

CRANFIELD INSTITUTE OF TECHNOLOGY

SCHOOL OF AUTOMOTIVE STUDIES

Ph.D Thesis

Dušan Kecman

BENDING COLLAPSE OF RECTANGULAR SECTION TUBES
IN RELATION TO THE BUS ROLL OVER PROBLEM

Supervisor: G. H. Tidbury

February 1979

ACKNOWLEDGEMENTS

I would like to express my sincere thanks to all those in authority in the School of Automotive Studies who enabled me to undertake this work and to the Department of Transport for funding the project. I am also very grateful to the British Scholarship Trust for Yugoslavs and Republički Sekretarijat za Obrazovanje i Nauku SR Srbije for providing a part of my first year grant. The British coach manufacturers Walter Alexander & Co., Duple Coachbuilders Ltd. and Plaxtons (Scarborough) Ltd. have provided much information and the test specimens. Their invaluable collaboration is also gratefully acknowledged.

My special thanks to my supervisor, Mr. G. H. Tidbury, for many useful discussions, help and comradeship from the time when we first met.

Investigation of the bus roll over accidents was carried out by the following members of the Structural Design Group: R. N. Hardy, J. C. Miles, D. Kecman, C. J. Knight, M. M. Sadeghi and G. H. Tidbury. Permission to summarise the main conclusions in the second Chapter of the thesis is gratefully acknowledged.

The theoretical analysis of the complete bus body, reported in Chapter 3, represents a part of the project supervised by Mr. G. A. Wardill with whom I worked with great satisfaction. I am also grateful to Mr. S. P. Healy for his assistance in the data preparation for the finite element model.

Many thanks to the workshop and technical staff, and in particular to Mr. C. J. Knight for help with the experimental work.

My gratitude also extends to the staff of the Computer Centre, Aircraft Design, Materials and Photographic Departments for their assistance with computing, testing and technical preparation of the thesis.

My wife Nina and children have done their best to provide me with normal working conditions and I hope that we shall see more of each other now that the thesis is finally complete. I am also very grateful to my parents for the help they have given me.

The best looking drawings in the thesis were neatly traced by Mrs. J. Saunders and finally, but certainly not least, my sincere thanks to Mrs. S. Watts, whose typing of the thesis was simply excellent.

SUMMARY

The thesis is concerned with the theoretical determination of the overall and local effects on the collapse behaviour of bus structures in a roll over situation. The aim is to enable an early selection of structural components, so that the finished body can absorb enough energy and preserve sufficient strength to meet the roll over safety requirements.

Chapter 1 gives an introduction into the bus roll over problem, discusses the present safety legislation and reveals that there is very little information on the performance of buses in real accidents and that no collapse analysis of the complete structure or bending collapse of its details had been undertaken.

The investigation into 21 bus roll over accidents, summarised in Chapter 2, showed that structural safety relies on both the overall collapse modes and hinge properties. Theoretical determination of the overall collapse mechanism and maximum strength of a typical British coach is carried out in Chapter 3 using the CRASHD collapse program. Some peculiarities of the finite element modelling are demonstrated and the analysis indicates that the collapse mechanism can be controlled by careful selection of various structural components. Chapter 4 emphasises the importance of a better understanding of the hinge behaviour in vehicle structures.

Bending collapse of rectangular section tubes is investigated in Chapter 5 for hinge rotation angles up to 30-50 degrees. The analysis starts with determination of the maximum strength of sections which may buckle within elastic range. Repeatability of local collapse mechanisms enabled the definition of the appropriate theoretical model. Kinematic theorem of the limit analysis is then applied to derive the formula for the hinge moment-rotation curve. Particular attention is paid to the selection of the appropriate material properties. The agreement with experimental evidence (Chapter 6) was very good for the complete range of tubes tested. This range includes practically all the standard sections that are used in the general structural design.

The theory is used in Chapter 7 to optimise sections from the safety point of view and, in combination with the CRASHD program, to predict the collapse behaviour of beams, bus rings and complete structure entirely on the theoretical basis. Static and dynamic tests of bus rings gave good agreement with theory.

The practical aspects of the work have been emphasised throughout the thesis. Detailed explanation of all the major decisions has increased the volume of the text, but the author believes that this will prove useful for practicing engineers. People interested in essentials only are referred to Chapter 8 where all the most important conclusions are given.

CONTENTS

	Page
1. BUS ROLL OVER SAFETY AND THE ASSOCIATED ANALYTICAL PROBLEMS	1
1.1 INTRODUCTION	1
1.2 GENERAL CHARACTERISTICS OF THE VEHICLE COLLAPSE BEHAVIOUR	2
1.3 THE PRESENT STATE OF THE ROLL OVER SAFETY LEGISLATION	4
1.4 RESULTS OF RESEARCH INTO THE VARIOUS ASPECTS OF THE VEHICLE ROLL OVER PROBLEMS	5
1.4.1 Analysis of the General Structural Behaviour in a Roll Over Situation	6
1.4.2 Analysis of the Collapse of Structural Components	12
1.4.2.1 Stable Section Beams	12
1.4.2.2 Sections Which Buckle Before Plastic Deformation	14
1.4.2.3 Beam Collapse Analysis	15
1.5 CONTRIBUTION OF THE THESIS	19
2. GENERAL CHARACTERISTICS OF PSV STRUCTURAL PERFORMANCE IN ACTUAL ROLL OVER SITUATIONS	20
2.1 INTRODUCTION	20
2.2 ACCIDENT CAUSES AND TYPES	20
2.3 OVERALL COLLAPSE MODES OF PSV STRUCTURES	23
2.4 LOCAL FAILURES	29
2.5 OTHER EFFECTS ON THE DRIVER AND PASSENGERS' SAFETY	30
3. THEORETICAL DETERMINATION OF THE OVERALL COLLAPSE MODE OF A TYPICAL BRITISH COACH IN A ROLL OVER	36
3.1 INTRODUCTION	36
3.2 QUASI-STATIC ANALYSIS OF A DYNAMIC ROLL OVER PROBLEM	37
3.3 DEFINITION OF LOADING CONDITIONS FOR COLLAPSE ANALYSIS	38
3.4 IDEALISATION OF THE STRUCTURE	40
3.4.1 The Actual Structure	40
3.4.2 Justification of the Modelling Technique	41
3.4.3 The Elastic Model	44
3.4.4 Effect of Incomplete Rings on Load Distribution in the Elastic Model	46
3.4.5 The Model for Collapse Analysis	49
3.5 THEORETICAL COLLAPSE MECHANISM AND STRUCTURAL STRENGTH	57
4. BENDING COLLAPSE CHARACTERISTICS OF VEHICLE STRUCTURAL COMPONENTS	63
4.1 INTRODUCTION	63
4.2 STIFFNESS, STRENGTH AND ENERGY ABSORPTION PROPERTIES OF HINGES	63
5. BENDING COLLAPSE OF RECTANGULAR AND SQUARE SECTION TUBES	72
5.1 INTRODUCTION	72
5.2 THE MAXIMUM BENDING STRENGTH OF A RECTANGULAR SECTION TUBE	73

5.3	THE ACTUAL BENDING COLLAPSE MECHANISM	81
5.4	THE THEORETICAL BENDING COLLAPSE MECHANISM	89
5.5	THE THEORETICAL ENERGY ABSORBED IN THE HINGE	97
5.5.1	The Energy of Plastic Bending and Rolling	97
5.5.2	The Compression Flange	98
5.5.3	The Web	99
5.5.4	The Tension Flange	102
5.5.5	The Total Energy Absorbed	104
5.6	THE THEORETICAL VARIATION OF THE HINGE MOMENT	104
5.7	DETERMINATION OF MATERIAL PARAMETERS	105
5.7.1	Pure Bending of an Ideally Plastic Sheet	105
5.7.2	Effect of the Actual Material Properties	108
5.7.3	Effect of the Loading Conditions	112
5.7.4	Selection of the Material Parameters	113
6.	EXPERIMENTAL VERIFICATION OF THE THEORY	117
6.1	INTRODUCTION	117
6.2	THE TEST METHOD	117
6.3	DETERMINATION OF MATERIAL PROPERTIES	125
6.4	PRELIMINARY TESTS AND THEORY MODIFICATION	126
6.5	THE FINAL PROCEDURE TO CALCULATE THE THEORETICAL MOMENT-ROTATION CURVE	135
6.5.1	Input Data	135
6.5.2	The Maximum Bending Strength	136
6.5.3	Hinge Dimensions	137
6.5.4	The Basic Moment-Rotation Curve	138
6.5.5	The Modified Moment-Rotation Curve	141
6.6	COMPARISON BETWEEN THE THEORETICAL AND EXPERIMENTAL RESULTS FOR VARIOUS TUBULAR SECTIONS	143
6.6.1	Introductory Remarks	143
6.6.2	The Maximum Strength Prediction	172
6.6.3	Prediction of the Moment Variation and Energy Absorbed	175
6.6.4	A Comment on the Accuracy of the Theory Presented	175
7.	APPLICATION OF THE THEORY OF HINGE BEHAVIOUR	177
7.1	INTRODUCTION	177
7.2	OPTIMISATION OF SECTION DIMENSIONS FROM THE SAFETY POINT OF VIEW	177
7.3	COMBINATION OF THE THEORY OF HINGE BEHAVIOUR WITH THE PROGRAM CRASHD	181
7.4	THEORETICAL PREDICTION OF THE LOAD-DEFLECTION CURVES IN BEAM TESTS	185
7.5	THEORETICAL PREDICTION OF THE BUS RING COLLAPSE BEHAVIOUR	192
7.6	APPLICATION OF THE THEORY TO THE ROLL OVER ANALYSIS OF THE COMPLETE COACH	203
8.	CONCLUSIONS AND RECOMMENDATIONS FOR FURTHER WORK	207
8.1	CONCLUSIONS	207

8.1.1	Chapter 1	207
8.1.2	Chapter 2	208
8.1.3	Chapter 3	209
8.1.4	Chapter 4	211
8.1.5	Chapter 5	212
8.1.6	Chapter 6	214
8.1.7	Chapter 7	215
8.2	RECOMMENDATIONS FOR FURTHER WORK	217
9.	REFERENCES	220
10.	APPENDIX	226
10.1	THE FIRST MODEL OF THE HINGE COLLAPSE BEHAVIOUR	226
10.2	ENERGY OF ROLLING DEFORMATION IN TERMS OF THE THEORETICAL ROLLING RADIUS OF THE HINGE MECHANISM	228
10.3	THE STRESS-STRAIN CURVES OF THE MATERIAL	229
10.4	TABLE CONTAINING THE COMPARISON BETWEEN THE THEORETICAL AND EXPERIMENTAL RESULTS	235

NOTATION

The SI system of units has been used in the thesis. It is common, however, to use N/mm^2 rather than pascals (N/m^2) for stresses, so that it was more convenient to measure lengths in millimetres and use a factor of 1000 when calculating hinge moments (in Nm) and energies absorbed (in J).

a (mm)	= width of the compression flange;
a_e (mm)	= effective width of the compression flange;
b (mm)	= depth of the beam cross section;
d	= subscript indicating values under dynamic conditions;
E (N/mm^2)	= Young's modulus;
e (%)	= engineering strain;
F (N)	= force;
h (mm)	= length of the hinge;
M (Nm)	= moment of the hinge;
M_p (Nm)	= fully plastic moment of the beam;
M_{\max}, M_m (Nm)	= maximum moment of the hinge;
m_0 (Nm/m)	= fully plastic moment of a unit width of the section wall in pure bending;
m_p (Nm/m)	= effective fully plastic moment of a unit width of the section wall;
r (mm)	= rolling radius;
t (mm)	= wall thickness;
W (J)	= deformation energy along the yield lines of the hinge;
X, Y, Z (mm)	= global co-ordinates;
x, y, z (mm)	= local co-ordinates;
Y (N/mm^2)	= yield stress in uniaxial tension;
Δ	= symbol indicating a small, finite increment of a variable;
δ (mm)	= deflection;
ϵ (-)	= strain;
$\dot{\epsilon}$ (/sec)	= strain-rate;
ν (-)	= Poisson's coefficient;
π	= 3.141592...;
σ (N/mm^2)	= direct stress;
σ_{cr} (N/mm^2)	= buckling stress of the compressed flange;
σ_e (N/mm^2)	= edge stress of the compressed flange;
σ_0 (N/mm^2)	= nominal stress (with reference to the initial area of the specimen);

- σ_p (N/mm²) = nominal yield stress;
- σ_{pu} (N/mm²) = maximum nominal flow stress ("yield strength");
- σ_{ult} (N/mm²) = maximum average stress in the compression flange;
- τ (N/mm²) = shear stress;
- ρ (rad) = half of the angle of hinge rotation;
- θ (rad, °) = angle of hinge rotation (in radians when used in the formulae for the hinge moment and energy absorbed, but it was also shown in degrees for better understanding of diagrams);
- θ_J (rad, °) = angle of jamming of the hinge;
- θ_T (rad, °) = angle of hinge rotation at which transition between the original and modified moment-rotation curve is made;
- ÷ = division symbol is used to indicate the range of a variable, e.g. 10÷20 means "from 10 to 20".

Other symbols are also used occasionally, with the appropriate explanation. Notation of some references had to be changed to obtain consistent notation for the main quantities.

CHAPTER 1

BUS ROLL OVER SAFETY AND THE ASSOCIATED ANALYTICAL PROBLEMS

1.1 INTRODUCTION

Traffic safety has become a matter of a major public concern. It includes various aspects ranging from the adequate road construction, over the primary and secondary safety of motor vehicles, to very complex "human factors". Serious and often tragic consequences of traffic accidents have imposed a series of problems to be tackled by the related government institutions, research organisations and particularly by the motor industry. Accidents often happen in spite of the considerable achievements in the field of their prevention. It is very unlikely that human error, as a major cause of accidents, can be eliminated in the foreseeable future, so that research into vehicle secondary safety becomes very important.

The central objective of all secondary safety studies is the protection of human life. The second, but also extremely relevant task, is the reduction of injuries.

The vehicle body is the main factor in passive safety. It is no exaggeration to say that to design a body for safety means to design it for the situation when the user needs it most.

Roll overs are very dangerous accidents for public service vehicles (PSV). A large number of people are directly exposed to a severe structural deformation of the entire passenger compartment. The chance of passengers falling out of the vehicle is greatest in a roll over situation. These accidents are not rare either. Twenty one PSV roll overs in Britain have been investigated by the Structural Design Group of the School of Automotive Studies, C.I.T., since 1975 (1,2)*. The importance of the same type of PSV accidents has been recognised in other countries (3,4,5). The relevance of the problem is further proved by the decision of the British Government to sponsor an extensive investigation into various aspects of the PSV roll over problem.

Vehicle safety is also affected by more and more severe safety legislation. This confronts the manufacturers not only with a moral obligation to make their vehicle safer, but also with a possibility of having their products banned from the market.

The collapse of a vehicle structure in an accident is caused by loads which are substantially different in direction, intensity and place of application from the normal service loads. This means that extensive redesigning of current models may be required to meet some safety criteria. Destructive testing is, of course, the most reliable method to check the structural performance in a selected accident situation, or the effect of some design alterations. However, this is also a very expensive exercise, since the structure becomes useless after the experiment. The process may also be very time consuming if the new specimens are not readily available, which is often true in the prototype phase. The most important decisions in the development of a new body are made in the early stages of the design when most of the components may not be available

* Numbers in parentheses designate references at the end of thesis.

for testing. Later changes of the original proposal are very expensive and time consuming. All these facts justify the attempts to predict the collapse performance of vehicle structures theoretically. This would not only enable a better understanding of the collapse phenomenon, but also provide significant economic gains.

This thesis provides information on the behaviour of PSV structures in actual roll over accidents. It also proposes a method of the appropriate collapse analysis of a complete PSV structure. A very relevant factor in this analysis is the bending collapse of rectangular section tubes. A theoretical method of predicting the collapse behaviour of such components has also been developed and verified experimentally.

In this way, the thesis indicates the important effects on the PSV structural performance in a roll over situation and provides useful theoretical means of predicting this performance in the early stages of design.

1.2 GENERAL CHARACTERISTICS OF THE VEHICLE COLLAPSE BEHAVIOUR

A general accident for design purposes cannot be defined due to the random character of accident conditions. Some systematization is still possible by selecting certain characteristic types of accidents such as frontal, rear or side impact and roll over. A variety of events may still exist within each group, but the reduction of scope increases the chance to clearly define the problem, select an appropriate method of analysis and, perhaps, obtain satisfactory results.

Vehicle collapse at impact or roll over is a short lasting process, but it is still possible to distinguish several phases. Leaving the dynamic effects aside for the time being, the increase of the external load usually causes the following sequence of events:

1. The initial elastic deformations of the structure increase linearly until plastic deformations, buckling, tearing, fractures or other sources of non-linearity occur at some places. The stiffness of the structure decreases, but the internal loads find new paths through a statically highly redundant vehicle body.
2. Further increase of the external load produces similar effects on more and more components. Each local overloading causes a redistribution of internal loads through the elements whose load carrying capacity is still not fully exhausted. The areas of plastic deformation, local buckling or fracture are relatively small and have a role similar to the hinges of mechanisms. The critical state occurs when the number and distribution of these "hinges" becomes sufficient to convert the structure into a kinematically movable system - the collapse mechanism. At this moment the structure usually passes through the state of maximum resistance. Components in bus and some special vehicle bodies, truck and tractor cabs and in passenger compartments of cars work primarily in bending. The beam local failures are very similar to mechanism hinges in the sense that the relative rotation of the two elastically deformed segments of a collapsed beam takes place about a localised area of the plastically deformed, buckled or fractured material. In sheet metal structures without distinct closed section beam elements the hinges are created along the lines of sheet metal folding or rolling.

3. The largest deformations take place in the third phase. The external load usually starts dropping off. However, in some special cases, like door intrusion due to side impact, after initial stagnancy or drop in resistance tension may build up in the collapsed element thus producing a further increase of load. The extent and shape to which the structure eventually deforms depends on the amount of energy to be absorbed by deformation and on its energy absorbing capacity. Absorption of the total kinetic and potential energy of the vehicle before impact is shared among the structure, obstacle, ground, suspension, tyres, etc. Relative contribution of these depends on the crash kinematic and properties of each energy absorbing medium. The more energy is absorbed during the first impact the better the chance will be to stop the vehicle and prevent further crashes or rolling. It is therefore desirable to let the structure contribute to the energy absorption by permanent deformation, but without intruding into the survival space. A rigid structure would tend to roll further than a collapsible one.

The final state is reached after recovery of the elastic deformations.

Dynamic influence includes the inertia effects on the collapse mode and material behaviour under high strain rate conditions. The difference between the static and dynamic collapse behaviour of a structure varies depending on the type of structure, point and direction of load application, impact speed, barrier or impactor properties, etc.

Some changes in the collapse mode are possible during the course of an accident. Relative vehicle to barrier (or other vehicle) motion may cause a significant variation in the intensity, direction or point of application of the external load. Structural changes due to door opening, glass breaking, jamming of the initial collapse mechanism, etc., may also effect the structural performance in an accident situation. However, a "weak" mode has been established by the first collapse mechanism, and in most cases the structure will persist collapsing in the initial mode.

The list of the important phenomena is further extended by the interaction between the passengers and their own vehicle in an accident situation. Apart from the direct collision between the human body and various parts of the vehicle, the passengers may fall out or be subject to dangerous (head) retardations. The effect of retardation has not been fully investigated, but the acceptable levels generally decrease with increased duration.

Auxiliary safety devices, such as safety belts are designed to restrain the passengers in their seats and help to cushion the impact. Such devices are not the subject of this thesis, but it is important to point out that they can be effective only if a sufficient survival space has been preserved. This space should accommodate the necessary movement of passenger bodies without impacting or crushing their vital parts.

In some cases the structure may be subject to a static load after the accident. This situation is common in roll overs, if the vehicle remains on its roof. It is necessary to support the weight of the vehicle by an already deformed roof structure. The load carrying capacity of a deformed structure may therefore become an additional problem in the collapse analysis. This point is particularly important in thin walled structures which may lose much of their load carrying capacity during deformation.

Each of the problems mentioned is complex in itself, but it is still possible to define the major objectives of structural design for safety, including the three important factors - stiffness, strength, and energy absorption:

A vehicle structure in an accident situation should deform in a reasonably controllable manner and absorb a sufficient amount of energy without intruding into the survival space and without producing fatal retardations. In the case of a roll over, the deformed roof structure should also withstand the weight of the vehicle without collapsing into the survival space.

The amount of energy to be absorbed and the survival space should be specified for each particular vehicle type (cars, buses, tractors, etc.) and for each typical accident. Capability of a vehicle to meet the safety requirements will then depend on:

- a. the general collapse mode of the structure;
- b. the energy absorbing capacity of the deforming components;
- c. the load carrying capacity of a deformed structure in the case of a roll over accident.

1.3 THE PRESENT STATE OF THE ROLL OVER SAFETY LEGISLATION

The complexity of vehicle passive safety makes the definition of a target performance very difficult. The advent of vehicle safety legislation has not only drawn more attention to safety, but has also helped a lot to define the safety requirements that a vehicle should meet. The present legislation is still based on a limited knowledge of the collapse phenomenon. It is therefore arguable whether all regulations prescribe requirements leading to safer vehicles in a most direct manner. However, they certainly do encourage research and hence gather information which will serve as a basis for future improved legislation.

The most important European legislative codes affecting the design of vehicles on an international scale are the European Economic Community (E.E.C.) and the Economic Commission for Europe (E.C.E.) regulations. These two were somewhat preceded by the American Federal Motor Vehicle Safety Standards (F.M.V.S.S.) which are mandatory for all vehicles in or entering the U.S.A.

The regulation F.M.V.S.S. 571-216 applies to cars and requires that a car should withstand a static crush load applied obliquely via a platten to the top of the windshield pillar without exceeding 5 in deformation. The load depends on the weight of the unladen vehicle. The platten is long enough to contact the top of the B pillar as the deformation progresses.

Some types of the agricultural tractors have roll over protective structures which are affected by the F.M.V.S.S. 1928, SAE J-395, and SAE J-1040. The prime requirement is to absorb a specified amount of energy without exceeding prescribed deflection limits. Tests are both static and dynamic. Proposal 18 of E.E.C. regulations also requires that the structure should withstand a sequence of pendulum impact and static crush tests.

E.E.C. regulation 29 applies to the cabs of commercial vehicles and specifies a vertical static crush load on the roof. There are some other specifications for commercial, or special purpose vehicles, which are not internationally approved. The Swedish test for commercial vehicle cabs specifies an impact load to the A pillar and a vertical static load on the roof. A requirement of twice the front axle load applied obliquely to the top of the A pillar of a fire-fighting vehicle was applied to the design of a new safety vehicle in Britain.

The area of PSV roll over legislation is most interesting for this thesis. Two regulations are currently in force: E.C.E. regulation 36/5.4 and the American S.B.B.M.A. School bus test qualification.

The E.C.E. requirement states that "It must be shown by calculation or by any other suitable method that the structure of the vehicle is strong enough to withstand an evenly distributed static load on the roof equal to the technical maximum weight of the vehicle up to a maximum of 10 tons". The American document also specifies a vertical static crush load applied via a rigid flat plate to the roof. Deflections must not exceed a specified maximum and the emergency exits should be operative during the course of and subsequent to the test.

Both regulations, in their present formulation, fail to take into account the two most significant effects on PSV roll over safety. Investigation into roll over accidents in Britain (1,2) has clearly indicated that the lateral component of the external load is far more dangerous than the vertical one. In only three out of twenty one cases observed so far was the lateral component of the load insignificant, implying that the vehicle rolled while the cant rail was either off the ground or subject to a small force before the vehicle landed "flat" on its roof. The lozenging mode of collapse which will be discussed in more detail in Chapter 2, and even simple portal frame calculations prove the priority of loads to which the structure should be tested.

The second arguable item is the maximum load requirement. It is possible to produce a structure with a load carrying capacity which may be high initially, but which would also drop off abruptly after collapse is initiated. Good examples are very thin walled structures or those in which brittle fractures occur. It is also possible to design a bus which would not deform permanently during roll over. However, weight penalty may be unnecessarily high and the tendency to roll further will be much greater than in collapsible bodies. The energy absorption requirement represents a more complex design task, but it allows for the need to preserve structural strength and arrest further rolling of the vehicle.

1.4 RESULTS OF RESEARCH INTO THE VARIOUS ASPECTS OF THE VEHICLE ROLL OVER PROBLEMS

In the light of the previous discussion it is convenient to organise the survey of the work relevant to PSV roll over into the following two groups:

1. Analysis of the general structural behaviour in a roll over situation.
2. Analysis of the collapse of structural components.

1.4.1 Analysis of the General Structural Behaviour in a Roll Over Situation

It is interesting to note that the first crash testing of vehicles involved the roll over of cars in 1933 (6,7). The roll was accomplished by driving a car onto a spiral ramp or into a skid on a sod field, or pushing the vehicle off a steep cliff. Later tests ensured an improved repeatability by using specially designed car roll over simulators. The first tests were monitored merely by observation and filming and the amount of information was later extended by applying a wider range of instrumentation - load cells, accelerometers, dummies, etc.

It appears that the first attempts to assess the roll over performance of a vehicle structure by calculation were made in the field of earth moving machines, agricultural tractors and other similar special purpose vehicles. Roll over protective (ROPS) or the falling objects protective (FOPS) structures of these vehicles are relatively simple and made of sturdy components so that they lend themselves to the application of the classical plastic analysis.

The engineering basics of ROPS illustrated with the full size and model tests of an earth moving machine were reported by Klose (8). This paper may serve as a good introduction into the field of roll over safety problems. The matrix method of elastic analysis was employed, but did not generally produce a good agreement with the collapse test data. This was attributed to the effects which seem to be more important for elastic than plastic analysis, but the results do point out the inadequacy of the purely elastic approach to the collapse problems.

A comparative study of the energy absorption of tractor cabs when rolling into ditches of various depths and under pendulum test conditions was reported by Steinbruegge (9). The more the structure deflects during roll into a ditch, the more potential energy has to be absorbed due to lowering of the centre of gravity. On the other hand, rotation and lifting of the pendulum during test reduces the energy input for larger ROPS deflections. This observation is correct, but it is still possible to ensure a good energy correlation between the laboratory and field test if the allowed deflection is specified. The cabs absorbed up to 42% of the total roll over energy, the rest being taken by the soil and tyres.

A simple plastic analysis of a portal frame was suggested by Macarus (10) to guide the designers in sizing the ROPS to meet the SAE J-395 regulation. Local buckling of relatively thin walled rectangular section tubes was noted and it was "felt that local buckling reduces the energy capacity and confidence level of the frame". A closer insight into the actual SAE testing procedure of ROPS and FOPS in tractors was reported by Wetjen (11).

A design procedure based on the simple plastic analysis, but allowing for the elevation of the material yield stress due to impact loading was described by Ashburner (12). This elevation was of the order of 20% for impact velocities between 2.7 and 4.44 m/s. Scale models were tested and recommended to provide a cheap and more accurate prediction for more complex frameworks. Model testing of ROPS was also considered by Srivastava et al (13) and compared with full scale experiments. It was concluded that this approach can be utilised to evaluate new designs

of ROPS and to study accident behaviour.

The experimental load-deflection curves for ROPS were approximated by a mathematical function and used in the analysis of roll over dynamics by Cobb (14). Soil properties were also allowed for and the limits of the load carrying capacity of the ground established. Since the allowable deflections of the ROPS are specified, the result is that the energy that can be absorbed by the structure is also limited whatever the mass of the tractor is.

Development of sophisticated finite element programs for the large displacement, non linear and collapse analysis has offered substantially new possibilities in the theoretical analysis of the ROPS. Yeh et al (15) have described the application of an elastic-plastic non-linear program to the space ROPS. An incremental elastic analysis is combined with the von Mises yield criterion for an elastic-ideally plastic material to introduce plastic hinges wherever the local loads exceed the plastic limit. The geometry of the structure and its stiffness matrix are updated after each increment to allow for the non-linear effects. The program calculates automatically the energy absorbed by the structure and plots the collapse mode. The agreement with the static test data was good. The program does not take into account either Euler or local buckling, section weakening with the hinge rotation, or any dynamic effects. A very similar program (SAGS) which allows for strain hardening effects in stable section beams was described by Pistler (16) and its application to a tractor ROPS was reported by Easter (17). Deflections of the deformed structure were fairly small with hinge rotations less than 10° . The theory predicted the peak load of the ROPS very well.

The application of the recently developed finite element techniques has been published in numerous references. Extensive lists and original contributions can be found in refs 9 and 10. Thompson (18) and Saczalski et al (19) have developed complex programs allowing for the inertia and strain rate effects. These techniques are particularly useful in cases where the impulsive loading produces collapse modes different from those in static conditions. The methods gave good agreement with experiments performed on simple structures. Although both achievements are theoretically advanced, it is believed that the PSV roll over problem can be tackled using a simpler and more economic approach. The above references do not include the moment drop off at the hinge, which is a significant factor in the collapse analysis of thin walled structures.

Kirioka et al (20) have developed a program very similar to (15) but they also include the geometric stiffness matrices (21) to allow for the effects of the axial loads on the stiffness and stability of the structural components. The method was used to determine the collapse load of a car structure subject to the seat belt forces. The mathematical model consisted of beam elements and a good agreement with experiment was obtained.

Kajio et al (22) have also produced a similar collapse program, with the beam stiffness matrices consisting of the linear, geometric and the initial displacement matrix. It is admitted, however, that the first two matrices cover most practical problems quite sufficiently. The program was used to predict the maximum load carrying capacity of a car roof subject to the F.M.V.S.S. Roof Crush test. The agreement with experimental data was good up to the point where the pillars buckled locally. It was not possible to allow for the drop in resistance and

the shifting of the load from the A to B pillar was not included. The same effects and a new form of local deformation were observed in the seat anchorage loading. The dynamic analysis of the roof crush was performed and the yield stress of the material was rather arbitrarily increased to allow for the strain rate effects.

Investigation into the collapse behaviour of vehicle structures, carried out in the School of Automotive Studies, C.I.T., has been broadly aimed at a hybrid approach combining development of the computer program for the analysis of a complete structure with theoretical and experimental study of the collapse of structural components. One of the current results of this research is the non-linear matrix analysis computer program, named CRASHD (Cranfield Structural High Displacement), developed by Miles (23) on the basis of a three dimensional, beam element, elastic program written by Wardill (24). The program will be mentioned again later in the thesis, but suffice it to say now that it can deal with material and geometric sources of non-linearity. It includes the linear and geometric stiffness matrices and employs the incremental increase of loads or displacements in a similar manner to the programs described above. The option that is very important when dealing with thin walled beams is the capability to handle a variety of relations between the moment and the appropriate hinge rotation (constant or decreasing moment and also the "brittle fracture" in bending). The hinge behaviour of a particular structural component is experimentally determined and the moment/hinge rotation curve approximated by an exponential function. These data are then used in the program to analyse the static or quasi-static behaviour of a complete structure composed of beam elements.

Apart from the general description and application to simple structures (25) the program has been used to analyse two more complex systems. The author of this thesis has taken an active part in both projects. The first one (26) concerned the collapse analysis and design of a fire engine safety cab which had to pass stringent roof crush, (maximum load within specified deformation), frontal oblique impact and door intrusion tests. After a preliminary elastic analysis the simplified models for the roof crush and frontal impact were established. The cab was built of very stable section tubes so that no significant decrease in hinge moments could take place before the structure reached its maximum roof crushing resistance. The first test of the prototype cab showed a very good agreement with the predicted collapse mode and maximum load which was only about 20% higher than the test requirement. The frontal impact was mainly an energy absorption problem and the results were obtained by combining the program with the information in Ref 74. A possibility to extend the deformation beyond the maximum resistance point was particularly useful. A very good agreement with experiment was achieved in the first test. Very good agreement was also obtained in the case of door intrusion, which was tackled by applying the data from Ref 67.

The second project (27) concerned the analytical check on whether a new prestige car would meet the F.M.V.S.S. roof crush and door intrusion tests. It was necessary in both cases to estimate the load carrying capacity of the structure within prescribed limits of deformation. The roof crush analysis indicated that the front half of the roof will collapse first, but then the loads would be transferred mainly to the top of the B pillar. The calculation was carried out in two stages,

allowing for the reduced strength of the rear structure after the front one collapsed. The results were not checked experimentally, but they look very reasonable and agree qualitatively with test data of another car. The door intrusion analysis also produced a very realistic character of the collapse mode and load, but the structure has not yet been tested. Particular attention was paid to the adequate design of joints and some other highly stressed details.

The Bus Roll Over Investigations

The investigation into the PSV roll over safety is still rather limited and confined to a few sources of information. The earliest record concerns the already mentioned American School Bus test described in the reports by Rumph (28) and Severy et al (29). Later report by Adams et al (4) on the development of a unitized school bus includes a chapter on roll over safety. The design requirements were that the roof should withstand the vertical distributed load of 1.5 times the gross vehicle weight, and also 6 times the gross vehicle weight applied at 45° to a limited portion of one cant rail. No explanation was given for the selection of those load factors and loading conditions. An elastic finite element analysis was performed for the two loading cases. The model for the vertical load consisted of beam elements and included five bays supported at four points. The first diagonal loading model included three bays, with the load applied to the middle ring only. This analysis indicated the load diffusion through the roof panels to the adjacent rings. The second model was composed of a middle ring simulating a 3 bow segment and two bays on either side of the middle ring. The roof structure included the diagonal tension "cables" to simulate the shear effects in panels. The load was applied to the middle ring only, as required by specification. The body was supported on five supports one of which was diagonally opposite from the loading area and carrying mainly the diagonal load. The calculated stress states were then compared with the load carrying capacity of the structural components, and the appropriate "section safety factors" estimated. This implies that the structure should not collapse in a standard roll over test.

The test was done on the front half of the body by applying a static oblique load to the cant rail over the length limited by the three rings. Diagonal tension fields have developed in the roof skin transferring the load to the rest of the body. Localised tension failures occurred during the test.

The approach in this thesis is much different from the American method. Their loading conditions are not representative for the roll overs that took place in Britain. The loaded portion of the structure is greatly assisted by the rest, which does not happen if the whole roof is pushed sideways. The resulting structure is grossly overdesigned (twelve 76 x 76 x 3 mm pillars) and is not supposed to deform. Such a vehicle would tend to roll further than if some kinetic energy were absorbed by an allowable structural deformation. The analysis is virtually elastic.

The other bus safety investigation coming from U.S.A. is the frontal impact test reported briefly by Lundstrom et al (30).

A bus roll over test in U.S.S.R. was reported by Ryabichinski et al (5). Particular attention was paid to survival space, prevention of passengers falling

out, acceleration levels and fire safety. Nineteen dummies fastened with safety belts and three unfastened dummies were placed in the test vehicle. The vehicle with a running engine was rolled down a slope at 33°, so that it completed 4.5 revolutions about the longitudinal axis. Such a test is too severe, but the results are interesting. No appreciable deformation of the body took place during the first three revolutions(!). Six fastened and one unfastened dummy were ejected through the window apertures and crushed during the second and third revolution. One of the restrained dummies fell out through one window, and came in through the other, whipping the safety belts around the window pillar. The fourth revolution forced the front part of the roof down to the lower edge of the windshield aperture, but it subsequently sprung back to approximately half of its original height. The loosening mode of roof collapse was observed with lateral deformations ranging between 275 and 660mm. Fractures of welded joints occurred at several places. The maximum accelerations recorded at the top of one pillar and at the floor level were: in the lateral direction 6g and 5g respectively, in the vertical direction 6g and 7g and 3.5g and 5g longitudinally. No comment was made on the duration of these maximum values. The vehicle did not catch fire, but some fuel leakage at the filler cap was recorded. The importance of retaining passengers within the bus during roll over was emphasised, and a somewhat exaggerated survival space (900-950mm above the top of the seat backs) suggested.

Hungarian research into the bus safety has been reported by Voith (31,32) and Matolcsy (3,33). Various structures and models were tested in the vertical and oblique loading conditions and some buses were actually rolled down the two different slopes, both allowing at least 360° rotation about the longitudinal axis. The energies (W_i) to be absorbed by the structure during the first ($i=1$) and second ($i=2$) cant rail impact were estimated taking into account the kinetic energy of the vehicle before and after impact, energy absorbed by the soil and the energy stored in the vehicle suspension. The formula derived for a "standard" slope at 33° to the horizontal was:

$$W_i = \alpha_i \cdot G - \beta_i \cdot F_{i,max} + \gamma_i, \quad i = 1,2 \quad (1.1)$$

where: G = total weight of the vehicle;
 α_i, β_i and γ_i = constants depending on the bus type and whether the passengers are wearing seat belts;
 $F_{i,max}$ = maximum force applied to the cant rail during roll over, limited by the strength of the structure.

Two substantial reinforcing rings situated in the front and rear were suggested as the most efficient means of producing an adequate passenger protection.

The theoretical analysis was limited to a predetermined collapse mode with hinges at the waist rail and cant rail, which seems to be the only collapse mode taking place in their buses.

A static or pendulum test device (Fig. 1.1a) is suggested for laboratory testing. The loads are applied at 45° to the floor beam and the tests are designed to produce the above energy inputs followed by oblique static loads which the structure should withstand without collapsing into

the prescribed survival space (Fig. 1.1.b). The test should simulate a roll over down an embankment where the bus rolls on its roof and further. This appears to be the most frequent type of PSV roll over accident (37%) registered in Hungary. Other cases involved rolling on the side only (31%), on the roof on level ground or from a small height (21%) and fall from an "overcrossing" (11%).

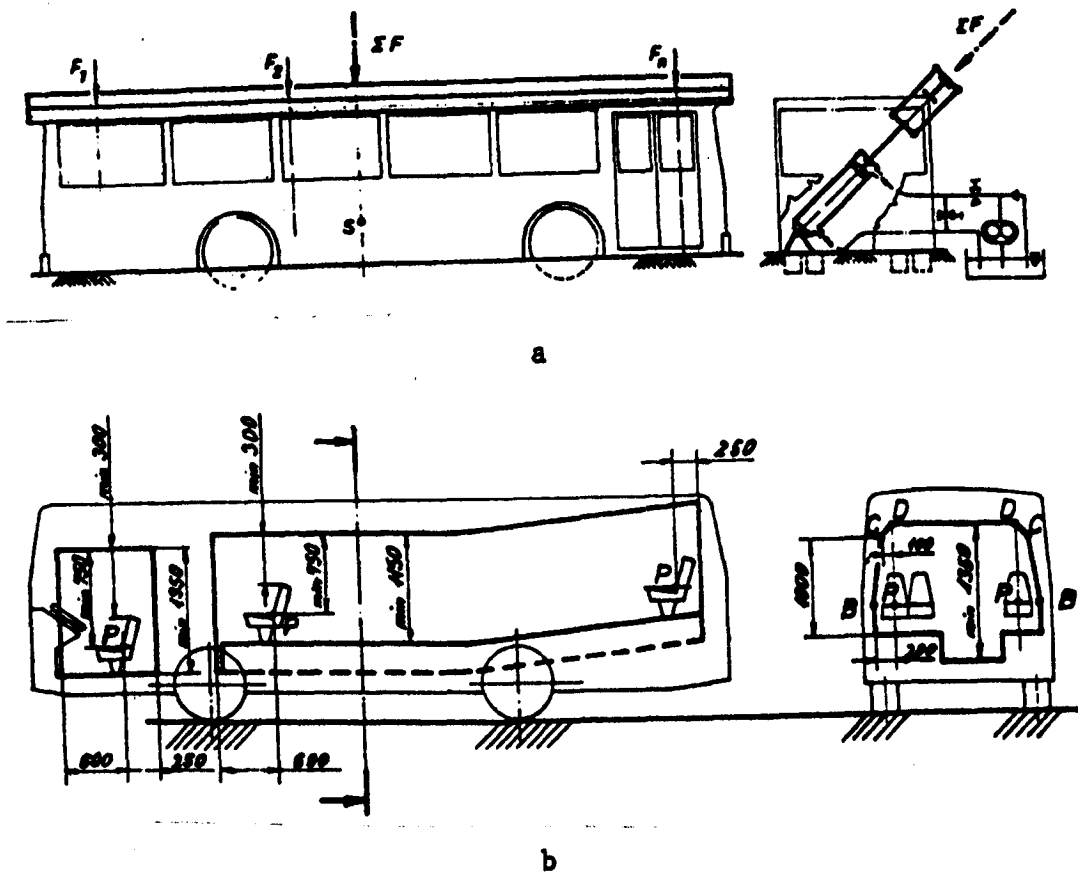


Fig. 1.1 (Ref. 32)

The first British results of the experimental and analytical treatment of the PSV roof strength were reported by McHugh and Tidbury (34). The later investigation carried out in the School of Automotive Studies (1, 2,35-38) included on-the-spot accident investigation, theoretical study of the roll over kinematics and the energy to be absorbed by the structure, testing of bus rings and models, analytical prediction of the ring and complete structure behaviour in a roll over situation and energy absorbing properties of hinges produced by bending collapse of rectangular section tubes.

Roll over dynamics were studied using a two-dimensional rigid body theoretical model (1,23) rolling on a level or inclined rigid surface. The energy and angular momentum conservation was employed to obtain the kinematics and energies to be absorbed by the structure. The program gives a graphical output. Work is in hand to improve the model by introducing a deformable structure.

Model testing (37,38) did not produce satisfactory information in the initial stages, so it was temporarily discontinued.

Analytical prediction of the bus ring behaviour under test conditions was performed using the already mentioned CRASHD program (23,36). The experimental moment/hinge rotation curves of the ring components were fed into the computer to obtain the collapse mode and a load/deflection curve of the complete ring.

Other results of the Cranfield research are discussed in detail in this thesis.

1.4.2. Analysis of the Collapse of Structural Components

The relatively recent development of plastic and impact analysis has drawn considerable attention to the load carrying capacity of structural components. The fundamentals, later work and extensive reference lists in both fields can be found in the standard textbooks (39-47). The amount of published work is great and only those references which are closely related to this thesis are discussed below.

It is possible to classify the relevant references into three groups according to the specific problems:

- A. determination of the fully plastic state in stable section beams;
- B. determination of the maximum load carrying capacity in beams where section buckling precedes the collapse. Some form of kinematics of the section deformation being established, this makes an important difference from group "A";
- C. determination of the beam behaviour after collapse has been initiated; this will be referred to as "the beam collapse analysis".

Each of these groups may include both static and dynamic problems. Most of the available information falls into the group "A", some into section "B" and the third selection of problems is still in its early stages of development. The main concern of structural engineers was to prevent collapse rather than analyse how it progresses. Design of energy absorbing devices has introduced the necessity of analysing the collapse behaviour as well.

1.4.2.1 Stable Section Beams

The partly or fully plastic stress state in beams subject to combined bending and twisting loads has been studied by several authors (48-54). Hill and Siebel (48) have applied the Reuss stress-strain relations (39) to find the combinations of moment and torque which render the circular, thin walled but stable steel tube fully plastic. Reuss relations assume that any infinitesimal increment of strain is a combination of the elastic part given by ordinary elastic equations and the plastic part to which Levy-Mises yield equations apply. The same authors have applied the variational principle (49) to find the upper and lower bounds of the fully plastic state in solid circular bars. The lower bound refers to the condition that the rate of work of external forces expressed in terms of direct and shear stresses is less or equal to the rate of work performed by the actual external forces. The upper bound is obtained

by putting the rate of work of the actual external forces less or equal to the rate of work derived from a fictitious velocity distribution (39) with the section warping function zero. The Reuss equations were tested (50) under conditions where the plastic and elastic components are comparable and where the strains are not uniformly distributed. Experiments were performed by simultaneous bending and twisting of thin, but stable cylinders. The theory predicted very good results in terms of deformations and definition of the fully plastic state. In the second case (51) the specimens were circular section solid bars, and the agreement with experimental data was again very good.

The effect of a combination of moments and torques on the fully plastic state in a square, solid section beam was studied by Steele (52). The material was considered rigid-ideally plastic, obeying the Levy-Mises yield criterion. The partial differential equation due to Handelman and Hill was derived first by maximising the rate of work done by external forces in terms of the direct and shear stresses. The equation was solved numerically for the two values of ratios between the rate of twist and curvature. The results agreed well with the bounded solutions proposed in (49). Similar bounded solutions for rectangular, I and box sections in bending and torsion were reported by Gaydon and Nuttal (53), and for solid circular, square and triangular sections by Imegwu (54). The interesting conclusion was that the relationship between the ratios M/M_0 and T/T_0 (M and T are the combined moment and torque producing the fully plastic state and M_0 and T_0 are the values which give the full plasticity when acting alone) is almost independent of the shape of the cross-section.

Plastic yielding of I section beams subject to bending and shear was considered by Green and Hundy (55). Model I beams made of mild steel were tested and yielding and deformations investigated. Comparison of experiments with several design formulae showed that the formulae suggested by Heyman and Dutton (56) were most suitable. Radomski and White (57) have shown that in elastic-perfectly plastic material short plastic zones may develop large strains even though the deflection corresponding to the first yield is not greatly exceeded. Strain hardening of the material reduces this strain concentration, but it may cause fractures soon after the yielding has started. Rectangular solid sections only were considered and the sections were assumed to remain plane.

Theoretical and experimental investigation into the elastic-plastic behaviour of I and channel sections subject to bending and torsion with restrained warping was reported by Strel'bickaya and Yevsenko (58). Vlasov's theory of thin walled beams was combined with the Mises yield criterion of an elastic ideally plastic material. Combined effect of biaxial bending and axial force in stable rectangular and I section beams was analysed by Santathadaporn and Chen (59). Variational principle (49) was applied and the effect of warping included.

Morris and Fenves (60) have derived the approximate lower bound yield surface equations for stable I, rectangular and circular tubes, subject to any combination of external loads. Material was rigid-plastic, the shape factor of the section = 1 (abrupt transition from elastic into fully plastic state), von Mises yield criterion was applied and no increase in the fully plastic torque due to warping restraints was assumed. The yield surfaces were expressed in terms of ratios between

the axial force, torque and the two bending moments and their respective "pure" fully plastic values. An iterative procedure for calculating a load factor for any combination of external loads is described. A similar analysis of rectangular tubes was presented by Shakir-Khalil and Tadros (61). The problem was investigated by analysing the possible position of the neutral axis and the effect of torque was allowed for by assuming that the shear stress is equally distributed and proportional to the one in the fully plastic shearing. Von Mises yield criterion is then applied to define the appropriate reduction factor of the maximum bending moment. The theory gave good agreement with experiments, which were also reported in ref. 62.

Dynamic load carrying capacity of stable section members may vary within broad limits depending mainly on the inertia properties of the impacted structure, loading direction and rate and material properties with respect to strain rate effects. The work published so far deals mainly with simple, solid section beams or structures and the following main assumptions are widely accepted:

- bending stresses only are considered;
- material is rigid-perfectly plastic, and the strain rate effects are being included indirectly, by appropriate factors;
- local deformations at the point of impact are neglected.

An excellent review of the published work can be found in the books by Goldsmith (46) and Johnson (47). However, since the problem dealt with in this work lends itself to a quasi-static method of analysis, the papers considering the dynamic effects in the group "A" will not be considered.

1.4.2.2 Sections Which Buckle Before Plastic Deformation

Rectangular section tubes with sufficiently small ratio between the thickness and width of the compression flange may buckle locally before the full plasticity of the section takes place. Determination of the maximum moment carrying capacity of such elements is of great importance in vehicle design for safety. Many basic structural elements of vehicle bodies are made as thin walled tubes which buckle within elastic range.

The British Standard B.S. 499:1959 and the American Iron and Steel Institute (AISI) manual use the concept of the effective width (a_e) of the compressed plate which is uniformly stressed by the edge stress σ_e . The AISI formula is based on the work by Winter (63), and the 1970 version is:

$$a_e = 1.9t \sqrt{\frac{E}{\sigma_e}} \left[1 - 0.415 \frac{t}{a} \sqrt{\frac{E}{\sigma_e}} \right] ; \left(\frac{a}{t} \geq 0.95 \sqrt{\frac{E}{\sigma_e}} \right) \quad (1.2)$$

where t and a are the thickness and width of the compressed flange of a lipped channel in pure bending, and E is the modulus of elasticity. This equation is similar to the one obtained by von Karman et al (64) for a simply supported flat plate. The effective width specified by B.S. 499

is based on the expression

$$\left(\frac{a_e}{t} \right)_{ult} = 0.66 \left(\frac{\sigma_{cr}}{\sigma_p} \right)^{1/3} \quad (1.3)$$

where σ_{cr} and σ_p are the theoretical flat plate buckling stress and the yield stress respectively. The last formula was derived by Chilver (65) to fit the lower scatter bound of results from some 200 tests on short length concentrically loaded steel struts of various sections and yield stress. It overcomes the trial and error method required by (1.2).

Rhodes (66) has investigated the problem of the load carrying capacity and deflections of a lipped channel section subject to pure moment. The design aspects of this work were summarised in (67). The beam was treated as a system of plates joined along the common edges and loaded by an axial stress system. Dawson and Walker (68) have developed a similar procedure to ref. 67, but assumed that the compression flange has an initial geometric imperfection and that the side plates do not buckle. Both of these references are considered in more detail in section 5.2.

1.4.2.3 Beam Collapse Analysis

The author has not been able to find a single paper dealing with the theoretical analysis of the bending collapse behaviour of beams. All the theoretical work published concerns the collapse of various elements in axial or lateral compression. However, these results have some relevance for this thesis and will be briefly reviewed below. Information will also be given on some experimental investigation into the collapse behaviour of beams in bending.

Tubes in axial compression

Large scale collapse of very thin walled cylindrical columns was analysed by Pugsley and Macaulay (69). A diamond pattern of deformation of the walls was observed and modelled by a mechanism consisting of bending and shearing plastic deformations. The average axial force was experimentally determined by calculating the area under the characteristically "wavy" force-deflection curve produced by subsequent diamond-shape buckles. The calculated results underestimated the actual value of the average force by approx 40%. It is difficult now to comment on these results, but it appears that the shear deformation was over-estimated, while rolling deformation was not included, and strain hardening was also disregarded.

The same problem was tackled by Alexander (70). Two collapse modes were observed: symmetrical convolutions (bellows) and the other where both "transverse and longitudinal waves have formed". The second mode was considered too complicated and the first one was used as the analytical model. Two extreme cases were considered and averaged, and the test results agreed well with the theoretical values. However, the yield stress of the material was calculated to fit the experimental average force, and was not measured independently.

Static and dynamic axial compression of closed top-hat sections was studied by Ohkubo et al (71). Bending and a constant radius rolling deformation were included into the collapse mechanism. The agreement with experimental results was good after a significant constant in the average force equation was experimentally determined. A simple linear empirical function in terms of the impact velocity was derived to calculate the ratio between the dynamic and static mean resistance to compression.

Static axial crushing of very thin walled ($a/t > 300$) square box sections was analysed by Rawlings and Shapland (72). Bending deformation only was observed and the contribution of local kinks at corners to the energy absorbing process was significant. The theoretical model predicted approximately 80% of the actual compressive load, and the analysis was limited to shortening of less than 10% of the original length. Johnson et al (73) have recently published results of the analysis of a rectangular tube in compression. Several possible collapse modes of circular and rectangular tubes have been studied and the appropriate mean collapse loads calculated. Tests on circular tubes have indicated the existence of "travelling hinges" which resemble a form of a rolling deformation. Inextensibility of the mean surfaces of plates was assumed and confirmed as reasonable. A constant rolling radius was assumed and derived from the condition of the minimum mean axial load. The agreement with experimental results was reasonable.

Wimmer (74) has studied the effect of loading rate on the strength and deformation behaviour of rectangular section tubes used in vehicle bodies. His results indicate that higher loading rates and a multi-axial stress state not only increase the effective yield stress of the material, but also raise the tendency to brittle fracture. The ultimate strength of material remains almost unaffected. The average resistance of the tube was derived neglecting the rolling deformation (this was corrected in (75)), but useful experimental diagrams giving the average axial force in terms of impact speed were produced. Wierzbicki and Akerström (75) have also studied the static and dynamic axial crushing of rectangular tubes. The idealised deformation mechanism consisted of bending and rolling deformation and a simple formula was derived for the mean crushing load. The rolling radius was considered constant and determined experimentally. A strain rate correction factor was derived theoretically by considering the segments of the collapse mechanism as dynamically loaded visco-plastic cantilevers. In one special case good agreement with results by Wimmer was obtained.

Newman and Rawlings (76) have tested thin circular tubes in static and dynamic conditions. Boundary conditions had an important effect on the peak static load, but a very small one on the mean crushing load particularly with larger deformations. Dynamic tests were conducted with different structural and mass arrangements and significant scatter of results was observed both within limits of one set of results and between different sets. Further research was strongly recommended before a more general analytical treatment of collapse of more complex structural systems becomes possible.

Correlation between the static and dynamic energy absorbing capacity of rectangular tubes in compression was experimentally analysed by Molnar (77).

Dynamic tests were carried out with three different weights and three impact speeds (the maximum being 4.5 m/sec). The energy absorbed over the same shortening of the tube was always greater in dynamic conditions and the increase ranged from 50% at smaller deflections to 20% when the length was only 35% of the original one.

An analysis of the collapse behaviour of an axially loaded simply supported plate was reported by Davies et al (78). A rigid-plastic analysis of the idealised mechanism was carried out and the Tresca's yield criterion was applied to the plastic zones. The mechanism was such that the shearing forces had to be included into the yield criterion for the "inclined" yield lines. The theoretical and experimental unloading curve was shown which offers some possibility of estimating the load-shedding characteristics of inter-related elements of a composite structure.

Johnson et al (79) considered experimentally orthogonal layers of aluminium and mild steel tubes under lateral compression. Two collapse modes were observed: one where tubes flatten uniformly along their lengths and the other where reversing ovality precedes the flattening. The specific absorbing capacity of both modes was close one to another.

Bending collapse of tubular sections

The gradual decrease of resistance associated with the rotation of hinges in tubular section beams has been tested recently by several authors (25, 80, 3). However, this problem has not been the main subject of interest and the experimentally established moment/hinge rotation relationship was approximated by a mathematical curve.

Miles (25) has investigated the possibilities of the analytical determination of the collapse load and energy absorbing properties of thin walled beam structures using matrix methods of analysis. The beams were tested in bending and the theoretical curve was approximated by an exponential equation:

$$M = A + B.e^{-c\theta} \quad (1.4)$$

- where
- A = the moment value which is stabilised at larger values of the angle of the hinge rotation;
 - B = the difference between the maximum moment and the quantity A;
 - c = empirical constant;
 - θ = the angle of hinge rotation;
 - e = basis of the natural logarithm.

The above formula is then used to determine the current values of the fictitious springs attached to the collapsed ends of beam elements in the finite element model. The formula applies to the collapse state only, while the elastic deformations are allowed for separately in the preceding elastic calculations.

McIvor et al (80, 81) introduce an interesting method of the collapse analysis of beam structures in which the component resistance drops-off after collapse has been initiated. The behaviour of the hinge is determined

by a scalar generalised yield function:

$$f(\xi) = 1$$

where $\xi_j = \frac{Y_j}{\alpha_j}$, $j = 1, 2, 3, 4$

in which the elements Y_j denote the current values of the axial force, bending moments about the principal axes and torque respectively. The components of ξ are the normalised stress resultants in local beam co-ordinates. The scaling parameters α_j are considered as properties of the hinge whose values depend on the history of plastic deformation. In particular:

$$\alpha_j = \alpha_j(\theta_j), \quad j = 1, 2, 3, 4$$

where θ_j denote the accumulated plastic deformation in extension, biaxial bending and torsion respectively. The experimental elastic-plastic moment/hinge rotation curve is used to produce the appropriate variation of α_j , which is then approximated by:

$$\alpha = M \{ a_i + b_i [1 + k_i (\theta - \theta_m)] \cdot e^{-k_i(\theta - \theta_m)} \} \quad (1.5)$$

where M is the maximum elastic moment, θ is the total plastic rotation, and θ_m corresponds to the maximum value of α . For $\theta < \theta_m$, $i = 1$ and

$$a_1 = (1 - f \cdot y) / (1 - y)$$

$$b_1 = (f - 1) / (1 - y)$$

$$y = (1 - k_1 \theta_m) e^{k_1 \theta_m}$$

In the collapse stage $\theta > \theta_m$, $i = 2$ and

$$a_2 = \beta, \quad b_2 = f - \beta$$

where f is the ratio of the maximum value of α to M , β is the ratio of the asymptotic value of α for large θ to M , and k_i are the empirical constants to fit the experimental curve.

The same approach is applied to tube extension and torsion tests and the collapse calculations were in good agreement with the load deflection diagram of an elbow-shaped square tube cantilever loaded by an inclined load and also for a simple space framework loaded by a single force.

Both elastic and collapse stages of a force(F)-deflection(s) curve of a bus ring made of rectangular section tubes was covered by a single equation suggested by Hungarian researchers (3):

$$F = a \cdot s^b \cdot e^{-cs} \quad (1.6)$$

where a, b, c are the experimentally determined constants. The last equation is not a moment drop-off curve, but it is a direct consequence of the phenomenon discussed.

1.5 CONTRIBUTION OF THE THESIS

The theoretical analysis of structural behaviour after collapse has been initiated (which will be referred to as "collapse analysis") is still in its infancy. However, a sound basis for further research is established and new contributions are turning up frequently.

Improvements of the vehicle passive safety is too urgent a matter to wait until all the theoretical problems are solved. The delay would be infinite since most of the problems are actually open ended. The quality of an analytical approach depends therefore not only on the theoretical level, but also on the relative significance of the selected problem and on the suitability of the method for a wide practical application.

The relevance of the problem and the practical inclination of the analytical approach were the governing ideas in the definition of the objectives of this thesis.

The survey of the published works has indicated an apparent lack of information in the following areas:

1. Little is known about the behaviour of PSV structures in actual roll over accidents;
2. The real collapse analysis of a PSV structure in a roll over situation has not been undertaken;
3. The very relevant bending collapse of rectangular section tubes has not been treated theoretically, and the amount of experimental evidence is still very limited.

This thesis attempts to shed light on these problems. The first one provides information on the points which are most relevant for PSV design for safety. The second item suggests a suitable method of PSV collapse analysis which should become an important design tool reducing the time and costs in the development of safer structures. The third problem is of more general application to structures composed of rectangular section tubes. Many components may not be available for testing in the early design stages and the method suggested should provide an estimate of the actual collapse performance of a wide range of rectangular section tubes. This would enable an entirely theoretical prediction of the PSV behaviour in a roll over, allowing for both the overall and local effects. It would also enable optimisation of section dimensions from the safety point of view.

CHAPTER 2

GENERAL CHARACTERISTICS OF PSV STRUCTURAL PERFORMANCE IN ACTUAL ROLL OVER SITUATIONS

2.1 INTRODUCTION

The investigating team of the School of Automotive Studies, Cranfield, has studied 21 PSV roll over accidents from 1975 until May 1978. The number of accidents, loss of at least 73 lives and often irreparable damage to health and property have drawn much public concern.

The accident investigation included the following main tasks:

1. To reconstruct the dynamic behaviour of the vehicle before and during roll over. The probable cause of the accident has also been examined but without being involved in establishing any legal responsibility. This part of the work has been carried out on the accident site and included the description of the general configuration of the ground and of the basic characteristics of the soil on which the vehicle rolled.
2. To study the overall collapse mode of the vehicle structure in the light of the accident dynamics and of the way in which the vehicle had been designed and built.
3. To analyse the local failures of the collapse mechanisms, particularly from the energy absorption point of view.
4. To investigate other important effects on the driver and passengers safety during roll over.


All vehicles had been recovered from the site before inspection. However, Police, press or private photographs of the vehicle shortly after the accident were obtained on several occasions. These were invaluable in determining the final position of the vehicle, state of the structure before and after recovery, etc.

Characteristic features of the accidents observed are presented in Table 2.1. In spite of a variety of accident conditions and vehicle behaviour, it was possible to identify certain trends in structural performance. The most important conclusions were divided according to the four groups above and summarised below.

2.2 ACCIDENT CAUSES AND TYPES

Human error is a frequent cause of roll over accidents. It varies a lot from one case to the other, but inadequate manoeuvres when negotiating bends or avoiding the oncoming traffic are more typical than others. Seven accidents (33%) happened on slippery roads due to rain, ice or 'black ice', so it would be difficult to decide on the drivers responsibility. However, in at least 3 accidents (14%) the direct cause was a severe brake failure. The investigation also indicated the necessity to examine the effects of telmar retarders on slippery roads.

Table 2.1

SITE	DATE	ACCIDENT TYPE	ROLL KINEMATICS	MAKE OF COACH	DESCRIPTION OF THE MAIN STRUCTURAL ELEMENTS	OVERALL COLLAPSE MODE A B C D E	LOCAL FAILURES	PASSENGERS		ADDITIONAL COMMENTS
								NO.	KILLED INJURED	
HEBDEM BRIDGE	May 1975	Destroying a stone parapet and fall from a 5m high bridge almost vertical fall	Bus fell obliquely on to its roof with almost vertical fall	Duple Viceroy	Composite steel - wooden body on a separate chassis. Steel top hat sections with wooden inserts for pillars. Wood screw joints at 3,4,5&6		Buckling of the metal parts and fracture of wood. Joint failures with complete separation - screws pulled out.	43 (all in)	Others	Extremely severe case, beyond reasonable legal requirements. Brake failure.
NORTHERN IRELAND	Summer 1975	Roll on the roof on level ground	Dropped in into a field continued to travel shortly, then turned and rolled on the roof	Duple Viceroy	Composite steel - wooden body on a separate chassis. Steel top hat sections with wooden inserts for pillars. Wood screw joints at 3,4,5&6	Collapse mode "A" with roof resting on the seats (-1°-2°)	Primarily joint fractures with occasional separation	5 (in)	10	This accident indicates the essential importance of the strength of joints in the main structural framework
"MG" COACH	August 1975	Rolled through 90°. Rear hitting an elevated embankment	Spun about vertical axis before roll, some backwards movement	Plaxton	Composite steel wooden body on a separate chassis. Bolted steel plates at 1 & 2. Steel channel with wood filling for pillars	Collapse mode "A" with an impact between the waist rail & seats. More damage to the seat tops in the rear. Angle of rotation 90°. Little deformation observed at joints 1 & 2. Stiffening effect of the boot apparent.	Buckling of the metal parts, rear w/rail joint separated	4 (back row)		The most likely mode of further collapse was the mode "A"
"ATHENS" COACH (site unknown)	August 1975	Rolled on side only	Almost pure sideways movement	Plaxton	Composite steel wooden body on a separate chassis. Bolted steel plates at 1 & 2. Steel channel with wood filling for pillars	Collapse mode "A" with an impact between the waist rail & seats. More damage to the seat tops in the rear. Angle of rotation 90°. Little deformation observed at joints 1 & 2. Stiffening effect of the boot apparent.	Buckling of the metal parts, no separation of joints	Unknown		The most likely mode of further collapse was the mode "A"
BLACKFOOT COACH (site unknown)	March 1976	Localized cant rail impact	Unknown (believed on level ground)	Duple Dominant Bus	Butt welded steel tube frame mounted on a separate chassis	Local dent on the roof combined with an initial "A" mode	Buckle of a box beam at 4 & a complex pillar & joint buckling & fracture at local points 6 & 8	Unknown (believed 0)		Buckling of the box beam identical to the modes obtained by laboratory tests
A74 BETWEEN CARLISLE & GLASGOW	March 1976	Rolled on to the roof on level ground	Spun about vertical axis before roll, almost pure sideways movement	Alexander "M" Type	Closed top hat aluminium sections for pillars and roof cross members. Aluminium casting connections at 5 & 6. Separate chassis	"A" collapse mode combined with the "C" mode at the entrance door -10°-30°, bigger at the back, -2°-30°-45°	Inverted buckle at the waist rail joint. Aluminium casting & joint fractures at 5 & 6, separating pillars from the roof	1 (partially out)	several	Fractures of the aluminium castings reproduced by the dynamic ring tests, but not by static ones. Compression panels in the side buckled.
GIRVAN	June 1976	Rolled 2.5 times down a 30m long slope at about 35°	Two separate impacts before "continuous" rolling, pure sideways movement	Duple Viceroy Bedford Chassis	Composite steel - wooden body on a separate chassis, steel angles with wood filling for pillars, wood screw joints at 3,4,5 & 6. Double skins in the side.	Collapse started in mode "A", followed by partial roof separation and by severe lateral impacts pushing both sets of seat towards each other. Gangway disappeared	Brittle fractures of wood combined with separation of joints at the waist rail and cant rail levels	45 (6 some out)	30	Severe accident, beyond reasonable legal requirements. Much energy absorbed by seats which served as an important safety factor. Very little damage to the chassis.
HOPLEY	July 1976	Flip over	Spun about vertical axis, hit the offside kerb and toppled on to the roof straddling a ditch	Plaxton (early) Supreme	Pillars made of steel channel sections with wood filling, bolted joints at 1, 2, & 6. Wood screw joints at 3,4,5 & 6	The main structure substantially undamaged, roof dented locally out (at the rear), unexplained damage of the nearside skirt	Joints 'shaken' but withstood the impact, signs indicating high compression in pillars	3 (out)	several	Accident confirms that little lateral force is imposed on the roof in a flip over. It also indicates the advantages of keeping the passenger movement under control even in cases when sufficient survival space exists
ABERFOYLE	Sept. 1976	Roll over after running down a 50m slope at 40°	Vehicle rolled through 180° as it veered to the right	Duple Viceroy on Bedford chassis	Closed top hat aluminium sections for pillars and roof cross members. Aluminium casting connections at 5 & 6. Separate chassis.	Front part severely damaged. Collapse mode "A" & only the door ring failed in mode "C", -1°-20°	Primarily joint brittle fractures with separation in the front half of the bus	2 (driver & pass.)		Most of the weight of the bus supported by seats after the accident, providing significant protection of passengers.
SHEFFORD	Sept. 1976	Flip over	Spun about vertical axis, the offside wheels dug in & toppled on to its roof leaning against a tree	Marshall on Bedford VAS	Steel framed structure, top hat section pillars and roof bows, double aluminium skins in the complete roof & sides	Local deformations at the rear and nearside middle of the roof, no overall collapse	Joint failures, fractures of wood & channel around the screw holes	1 (out driver)	several	Remarkable performance of the double skinned aluminium panelled roof. Need of controlling the movement of passengers emphasised again.
MALTRAVISTLE	Nov. 1976	Similar to a flip over	Spun about vertical axis, hit the offside kerb and rolled on the roof into a depression, leaning against a tree	Plaxton	Pillars made of steel channel sections filled with wood, bolted joints at 1,2,3,4,5 & 6	Collapse mode "A" with 75-90° except in one locally impacted ring 1 & 2 angles occurred at 1 & 2 angles. High compressive loads in pillars.	Joint failures, fractures of wood & channel around the screw holes	None	None	None of the passengers fell out of the bus, which contributed to their safety.
WIMBORNE	Jan. 1977	Destroyed a 0.5m thick stone wall, rolled & finished on its roof supported at the front and rear	Most of forward speed lost before roll, high vertical & lateral loads	Park Royal body on an ABC DeLance chassis	Two top hat sections crimped together with wood filling for pillars, double aluminium skins along the whole side, steel cant rails, strong joints at 5 & 6.	Severe damage at the offside front, inner roof collapsed, at the rear the door ring collapsed in the mode "C".	Primarily beam failures with buckling on the cant rails, side and some compression side and some side fractures on the tension side	1 (in driver)	Several	Severe accident combining frontal impact with roof failure. Very narrow survival space still adequate. Minor failure.
NEWPORT	Spring 1977	Rolling on to the roof & back from an elevated embankment	Rolling up an embankment with a continuous forward sliding	Plaxton	Channel section pillars with wood inserts. Rings interrupted at 7 & 8 by the wooden roof longitudinals	Collapse mode "E" with excessive damage in the rear part, including the front which was impacted first	Joint failures with brackets or bolts broken at 7 & 8, fractures in wood at 3 & 4 as well	2 (out)		The roof has loosened purely sideways in spite of the continuous forward sliding. The soil was fairly soft & could have absorbed a considerable amount of energy.
GLENFANS	Nov. 1976	Destroying a small stone wall and fall rolling on the roof	Almost pure sideways movement and fall from a 2m elevation	Duple Dominant	Composite steel - wooden body, bolted plates at 1 & 2 & screw joints at 3,4,5 & 6	Collapse mode "C" dominant with the lowest hinge at the seat to side connection. Nearside seats pushed in, -1°-2° when in the roof.	Primarily joint failures combined with wood fracturing in places	None	Several (light)	Considerable spring back of the roof after recovery. The nearside roof rick fractured at all supports. Nearside seats bearing much vertical load. Slow roll.
MIDB NEAR EARLSTUN	Sept. 1977	Rolled on to roof across drainage, almost no forward speed.	Rolled after running on the four wheels down a 30m long slope at approx. 45°	Plaxton on Leopard chassis	Wood filled channel sections for pillars, cant rail welded to the pillars	Collapse started in mode "A", but the roof was eventually completely sheared off	Cant rail wall torn away locally by the pillar, & local fractures at screw holes at the waist rail joints	3 (all out)	20	Impact against a concrete surface, so that almost all deformation energy was absorbed by the body. Seats had a particularly important role in preserving survival space. Very severe case.
ACLE	Oct. 1977	Rolled on to the side only	Rotation in yaw and roll until it came on the side with low forward velocity	Plaxton Panorama Elite III	Channel section pillars with wood filling bolted to the wooden waist rail & cant rail. Roof bows interrupted by two longitudinals.	Little damage, more at the front. Started collapsing in mode "A".	Joints shaken, but could not be inspected in detail.	None	Minor Injuries only	None of the passengers were thrown out of the bus.
LLANHILETH	Jan. 1978	Two (or one) rolls down a 30m steep drop	Rolling sideways: the angle of slope = 60-70°	Duple Viceroy on Ford D Chassis	Pillars were wooden composite members with steel cladding strips. Bolted joints at waist rail & screws at 5 & 6	Front part completely destroyed. Middle & rear parts had a combination of modes "A" & "C". Seats provided little lateral restraint.	Joint fractures at 5 & 6 with separation in places, brittle fracture of timber in pillars.	2 (one in one out)	4 serious	Very severe accident beyond reasonable legal requirements. Indicated the necessity of providing lateral strength by seat mounting design.
SCARBOROUGH	Feb. 1978	Spun on icy road & overturned coming to rest on its roof	Sideways movement with the rear moving faster than the front	Plaxton Elite III	Channel section pillars with wood filling bolted to the wooden waist rail and cant rail. Roof bows interrupted by two longitudinals.	The general collapse mode of the type "D", 4th to the 9th rows of nearside seats with damaged head-rests	Joint failures with fractures of the wood and channel near the holes & brackets in the roof (at 8)	1	1	This accident demonstrated the necessity of providing continuous cross members in the roof.
HADLY	March 1978	On the roof, front on flat ground, rear over ditch	Spun about vertical axis and rolled to rest on the roof with little fore & aft speed	Plaxton Elite III	Channel section pillars with wood filling bolted to the wooden waist rail & cant rail. Roof bows interrupted by two longitudinals.	More damage to the rear part with collapse mode "A", -1°-70° at the rear, increasing towards the front	Joint failures with fractures of the wood & channel near the bolt or screw holes	2	10 (3 serious)	It appears that not much lateral force was imposed on the roof. The accident was therefore between a roll over on flat ground and a flip over.
(WORTH)	April 1978	Roll on the roof from a 0.5m elevated road on to a 30° slope	Bus rolled from almost standstill because the road verge gave way	Duple Dominant	Basic framework made of 2"x2" hollow section steel tubing, joints welded along lateral connections only (with reference to the vehicle longitudinal axis)	Collapse mode "A" clearly dominant except in one middle ring where a mixture of "A" & "B" modes took place.	Typical box beam buckles at the waist rail level & cant rail longitudinal buckling at 5 & 6, pillar fractures on the tension side of hinges.	2	several	The roof rack on the nearside was brought into heavy contact with the seats on the offside causing crushing of the headrests and fracturing the roof rack support legs. Majority of injuries caused by glass as passengers escaped after roll.
NEWTON BAR	May 1978	Roll over with considerable forward speed (45-70 km/h)	Spun about vertical axis through 30° 180° & slid like that = 30m	Duple Dominant on Ford Chassis	Channel section with wood filling for pillars, bolted joints at waist rail & rather poor welds at 5 & 6.	Collapse mode "A" dominant in places also "B" & "C". Some local damage in the roof. Seats head-rests smashed sideways.	Joint fractures with separations at 5 & 6, fractures & severe bending without separation at waist rail.	5 (inside)	11 serious	High kinetic energy to be absorbed. A significant part absorbed by the soil and bushes. Similar to 25, but here the sliding had a much greater lateral component. Brake failure.

The first impact is applied either at the cant rail or waist rail level, depending on the roll kinematics and ground shape. In the more severe cases the lateral load is applied first to the cant rail. Presence of lateral force on the roof structure serves as a distinct criterion for accident classification. Accidents with little or no lateral force on the cant rail usually cause far less damage (injuries or loss of lives) than those where lateral force is significant. The actual roll kinematics depends both on the vehicle behaviour before roll and on the general configuration of the ground. Little or no side force was applied to the cant rail if the vehicle rolled on its side only, or if the roll took place while the cant rail was off the ground. In the latter case the coaches landed "flat" on their roofs and further roll was arrested by trees (accidents 10 and 11) or ground (accident 8). It is suggested (1) that these accidents should be called "flip-overs". Statistical information on the accident types is summarised in Table 2.2.

Table 2.2

Type of Accident	Configuration of the Ground	No.	Percentage %	Total	Total Minus 3.1
PSV roll over on to the roof with lateral force on cant rail	1.1 On level ground	3	14.28	13 (61.9%)	13 (72.2%)
	1.2 From a moderately elevated road (approximately 1m height difference)	3	14.28		
	1.3 After running down a slope	3	14.28		
	1.4 Oblique roof impact after a fall from a 5m high bridge	1	4.76		
	1.5 After demolishing a stone wall and resting on the roof supported at the front and rear	1	4.76		
	1.6 Rolling on to an elevated embankment with considerable forward speed	1	4.76		
	1.7 Rolling through approximately 135° and then skidding 30m on level ground	1	4.76		
PSV roll over more than 180° about longitudinal axis	2.1 2.5 full revolutions down a 30m long slope at about 35°	1	4.76	2 (9.52%)	2 (11.1%)
	2.2 2 full revolutions down a slope at about 60-70°	1	4.76		
PSV roll over with little or no lateral force on the cant rail	3.1 Roll on side only on level ground	3	14.28	6 (28.57%)	3 (16.7%)
	3.2 Flip over into a depression in the ground	3	14.28		
Total		21	100	21 (100%)	18 (100%)

Table 2.2 indicates that most of the accidents occurred on level ground or from moderately elevated road (66.7%). If we include here the nearest accident type "after running down a slope" the percentage rises to 76%. In a majority of cases the vehicles rolled once on to the roof with lateral force on the cant rail (62%). Both conclusions do not agree with Hungarian statistics which point out that most of their accidents (37%) refer to a 360° roll over down embankments. Disagreement of national statistics has to be seriously borne in mind if any international PSV roll over safety legislation is to be accepted. It should also be mentioned that the accidents which had more than 180° roll (nos. 7 and 17 in Table 2.1) were beyond any reasonable legal requirements. The difference in statistics may be due not only to the environmental circumstances but also to the collapse behaviour of respective structures. Unfortunately, little evidence is available on the collapse performance of Hungarian buses.

Energy absorbing characteristics of the ground were not investigated in detail. However, a note was made on the surface appearance, and in most cases it consisted of a layer of soil and grass. This soil is a better energy absorber than harder, stony or concrete surfaces which were observed in some accidents. The conclusions regarding soil characteristics generally agree with refs 31 and 32.

Vehicles have generally lost most of their forward speed (or rearwards - if spinning about vertical axis took place) before the roll over started. The longitudinal component of speed was lost due to braking, hitting an obstacle or ground, or due to spinning about vertical axis, so that the actual roll represented almost a pure sideways movement. Accidents 12 and 21 (Table 2.1) were the only ones with considerable forward movement during roll over.

2.3 OVERALL COLLAPSE MODES OF PSV STRUCTURES

Overall collapse modes depend on the dynamics of a roll over accident, configuration of the ground and on the structural properties of the PSV body. In most accidents the vehicle rolled on to its roof with an almost pure sideways movement and on relatively even ground. The strengthening effect of glazing in the longitudinal direction could have been important in cases where fore and aft speed of a rolling vehicle was initially present. The overall collapse modes have always displayed an almost pure sideways movement of the roof, even in cases where considerable forward speed was evident (accidents 13 and 21). Collapse is governed by the behaviour of rings enclosing the passenger compartment, and the usual modes are indicated in Table 2.1 and Fig 2.1.

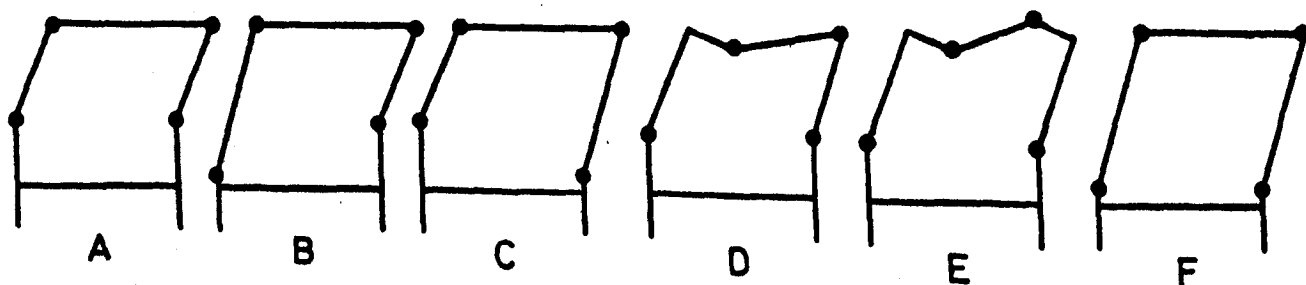


Fig. 2.1

Collapse mode A in Fig. 2.1 with hinges at the waist rail and cant rail was most frequent, but sometimes combined with some of the other forms. An example of the collapse mode A is shown in Fig. 2.2a* (accident no. 20).

Modes B and C were found mostly at the front door apertures, but also as a dominant collapse mode C in Fig. 2.2b** (accident 14). The lowest hinge occurred either where the seats were attached to the side, or at the floor level next to the bracket connecting the pillar and the floor member. Mode B is likely to be transformed into mode A after the waist rail contacts the seats.

Collapse modes D (Fig. 2.2c - accident 18) and E (Fig. 2.3a - accident 13) were produced in structures which had the roof cross members interrupted by the two longitudinal rails. The appropriate joints were weak in bending.

Excessive local roof damage is also possible (Fig. 2.3b*** - accident 12) if the vehicle lands on a hard and very uneven surface. In some cases an extra hinge in a pillar occurred due to the effect of seats (Fig. 2.3c - accident 21).

Neither of the three flip-overs - Figs. 2.4a* (accident 8), 2.4b (accident 10) and 2.4c++ (accident 11) caused intrusion of the roof structure into the passenger compartment. The main reason is the absence of lateral load on the roof.

Three accidents were very severe indeed. Accident number 1 (Fig. 2.5a) was the worst road accident that ever happened in the UK. The near side lower part of the body was severely damaged before the coach fell from the bridge, giving little support to the rings. In the accident no. 7 a composite construction coach rolled 2.5 times down a 35° slope. The roof was partially separated from the rest of the body and the seats absorbed much of the kinetic energy. Lateral movement of the seats was so extensive that the gangway disappeared completely (Fig. 2.5b). The third case (accident 17) happened when a coach rolled twice down a 30m long steep slope at 60-70° (Fig. 2.5c+++). These cases are beyond reasonable safety requirements, but the improved current designs would certainly provide a better passenger protection even under such extreme conditions.

The general collapse mode was affected not only by the distribution of strength around the rings, but also by the side structure below the waist rail and by the seats. The outer side panels were often buckled on the compression side only. Waist rail deformations indicated in some cases the restraining effect of the adjacent stump pillars or rings, particularly where lateral displacement of the roof was uneven.

-
- * by courtesy of the West Yorkshire Metropolitan Police
 - ** by courtesy of the Dundee Courier newspaper
 - *** by courtesy of the Dyfed-Powys Police
 - + by courtesy of Crawley Gazette
 - ++ by courtesy of Mr. Carney, coach operator
 - +++ by courtesy of South Wales Argus



a

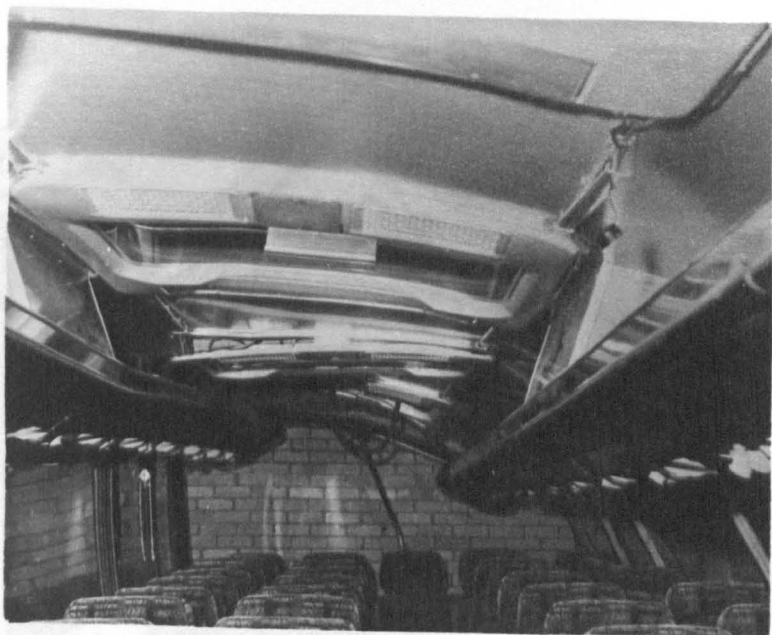


b



c

Fig. 2.2



a



b



c

Fig. 2.3



a



b

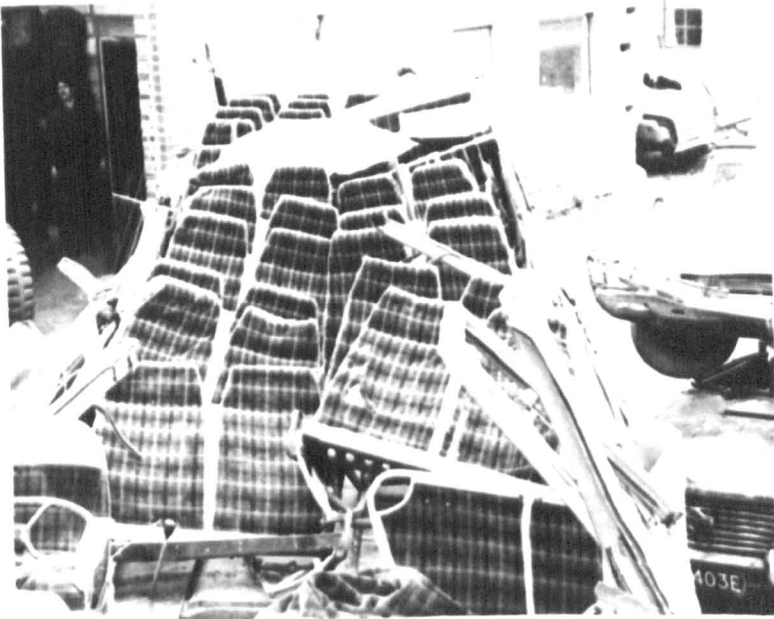


c

Fig. 2.4



a



b



c

Fig. 2.5

Seats made a very important contribution to the strength of the structure in both lateral and vertical directions. The lowest hinges in collapse modes B and C (Fig. 2.1) usually occurred at the seat to side connections. In some cases mode C was created after the ring started collapsing in mode F until one waist rail hit the seats. In accident 7 (Fig. 2.5b) seats had a particularly important role in the energy absorption process. They have often supported the weight of the bus at least on one side, thus preserving some survival space for passengers.

The floor cross members and chassis suffered little or no damage in all accidents (except no. 1).

In conclusion we can say that several different collapse modes have been observed in otherwise similar roll over conditions. A real comparison in terms of safety requirements can be made only if the other relevant parameters (direction and point of load application, impact speed, amount of energy to be absorbed before intrusion into the specified survival space, load that the structure should support after impact and hinge properties) are assumed common to all structures. The problem can also be tackled if a particular coach is considered with different collapse modes aiming to satisfy the same complex safety requirement. Assuming again that the hinge properties in a particular component will not depend on the hinge position, the energy absorbed will be proportional to the amount of rotation in hinges of the collapse mechanism. Simple comparison of collapse mechanisms in Fig. 2.1 with reference to a common survival space, defined for example as in Fig. 1.1, shows that the mechanism A allows most rotation in hinges before the structure starts intruding into the survival space. A relatively higher strength and smaller elastic deformations can be achieved. Gussets in the roof pillar joint or roof racks may further reduce the length of the arms of the collapse mechanism, thus enhancing the effects mentioned. However, an increased hinge rotation may not be desirable in components which lose abruptly their load carrying capacity during deformation. Such components may not be strong enough after the impact to withstand the weight of the bus, and should be avoided. A comparison of performance of different structures cannot be based, therefore, entirely on the overall collapse mode.

2.4 LOCAL FAILURES

As the structure starts collapsing, a major part of the energy is absorbed by permanent deformation of the material which is concentrated in hinges of the collapse mechanism. The energy absorption process in hinges will be discussed in more detail in section 4.2. Let us mention though that a good energy absorber of this type should have sufficient strength and also maintain its resistance through fairly large angles of hinge rotation. The angles to be considered in design depend on the overall collapse mechanism and the allowed survival space.

The survey of accidents has shown that the local failures can be broadly divided into three groups:

- a. joint failures,
- b. beam failures with material separation,
- c. beam failures with local buckling.

Joint failures occurred in all accidents and were particularly common in composite structures. This type of failure can drastically reduce the hinge strength and energy absorption since the load carrying capabilities of the beams connected are not utilised. The pillar to cant rail joint was particularly critical in composite (Fig. 2.6a - accident 21) but also in steel (Fig. 2.6b - accident 15) or aluminium (Fig. 2.6c - accident 6) versions. The main problem in composite structures is wood joining, while better design or welding would be required in some steel joints. It is believed that fracture in the aluminium insert in Fig. 2.6c was due to stress concentration and brittle behaviour of the material under high strain rate conditions.

An abrupt drop in ring strength was sometimes apparent in places where the roof member was interrupted and connected to the longitudinal roof rail (Fig. 2.7a - accident 13), or at the pillar/waist rail joint (Figs. 2.7b - accident 8 and 2.7c - accident 15).

The main causes of beam failures with material separation were insufficient material ductility and presence of stress concentration. Lack of ductility was always observed in wooden elements of composite designs, e.g. Fig. 2.8a - accident 21. However, separation of material also occurred in steel beams (Fig. 2.8b - accident 20). Adjacent welding might have influenced the beam in Fig. 2.8b, and this effect is studied in more detail in section 4.2. The same type of failure was observed in laboratory tests of aluminium beams.

Stress concentration, or local section weakening in continuous beams were usually caused in places where the beam was joined to the adjacent elements. Fig. 2.8c - accident 19, depicts a stress concentration effect in wood, while the same type of failure was observed in laboratory tests of steel or aluminium beams.

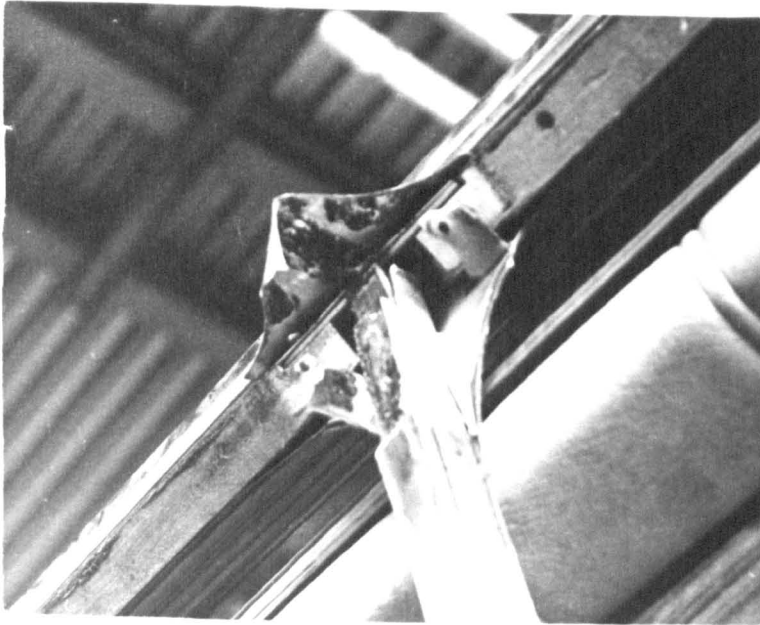
Local buckling occurred in steel box beams (Figs. 2.9a and b - accident 20). Fractures were produced by pulling the roof back during recovery. The failure in Fig. 2.9a was most common (accidents 5 & 20) in box beams. The second mechanism (b) represents an "inverted" form of the first one and was also observed in aluminium closed top hat sections (Fig. 2.9c - accident 6 - cut was made during recovery).

The metal mounts of seats or roof racks had the same general pattern of joint or section failures as the beams.

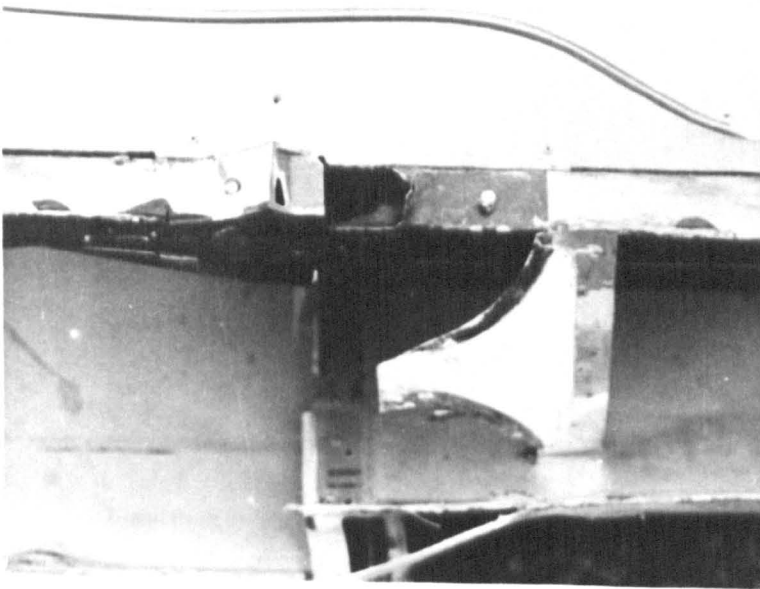
The energy absorption properties of the local failures will be reviewed in section 4.2.

2.5 OTHER EFFECTS ON THE DRIVER AND PASSENGERS' SAFETY

Protection of driver and passengers in a PSV roll over accident can only be discussed in terms of probabilities of a certain outcome. There is, unfortunately, no way to provide absolute safety and the events which appeared generally similar did not always produce the same consequences. However, definite trends have been observed on at least two major points. Driver and passengers stand a much better chance to survive if:-



a

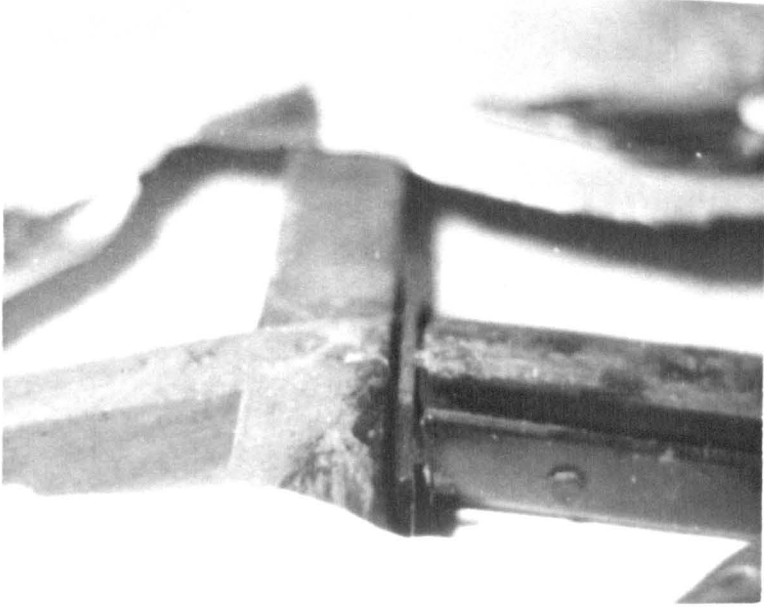


b

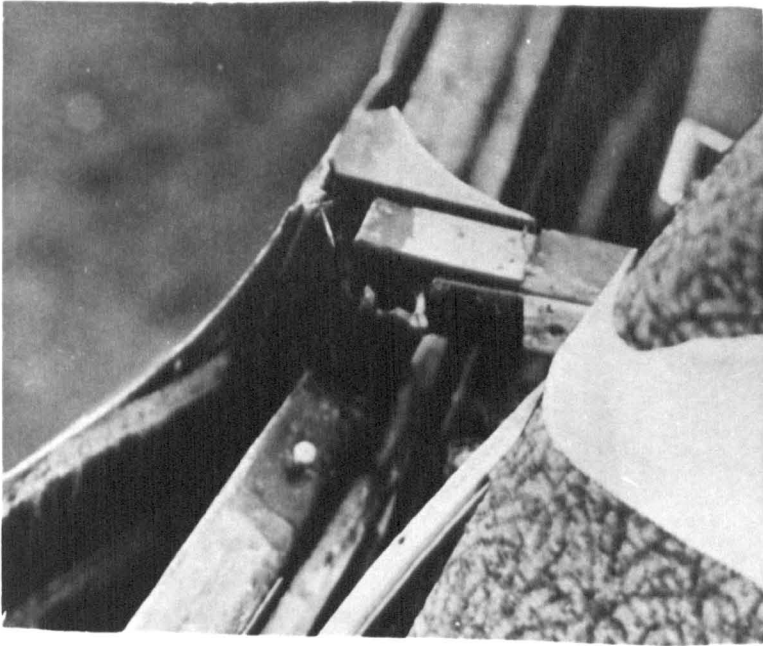


c

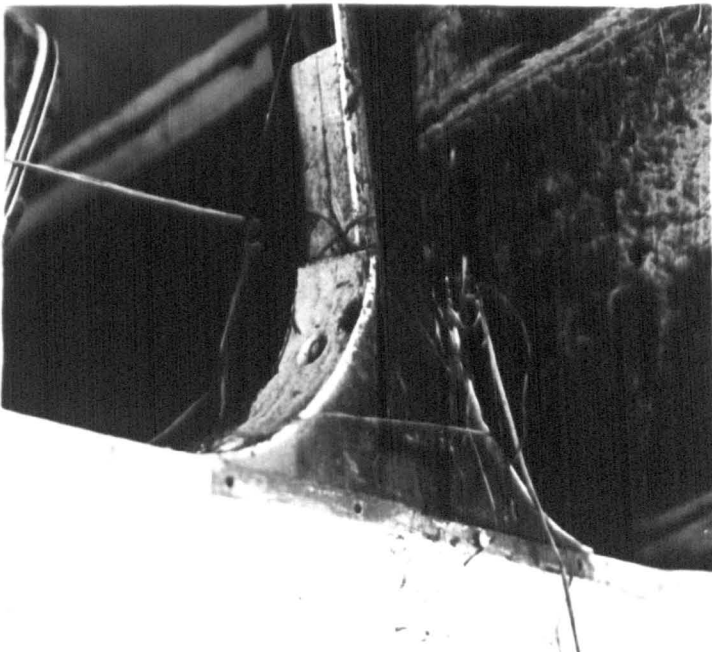
Fig. 2.6



a



b

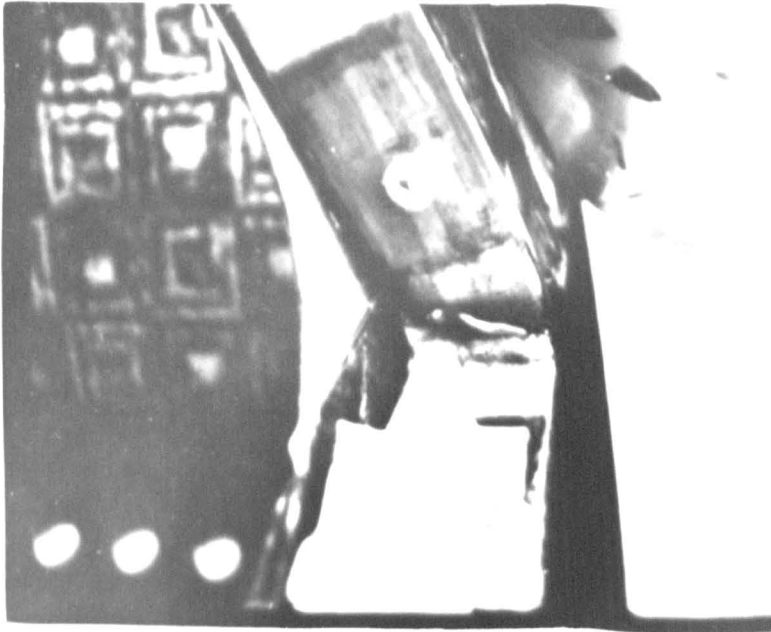


c

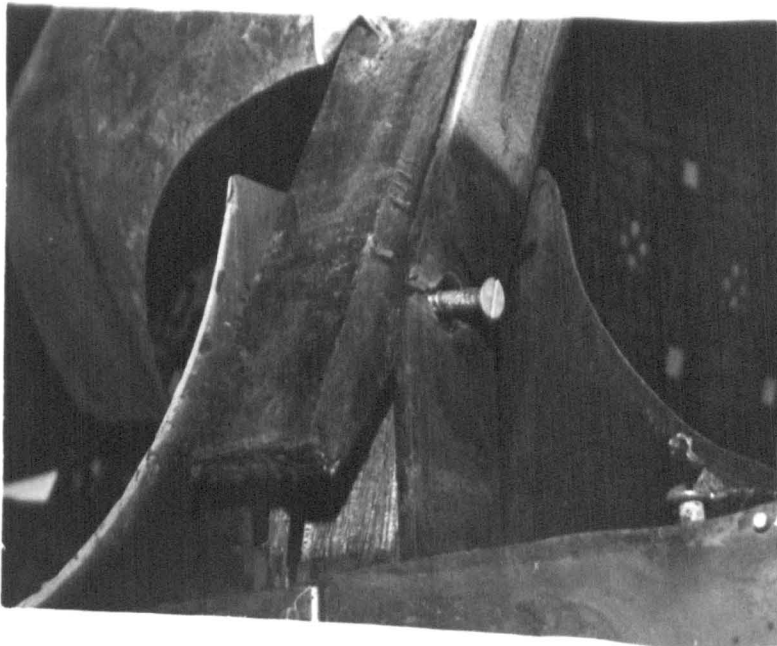
Fig. 2.7



a

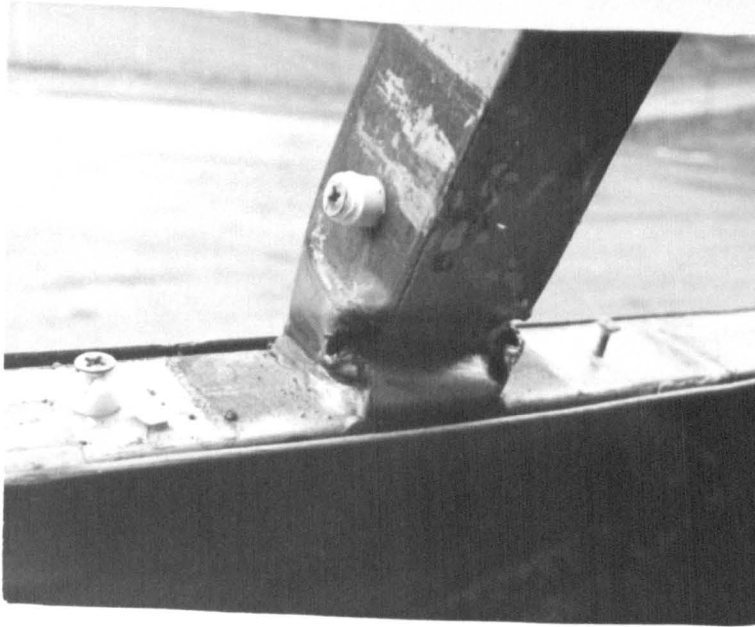


b

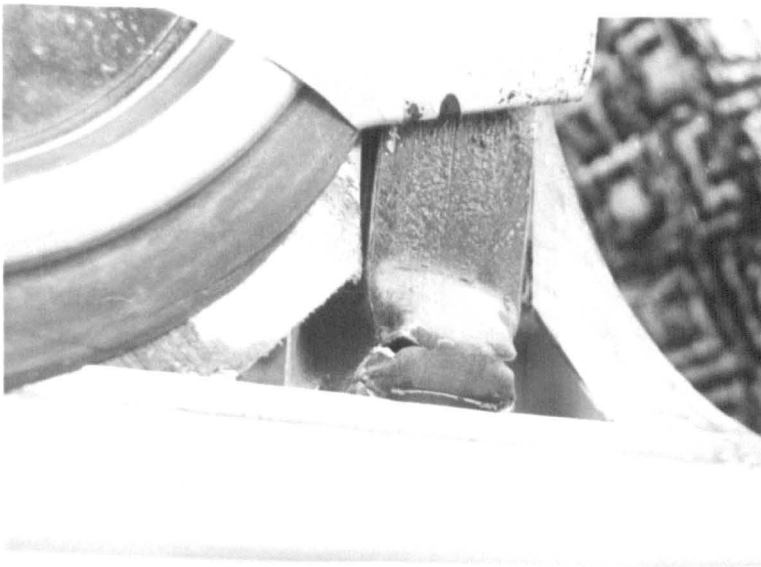


c

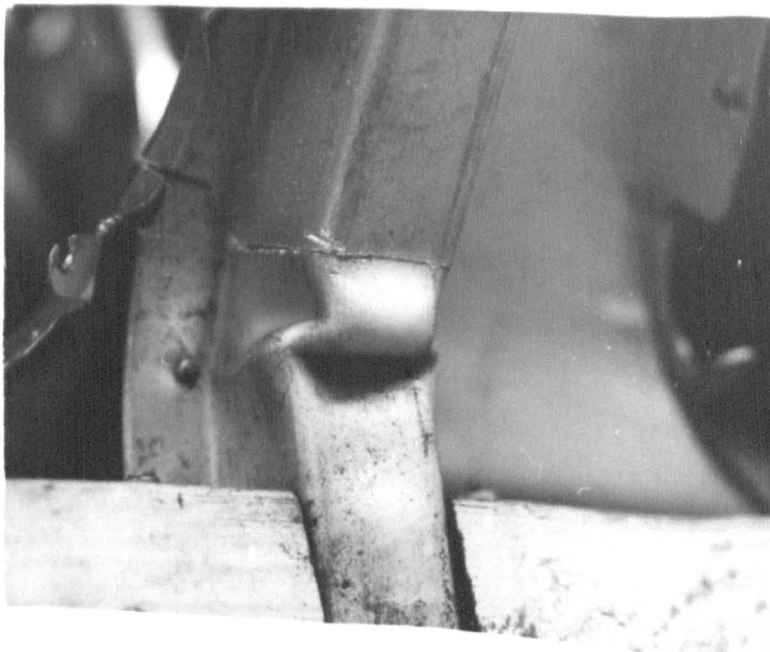
Fig. 2.8



a



b



c

Fig. 2.9

- a. they are retained within the passenger compartment, and
- b. sufficient survival space is preserved during the course of the whole accident.

Retention of occupants by means of seat belts could be effective, but is hardly applicable in the foreseeable future. Smaller window apertures and safety glazing would be more appropriate.

The safest area is between the seats and below the head rests, but it is also necessary to preserve some survival space above the head rests. The suggestion in Fig. 1.1 is reasonable, but it is not intended to discuss specific dimensions of the survival space within the limits of this report.

Hard and sharp surfaces should be avoided, which is another reason for avoiding fractures in the structure.

The head retardations of occupants are primarily governed by the speed of impact against the vehicle interior. Retention in seats would help to reduce this speed as well. Energy absorbing surfaces could be provided in the places where heads are known to impact the structure, e.g. the undersides of luggage racks and the roof lining itself between the racks.

3.1 INTRODUCTION

The accident survey has emphasised the importance of analysing both the overall collapse mode of a body and the hinge behaviour. This chapter will now present an approach to the theoretical determination of the overall collapse mode of a coach in a roll over and the discussion will be illustrated by an example calculation.

Theoretical analysis is usually employed either to check whether an existing structure can meet some safety requirements, or to ensure that a future design converges to a satisfactory solution in a most direct and economic manner. Most of the problems, however, are common to both options and are determined by the physical complexity of the roll over phenomenon and by the available analytical method. This study employs the already mentioned finite element program CRASHD for the collapse analysis of spatial frameworks.

The advantage of the program CRASHD is the ability to include various relationships between the moment and rotation in hinges of the collapse mechanism. This feature is particularly useful in the collapse analysis of vehicle structures consisting of thin walled components. The main limitations of the program in its present state are the quasi-static incremental approach to analyse dynamic events, the inclusion of beam elements only and the necessity to establish the hinge characteristics by a separate experimental exercise.

Development of the finite element method has opened substantially new possibilities in any area of structural analysis. However, inadequate modelling of the actual physical situation or inaccurate interpretation of results can still cause misleading conclusions. This is particularly true for collapse analysis since the amount of experimental evidence to check the theory is still very limited. Disappointment may become even more unpleasant due to a relatively greater expectation from results of a finite element analysis. A sound engineering application is therefore required to produce answers which would be not only reliable, but also reasonably accurate, cost effective and supplied in the right time. It is still the man and not the computer that eventually creates the quality of the theoretical results.

The major problems that should be solved in the current analysis are:

- a. Implications of a quasi-static approach to a dynamic roll over problem,
- b. Definition of loading conditions,
- c. Idealisation of the structure,
- d. Interpretation of results.

3.2 QUASI-STATIC ANALYSIS OF A DYNAMIC ROLL-OVER PROBLEM

In the present context the term "quasi-static" is used to describe a process in which external loads (or specified displacements) are incremented in steps and a static finite element analysis of the current form of the structure is performed in each step. The structural stiffness matrix is updated after each step to allow for the non linear effects of large displacements, axial load in members, occurrence of hinges and some forms of hinge behaviour. In this way the analysis allows for the varying properties of a structure which is a very important feature of the actual dynamic collapse. However, no inertia, damping or any other dynamic effects are included.

The actual dynamic influence includes the varying loading conditions during collapse, the inertia effects on the overall and local collapse modes and material behaviour under high strain rate conditions. The difference between the static and dynamic collapse behaviour varies depending on the type of structure, point and direction of load application, impact speed, barrier or impactor properties, etc.

The varying loading conditions will be discussed in the next section. In the author's opinion the other dynamic effects allow the application of a quasi-static analysis because:

- a. The cant rail impacts the ground with a relatively low speed. It can be easily calculated by considering a rolling bus as a rigid body whose potential energy is being transformed into kinetic energy of rolling. For a typical bus (mass 8000 kg, roll moment of inertia 8000 kgm^2 , height 3m, width 2.5m, height of centre of gravity 1m) rolling on a flat ground with zero initial angular velocity about the nearside wheels, the speed of the first impact between the cant rail and ground is 4.16 m/s.
- b. Extensive static and pendulum impact testing of a range of bus rings carried out in the School of Automotive Studies (2) always produced exactly the same overall collapse modes in static and dynamic conditions. Static and dynamic loads were applied to the cant rail at 30° to the floor member. Impact speed of a rigid pendulum was 4.6 m/s. Collapse modes were in reasonable agreement with the evidence of the accident investigation.
- c. A great majority of the bus mass is distributed in the area away from the collapse mechanism. No larger lumped masses are directly involved in impact and no appreciable deformation takes place in the area of major mass concentration (floor level, chassis). The energy absorber mass is therefore much smaller than the mass retarded, hence the propagation of stress waves can be ignored.
- d. Static and dynamic tests on rings of the type considered here have produced the same continuous hinge failures within comparable deflection range. The strain rate effect in dynamic tests was evident in terms of the increased energy absorption for the same deflection. The strain rate did not affect the relative strength of hinges and the collapse mode remained unchanged.

However, the above arguments are primarily concerned with the relative strength distribution and do not necessarily apply to the quasi-static analysis of the energy absorption in dynamically produced hinges. The difference in the static and dynamic hinge behaviour may be important, particularly due to the possible change in properties of the deforming material. Apart from the strain rate effect on the yield stress, an increased tendency to fracture has also been observed in tests of some designs (for example the one in Fig. 2.6c). The energy absorbing process will be discussed in more detail in section 4.2.

3.3 DEFINITION OF LOADING CONDITIONS FOR COLLAPSE ANALYSIS

The accident investigation has shown that 76% of accidents involved coaches which rolled once on to their roof on a fairly even ground in level with or moderately lower than the road surface. All these vehicles did not roll any further and remained in an upside down position. They also lost most of their fore and aft speed before the structure started collapsing and the roofs always displayed an almost pure lateral movement. The deformations were fairly evenly distributed along the whole vehicle, with some tendency to produce more deflection in the front half. This may be due to the roll kinematics exposing the front half of the roof more in the initial stages of collapse and/or due to the uneven distribution of strength along the structure. The first reason is possible, but the second is certain because the door is located in this area, and there may also be another small auxiliary door next to the driver. In front-engine coaches the front rings may have gaps in the floor members to accommodate the engine and transmission.

In more severe accidents the first contact with the ground took place along the cant rail. Assuming the most frequent case of a pure lateral roll on reasonably even ground the load would be distributed along the whole cant rail. The time interval between the first contact with the ground and start of collapse (period of elastic-plastic deformations) is very short. Uneven distribution of the roof lateral stiffness may cause uneven ground reaction forces along the cant rail. However, it is very unlikely that these uneven and transient forces could disturb the rolling axis of the heavy vehicle rolling with maximum momentum. The inertia resisting this action is particularly great because it refers to rotation about lateral axes of greatest moments of inertia. It is argued therefore that under the assumed conditions the whole cant rail should start moving laterally by the same amount. Of course, during roll and particularly after the coach finishes on its roof these deflections may become different depending on the strength distribution. This argument is supported by evidence seen in filmed bus roll over tests by Hungarian and American researchers. The previous experience indicates also that the collapse mode is not altered if the increase of all external loads is not exactly proportional.

This was the first reason to apply lateral displacement rather than load increments to the cant rail in the theoretical analysis.

The second argument in favour of displacement incrementation is the fact that loads can be incremented only up to the maximum value when the collapse starts. From there on it is only the displacement incrementation that can produce a unique solution to the system of load-deflection equations of the finite element model.

And finally, the load incrementation may produce a mechanism in only a part of a structure, say front ring, which prevents a further automatic load incrementation in the areas that are still intact.

The final problem is to decide on the direction of displacement incrementation. The load applied to the cant rail changes direction relative to the structure as it rotates about the contact line (Fig. 3.1a). A quasi-static analysis cannot predict this load variation. (Work is in hand in Cranfield to develop this, dynamic, facility.) However, the collapse mechanism is created soon after the impact and subsequent variation of load direction will not alter the initial mode. A load angle of 30° to the floor member of the ring (Fig. 3.1b) was assumed as a reasonable mean value.

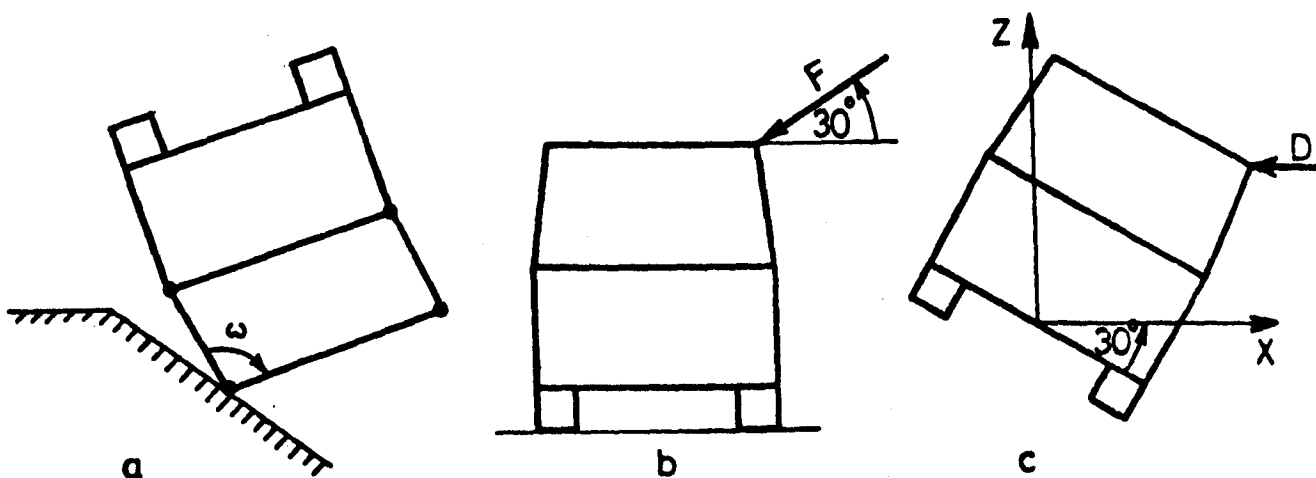


Fig. 3.1

Another reason in favour of assuming a single value of the load angle is the fact that assessment of the roll over safety characteristics may be based on laboratory tests rather than actual roll over of the vehicle. This is due to difficulties in providing uniform and repeatable test conditions in actual roll overs. If a laboratory test is accepted then it is most likely that a load would be applied obliquely to the cant rail in only one direction, presumably as a pendulum impact.

The somewhat conflicting requirements of applying lateral displacements to the cant rail and getting a reaction at 30° to the floor can be simultaneously met. The structure is therefore rotated about the longitudinal axis (Y) through 30° as shown in Fig. 3.1c, where axes X and Z belong to the global co-ordinate system of the finite element model. Displacements are now applied to the cant rail along the -X axis, while all the other degrees of freedom of the cant rail are set free. The structure will deform naturally with the cant rail rotating about the lower hinge and reaction will always lie along X axis. One should bear in mind that this rotation changes not only the node

co-ordinates, but also the relative position between the global and local co-ordinate systems.

3.4 IDEALISATION OF THE STRUCTURE

3.4.1 The Actual Structure

The coach chosen for the example calculation has an all-metal body mounted on a separate chassis. The engine and gearbox are situated in the front and the boot is behind the rear axle. The chassis side members stop in front of the boot, but two aluminium "T" sections are extended further back to support a part of the luggage load. The door is in the front of the near side wall, while the emergency door is located on the off side between the last two rings. Windows are mounted on rubber seal mounts fitted into the framework.

The body framework is composed of standard mild steel rectangular and square section tubes with wall thickness ranging from 1.2 to 3.2 mm. The rings are assembled of four continuous beams: two pillars, roof and floor members. No significant section weakening or stress concentration was apparent in rings, apart from some possible effects due to welding. The main structural rings start at the rear door pillar and the structure in the very front is less substantial employing primarily open section beams. The pillars of the front two rings are connected to the continuous floor members via adjacent stump pillars as will be shown later in the finite element model (Fig. 3.5). The first floor member in line with the first ring is interrupted between the chassis side members to accommodate the engine and transmission. Additional floor members and stump pillars are arranged between the rings. The waist rail and two more longitudinal rails run along the side with three diagonals behind the rear axle to strengthen the side of the luggage compartment. The frameworks of the front and rear bulkheads are made of relatively light open section members.

Four longitudinal roof rails and cant rails run along the roof, but they are all interrupted by the roof cross members and welded together.

Most joints in the main load carrying structure are continuously welded, and brackets with bolts are used to connect pillars to the floor members.

The roof and sides are clad with aluminium skins. Steel sheet is also attached to the inner side structure between the waist rail and the middle rail running above the wheel arches. The aluminium segments are pop riveted to the roof framework and only to the horizontal beams in the side, while spot welding is employed to fix the interior steel sheets to the side skeleton. The front and rear bulkheads are made of glass reinforced plastic. Hardboard panels are used to build the luggage compartment.

The effect of floor panels and seats on the collapse mode has not been included for reasons explained in section 3.4.3.

3.4.2 Justification of the Modelling Technique

A variety of collapse modes (Fig. 2.1) has been observed in real accidents. They have been determined by the collapse mechanism of structural rings surrounding the passenger compartment.

Consider an isolated bus ring loaded by an arbitrary oblique load ($F = 1.65 \text{ kN}$) as shown in Fig. 3.2a. The ring is assembled of uniform section, continuous members so that the collapse moment can be assumed constant anywhere along a particular component. It is also assumed that the joints are stronger than the beams they are connecting. Nodes 5 and 6 are located at the waist rail level.

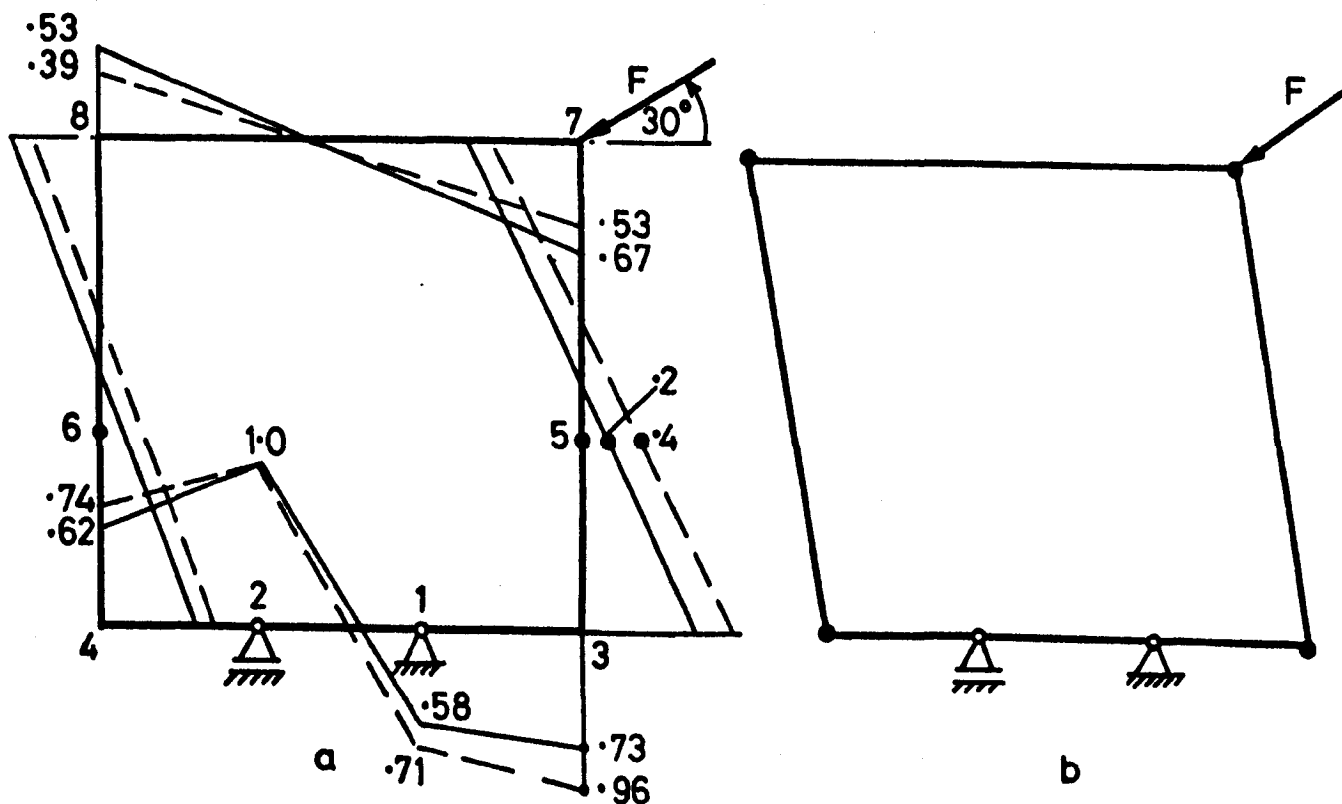


Fig. 3.2

The bending moment diagrams in kNm are plotted as solid lines in the same figure. The peak moments occur at the pillar ends while the loading of the waist rail joints is very low. Collapse analysis of such a ring gives a collapse mode in Fig. 3.2b, which was also produced experimentally (2). Hinge at node 2 does not occur because the floor member is much stronger than the pillar.

This simple example shows that the ring in the complete structure acts under conditions which are much different from the ones in Fig. 3.2. The actual collapse mode is affected by the rest of the structure, i.e. the skeleton of the side (stump pillars, other rings, waist rail and other longitudinal members), the roof and the sheet metal cladding.

The usual attempt made in the elastic analysis would be to increase the effective second moment of area of the pillars below waist rail to allow for the contribution of the adjoining elements. However, this approach should not be applied in the current study. For example, if the second moments of area of elements 3-5 and 4-6 in Fig. 3.2 are increased five times and same loading applied, the bending moment diagram will follow the dotted lines in Fig. 3.2a. The stiffer elements have taken more load, but the moment distribution is virtually unchanged. The waist rail nodes are again loaded substantially less than the nodes 3 and 4. The load carrying capacity of member 3-5 and 4-6 would have to be doubled at least ($0.96/0.4 = 2.4$) in order to produce a hinge at node 5 rather than 3. The longitudinal members joined with the pillar do not increase the strength of the pillar. The skins in the sides are often attached to horizontal beams only, hence their contribution to the strength of the pillar cannot be sufficient to alter the collapse mechanism.

The above argument was used to suggest a new modelling technique presented in Fig. 3.3a, which employs a fictitious "spring" elements 5-9 and 6-10 simulating the restraining effect of the side structure on the pillars at the waist rail level. For example, the restraining effect in lateral direction of the adjacent stump pillars and waist rails can be simulated by attributing an axial stiffness (c) only to both springs, where $c = AE/l$ (section area times modulus divided by beam length). A gradual increase of this stiffness will alter the moment diagram in pillar 3-5-7 until the moments at waist rails become greater than moments at the floor level. A collapse analysis of such an arrangement has been performed using the CRASHD program and it was found that, for this particular ring, the axial stiffness of minimum $c = 150 \text{ N/mm}$ in both springs would convert the collapse mode in Fig. 3.2b into the required form "A" shown in Fig. 3.3b. The above stiffness should be maintained through approximately 20 mm of lateral deflection of nodes 5 and 6. It will be shown in section 3.4.5 that the spring bending stiffness may be even more important.

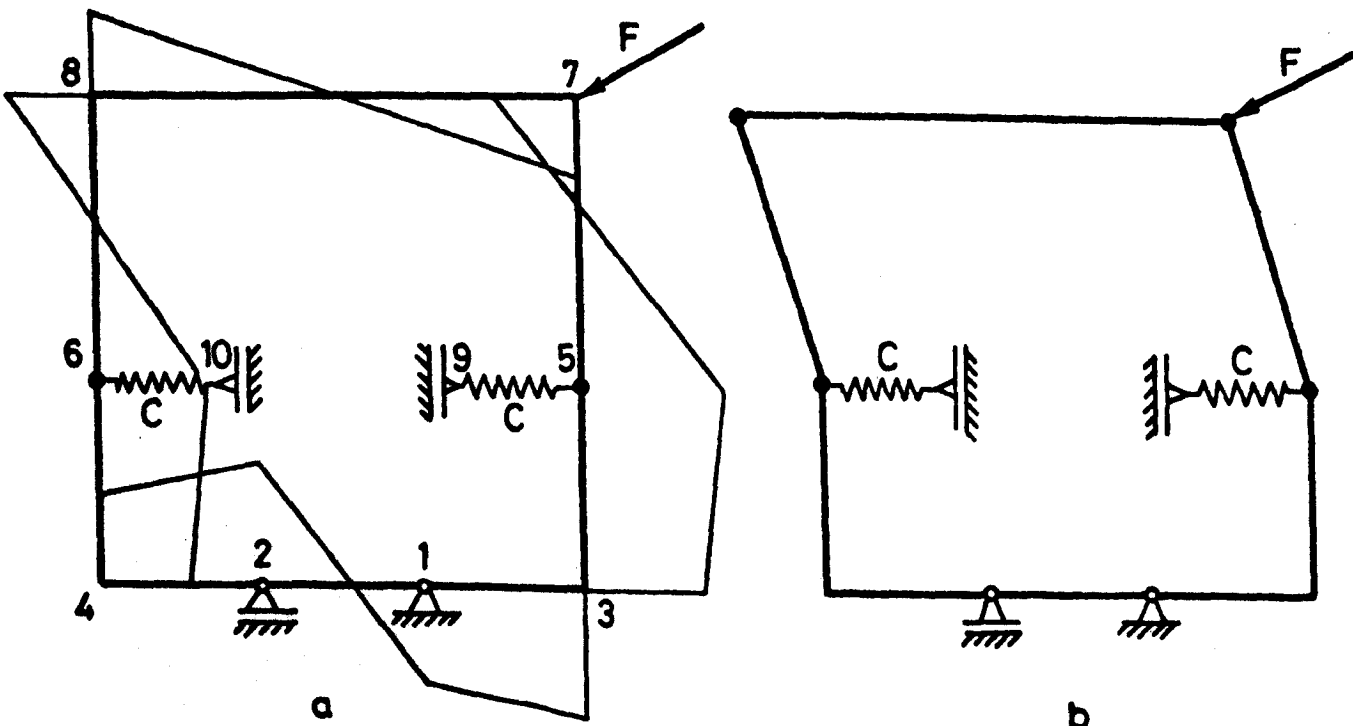


Fig. 3.3

The last sentence pointed out an important assumption that the effect of components simulated by the spring remains linearly elastic until the maximum resistance of the structure has been achieved. In practice this implies good beam joints and skin attachments.

Shortening of arms of the collapse mechanism has increased the strength of this ring by 64% which can be easily derived by applying the energy principle of elementary plastic analysis. The energy absorption for the same lateral movement of the roof has also been increased.

A similar study has been applied to an incomplete ring (Fig. 3.4a), appearing in areas where engine or transmission should be accommodated. Such a ring is very flexible in both vertical and horizontal directions. However, in a real structure it is restrained by the rest of the side structure. Assuming that the lateral stiffness $c = 150 \text{ N/mm}$ is relatively constant, it is possible to calculate the critical stiffness of springs c_1 which would produce the collapse mode in Fig. 3.4b. In the case considered this minimum value was approximately $c_1 = 100 \text{ N/mm}$, which already exists in current bus designs.

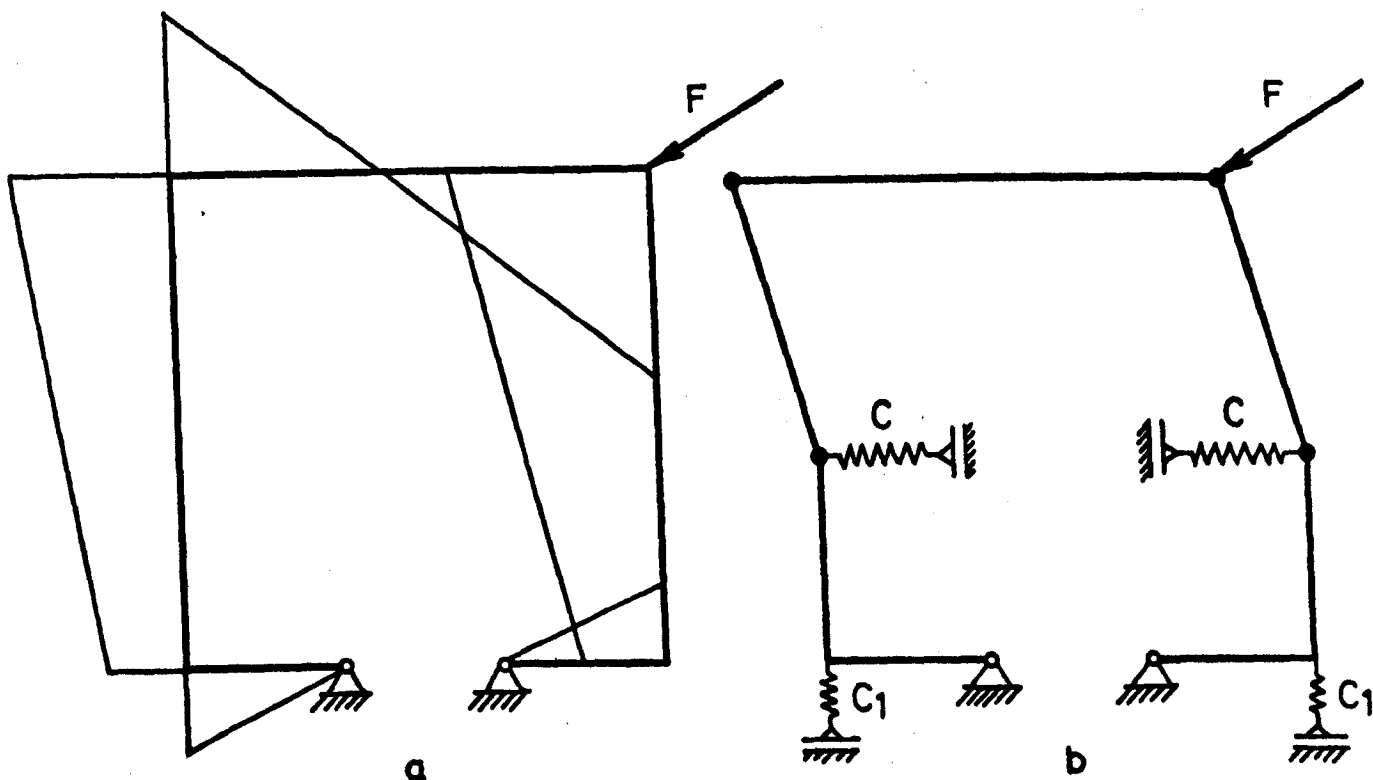


Fig. 3.4

This simple analysis has shown that collapse mode can be controlled by the appropriate selection of various body components. The number of incomplete rings should be minimised, but the potential drawbacks which they imply can be successfully eliminated.

The above examples have been used to illustrate the preceding argument. The quoted spring characteristics may or may not be exceeded in a real structure. Each ring may be subject to different conditions and the effect of skin has not yet been considered. In order to create a more realistic idealisation for collapse analysis, a fairly comprehensive elastic model has been introduced first.

3.4.3 The Elastic Model

The elastic model (Fig. 3.5) has been produced following the general procedure of finite element modelling. The actual structure was observed first on the production line, but the basic geometry, beam section dimensions, methods of joining and panelling were taken from drawings.

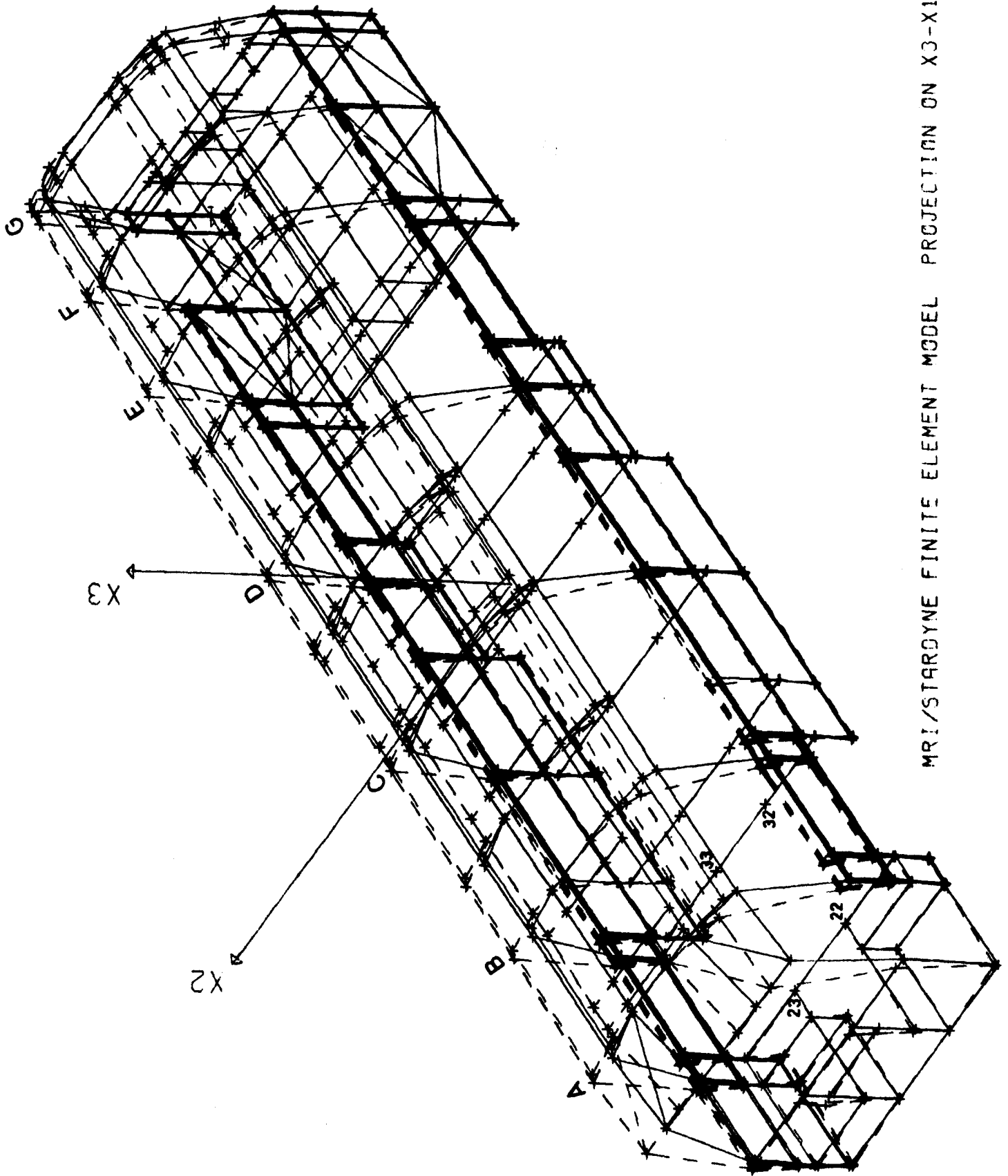
All structural members of the skeleton and all panels except the floor have been allowed for. Floor, seats, windows and all moving parts of the body (doors, skylights, covers, etc.) have been left out. Properties of the floor to side connection may vary a lot and the effect of seats on the collapse mode in actual accidents was not always evident. The prime interest of the analysis is to consider the effects on the structural behaviour before the contribution of seats may become important. Windows may increase significantly the strength of the roof, particularly in the fore and aft and vertical direction. However, their effect on lateral strength is less pronounced, and, what is more important, their contribution is very unreliable because most of them break during the accident. The effect of the moving parts is also either negligible or very unreliable.

All joints between beam elements are assumed rigid. This is a reasonable assumption for the welded joints between rectangular tubes. Satisfaction of the joint strength requirements brings them very close to the theoretical assumption. The pillar to floor member bolted joints can also provide reasonable rigidity.

Roof panels have been idealised by flat membrane elements, following the actual sheet segments. Care was taken that the aspect ratio does not exceed the limits suggested by the program manual in order to make the results as accurate as possible. Four triangular elements were used in the very front of the roof. The modulus of elasticity of aluminium was taken as 69000 N/mm^2 .

Front and rear bulkheads are produced from glass reinforced plastic. The exact properties of that composite and anisotropic material were not known and a fairly low modulus of 23000 N/mm^2 with Poisson's ratio 0.15 was assumed. The possible error in properties could not have affected the results significantly, because these panels are mounted on a relatively flexible, open section framework.

If the panels of the luggage compartment are connected efficiently, they can make a significant contribution to rear end stiffness. Good joints can be manufactured even when, as in this case, hardboard panels are used. The analysis assumes good joints and does not, therefore, take into account any possible deterioration of this material in service. A modulus of 23000 N/mm^2 and Poisson's ratio of 0.33 were assumed.



MRI/STARDYNE FINITE ELEMENT MODEL PROJECTION ON X3-X1 PLANE

Fig. 3.5

The panelling of the sides was offset from the beam axes by inserting short, stiff beam elements between the appropriate main beam nodes and corners of the plate. No numerical problems were reported by the program which continuously monitored the matrix decomposition process. Rectangular membranes were distributed to follow the actual sheet metal segments, and the element aspect ratio was again kept within specified limits.

Floor panelling on either side of engine bay has also been included in the model.

The structure was supported at each floor member to chassis connection. All supports were fixed in translation, but free to rotate. This arrangement is most appropriate for the actual body to chassis fixings. Here again one had to abandon the real roll over situation in which the actual support is at the cant rail while chassis flies in the air. However, supports are away from the collapse mechanism and no chassis deformation has been observed in accidents. It therefore appears reasonable to assume a constant relative distance between support points. The two aluminium "T" sections extending behind the rear axle run along the whole chassis, so they were idealised as cantilevers starting from the rear end of the chassis.

The complete model had 400 nodes with 2328 degrees of freedom, 556 beam elements, 4 triangular membrane elements and 141 quadrilateral membrane elements. The program used was STARDYNE-STAR for static, elastic analysis, supplied with computing facilities by the Control Data Corporation (CDC) service centre in London. The beam elements were based on the engineering theory of bending without section warping effects. These are quite adequate for rectangular or square tubes, and the open section beams were not used as a part of the main load carrying assembly. The simple triangular or quadrilateral membrane elements were used because the actual metal sheets have a low bending stiffness (membranes), the real interest was concentrated on the load distribution in the skeleton rather than panelling and finally, the elements employed ensure a sufficiently accurate solution in a most economic manner.

The external loading was applied to the tops of the nearside pillars. This was the simplest way of producing the required lateral movement of the roof.

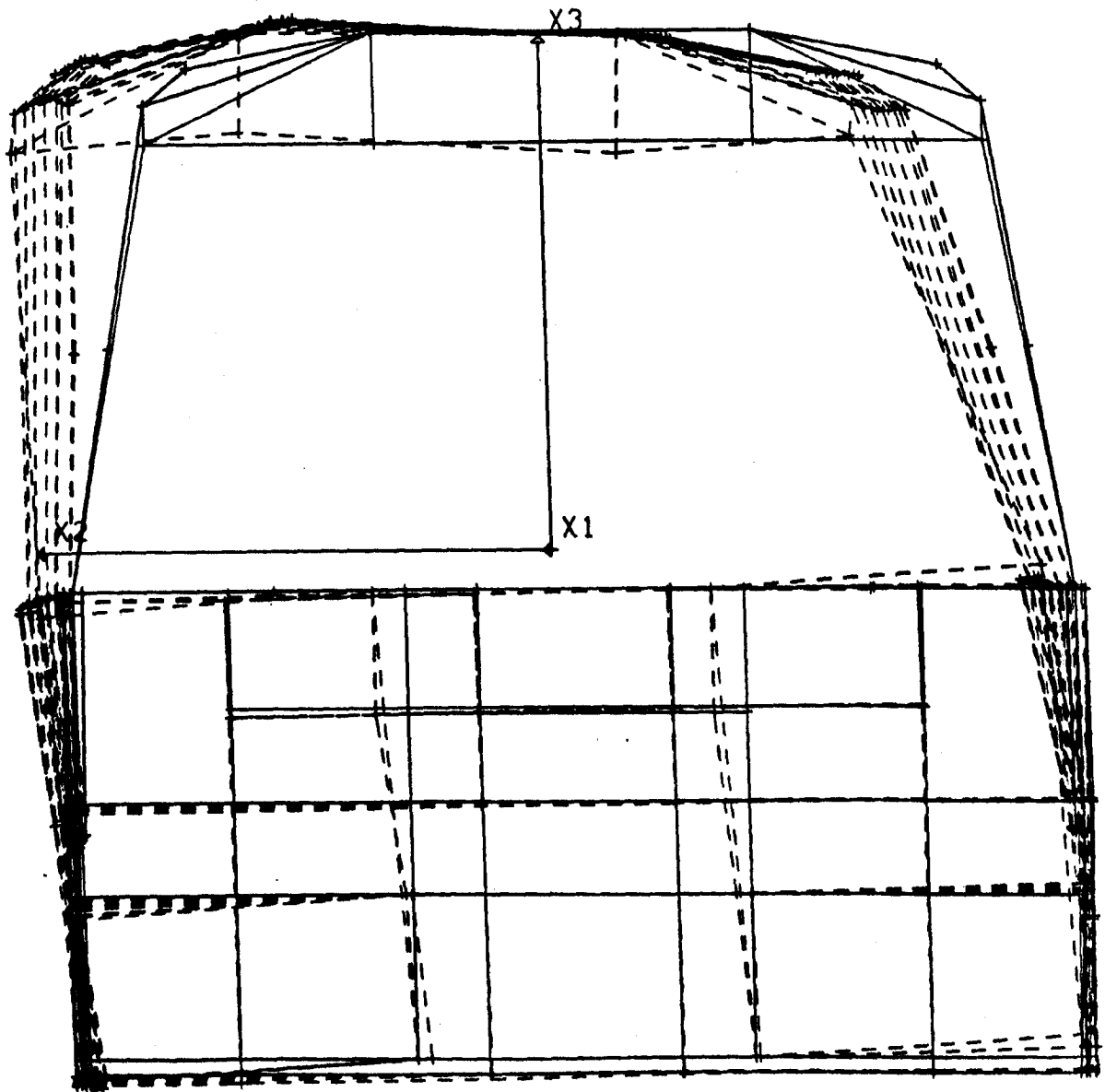
After geometry check the calculation was performed on a CDC CYBER 175 computer. The results included the nodal displacements, internal loads at the ends of each beam and corner forces of each plate element. The plots of deflected shape were also produced in one case.

The dotted lines in Fig. 3.5 and 3.6 represent deflected shape of the structure subject to 5500 N oblique loads applied to the joints between the pillars and near side cant rail at 30° to the floor member. Note the twisting deflection of the body due to an uneven distribution of lateral stiffness along the body.

3.4.4 Effect of Incomplete Rings on Load Distribution in the Elastic Model

Simple analysis in Fig. 3.4 indicated that the potential drawbacks of incomplete rings may be eliminated in an actual bus structure. The intention of the following study is to examine the same effect under more realistic conditions.

CRANFIELD BUS



MRI/STARDYNE FINITE ELEMENT MODEL PROJECTION ON X2-X3 PLANE

Fig. 3.6

Two models as shown in Fig. 3.5, with the exception of inner skins, were compared under identical loading conditions obtained by applying a pure lateral displacement (inwards) of 60 mm to the nearside cant rail. This value was chosen because at that deflection the rings gave maximum resistance in laboratory tests. The only difference between the two models was that in the second case elements 22-23 and 32-33 (Fig. 3.5) have been deleted.

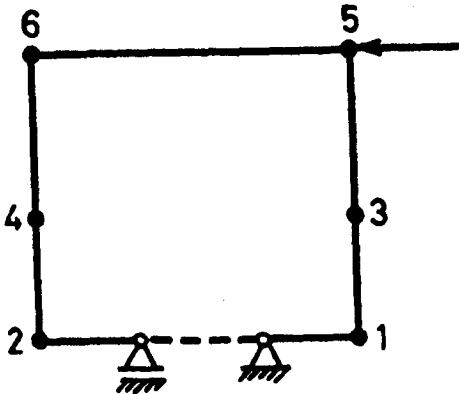


Fig. 3.7

The analysis has shown that rings play a major role in resisting the described loading conditions. Longitudinal members in the whole structure are loaded much less, which is not surprising. The pillars and roof cross members in rings were stressed most. Bending moments in floor members were relatively larger in places, but these beams are much stronger than the pillars.

Absolute values of maximum bending moments at characteristic places in rings were compared and summarised in Table 3.1. The reference points in rings are marked in the simplified diagram in Fig. 3.7. The ring notation is taken from Fig. 3.5. Moments M_1 in Table 3.1 refer to the model with all rings complete, and M_2 to the second case. The front and rear bulkheads are not included in the Table since their contribution to the collapse behaviour is less important.

Table 3.1

Ring	Reference Point	1	2	3	4	5	6
A	M_1 (Nm)	1010	360	-224	537	-1259	1325
	M_2 (Nm)	712	288	-196	430	-1029	1143
B	M_1 (Nm)	-300	250	-283	234	-1360	1022
	M_2 (Nm)	-224	201	-230	210	-1222	914
C	M_1 (Nm)	1464	1394	-542	536	-1733	1590
	M_2 (Nm)	1339	1290	-480	489	-1610	1515
D	M_1 (Nm)	1340	1251	-704	701	-1705	1435
	M_2 (Nm)	1325	1265	-686	694	-1670	1442
E	M_1 (Nm)	-2383	-2126	-975	959	-1912	1530
	M_2 (Nm)	-2383	-1214	-975	957	-1909	1534
F	M_1 (Nm)	-1060	1244	-1334	823	-2170	1380
	M_2 (Nm)	-1194	1415	-1342	826	-2173	1384
G	M_1 (Nm)	229	238	-2698	2331	-2394	1430
	M_2 (Nm)	334	248	-2671	2251	-2519	1512

The results in Table 3.1 show that the front rings take less load than the rear ones due to an uneven distribution of lateral stiffness. The rear part is stiffer than the front, and only the rear rings would collapse at 60 mm lateral deflection of the roof. The two incomplete rings make the front half even more flexible, and cause a further relative drop of loads. The effect is much less towards the rear of the bus, but even in the front the difference is not great. This proves again that if the number of incomplete rings is relatively small their potential drawbacks are minimised. However, excessive elastic deformations of a too flexible structure reduce the available plastic deformation before intrusion into the survival space and hence reduce the energy absorbing capacity of the structure.

A comparison of the same structures has been made when applying an oblique lateral force of 5500 N at 30° to the floor to each joint between pillars and cant rail on the rear side. The selected load was close to the maximum resistance of pillars in laboratory tests. The results are summarised in Table 3.2 with the same meaning as in Table 1.

Table 3.2

Ring	Reference Point	1	2	3	4	5	6
A	M ₁ (Nm)	1590	464	-496	770	-1970	2230
	M ₂ (Nm)	1340	420	-490	725	-1890	2225
B	M ₁ (Nm)	-330	274	-460	257	-1750	1264
	M ₂ (Nm)	-330	300	-460	250	-1770	1275
C	M ₁ (Nm)	1675	1575	-785	620	-2176	1805
	M ₂ (Nm)	1690	1600	-780	616	-2240	1860
D	M ₁ (Nm)	1396	1354	-862	762	-1886	1532
	M ₂ (Nm)	1490	1460	-900	808	-1980	1640
E	M ₁ (Nm)	-2105	-1958	-1004	905	-1844	1482
	M ₂ (Nm)	-2160	-2010	-1030	930	-1890	1530
F	M ₁ (Nm)	-1025	1312	-1243	719	-1983	1315
	M ₂ (Nm)	-1050	1330	-1250	726	-2000	1330
G	M ₁ (Nm)	329	-252	-2261	2019	-2123	1499
	M ₂ (Nm)	300	-224	-2240	2000	-2110	1485

The internal load distribution is more even than in the displacement case because the stiffness variation along the structure has less effect. The difference in internal loads between the two structures is even less than in Table 3.1, confirming the previous comments on the effect of a small number of incomplete rings.

3.4.5 The Model for Collapse Analysis

Identification of the collapse mode allows generally a more crude idealisation of the actual body than does the elastic analysis. The collapse model may

include only a part of the complete assembly which will envelope the collapse mechanism.

The other reason for making the collapse model as simple as possible are computing costs. The "quasi-static" calculation process described in section 3.2 requires the assembly and decomposition of the stiffness matrix for each loading increment, which is the most expensive part of calculation. However, the collapse analysis model must include the important effects on the actual collapse mechanism.

The collapse model in Fig. 3.8 was developed using the results of the elastic analysis. The structure in Fig. 3.5 with double skins in sides was loaded by oblique concentrated loads of 5500 N applied to the joints between pillars and the nearside cant rail, at 30° to the floor. The deflection shape is shown in Figs 3.5 and 3.6, and the bending moment diagrams in rings are given in Figs. 3.9, 3.10, 3.11 and 3.12.

It was mentioned in section 3.3 that displacement increments were to be applied in the collapse analysis, but such that the reactions are at 30° to the floor beam. These conditions are not quite the same as the ones with equal loads at each joint. However, if the elastic and plastic models behave similarly under common constant loads as above, then the plastic model can be reliably used for slightly different conditions as well. An exact reproduction of collapse loading conditions would have required rotation of the complete elastic model through 30° and repeating the run, but this could not be justified in terms of labour, time and costs.

The collapse model includes the structural rings A to G (Fig. 3.5), but not the front and rear bulkheads made of GRP and mounted on relatively light beams. The lower parts of pillars in rings F and G were also deleted because these rarely fail below waist rail due to the effect of the luggage compartment - this experience from the accident survey is confirmed by the bending moment diagrams in Figs. 3.11 and 3.12. The curvature of the roof bows did not shift the maximum moments from the cant rail nodes, so straight roof members were assumed.

The elastic properties of all beams in rings, cant rails, waist rails and lower rails in the sides are the same as in the elastic model. The roof structure behaves almost as a rigid body (this agrees with accident data) and the effect of the deleted roof skeleton and skins has been idealised by diagonals (Fig. 3.8) with a high stiffness axially and in the roof plane, but flexible in every other sense. Similarly, the diagonals in the side were stiff axially and in the vertical plane, but flexible otherwise. Selection of the other diagonals in each field might have been better to simulate the diagonal tension in skins due to twist of the whole structure. However, the diagonals selected simulate the effects of both skins and framework and equal cant rail displacements are assumed in the collapse analysis, so that the twisting effect will be negligible.

Rings A to E were supported in the same way as in the elastic model. Nodes 51 and 52 of the ring F were restrained in vertical translation only (due to the side stiffness), while nodes 57 and 58 of ring G were only allowed to rotate about the longitudinal (X1) direction. A fictitious beam 57-58 was then introduced to reproduce the bending

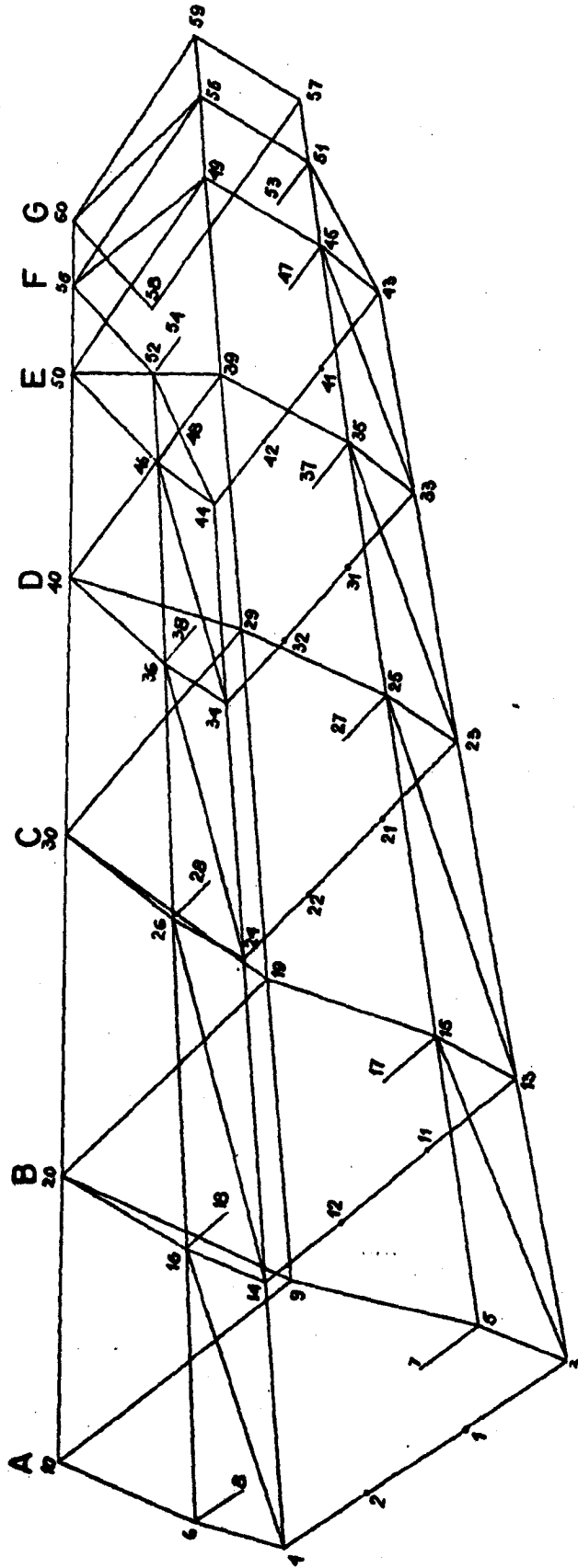


Fig. 3.8

moments at these nodes obtained in the elastic model.

Fictitious horizontal springs (Fig. 3.8) were attached rigidly to the waist rail/pillar joints, following the argument of section 3.4.2. Opposite ends of the springs were fixed in translation, but set free to rotate. The axial and bending stiffness of each particular spring were selected aiming to reproduce the bending moments at characteristic points in rings (floor, waist rail and cant rail joints). The actual bending moment diagrams have "steps" which are due to the effect of panels and adjacent beams. The steps in the collapse model are created by the spring bending and waist rail twisting and the effect of axial spring stiffness was described in section 3.4.2.

After the first trial and two corrections the bending moment diagrams at characteristic points of the collapse model got the values marked by small triangles in Figs. 3.9, 3.10, 3.11 and 3.12. The aim of the model is to identify a correct collapse mechanism, i.e. the location and sequence of hinge occurrence. This does not require an exact coincidence of moments, but the relative magnitudes should follow the same pattern. Ring A (Fig. 3.9a) gave a reasonable agreement except at node 4. The collapse moment of the pillar at node 4 was therefore doubled. A similar intervention had to be done at nodes 13 and 14 of ring B (Fig. 3.9b). These two rings are assumed with continuous pillars, while in the elastic model they are connected to the floor members via separate stump pillars (Fig. 3.5). The moments in stump pillars were also relatively low. Rings C and D showed a good agreement (Fig. 3.10) while the rotation about longitudinal axis of nodes 43 and 44 of Ring E had to be subsequently restrained in the collapse model (Fig. 3.11a) due to the effect of the luggage box. Rings F (Fig. 3.11b) and G (Fig. 3.12) also showed a good agreement within the included part of structure. Further improvements were possible, but the agreement achieved was considered sufficient for the purpose. A correct collapse mode and maximum resistance were expected, and the mentioned differences could have only a small effect on the load deflection curve before collapse.

All fictitious springs were 450 mm long and had properties listed in Table 3.3.

Table 3.3

Beam	Axial Stiffness (N/mm)	Second Moment of Area (mm ⁴)
5-7	0.005	10000
6-8	4.64	30000
15-17	0.046	1
16-18	0.046	1
25-27	0.046	20000
26-28	0.092	20000
35-37	0.046	60000
36-38	0.046	60000
45-47	0.005	70000
46-48	696	20000
51-53	0.005	100000
52-54	0.005	40000
(57-58)	/	1 = 2400 mm 800000

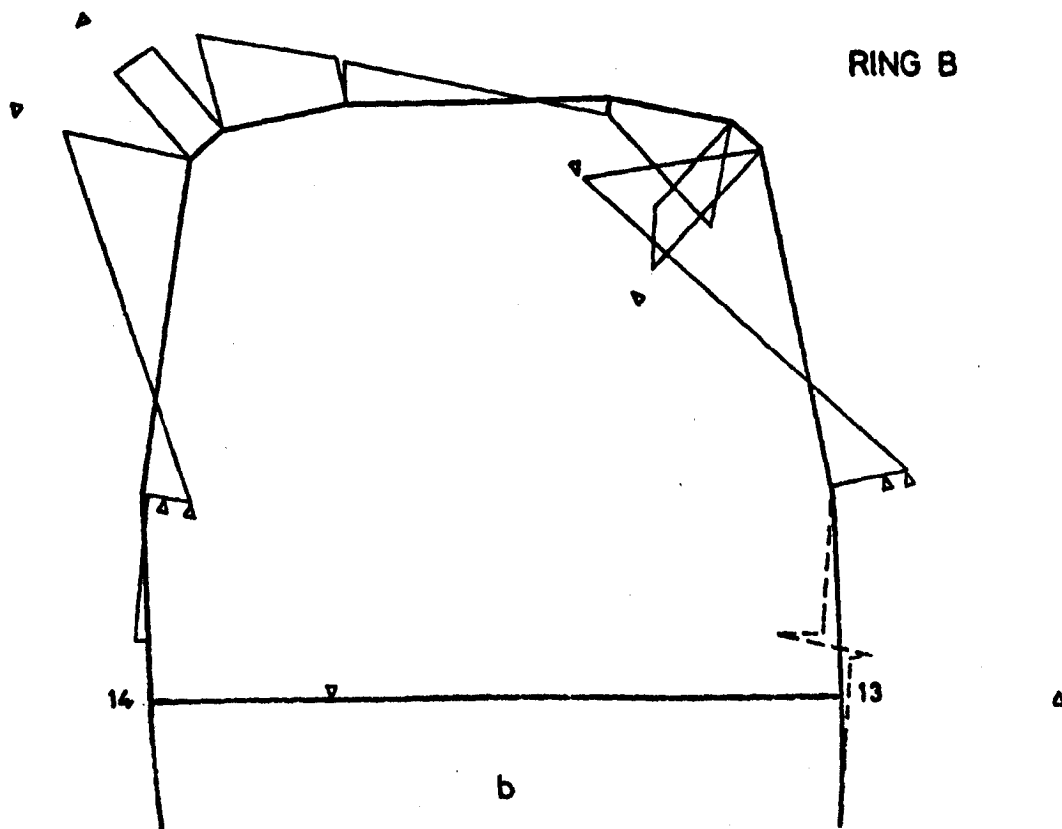
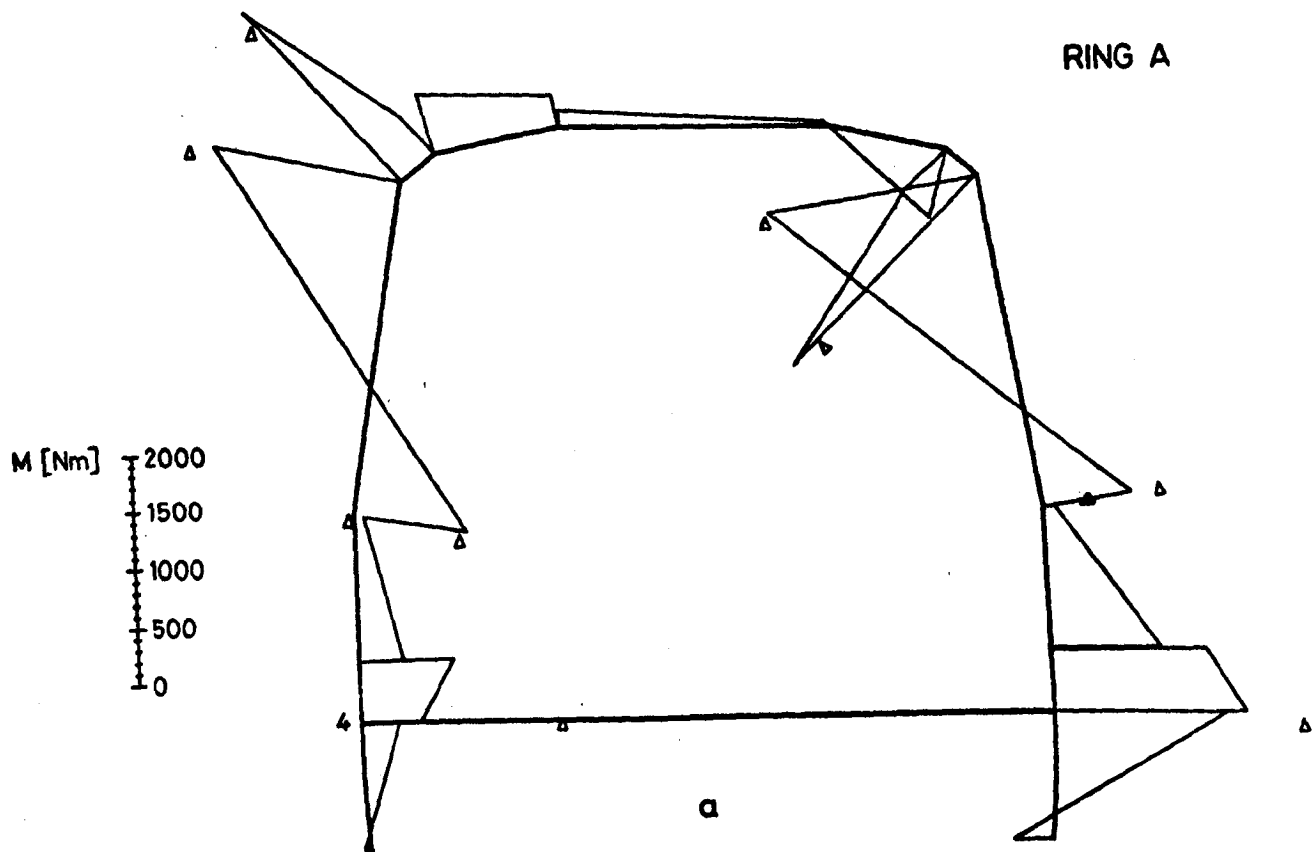
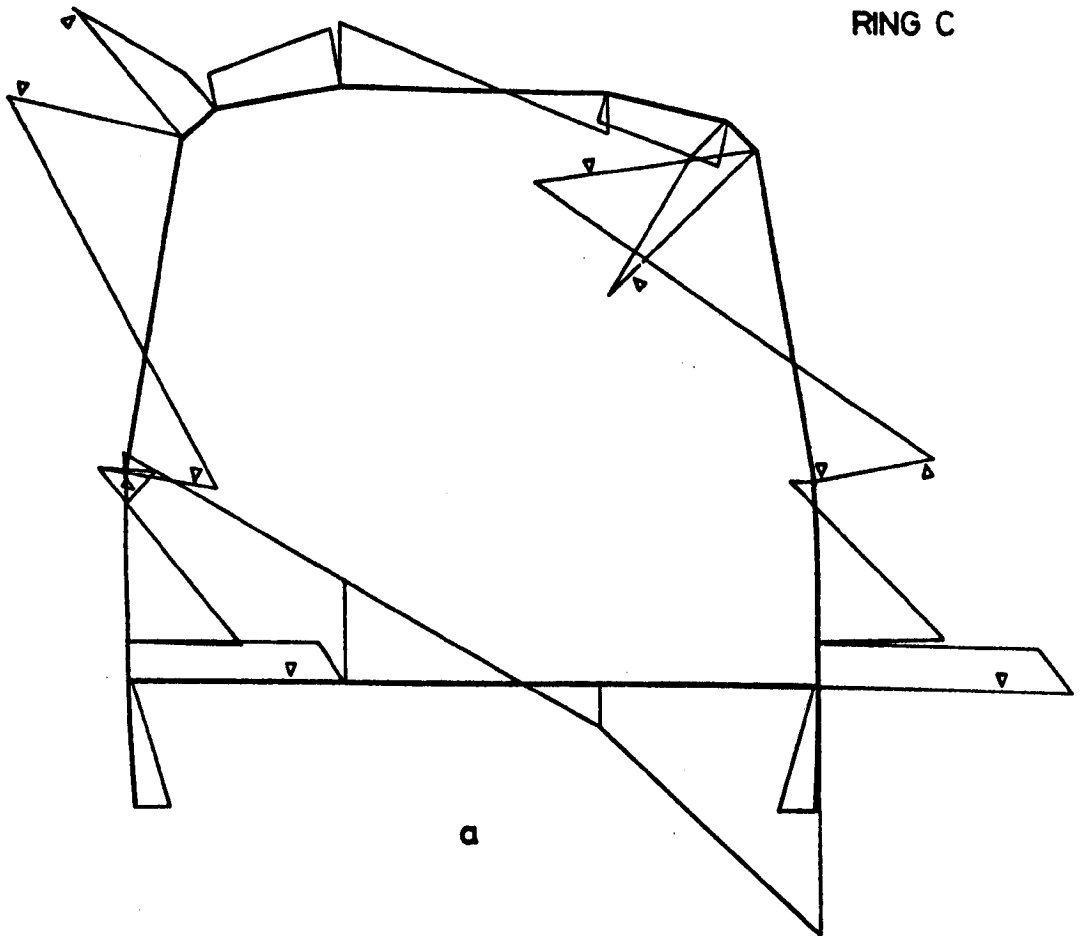
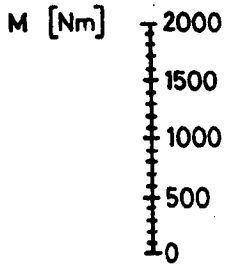


Fig. 3.9

RING C



RING D

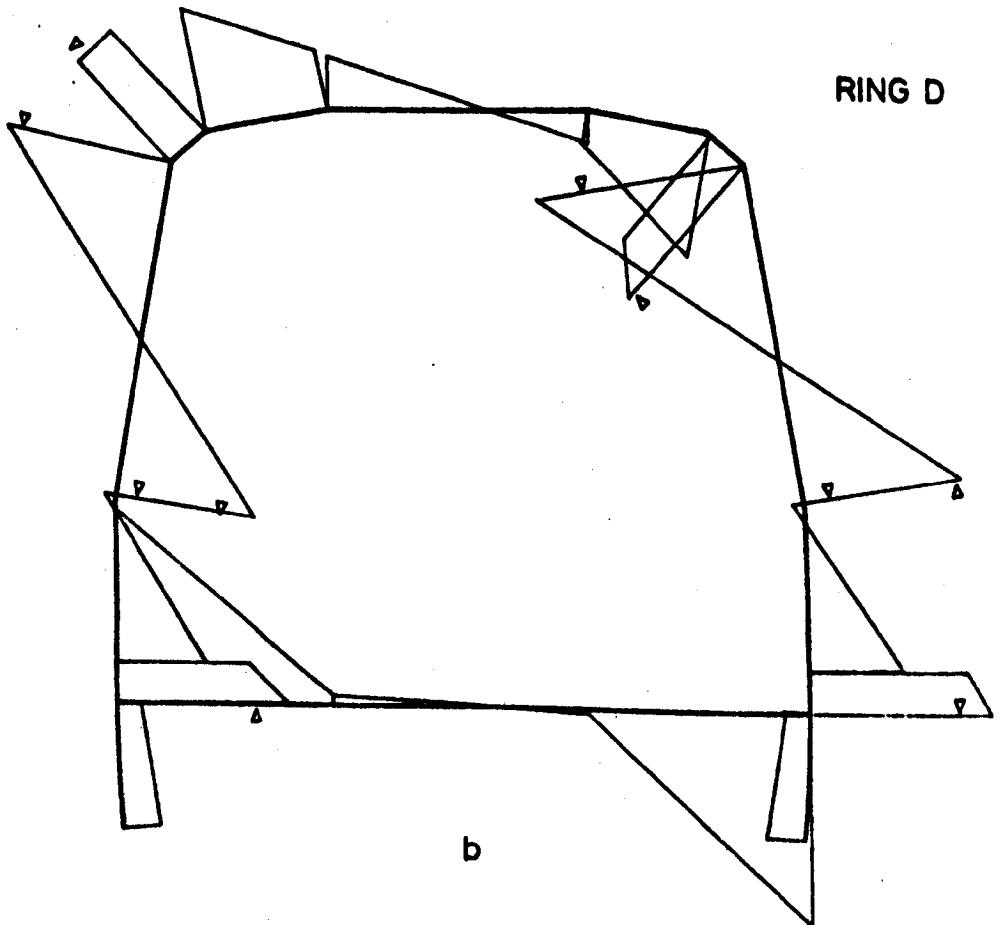
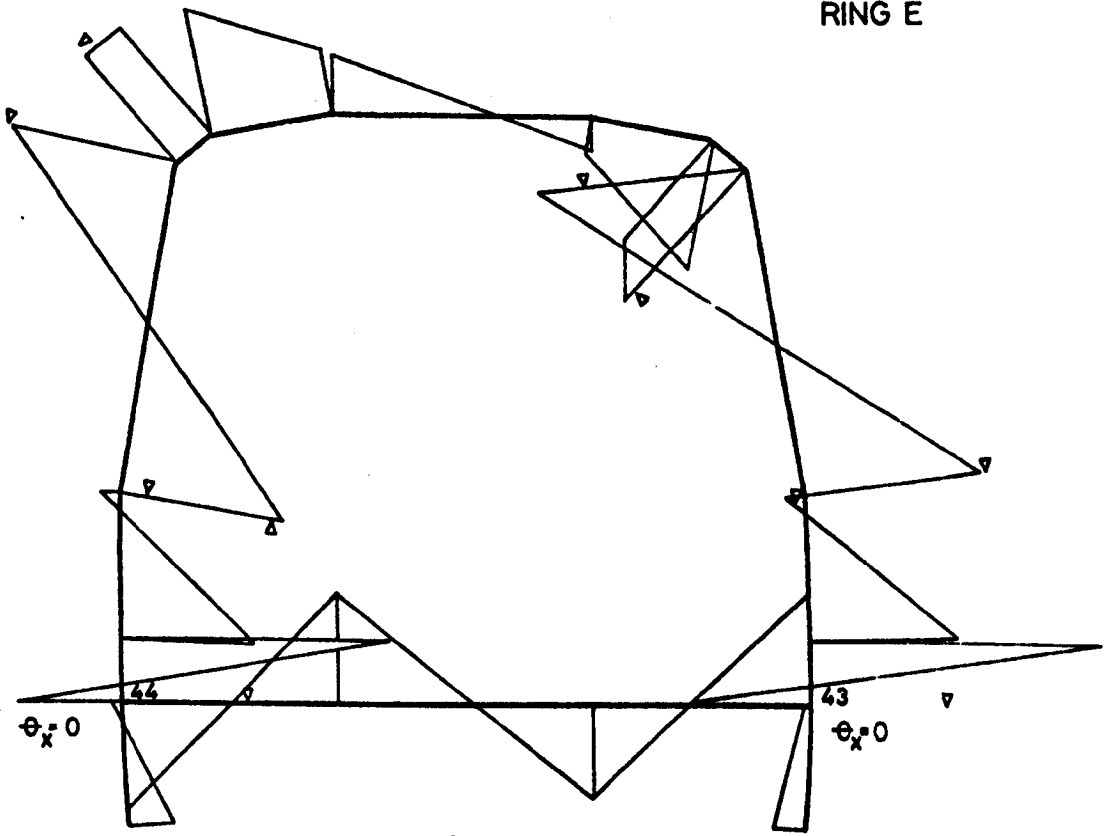
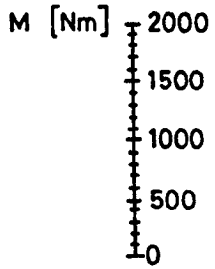


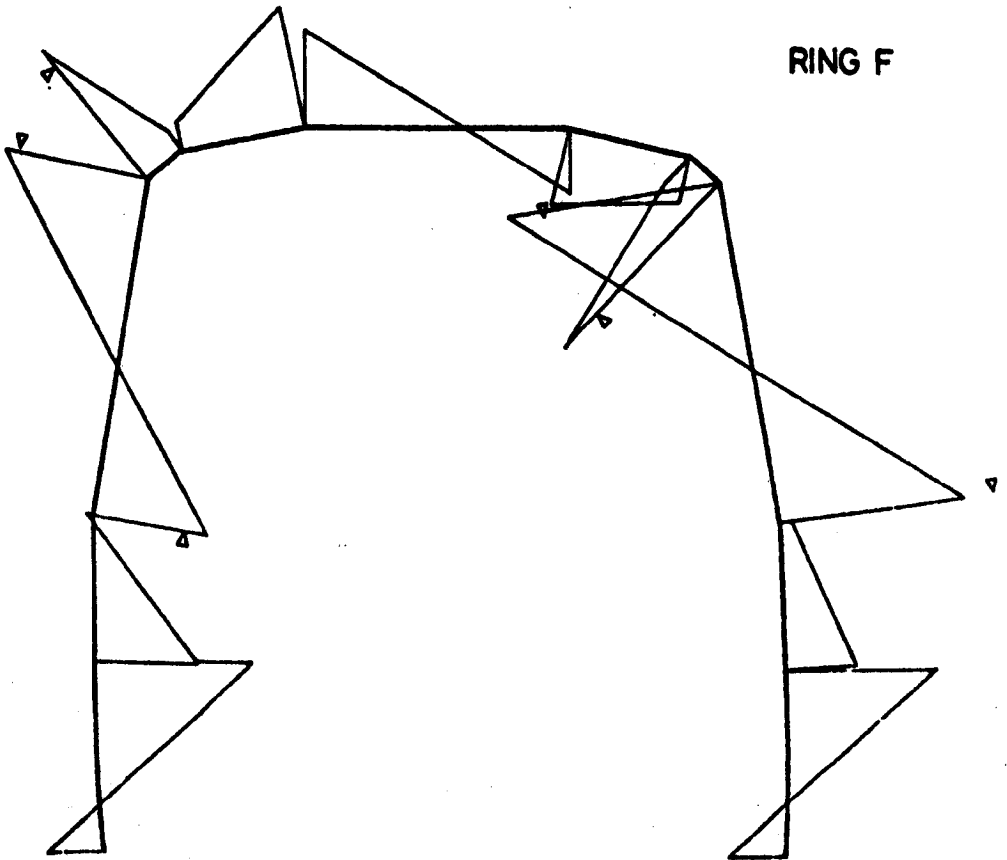
Fig. 3.10

RING E



a

RING F



b

Fig. 3.11

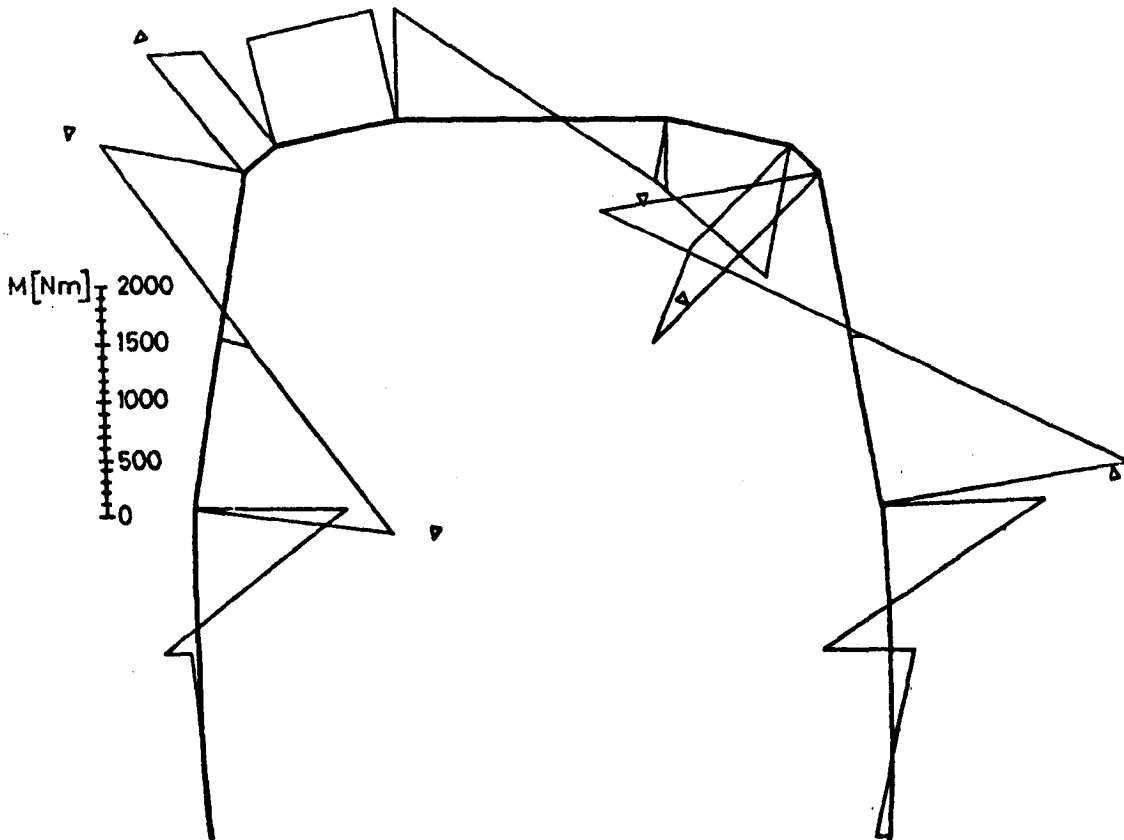


Fig. 3.12

A wide range of spring properties has been employed to match the moment diagrams of the elastic model. The big difference in axial stiffnesses obtained here and in section 3.4.2 is caused by the fact that springs in Table 3.3 simulate the effect of components which have been left out of the collapse model of a complete structure, while section 3.4.2 considers an isolated ring. Springs combining the above properties are not physically realistic and serve as a pure mathematical model.

Plastic properties of beams were calculated allowing for the elastic stability of compression flanges. All tubes had stable enough walls to develop fully plastic moments about both principal axes. Rotation in hinges before the peak resistance of the structure is relatively small, so that fully plastic moments were assumed constant.

An elliptic yield criterion:

$$\left(\frac{M_y}{M_{py}}\right)^2 + \left(\frac{M_z}{M_{pz}}\right)^2 > 1 \quad (3.1)$$

was adopted, where M_x and M_y are the current bending moments about local axes of the section, and M_{py} and M_{pz} are the respective "pure" fully plastic values. The shape factor of each section was taken as 1, which implies an abrupt transition from elastic into a fully plastic state. No normality condition was employed and a spherical hinge was inserted wherever the yield condition was satisfied. All these assumptions are justified by the facts that

- a. stresses due to bending are by far the highest in the type of structure considered;
- b. All thin walled sections have the shape factor close to unity and the difference produces negligible effects.
- c. The normality condition developed in the classical plastic analysis of stable section beams to define the position of the plastic neutral axis does not apply to sections which buckle locally after yielding has occurred. A spherical hinge relaxes the kinematical constraints and therefore the results err on the side of safety.

All diagonals in the collapse model had big collapse moments in order to maintain their role in the load distribution. Failures in diagonals would produce effects not experienced in practice.

The collapse moments of fictitious springs depend on the quality of the waist rail to pillar joint and on the behaviour of adjacent panelling. A drop in the load carrying capacity of a spring may be caused by failure in either beam or panel joint or by panel buckling. The experience of accident surveys shows that the above details are reasonably strong in metal structures and the occurrence of plate buckling was not always evident. Big collapse moments in springs have been assumed which again implies that the effect simulated will be linear and that joints will not fail.

All joints in the collapse model were assumed stronger than the beams they are connecting. This is a very important assumption which is often not satisfied in reality. However, the current analysis defines very well the loading conditions of all the important joints, so that the actual design can be checked for their strength. A detailed analysis of each connection would be required to make sure that the strength and energy absorbing properties of beams are utilised.

3.5 THEORETICAL COLLAPSE MECHANISM AND STRUCTURAL STRENGTH

Formulation and decomposition of the structural stiffness matrix has to be done for each increment separately, which makes the calculation relatively expensive. The rounding off errors tend to accumulate in such an incremental procedure, particularly as the structural stiffness starts decreasing. This had to be borne in mind since the collapse model was fairly big for the solution routine used in the CRASHD program. Equal increments have to be applied in the current version of the program, which does not provide an optimum utilisation of the number of steps available. Too small increments increase the number of steps, out of which many may be used before the structure even starts collapsing. Too large increments, however, tend to over-estimate the local and overall strength because the calculated yield criterion (3.1) may become considerably larger than unity and a mechanism with more than one degree of freedom can be produced eventually.

One way of improving the program would be to use an arbitrary load or displacement increment for each step and scale the results (internal loads and displacements) up or down to produce the next single hinge. This would be very good if the elastic deformations between subsequent hinges

are not large (so that the effect of changing geometry is lost), or if the total number of hinges of the collapse mechanism is not too big. If there are many hinges several small increments could be quite adequately covered by a single, but somewhat larger one. Another possibility may be to start with larger increments and reduce them gradually after occurrence of the first hinges.

The economic and computational reasons have been allowed for when deciding to select a constant 25 mm increment of lateral deflection applied to the near side cant rail (nodes 9, 19, 29, 39, 49, 55 and 59 in Fig. 3.8). Six steps were taken to produce a maximum displacement of 150 mm. The structure was arranged as in Fig. 3.1c in order to obtain a reaction at 30 deg. to the floor cross members.

The theoretical collapse mode with hinge locations predicted by the first collapse run is depicted in Fig. 3.13. The first hinges were produced in the rear part of the body after 50 mm deflection. As the deflections increased the hinges started appearing more and more towards the front which is normal since the structural stiffness decreases in the same longitudinal direction. The collapse mode "A" (Fig. 2.1), with hinges at the waist rail and cant rail levels, appears in all rings except in ring A which collapses in mode "B". The results also indicate that the pillars of rings C, D and E have also very high stresses at the floor level. For instance, ring C starts collapsing in the "F" mode after 100 mm deflection, but the rest of the structure converts the initial mode into mode "A" during the next two increments.

Hinges were also predicted at the top ends of each pillar. The roof cross members were only 14% less strong than the pillars, so that the local bending moments could exceed the strength of both members within one step of calculation. The moments at the cant rail joints are shared between the ring and cant rail, so that the pillar may theoretically fail first. The local moment distribution was therefore studied at each cant rail joint and it was decided that the actual hinges will occur in the roof members only (Fig. 3.13). A similar analysis had to be applied to the offside lower part of ring E.

The collapse moments of fictitious springs and pillars were equal, but the following springs still failed in bending: 51-53 after the 2nd step, 25-27 and 35-37 after the 3rd step and 15-17 and 38-36 after the 5th step.

Cumulative reactions at the loaded nodes are listed in Table 3.4.

Table 3.4

Ring	A	B	C	D	E	F	G	Total Reaction R[N]
δ [mm]	R ₉ [N]	R ₁₉ [N]	R ₂₉ [N]	R ₃₉ [N]	R ₄₉ [N]	R ₅₅ [N]	R ₅₉ [N]	
25	987	1439	2491	4123	5327	-2877	8742	20232
50	1904	2852	4932	8175	10807	-6034	17232	39058
75	2791	4218	7224	12028	16654	-11694	20071	51292
100	3822	6539	9247	11200	16564	-12943	21583	56012
125	4736	5313	12172	10020	16368	-13717	22638	57530
150	5656	5413	12077	9627	16394	-14434	23271	58004

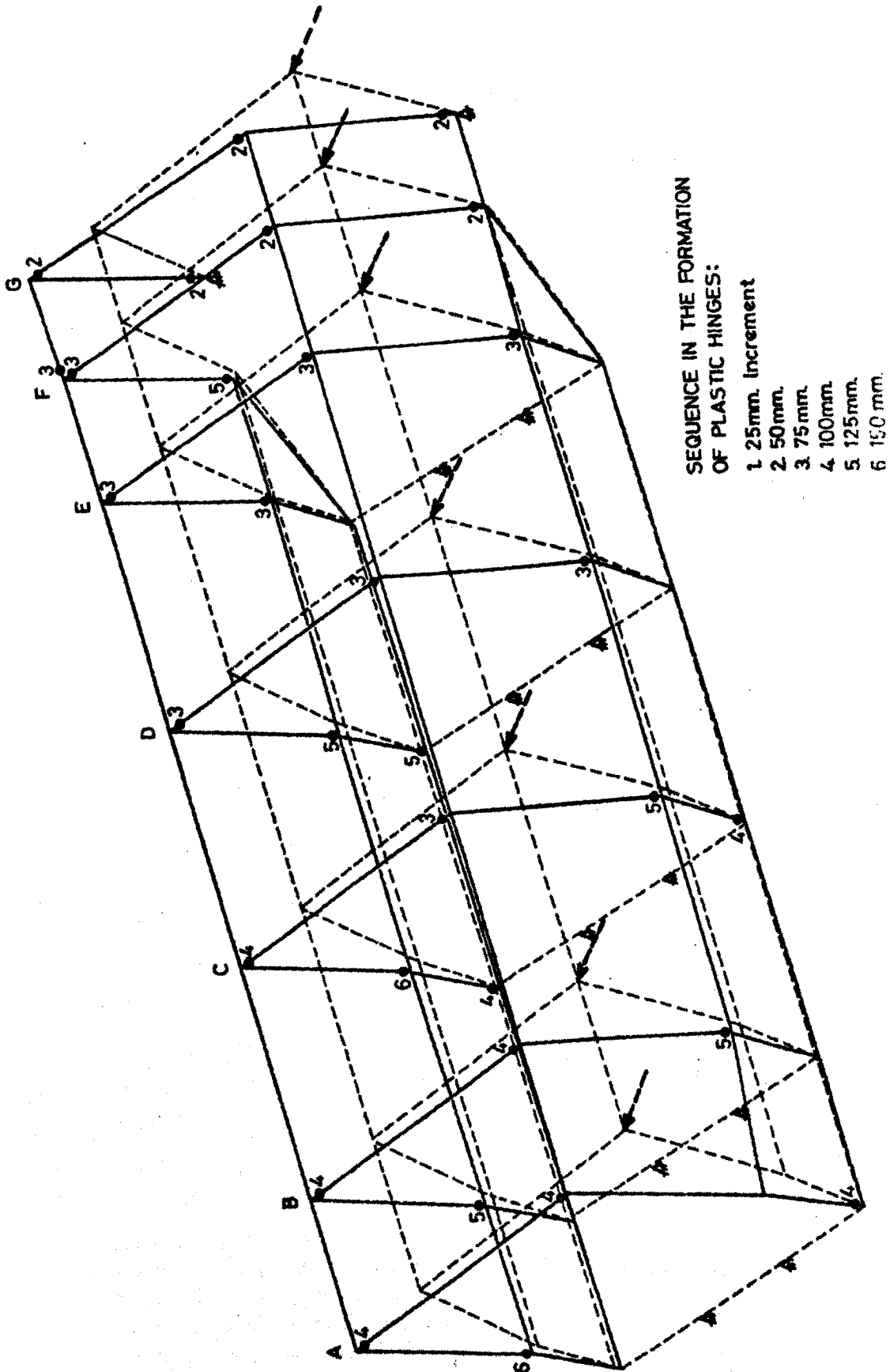


Fig. 3.13

The interesting and surprising point about Table 3.4 is the negative reaction at node 55 of ring F (Fig. 3.8). This implies that ring F tends to deflect slightly further if the rest of the roof is pushed by the same amount. A pulling force is therefore required to align node 55 with the rest of the cant rail. It was difficult to explain the cause of such a behaviour and the first step of calculation was repeated using the STARDYNE program. The results were within 1% of the values above, so the CRASHD calculation was accepted as correct. However, a pulling force cannot be supplied by the ground and it was decided to repeat the collapse calculation with modified loading conditions.

The second collapse run was done with seven increments of 25 mm displacement applied to nodes 9, 19, 29, 39, 49 and 59, leaving the node 55 unloaded. Collapse moments of fictitious springs were doubled.

The second collapse mode was the same as the first one in Fig. 3.13 with the same sequence of hinge occurrence. The only difference was that no springs failed and that hinges at 15, 16 and 26 occurred later than in the first attempt. This was due to a larger share of moments taken by the springs which did not fail. Other comments regarding the first collapse mode and internal load distribution in the rings apply here as well. Lateral displacement of node 55 was always slightly bigger than the rest of cant rail, the maximum difference being 0.97 mm at 175 mm lateral deflection.

Cumulative ring reactions of the second run are shown in Table 3.5 and plotted in Fig. 3.14 (curve R).

Table 3.5

δ [mm]	R_A [N]	R_B [N]	R_C [N]	R_D [N]	R_E [N]	R_G [N]	Total Reaction R [N]
25	1045	1372	2349	4217	3727	7387	20097
50	2019	2717	4654	8339	7534	14363	39626
75	2954	4001	6837	12276	10561	14248	50877
100	4020	6261	8809	11276	10203	14957	55526
125	4904	5130	11744	9797	10053	15434	57062
150	5739	5548	11346	9407	10046	15504	57590
(175)	(6562)	(6006)	(10923)	(9000)	(10000)	(15620)	(58111)

Having established the collapse mode of the rings B to G (Fig. 3.13) it is possible to use the isolated ring idealisation in Fig. 3.3a and repeat the collapse calculation with smaller displacement increments than for the complete body. The overshoot of local strengths is thus greatly reduced and the collapse load of a ring is much closer to its actual value. The stiffness of fictitious springs of $c = 200$ N/mm was chosen so that the lateral stiffness of the isolated ring gets close to the average lateral stiffness of the bus body (middle rings). The theoretical hinge moment drop off during rotation, as explained later (section 7.6), was also included and the maximum strength of 6913N at $\delta = 125$ mm was obtained.

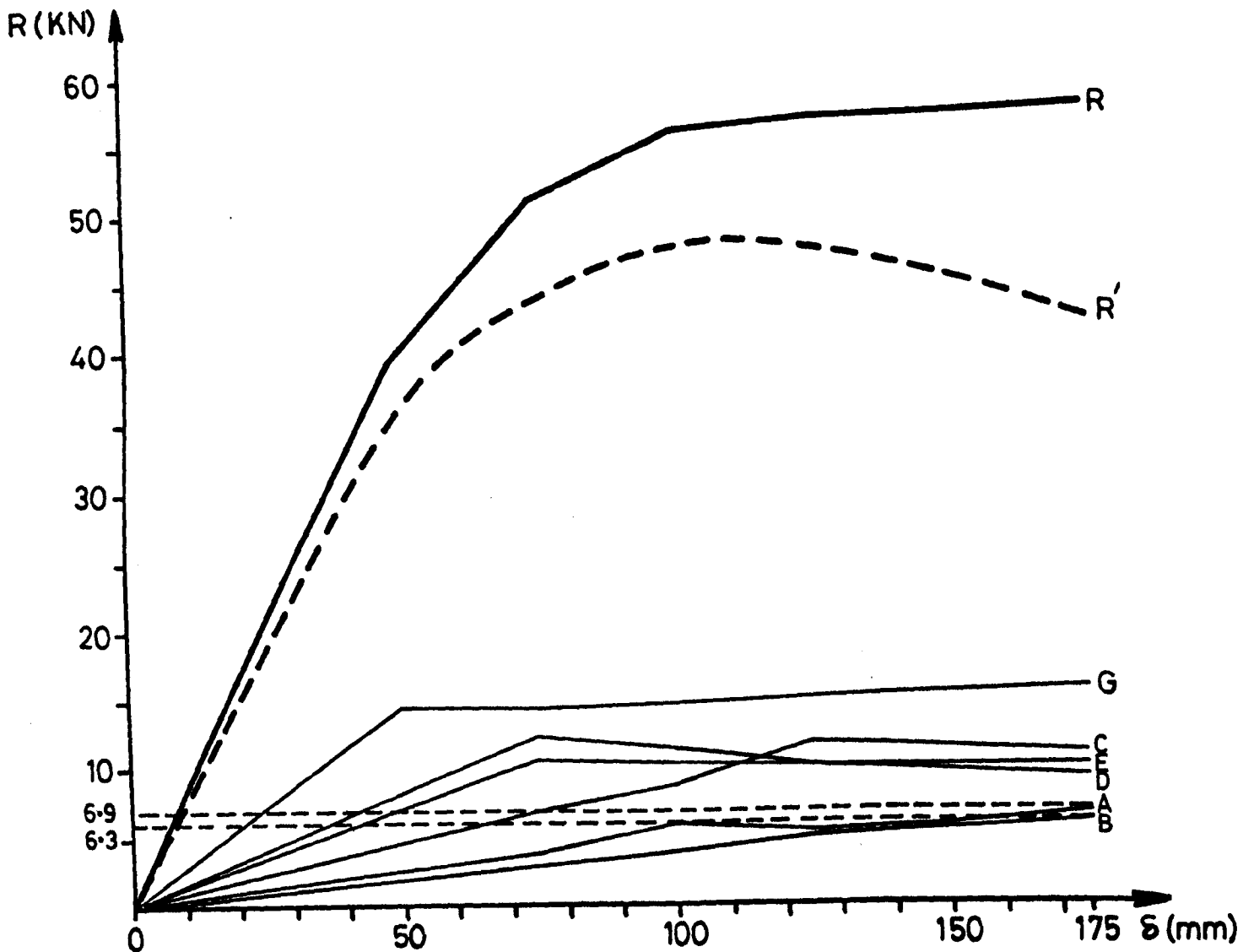


Fig. 3.14

A similar calculation was repeated for ring A (Fig. 3.8) with the stiffness of the nearside fictitious spring of 20 N/mm and the other one of 200 N/mm. The collapse mechanism was the same as of the ring A and the maximum strength was 6286 N, also at $\delta = 125$ mm.

The cumulative reaction of the six rings (B to G) collapsing in mode "A" (Fig. 2.1) and one (A) collapsing with one hinge at the floor level gives the dotted curve R' in Fig. 3.14 which is closer to the actual quasi-static reaction of the complete body. The maximum strength of 47767 N is 17% less than the original figure of 58000 (curve R). The subsequent reduction in resistance (R') is due to the gradual decrease of the hinge strength with rotation.

The initial stiffness of the actual body may be slightly lower than the curve R' would suggest due to the finite stiffness of structural joints prior to collapse. This effect cannot be allowed for by the present form

of the program CRASHD, i.e. only rigidly fixed or pinned beam ends can be specified.

Resistance of a ring in a bus body is produced both by the ring itself and by the effect of the surrounding structure. The effective resistance of the indirectly loaded ring F is therefore distributed to the other rings, particularly to the nearest ones. This is the main reason why some of the rings in Fig. 3.14 exceed the theoretical limit of 6.91 kN. The pulling force of ring F in the first collapse run (Table 3.4) was balanced by abnormally increased reactions of the nearest rings but the total reaction increase was the same as in the second case (Table 3.5).

Some overshoot of the theoretical strength is also due to the previously discussed effect of the increment size on the calculated value of the yield criterion (3.1). The overshoot was particularly large in the rear part of the structure, and could be reduced by taking much smaller increments.

The area under the curve R' is proportional to the estimated energy absorbed by quasi-static elastic-plastic deformation of the structure. This energy is 6.5 kJ for the lateral deflection of the roof of 175 mm. Energy accumulated in the fictitious springs is negligible. An increase of 10-30% may be expected under dynamic conditions due to strain rate effect, provided that fractures do not occur.

The structure considered in this report has not been tested or seen after a roll over accident. However, the collapse mode predicted (Fig. 3.13) reproduces the significant features observed during accident survey and bus ring tests:

- a. All rings have collapsed in mode "A" (Fig. 2.1) except the one next to the door which displayed mode "B".
- b. The pillars in rings C, D and E are highly stressed at the floor level, bringing the whole structure fairly close to a state from which various collapse modes may originate. For example, exclusion of the inner panels in the side would reduce the stress drop at the waist rail and increase the tendency to produce mechanisms with hinges at the floor level. Sheet buckling or bad joining to the side skeleton would have the same effect. On the other hand, additional support by the floor panels and particularly seats would enhance the tendency to produce collapse mode "A" with hinges at the waist rail.

CHAPTER 4

BENDING COLLAPSE CHARACTERISTICS OF VEHICLE STRUCTURAL COMPONENTS

4.1 INTRODUCTION

Determination of the PSV collapse mode in Chapter 3 was an essential step in the roll over collapse analysis. However, the actual performance of the structure after it starts collapsing will also depend on the behaviour of hinges of the collapse mechanism. A part of kinetic energy may be absorbed by permanent deformation of elements away from the main hinges (e.g. local dents in sides or roof not affecting the collapse mode), but in the most dangerous case of "pure" cant rail impact it is safer to assume that all the energy absorbed by the structure goes into the hinges only.

Load carrying capacity of a structure after impact will also be directly affected by the remaining hinge strength.

The original plastic analysis of frames was not concerned with the behaviour of a structure after it starts collapsing. The method was employed by civil engineers to calculate the strength of structures, avoiding some difficult problems of the elastic analysis: joint stiffness, support conditions, imperfect fabrication, initial stresses, etc. All these are often difficult to specify, but may influence significantly the results of an elastic analysis. Their effect on the maximum load carrying capacity is much less or non existent, hence it could be used as a more reliable theoretical information. The use of elastic beam properties was often unnecessary and that was a great help, particularly before the application of computers in structural analysis. The method was applied to structures with beams that were stable with respect to overall (Euler) buckling and also to local section buckling under elastic and plastic deformations. Deflections before collapse were assumed relatively small and the fully plastic moments developed at hinges were taken as constant throughout the hinge rotation. All these assumptions were often quite adequate for the purpose.

Collapse analysis of vehicle structures introduces, however, a number of peculiar problems. Vehicle bodies are built in different ways ranging from spot welded sheet metal pressings over composite designs to all steel skeletons clad with sheet metal or plastic skins. Connections between adjacent elements are also very versatile. Thin walled components are universally applied, raising the question of elastic and plastic stability before and after the local collapse has been initiated. Other forms of local failures affecting the load carrying capacity of hinges are also common. All these factors become particularly important in frequent cases where not only the initial strength, but also the behaviour of a collapsing structure and remaining strength should be determined.

4.2 STIFFNESS, STRENGTH AND ENERGY ABSORPTION PROPERTIES OF HINGES

Consider a simple test of a uniform cantilever AB in Fig. 4.1b. Gradual increase of the force F will produce initially elastic deformations of the beam. The maximum stresses occur at the root A because of the

maximum bending moment M at that point. The increasing load F will bring the moment M close to the maximum load carrying capacity of the beam and a non linear behaviour of the beam will be initiated. Non linearity may be caused by various effects (elastic buckling, partial plastic deformations, separation of fibres, etc.) depending on the beam design and material properties. In most practical cases the non linear behaviour will be confined to a localised area subject to highest stresses. Eventually the beam reaches its maximum load carrying capacity (M_{max}) and starts collapsing, usually in a form of a localised hinge failure. The slope at the hinge becomes discontinuous, enabling a definition of the hinge rotation angle θ . Further increase in force F may not be possible, but deflection δ can be incremented to obtain an appropriate $F-\delta$ diagram including both elastic and collapsing state of the beam.

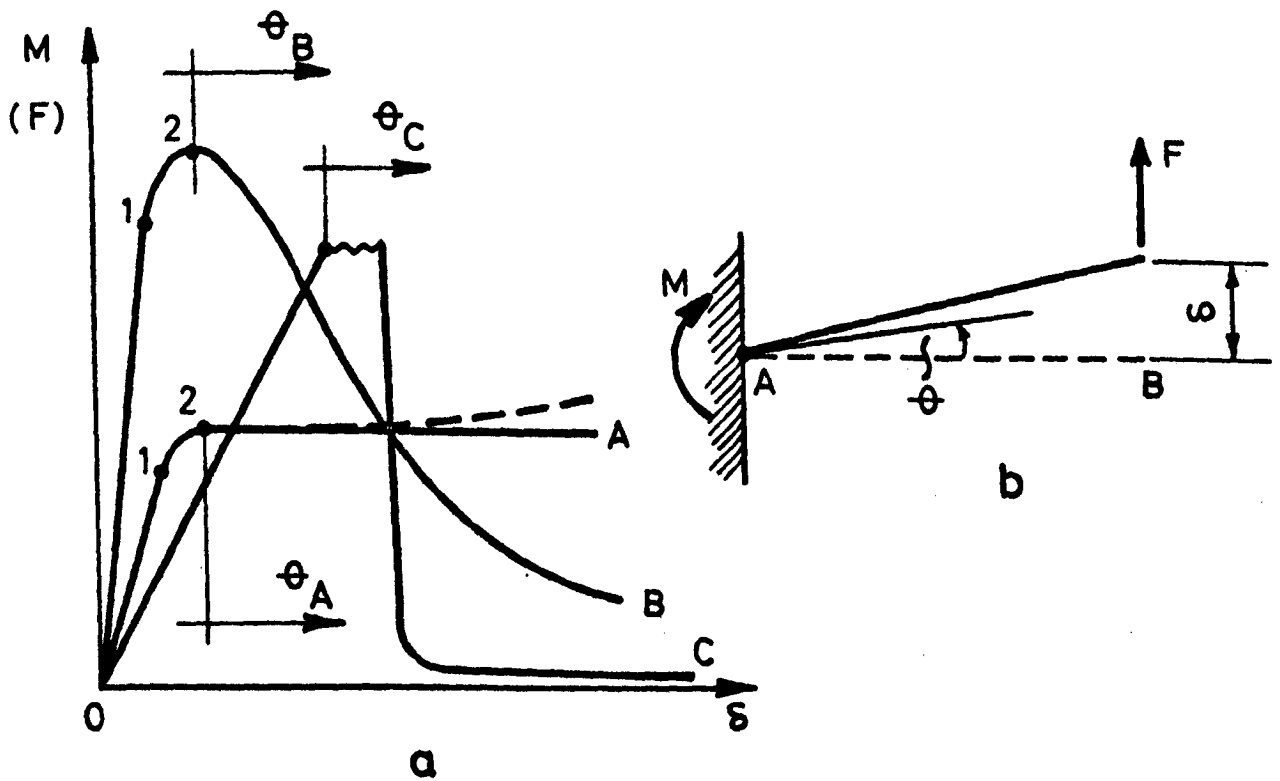


Fig. 4.1

A variety of load-deflection diagrams can be obtained by testing different beams and joints, and three possible cases are depicted in Fig. 4.1a to illustrate the argument to follow.

The STIFFNESS of the cantilever is an elastic property defined by the slope of the initial straight part of the $F-\delta$ diagram (in Fig. 4.1a cantilever B is the stiffest and C most flexible). The element stiffness in actual structures is determined by the elastic section properties of the beam and also by the stiffness of its joints. The joint stiffness

is a common and difficult problem in the elastic analysis of vehicle structures. It often varies depending on both direction and sense of bending. However, in a case of a welded steel tube skeleton it is often reasonable to assume rigid connections. This is particularly so if local reinforcements are employed to strengthen the joints.

The effective elastic properties of the beam depend on the design, manufacture and material. The effective bending stiffness of spot welded sheet pressings or composite beams may vary a lot depending on the characteristics of the connection (spot weld pitch, quality of bonding, anisotropic materials, etc.). It is generally less than the engineering theory of bending would suggest. The effective bending stiffness of spot welded (25 mm nominal pitch) closed top hat sections with welds in tension (23) ranged between 55 and 100% of the theoretical value, with higher percentage for smaller width to depth ratio. The deflections of open section beams also depend on the position of load with respect to shear axis and on the warping inhibition at ends. The effect of shear may become important in very short beams. In some aircraft elements the shear lag effect may also have to be included. Rectangular tubes considered in this thesis can be treated quite adequately using the engineering theory of bending.

Non linear elastic (buckling) and/or plastic behaviour takes place before the beam collapses - segments 1-2 in curves A and B (Fig. 4.1). The difference between the moments at points 1 and 2 depends on section design and material properties. In standard metal tubes this difference is relatively small, particularly if no elastic buckling of section walls precedes collapse (the plastic shape factor is close to unity). Deflections and energy absorbed within these limits are negligible, hence this non linear elastic/plastic range can be safely ignored. Hinge dimensions are generally small in comparison with the total beam length, so that the effective beam length can be assumed constant.

The term STRENGTH of a structure will be used to define its maximum load carrying capacity. It is not necessarily proportional to the stiffness (compare curves A and C in Fig. 4.1) and depends on the collapse mechanism and hinge properties. The strength of a structure changes during collapse which may be very important in a roll over accident since the deformed roof should support the vehicle weight. This variation is controlled by the hinge behaviour. It is convenient to discuss the hinge strength in terms of a moment that it can develop at a particular stage of deformation.

Curve A in Fig. 4.1 corresponds to the assumption of the classical plastic analysis that the collapse moment of a hinge remains constant. This is possible in solid section or thick walled beams made of a ductile material. There is little experimental evidence on the behaviour of these beams at larger angles of hinge rotation. The term "thick walled" cannot, therefore, be precisely defined. The ratio between the elastic buckling stress of the compressed flange (σ_{cr}) and yield stress of the material (σ_p) can be used as an approximate criterion. Local buckling during collapse was evident in beams with $\sigma_{cr}/\sigma_p \approx 13$ (test no. 6 in section 6.3), and little buckling and moment drop off was observed when $\sigma_{cr}/\sigma_p \approx 30$ (test no. 23 in section 6.3). Thick walled beams collapse with a continuous bend of a radius several times larger than the beam depth. Strain hardening of the material spreads the plastically deformed zones and some rise of the

effective hinge moment may even take place (dotted line in Fig. 4.1). Solid section or thick walled beams are hardly ever used as vehicle structural elements.

Curve B in Fig. 4.1 is characteristic for "semi thin walled" and thin walled beams which buckle locally either before or after the maximum strength is achieved. How thin walled a beam is depends on the ratio between the wall thickness and other section dimensions and on material properties (modulus of elasticity and yield stress). The more thin walled a beam - i.e. the smaller the ratio σ_{cr}/σ_p is, the steeper the moment drop off with hinge rotation will be. Vehicle body components generally fall into this category (e.g. Fig. 2.9), so that the classical collapse analysis cannot be applied to larger deformations. The necessity to evaluate and allow for the loss of strength with hinge rotation becomes essential in the collapse analysis of vehicle structures. The strength remaining in the structure after deformation does not have to be proportional to the maximum strength before collapse.

Curve C in Fig. 4.1 corresponds to a hinge collapse with separation of the material. Such failures were common in bus accidents (Figs. 2.6 - 2.8), especially in joints. Separation of material reduces abruptly the strength of the hinge, which usually falls very low. In some cases separation is complete, while in others the capability to transfer shear and axial force is preserved.

The ENERGY ABSORBED is proportional to the area under the $F-\delta$ curve (Fig. 4.1). The energy input is accumulated in the structure by elastic deformation of the beam and mainly plastic deformation of the hinge. The effective elastic and plastic contributions can be presented in a somewhat idealised form using the load-deflection diagram in Fig. 4.2.

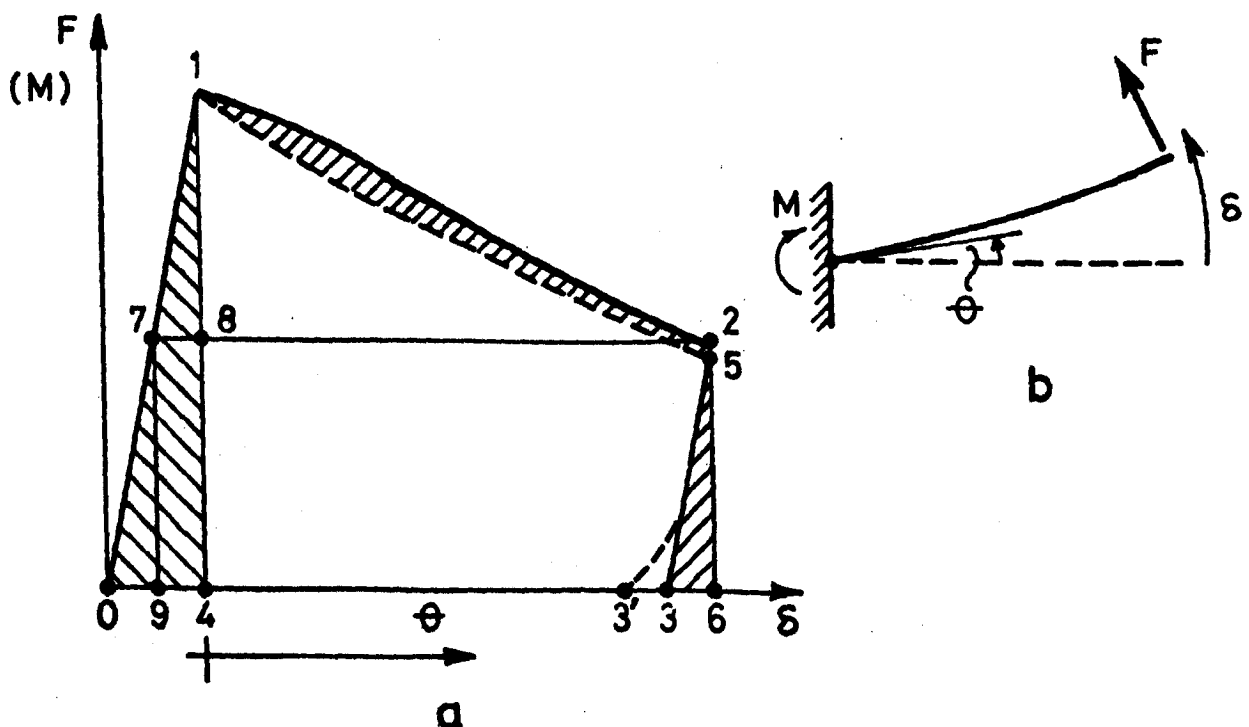


Fig. 4.2

The load-deflection curve of a structure, say the cantilever in Fig. 4.2b where F is always normal to the beam axis and δ is the arc drawn by the tip, is represented by an elastic part 0-1, segment 1-2 corresponding to the hinge rotation (θ) and an unloading, linear segment 2-3 (the actual unloading curve has a form 2-3' with a non-linear finishing part due to residual stresses after plastic deformation). Energy of elastic deformation accumulated in the beam is represented by the shaded area 0-1-4-0. Drop of the hinge strength will produce a drop in the load F along line 1-2. Bending moments in the beam will decrease producing a drop in the elastic energy proportional to the area 1-2-5-1, which is also equal to the area 1-4-9-7-1 (hinge dimensions are assumed negligible). Dotted line 1-5 can be determined by selecting a small decrement of load and subtracting the appropriate area under the curve 0-1 from the area under 1-2. If the hinge is small, lines 0-1 and 2-3 should be parallel, and the beam finally returns all the remaining elastic energy proportional to the area 2-3-6-2 or, equally, 0-7-9-0.

The energy absorbed in the hinge by pure plastic deformation is proportional to the non-shaded area 1-5-3-4-1 in Fig. 4.2. The elastic segment 0-1 is allowed for by the elastic calculation of the finite element program (compare with the elastic-partially plastic range of the load-deflection curve of the bus structure in Fig. 3.15). The rebound part 2-3 is not of interest if the vehicle finishes on its roof. The difference between areas 1-2-6-4-1 and 1-5-6-4-1 increases with the beam length, but in most practical cases it can be ignored.

Diagrams in Figs 4.1 and 4.2 show that the energy absorbing capacity of a hinge does not have to be proportional to either stiffness or maximum strength of a component. This is another reason why the hinge behaviour should be studied over the whole range of deformation.

An interesting practical example is shown in Fig. 4.3. Aluminium tube with thicker lips was tested as a cantilever in Fig. 4.1. The hinge characteristics are represented by the moment (M) - rotation (θ) curves. Curve 1 was obtained with lips in tension. The section was initially stable enough to develop a fully plastic moment, and the subsequent moment drop off was due to local buckling and material separation very similar to Fig. 4.4a. Separation occurred after $\theta = 20^\circ$. The second test (curve 2) was carried out with lips in compression. The same fully plastic moment was developed, but the thicker lips prevented local buckling at the hinge. The moment was almost constant up to 10 degrees of hinge rotation. However, excessive strains on the tension side produced separation of material (Fig. 4.4b) followed by an abrupt fall of resistance to a very low value. This shows that local buckling reduces the hinge moment, but may also have a positive effect by relaxing the tension side of the section from excessive strains. In the third case (curve 3) the tube was tested with an aluminium insert (Fig. 4.4a) and with lips in tension. The collapse mode of the section was not affected by the insert, but the total strength and energy absorbing capacity of the hinge were increased (Fig. 4.3).

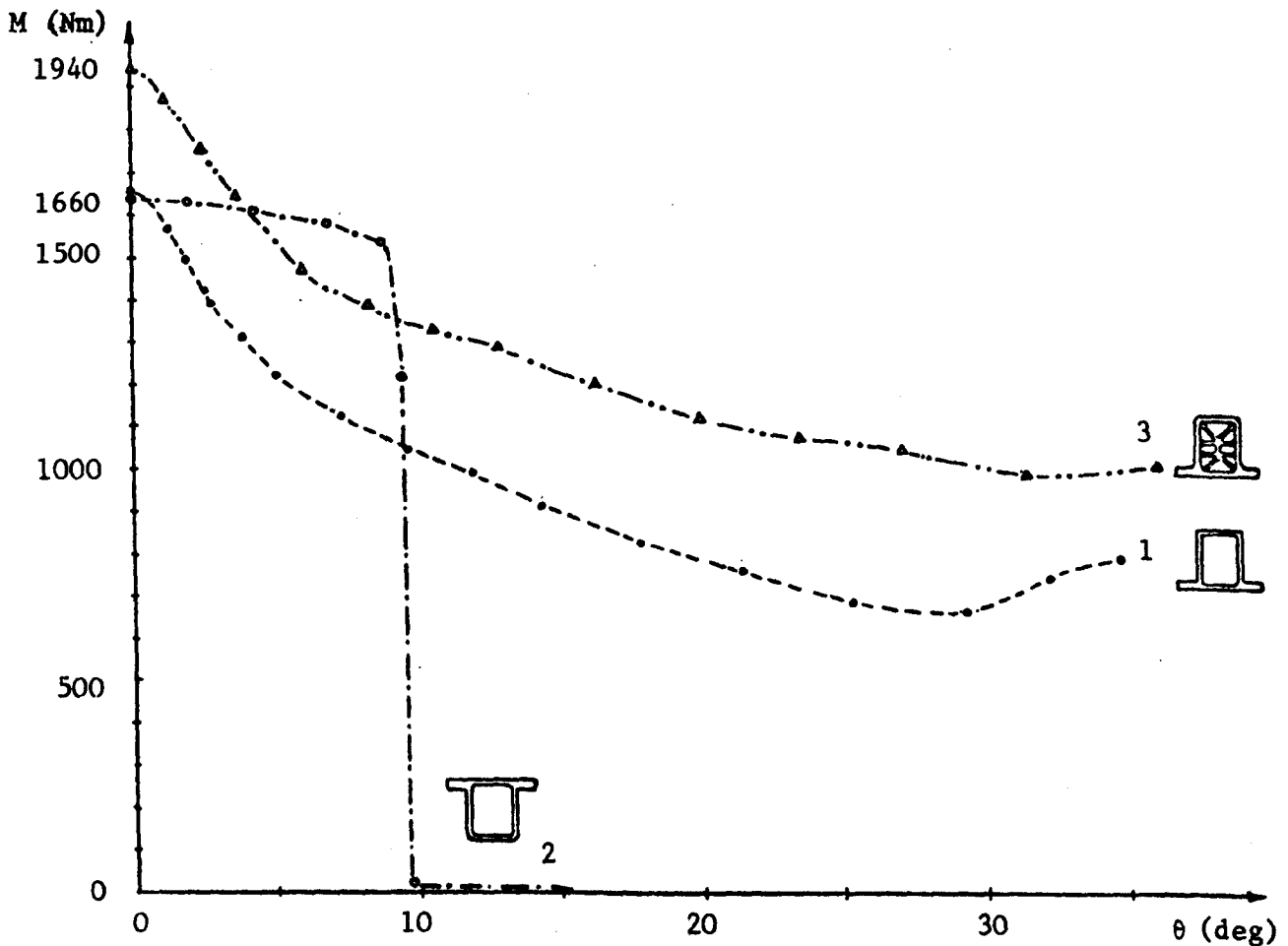
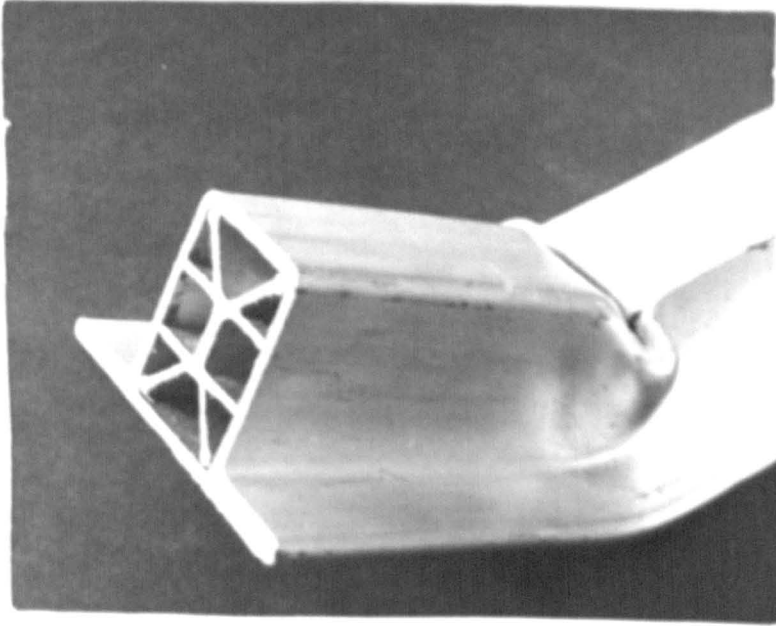


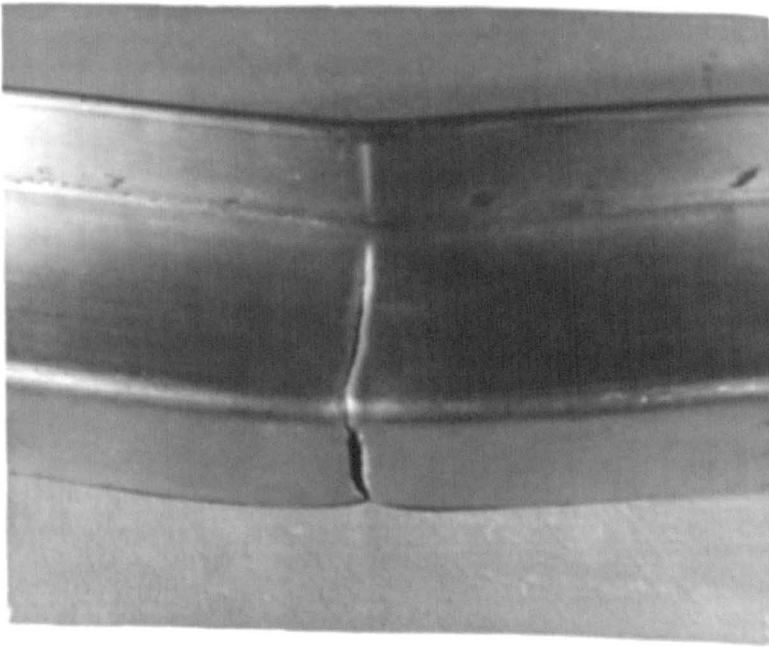
Fig. 4.3

Curve 1 in Fig. 4.3 is typical for the buckling collapse mode of rectangular section tubes. The energy absorbed at the hinge after it rotates through 30 deg. (proportional to the area under curve 1) is 510 J and it represents only 58% of the energy corresponding to a constant fully plastic moment. The remaining hinge strength is only 40% of the maximum value.

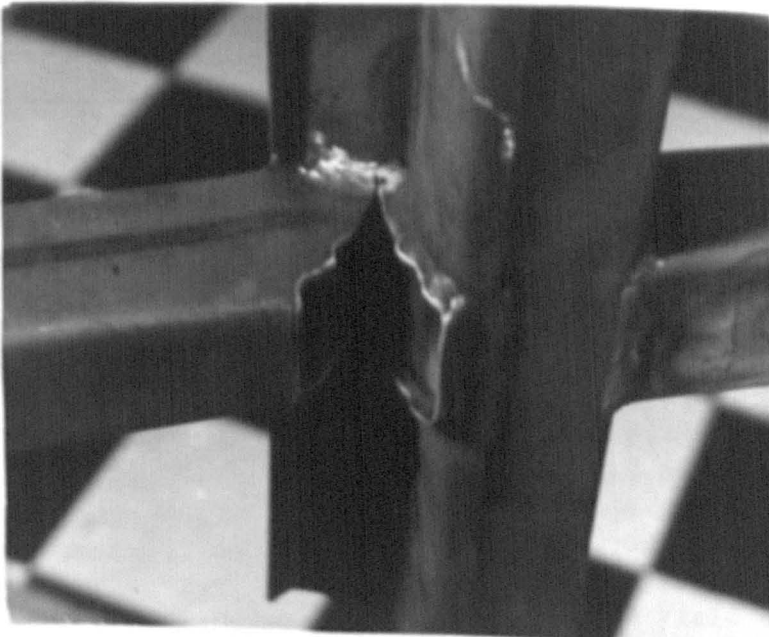
It is also interesting to compare the above energy with the energy absorbed by bending of a flat sheet of the same material whose width and thickness correspond to the respective circumference and wall thickness of the section 1 in Fig. 4.3. The same section area is thus obtained and it is also assumed that the average yield stress producing the fully plastic moment of 1660 Nm remains constant during sheet deformation. Bending of such a sheet through 30 deg. about a straight line would produce a theoretical energy (calculated on the basis of Chapter 5) of 53 J. This value is almost 10 times less than the above 510 J absorbed by a beam in spite of a significant drop off of the curve 1 in Fig. 4.3. This ratio is often even bigger, as will be shown in section 6.6. Superiority of beams in terms of energy absorption can be easily experienced by bending a sheet of paper and then producing a tight roll of the same sheet and bending it again.



a



b



c

Fig. 4.4

The last example supports the argument that the sheet metal cladding of structural skeletons used in vehicles may affect the load distribution, but is not so important during energy absorption. However, the above comparison refers to bending deformation only. In some cases sheet metal deforms by stretching or rolling with an increased capacity to absorb energy (the term "rolling" will be explained in detail in section 5.3). Relative contribution of sheets also increases by an increased length of sheet deformation.

The possible dynamic effects have already been discussed in sections 1.2 and 3.2. A high initial peak load, caused by structural inertia and stability, often occurs in dynamic load-deflection diagrams. It is very short lasting and followed by a much lower load fluctuating about some mean, gradually changing or constant value. It is this mean load, rather than initial peak, that is of real interest in the present context. The mean load affects the energy absorbed during deformation and usually ends very close to the remaining strength of the structure after impact. The initial peak can be reduced, if causing excessive deceleration, by local crimping of sections where the hinges are going to form.

Most of the tubular members in steel skeletons are joined by welding. The joint properties may vary a lot depending on the welding quality. The greatest bending moments occur usually at beam ends and it is advised therefore to produce good, continuous welds all around the section. However, in some materials, and under certain welding conditions local weakening of section may take place in the area next to the weld. This effect is illustrated in Fig. 4.5, where d.c.w denotes distance from the centre of the weld along the beam axis.

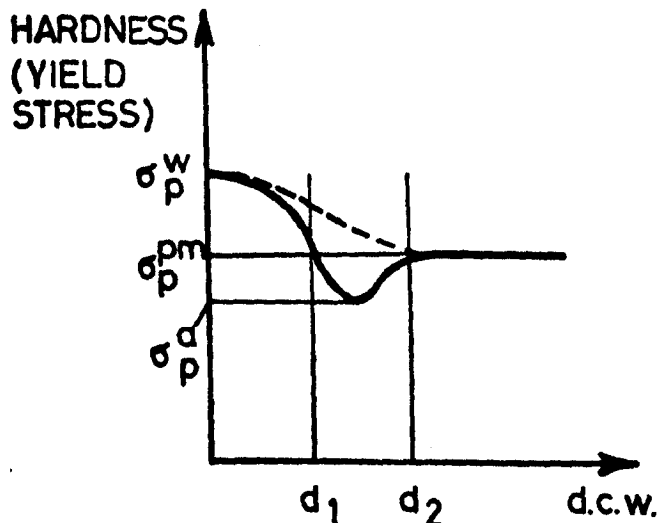


Fig. 4.5

Let the "parent material" of the tube have an initial yield stress σ_p^m at any point of the section. This stress depends on the material contents, metallurgical processing preceding the tube production and also on the way in which the tube has been manufactured. Strain hardening in plastically deformed parts of the section is particularly common, as will be shown in section 5.7.2. The actual weld joining the tube to an adjacent component has a relatively higher hardness or yield stress (σ_p^w) than the parent material. A zone d_1 - d_2 in Fig. 4.5 is affected by heat during

welding. This zone refers to the temperature range which can cause variation in material properties, and its dimensions vary with tube and weld dimensions, material properties, welding process, etc. In some materials, and under certain welding conditions the yield stress variation follows the dotted line in Fig. 4.5. In other cases, however, the

temperature in the vicinity of weld may cause local annealing of the material by rebalancing the dislocated segments of the material lattice. The yield stress of the annealed zone (σ_p^a) is lower than σ_p^{pm} and a narrow band of weaker material is created along the weld.

Excessive loading of a component with a locally reduced yield stress causes yielding at a lower average stress than σ_p^{pm} , and also concentrates the plastic strains into this weaker area, particularly on the tension side. A small rotation of the hinge produces large local strains, so that material separation may soon take place (Fig. 4.4c) even in relatively ductile materials. This form of failure has been observed in roll over accidents and in bus ring tests. The loss of strength was often very severe or complete. It appears that materials with higher nominal yield stress have a greater tendency to be adversely affected by welding, but there is not sufficient information to make any more specific comments.

Residual stresses due to welding do not affect the collapse load of stable sections since the stress variation is lost during material yielding. It should be noted, however, that this comment applies to good quality joints which are collapsed by a single overloading. Inadequately designed or manufactured welded joints may also contain areas of material with very low ductility or with fatigue micro-fractures. These may reduce significantly both the strength and energy absorbing capacity of a hinge by an increased tendency of material separation. Intensive corrosion may also influence the hinge collapse behaviour, but all these effects fall beyond the scope of this thesis.

5.1 INTRODUCTION

An attempt will be made in this chapter to derive a theoretical method of predicting the bending collapse behaviour of rectangular section tubes made of ductile material. Rectangular section mild steel tubes have been selected because they are standard structural elements with a very wide application in vehicle bodies and also in other areas of structural design.

The bending collapse is chosen because it is almost the only mode of local collapse found in structural frameworks when they are subject to large deflections.

The following analysis of hinges is closely related to the PSV roll over safety. It has been shown in Chapter 2 that the roof structure deflects in an almost pure sideways movement, producing a uniaxial bending collapse of ring components. The same collapse mode has been observed in other cases of structural collapse, as will be shown in section 5.3. Uniaxial bending is therefore chosen for theoretical treatment.

The bending stiffness of standard tubular components has been described in Chapter 4 as an elastic property that can be calculated using the engineering theory of bending. Reinforced joints may often be considered as rigid, so that properties to be determined in this chapter are:

- a. the maximum bending strength of a rectangular section tube;
- b. the strength variation with hinge rotation;
- c. the energy absorbed as the hinge rotates through an arbitrary angle.

The range of angles of hinge rotation should include the maximum angles developed before the structure starts intruding into a reasonable survival space. In most vehicles this maximum lies between 30 and 45 degrees ✓ which means that very large deformations should be allowed for.

The strength and energy absorption problems can be tackled in two ways similar to the variational principle mentioned in section 1.4.2. Both methods are based on the theorems of limit analysis and should provide reasonably close upper and lower bounds to the true collapse load and energy absorbed. General proofs of these theorems have been given by Prager and Hodge (82).

The lower bound solution requires a definition of a statically admissible stress field producing equilibrium of external and internal loads at each point of the collapse mechanism. However, the complexity of the hinge mechanism and load distribution during collapse make this approach inappropriate for the current analysis. Another disadvantage is that bending moment is not a convenient reference quantity since more than one deflection can be attributed to a single value of the moment (Fig. 4.1).

The second possibility is to use a kinematically admissible set of displacements (collapse mechanism) and calculate the work required to move the mechanism through a prescribed virtual displacement (hinge rotation angle θ). This approach leads to the upper bound solution and is much more feasible, provided that the energy absorbing process can be related uniquely to the hinge rotation angle. A model of the collapse mechanism should be established, but it is not necessary to consider the balance of internal and external loads. The hinge moment-rotation curve is obtained by differentiating the energy equation. Deformation is a good reference quantity because a unique moment can always be associated with any angle of hinge rotation (Fig. 4.1).

A correct upper bound solution produces minimum collapse load, so that several collapse mechanisms may have to be analysed. If the internal and external loads are at the same time in equilibrium, the upper and lower bound results are equal and represent the theoretically true collapse load. The agreement between the theoretical and actual collapse load depends then on the similarity between the theoretical and actual collapse mechanism and on the accuracy of defining the relevant material properties. If the theoretical mechanism is not fully compatible and/or if the yield and flow stresses are underestimated, the upper bound strength may become even lower than the actual one.

5.2 THE MAXIMUM BENDING STRENGTH OF A RECTANGULAR SECTION TUBE

The maximum bending strength of a rectangular section tube is usually achieved at the point where the tube starts collapsing. The collapse may be initiated by:

- a. plastic yielding of the material over the whole section,
- b. plastic yielding of the material over a part of the section, combined with elastic or inelastic buckling of some other segments of the section, and
- c. plastic yielding of the material over a part of the section, combined with material separation over another segment of the same section.

The first case is common in stable section tubes made of a ductile material.

The second collapse form applies to tubes which buckle locally before the maximum moment is achieved. Local buckling may be elastic or inelastic, depending on the stability of the compressed segments of the section. Most of the beams used in vehicle bodies represent thin walled tubes, so that buckling has an important effect on their collapse behaviour. Shear buckling is very uncommon in actual frameworks.

The third possibility is not typical in ductile materials, except in special cases of stress or strain concentration as shown in Chapter 4. This condition will not be taken into account in the following analysis.

Elastic stability of compression members has been treated in many standard textbooks. Inelastic buckling of plates is a more specialised subject approached in different ways by different authors. Bleich (45) defines

the inelastic critical stress as a function of the elastic critical stress, yield stress and maximum stress that is still linearly proportional to strain. Bulson (83) also discussed inelastic buckling of plates and referred to the Stowell's theory (84) that inelastic stresses and strains are related by the secant modulus of the material. Inelastic buckling stress of square tubes in compression is then obtained from the elastic critical stress by a factor depending on the Young's, secant and tangent moduli and Poisson's ratio of the material. However, the most relevant information for this thesis deals with the bending strength of complete beams, as described below.

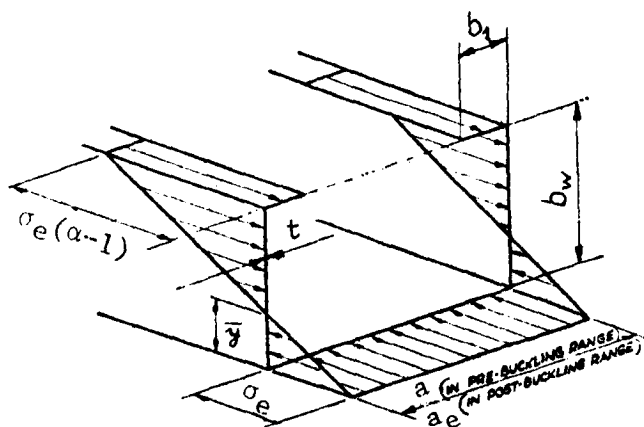


Fig. 5.1

Rhodes (66,67) has investigated the problem of the load carrying capacity and deflections of a lipped channel section in Fig. 5.1 subject to pure moment. The beam was treated as a system of plates joined along the common edges and loaded by an axial stress system, the lips being in tension and flange in compression. Von Karman's fourth order differential equations for local deformations of plates were employed and all buckles were assumed to have sinusoidal form with a common period. The strain energy of the deformed plates was evaluated in terms of the coefficients of functions

describing the idealised deflections. A system of algebraic equations was obtained by minimising the strain energy with respect to each coefficient and solved. The stress distribution over the whole section was then calculated for both linear and non linear (after buckling) stages of the elastic deformations.

Buckling of the compression flange occurs, theoretically, when the compressive edge stress on the flange (σ_e) becomes equal to the critical stress (σ_{cr}).

$$\sigma_e = \sigma_{cr} = \frac{K_f \pi^2 E}{12(1-\nu^2)} \left(\frac{t}{a}\right)^2 \quad (5.1)$$

where E and ν are respectively the Young's modulus and Poisson's ratio of the material, t and a are the flange thickness and width, and K_f is the flange buckling coefficient which can be approximated, using dimensions in Fig. 5.1, as:

$$K_f = 5.23 + 0.16 \frac{a}{b_w} \quad (5.2)$$

The last expression allows for the variation of flange boundary conditions with the ratio a/b_w .

If the critical stress σ_{cr} is less than the yield stress of the material σ_p the flange will buckle elastically producing a non linear stress distribution with the membrane stress in the middle much less than the edge stress σ_e . An "effective flange width" (a_e) is introduced to define the part of the flange which is still effective in withstanding compression. The product $a_e\sigma_e t$ gives the actual compressive force acting on a flange. The same mathematical model was applicable to this non linear elastic behaviour, so that a theoretical value of a_e/a could be determined in terms of the stress ratio σ_e/σ_{cr} (Fig. 5.2). A simplified design formula:

$$a_e = a(0.7 \frac{\sigma_{cr}}{\sigma_e} + 0.3) \quad (5.3)$$

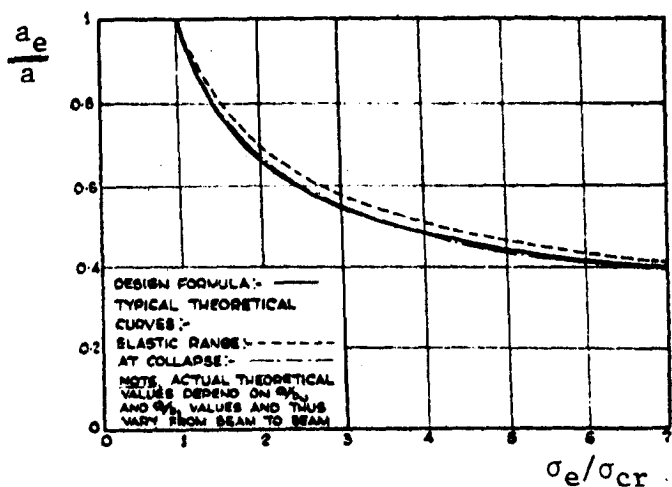


Fig. 5.2

was suggested to give a good agreement with the theoretical curve. The bending stresses within the effective width $a_e/2$ on either side of the flange, caused by buckling in the middle, and the periodically varying membrane stresses along the edges were negligible in comparison with σ_e .

Rigorous mathematical treatment of the linear and non linear elastic behaviour becomes inapplicable when the first yielding of the material takes

place. The elastic relations no longer apply and the stress system becomes biaxial. A simplifying assumption had to be introduced, based on finding that "... beams generally collapse soon after the onset of yield in the compression flange, although not at the first yield. Several different collapse criteria were tested theoretically, e.g. when the flange load decreases with increase in deflections, when plasticity first occurs at the section with the lowest edge stresses, and found to give little difference in the collapse moment, although deflections varied considerably". An assumption was then made that the maximum strength will be achieved when the effective width, determined by (5.3) goes plastic. Edge stress of the flange σ_e in (5.3) is then equal to the yield stress σ_p and the agreement between the theoretical and design curve becomes very good indeed (Fig. 5.2). Naturally, if $\sigma_{cr} \geq \sigma_p$, then $a_e = a$ in (5.3). The material is assumed elastic-ideally plastic with equal σ_p in tension and compression.

The actual maximum moment (M_{max}) depends on the total stress distribution when the compression flange yields. At that instant yielding may or may not take place on the tension side of the section. From the condition of zero axial load a characteristic ratio (α_e) defining position of the neutral axis (Fig. 5.1) is:

$$\alpha_e = \frac{b_w}{\bar{y}} = \frac{a_e + 2b_1 + 2b_w}{2b_1 + b_w} \quad (5.4)$$

If α_e is less than 2, the neutral axis is closer to the lips, hence plasticity will not take place on the tension side. Summing moments about an axis through the lips (Fig. 5.1), with $\sigma_e = \sigma_p$, the maximum load carrying capacity becomes:

$$M'_{\max, lc} = \sigma_p t b_w^2 \left[\frac{4b_1 + b_w + a_e \left(6 \frac{b_1}{b_w} + 2 \right)}{3 (2b_1 + b_w)} \right] \quad (5.5)$$

If α_e is greater than 2, the neutral axis is closer to the flange, hence plasticity on the tension side occurs before the flange yields (Fig. 5.3). Using again the zero axial force condition and summing moments about an axis through the lips, with $\sigma_e = \sigma_p$, the maximum moment is

$$M''_{\max, lc} = \frac{2}{3} \sigma_p t b_w \left[a_e + b_1 + \frac{b_w}{2} - \frac{1}{b_w} \left(b_1 - \frac{a_e}{2} \right)^2 \right] \quad (5.6)$$

Both expressions give the same value of M_{\max} if $\alpha_e = 2$.

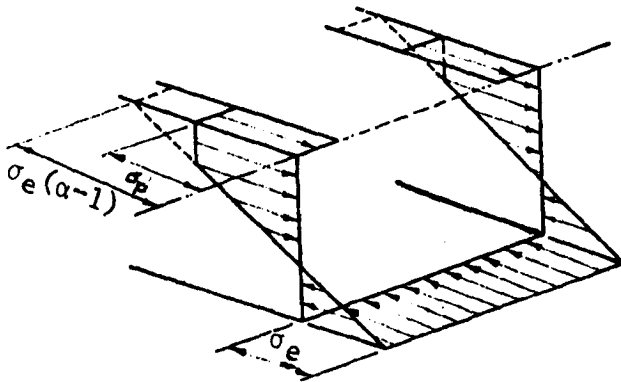


Fig. 5.3

The above formulae were checked against test results for $a/b_w < 4$ and $a/t < 220$. For sections outside this range it is suggested that $K_f = 5.4$ be used in (5.2) and if $a/t > 220$ then $a_e = a (0.8(\sigma_{cr}/\sigma_e) + 0.2)$, to produce a conservative result. The minimum ratio a/t was 51.6. The ratios σ_p/σ_{cr} ranged between 1.12 and 16.8, indicating that buckling always took place before collapse.

Dawson and Walker (68) have developed a method similar to Rhodes, but assumed that the flange of the lipped channel in Fig. 5.1 has an initial

imperfection and that the webs remain flat throughout the deformation process. The second assumption is justified by the fact that the periodically varying elastic membrane stresses represent a secondary effect, as stated in the comment following the equation (5.3). Yielding in the compression flange starts when $\sigma_e = \sigma_p$, so that the average flange stress reaches its maximum value σ_{ult} satisfying the relation:

$$\sigma_{ult} a t = \sigma_p a e t \quad (5.7)$$

Additional moment is resisted as yield spreads through the webs which undergo a fully plastic deformation.

The position of the neutral axis at collapse is determined from the zero axial force condition, and then the moment equilibrium about lips gives the maximum moment in the form:

$$M_{\max,lc}''' = \frac{\sigma_p t b_w^2}{2} \left[1 + \frac{b_1}{b_w} \left(2 - \frac{b_1}{b_w} \right) + \frac{a}{b_w} \left(1 + \frac{b_1}{b_w} \right) \frac{\sigma_{ult}}{\sigma_p} - \frac{a^2}{4b_w^2} \left(\frac{\sigma_{ult}}{\sigma_p} \right)^2 \right] \quad (5.8)$$

The ratio σ_{ult}/σ_p is obtained in the following manner. The compression flange is treated as a simply supported plate, giving the critical buckling stress:

$$\sigma_{cr} = \frac{\pi^2 E}{3(1 - \nu^2)} \left(\frac{t}{a} \right)^2 \quad (5.9)$$

The effect of plate imperfections is now introduced and results by Coan (85) and Walker (86) are used to relate the stresses σ_{ult} , σ_{cr} and σ_p at the point of collapse:

$$\frac{\sigma_p}{\sigma_{cr}} = \frac{\sigma_{ult}}{\sigma_{cr}} + 2.832 \left[\frac{\sigma_{ult}}{\sigma_{cr}} - 1 + \frac{e_o}{e_{ult}} \right] + \left[0.515 \left(\frac{\sigma_{ult}}{\sigma_{cr}} - 1 \right)^2 \right]; \sigma_{ult} > \sigma_{cr} \quad (5.10)$$

where e_o is the initial plate imperfection (maximum distance between the actual mid-plane of the unloaded plate and the ideally flat mid-surface), and e_{ult} is the plate imperfection at collapse, obtained by solving:

$$e_{ult}^3 - e_{ult} \left[e_o^2 + 4.25 \left(\frac{\sigma_{ult}}{\sigma_{cr}} - 1 \right) \right] - 4.25 e_o = 0 \quad (5.11)$$

Equations (5.10) and (5.11) can be solved for σ_{ult} and e_{ult} if e_o is known. A suitable generalisation of the initial imperfection amplitude in the form

$$e_o = 0.2 \frac{\sigma_p}{\sigma_{cr}} \quad (5.12)$$

is suggested in (68) to fit the lower bound results by Winter (63) and Chilver (65), Fig. 5.4. The lower two of the dotted curves in Fig. 5.4 are obtained by combining equation (5.7) with (1.2) and (1.3) respectively (68). The top curve, corresponding to Rhodes formula (5.3) or Fig. 5.2 is added here for comparison.

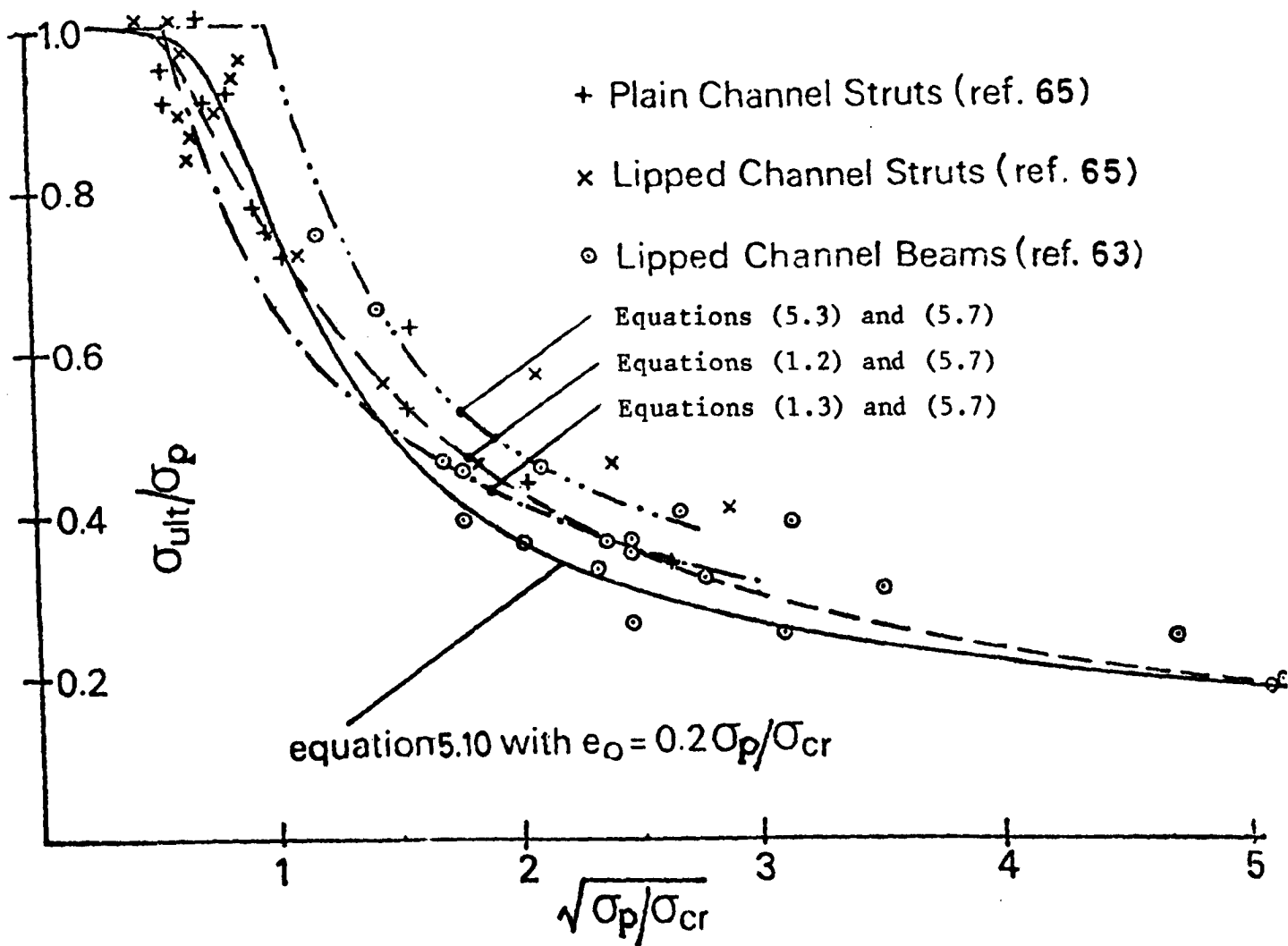


Fig. 5.4

Knowing the critical stress σ_{cr} from (5.9), the quantity $\sqrt{\sigma_p/\sigma_{cr}}$ can be evaluated. The required ratio σ_{ult}/σ_p is then taken from the solid curve in Fig. 5.4 and substituted into (5.8) to calculate $M''_{max,lc}$.

According to equation (5.10) in Fig. 5.4 the fully plastic moment ($\sigma_{ult} = \sigma_p$) will be developed if σ_{cr} is at least 2.5 times higher than σ_p , due to the initial imperfections.

The difference in maximum moments given by the two methods described is actually much smaller than the graphs in Fig. 5.4 would suggest. The first reason is that formula (5.9) produces a lower critical stress than (5.1) and (5.2). The first method (top curve in Fig. 5.4) does not allow full plasticity to develop in the webs while the second one (solid curve) always assumes full plasticity in the webs. Both methods gave, therefore, very similar results close to experimental data reported in ref. 66.

The lips in Fig. 5.1 are subject to equal tension. If their width is $b_1 = 0.5a$ and if they are joined together, no shear would occur along the joint. However, this would alter the boundary conditions along the lip

to web connections. The webs would become more stabilised, but the longitudinal membrane stresses would still be much larger than any other stress components. It was therefore decided to extend the above formulae to the rectangular tube case simply by putting $b_1 = 0.5a$. Such an extension would, of course, be wrong if the section in Fig. 5.1 were subject to any other loading conditions.

The first method (67) is easier to organise as a standard computing routine because the second one (68) requires either the solution of equations (5.10) and (5.11) or the use of the diagram in Fig. 5.4. Determination of the maximum bending strength of a rectangular tube in Fig. 5.5a with flange "a" in compression starts therefore as in the first case. The section dimensions shown in Fig. 5.5a will be used in the rest of the thesis.

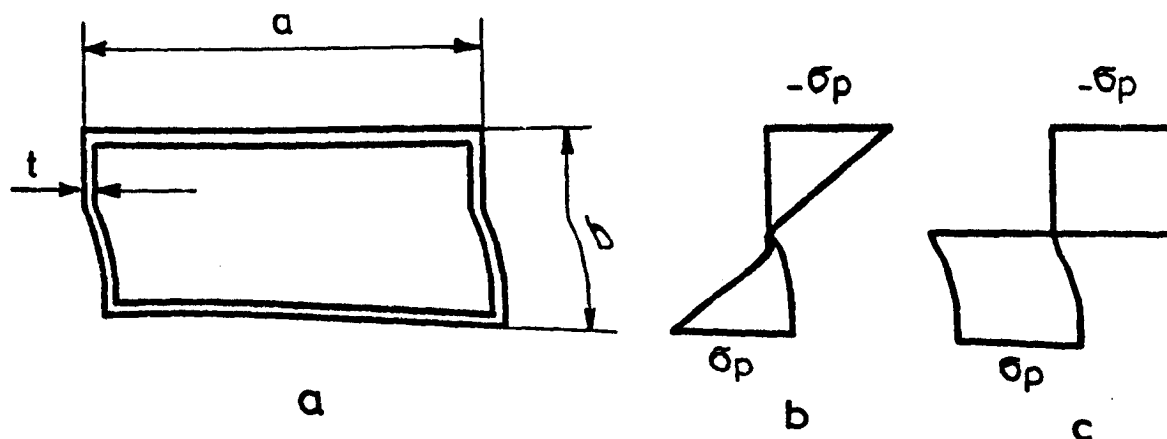


Fig. 5.5

The new situation should not change significantly the boundary conditions along the edges of the compressed flange, hence:

$$\sigma_{cr} = \frac{\pi^2 E}{12(1-\nu^2)} \left(\frac{t}{a}\right)^2 (5.23 + 0.16 \frac{a}{b}) \quad (5.13)$$

and the effective width of the flange becomes

$$a_e = a(0.7 \frac{\sigma_{cr}}{\sigma_p} + 0.3) \quad (5.14)$$

In the last equation $a_e = a$ if $\sigma_{cr} \geq \sigma_p$, which disregards the effect of initial imperfections for σ_{cr} bigger than but close to σ_p . However, this effect is often reduced by an increased yield stress near the edges of the flange as will be shown in section 5.7.2.

The coefficient α_e defining the position of the neutral axis is:

$$\alpha_e = \frac{a_e + a + 2b}{a + b} \quad (5.15)$$

Since $a_e \leq a$, $\alpha_e \leq 2$. If $\alpha_e < 2$ yielding occurs in the compressed flange first, while $\alpha_e = 2$ produces simultaneous yielding in both flanges. In any case, equation (5.5) now takes the form

$$M'_{\max} = \sigma_p t b^2 \left[\frac{2a + b + a_e(3a/b + 2)}{3(a + b)} \right] \quad (5.16)$$

If both flanges yield:

$$M'_p = \sigma_p t b \left(a + \frac{b}{3} \right) \quad (5.17)$$

which corresponds to the stress distribution in webs shown in Fig. 5.5b.

The new form of equation (5.8) is, after some rearranging:

$$M'''_{\max} = \frac{\sigma_p t}{8} \left[4b(a + b) - a^2 + 2a(2b + a) \frac{\sigma_{ult}}{\sigma_p} - a^2 \left(\frac{\sigma_{ult}}{\sigma_p} \right)^2 \right] \quad (5.18)$$

Yielding of both flanges ($\sigma_{ult} = \sigma_p$, i.e. when $\sigma_{cr} > 2.5\sigma_p$ from Fig. 5.4) will be accompanied by full plasticity in webs (Fig. 5.5c) and a fully plastic moment will be obtained:

$$M'''_p = \sigma_p t b \left(a + \frac{b}{2} \right) \quad (5.19)$$

Equations (5.15) - (5.19) are derived by assuming that the wall thickness (t) is much smaller than the depth (b) of the beam. In beams which develop fully plastic moments a more accurate formula using dimensions in Fig. 5.5a is:

$$M_p = \sigma_p t \left[a(b - t) + \frac{(b - 2t)^2}{2} \right] \quad (5.20)$$

Most structural tubes have $a/b \leq 2$, otherwise the load carrying potential of the material is not well utilised. Assuming a very high yield stress of $\sigma_p = 500 \text{ N/mm}^2$ and putting $\sigma_{cr} = \sigma_p$ into equation (5.13) with $a/b = 2$, we get $a/t = 45.7$ or $t = 0.04376b$ (lower σ_p produces an even smaller relative thickness). This thickness would produce full plasticity in the flanges, and substituting it into (5.17) + (5.20) the following ratios are obtained:

$$\frac{M_p}{M'_{\max}} = 1.04; \quad \frac{M_p}{M'''_p} = 0.95; \quad \frac{M_p}{M'_{\max}} = \frac{M_p}{M'''_p} = 0.998 \quad (5.21)$$

In structural tubes a/b is rarely less than 0.5. If $a/b = 0.5$ and the same procedure as in the last paragraph is repeated, the following results are obtained: $a/t = 44.7$, $t = 0.0112b$ and

$$\frac{M_p}{M''_{\max}} = 1.036; \quad \frac{M_p}{M'_p} = 0.98; \quad \frac{M_p}{M'_{\max}} = \frac{M_p}{M'_p} = 1.18 \quad (5.22)$$

The values of M''_{\max} in (5.21) and (5.22) have been found using Fig. 5.4.

The considerations above indicate that

- a. formulae (5.16) to (5.19) produce similar results for $\sigma_{cr} \leq \sigma_p$;
- b. formula (5.16) is more suitable than (5.18) and the stress distribution in Fig. 5.5b, assumed by (5.16), has a similar effect as the initial imperfection (5.12). Reduction of the relative wall thickness increases the chance of having an elastic stress distribution in the webs immediately before collapse;
- c. relatively thicker walls increase the tendency of web yielding, but at the same time formula (5.20) gains preference over the equation (5.19).

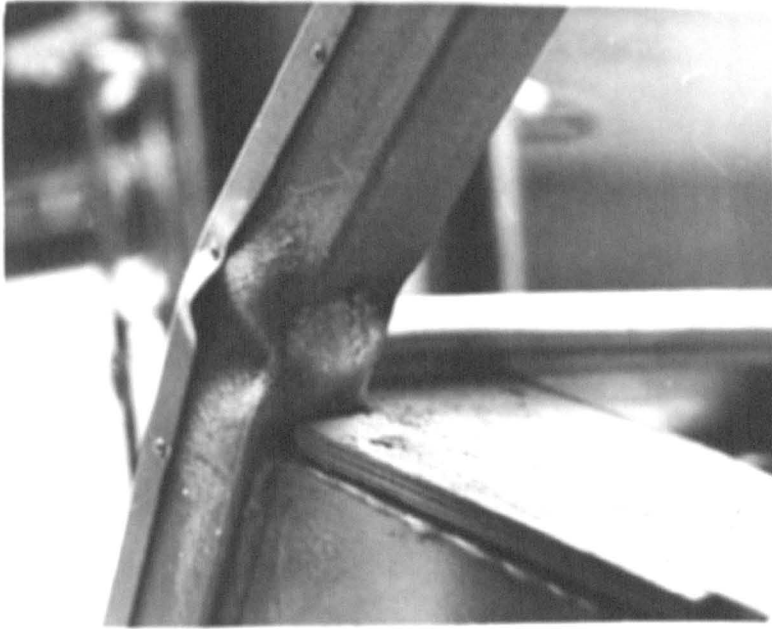
It is therefore suggested that the maximum bending strength (M_{\max}) of a section in Fig. 5.5a should be calculated by the following relations:-

$$M_{\max} = \begin{cases} M'_{\max}, & \text{for } \sigma_{cr} \leq \sigma_p \\ M'_p + (M_p - M'_p) \left(\frac{\sigma_{cr} - \sigma_p}{2\sigma_p} \right), & \text{for } \sigma_p < \sigma_{cr} \leq 3\sigma_p \\ M_p, & \text{for } \sigma_{cr} > 3\sigma_p \end{cases} \quad (5.23)$$

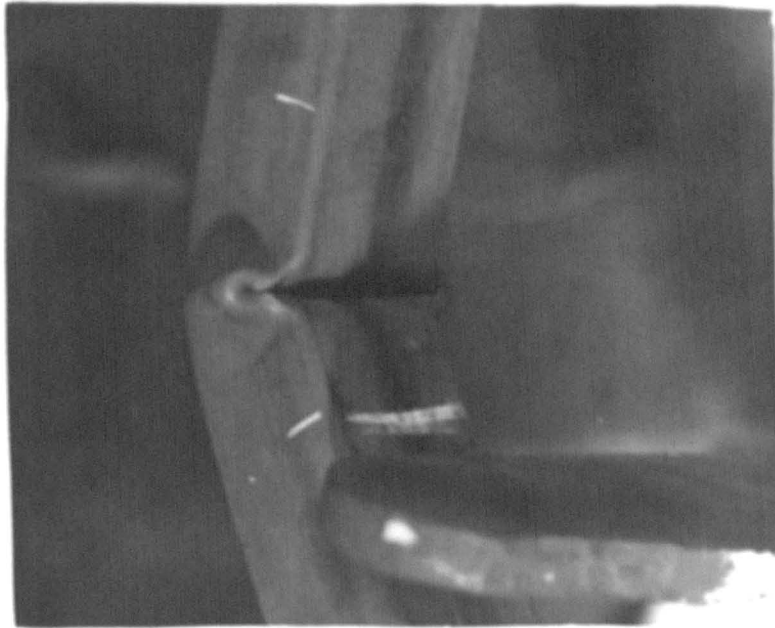
A factor of 3 rather than 2.5 is used in the last two lines because equation (5.9) gives a lower critical stress than (5.1) and (5.2). The yield stress σ_p to be used in (5.23) is discussed in section 5.7.4.

5.3 THE ACTUAL BENDING COLLAPSE MECHANISM

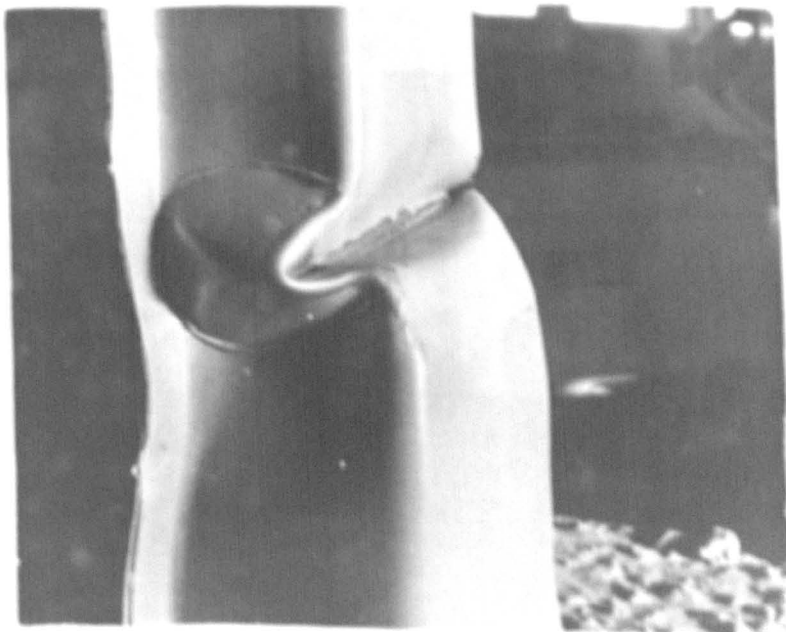
The collapse mode of the bus pillar observed in roll over accidents nos. 5 and 20 (Fig. 2.9a) proved to be very repeatable in rectangular section tubes. The same type of failure occurred in pillars of a fire engine safety cab (26) during the roof crush test (Fig. 5.6a), in both static and dynamic collapse tests (2) of bus rings with rectangular (Fig. 5.6b) or closed top hat section (Fig. 4.4a) members and also in pillars of a passenger car side frames (Fig. 5.6c) which also had a closed top hat section. All the cantilever tests of a range of rectangular section tubes produced the same hinge mechanism (Fig. 5.7). These tests were used to check the theory and are described in Chapter 6. All hinges in Figs. 2.9, 4.4a, 5.6 and 5.7 were created by internal loads only, i.e. away from the point of application of the external load.



a

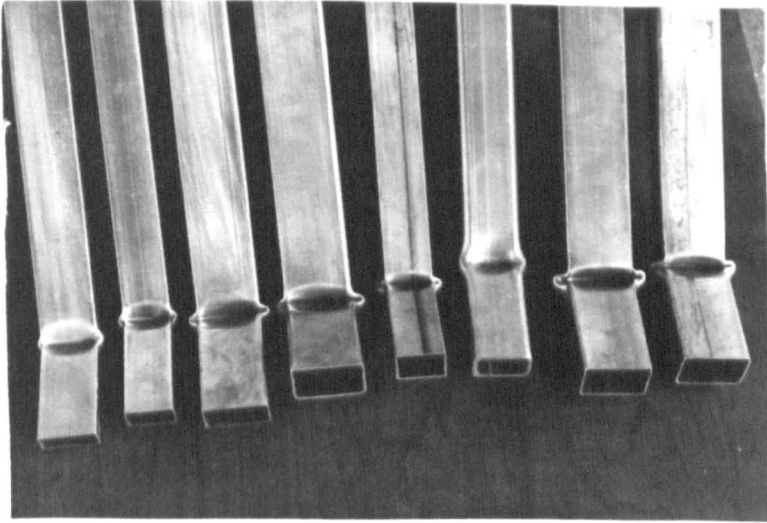


b

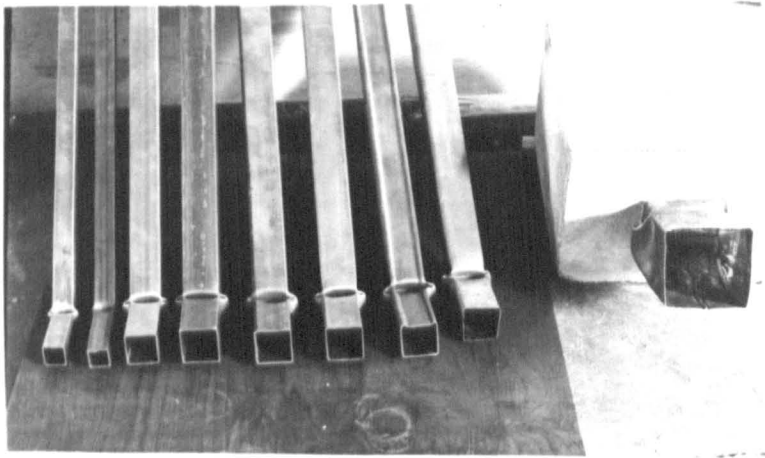


c

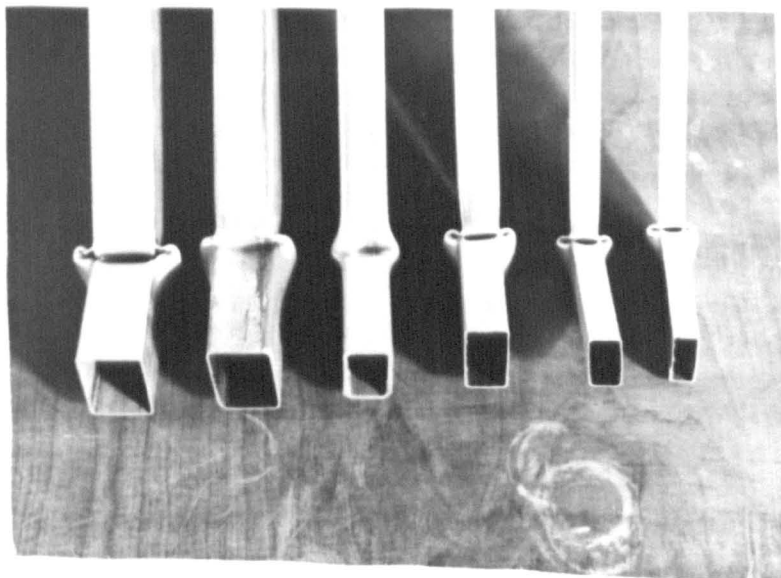
Fig. 5.6



a



b



c

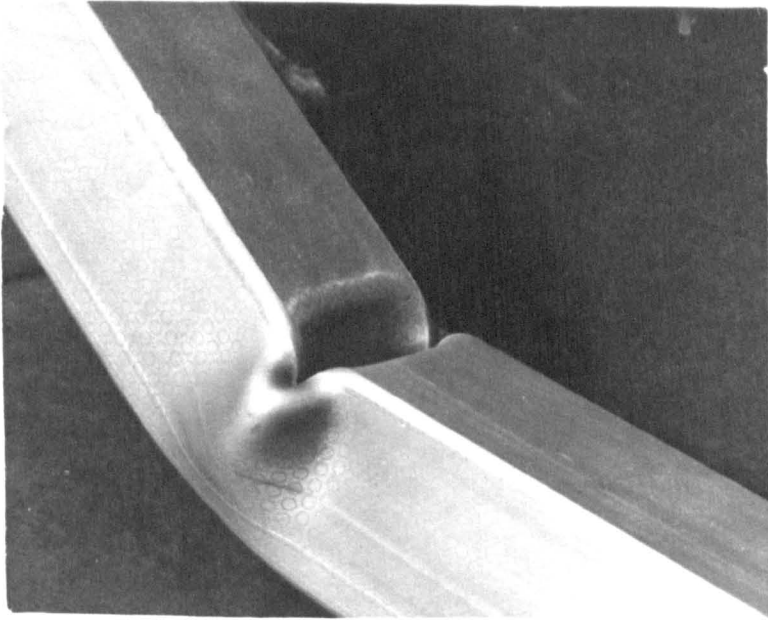
Fig. 5.7

A major part of the fixed length of the tube was cut off before taking the photograph in Fig. 5.7 in order to show the section more clearly.

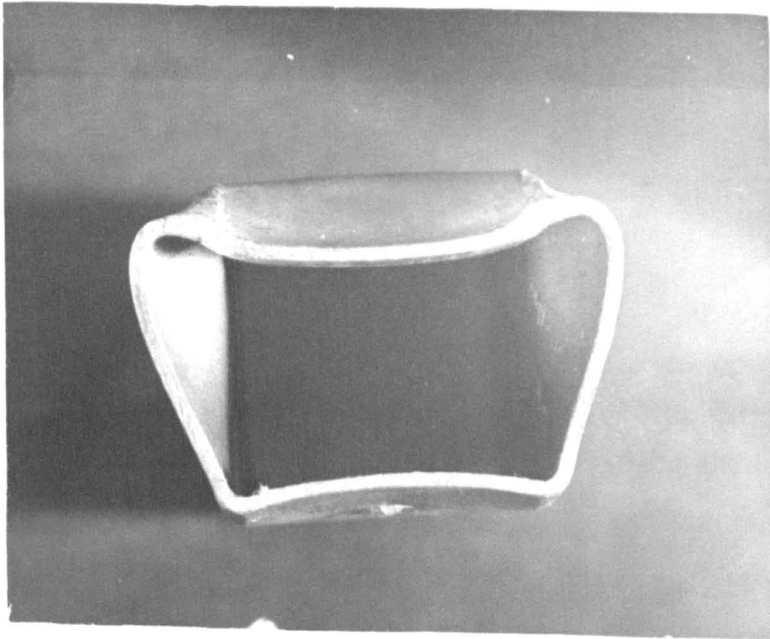
A detailed inspection of the hinge collapse mechanism was made possible by bending a square section cantilever (38 x 38 x 1.6 mm) which had a dense circular pattern grid applied electrochemically to all the four walls in the area of the hinge. The diameter of undeformed circles was 2.54 mm, representing 50 divisions on the optical instrument used for measuring dimensions. The distance between the middle of the hinge and the point of load application was 683 mm and the test apparatus is described in detail in section 6.2. The load was increased quasi-statically in 10 steps up to the maximum strength. Further increments of displacements corresponding to approximately 1° of hinge rotation were then slowly applied to continue the test. Load and deflection readings were taken and the hinge behaviour was observed carefully. The test was stopped after 9.5° , 19° and 29.8° of hinge rotation and the beam was removed from the rig in order to measure deformations recorded in the circular grid. The hinge appearance after the test is depicted in Fig. 5.8a, the cross section through the middle of the hinge in Fig. 5.8b and the longitudinal section in the plane of symmetry is in Fig. 5.8c (sections were produced by cutting the other two hinges of the same dimensions and shape in order to save the original one for future reference).

The observation indicated that the hinge mechanism occurs between the two plastically undeformed beam segments which can be treated as rigid "blocks" in the somewhat idealised form of the collapse mechanism in Fig. 5.9a. The boundaries between the hinge and blocks are clearly defined by the wall bending along lines GHNKG and EFMLE in Fig. 5.9a. The length of the hinge cannot be determined exactly because the bending lines have a radius, but an approximate measurement showed that the length of the hinge in the undeformed state is very close or equal to the section width or depth ($KL = GBE = GH = GK$). The hinge is reasonably symmetric with two planes of symmetry: one at the cross section through the middle of the hinge (Figs. 5.8b and 5.9b) and the other at the longitudinal section of the beam passing through the middle of the lines EF, GH, LM and NK (Fig. 5.8c).

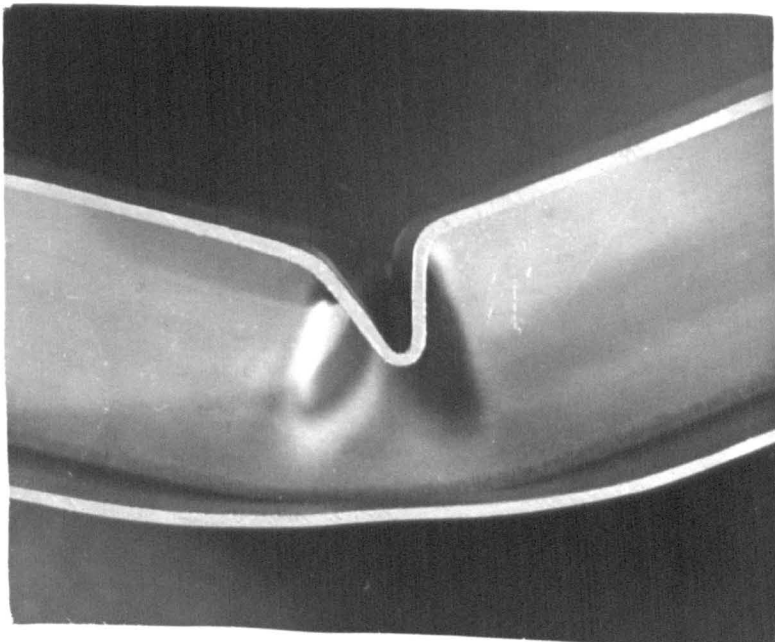
The compression flange EFCHGBE (Fig. 5.9a) buckles inwards with plastic deformation concentrated along the bending lines EF, GH, BC, GB, BE, HC and CF. This conclusion is based on the general appearance of the flange and on the deformation pattern of the circular grid. The lines of concentrated plastic deformation will be further referred to as "yield lines". The circles within the flange but away from yield lines remained almost undeformed (representative circle no. 2 in the plan view of the flange - Fig. 5.9d). The circles on the yield lines became elliptic due to a considerable local deformation. Representative samples of the circles on each line are shown in Fig. 5.9d as ellipses 1, 3, 4 and 5. The major (d_1) and minor (d_2) axis of each ellipse were arranged as in Fig. 5.9d and the approximate lengths of each axis in divisions of the optical instrument are listed in Table 5.1. Exact measurements could not be made because of difficulties when measuring circle dimensions on a curved surface. However, the accuracy was sufficient to indicate the direction of the plastic flow of the material.



a



b



c

Fig. 5.8

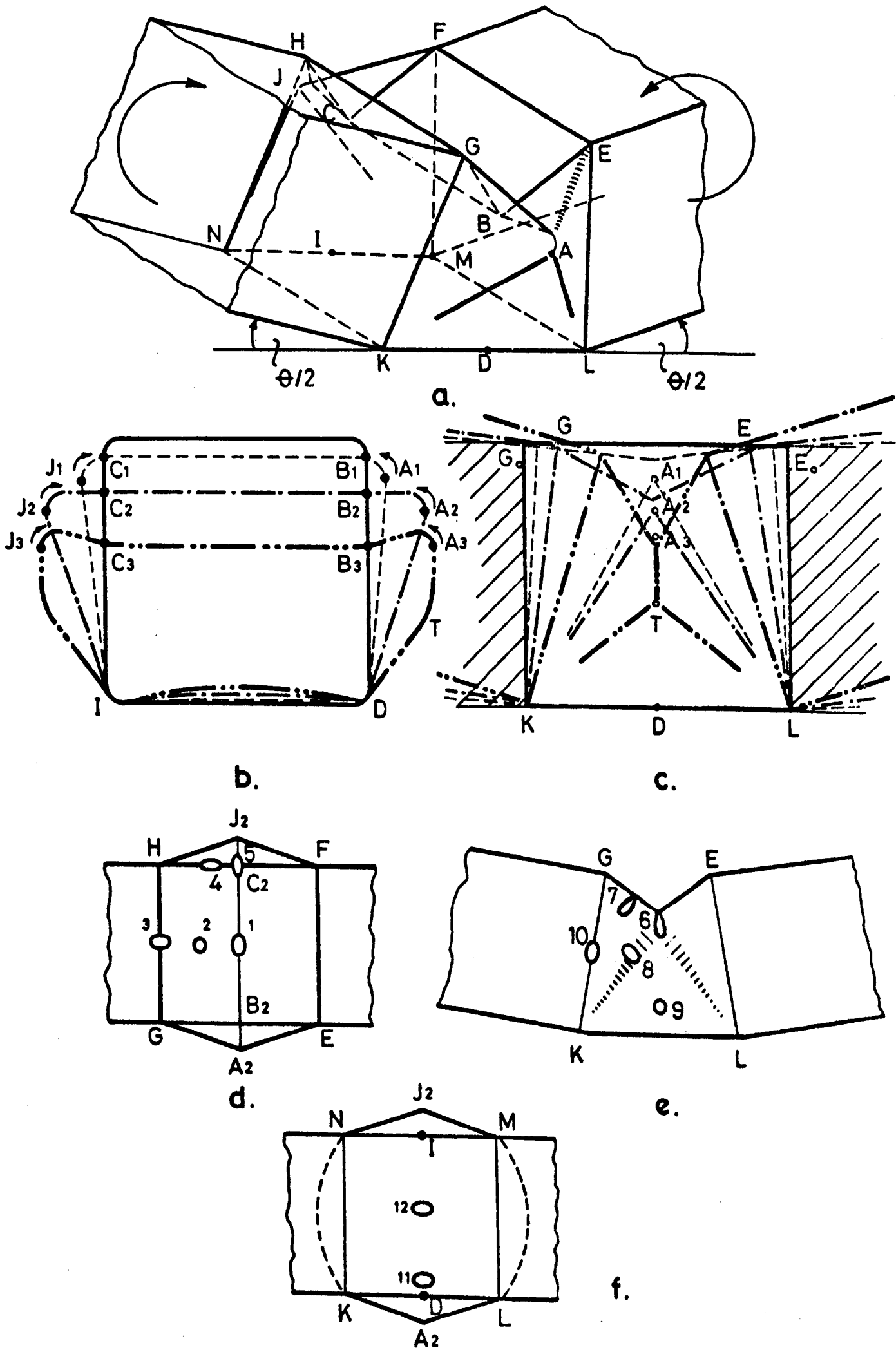


Fig. 5.9

Undeformed circle: 50 x 50 divisions

Table 5.1

θ	Circle Number	1	2	3	4	5	6	7	8	9	10	11	12
9.5°	d ₁	51	50	55	≈50	55	55	54	53	≈50	50	52	52
	d ₂	35	50	50	≈48	30	47	48	47	≈50	48	50	49
19°	d ₁	≈50	≈50	57	≈50	>75	60	58	54	≈50	50	53	53
	d ₂	≈30	≈50	50	≈40	<20	35	35	45	≈50	45	49	47
29.8°	d ₁	≈50	≈50	59	≈50	Fracture	>75	>75	54	≈50	50	51	52
	d ₂	≈20	≈50	50	≈40		<25	<25	45	≈50	45	47	48

Webs EBGKLE and FCHNMF deform in a fairly complex manner. The deformations of the circular grid in the side view of the beam (Fig. 5.9e) followed the general pattern indicated by representative ellipses 6 - 10. The web deformation is symmetric, so only one half may be considered.

The initial buckle of the flange is followed by a shallow "bulge" with an apex A₁ in Fig. 2.9b approximately 0.2 KG below the compression flange. After about 5 ÷ 10 degrees of hinge rotation the middle section takes the shape A₂DIJ₂C₂B₂A₂ in Fig. 2.9b and progresses in a similar shape through further 20 - 25 degrees, gradually approaching the shape in Fig. 5.8b and, still later, the curve A₃DIJ₃C₃B₃A₃ in Fig 2.9b. Points A₁, A₂, A₃ denote the current apex of the bulge and do not correspond to the same point on the cross section. The apex A gets further and further from point B which passes through the current positions B₁, B₂, B₃, etc., so that B₁A₁ < B₂A₂ < B₃A₃. This kinematics is possible only if a "rolling" deformation depicted in Fig. 5.10 takes place along GA about an axis approximately parallel to the same line GA. The term "rolling" is used to describe a deformation in which the sheet

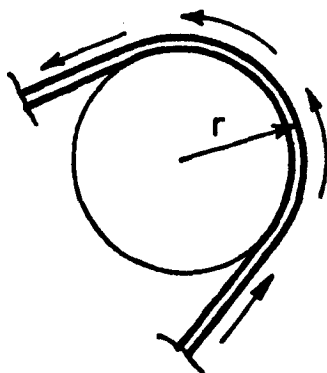


Fig. 5.10

moves about a "frictionless roller" of the radius "r" (Fig. 5.10). The sheet bends when entering the curvature and straightens again when leaving it, but without extension of the middle surface. Trajectories of the rolling points cannot be perpendicular to GA₂ because this would pile up the material on the current BA line. The actual trajectories are parallel to KG when entering the rolling segment, but approximately perpendicular to the GB line when leaving it. Some in-plane deformation is necessary to maintain the continuity of the walls. The rolling radius "r" varies slightly along GA, and reduces with the progress of collapse. This reduction makes the rolling deformation more and more "difficult" until, eventually, jamming takes place, starting the third phase

of hinge collapse. The radius was measured approximately by cutting at right angle to GA (as in Fig. 5.8b), and its estimated magnitude was

proportional to the length of the hinge; i.e. $(0.03 - 0.05) \cdot KL$. The rolling radius is bigger in thicker walled beams of the same depth and width, but no significant difference was noticed within the range of tubes tested in this thesis. The corner radius of the undeformed sections also did not seem to affect the rolling radius because of the initial "bulge" in the web created away from corners.

The circles in the area swept by GA, represented by deformed ellipses 6 and 7 in Fig. 5.9e, deformed very much (Table 5.1) with the major axis approximately perpendicular to the GA direction. The ellipses deformed into a "droplet" shape with the tip towards the line GB, thus indicating the accumulation of material in this area. Some increase in wall thickness around points B and C is noticeable in Fig. 5.8b as well.

Bending along BA must also take place in the symmetric collapse mechanism. The straining along this line is further increased, resulting in material separation around point B (and C) after the hinge rotated more than 20° . The crack in the outer surface was along the line BA and on the inner side (Fig. 5.8c) along GBE. The length of each crack was approximately $3t$ (where t denotes the wall thickness) after 30° of hinge rotation. This material separation did not have much effect in the hinge strength within the following $5^\circ - 15^\circ$ of rotation. However, if reverse loading is applied to such a beam the cracks propagate rapidly as in Fig. 2.9a and b, reducing significantly the remaining hinge strength.

A diffused deformation pattern was observed in the web area between points K and A. The major axes of ellipses, represented by ellipse 8 in Fig. 5.9, were approximately perpendicular to the KA direction. At any stage of collapse the deformations appeared rather concentrated along the line KA. However, the yield line KA was not as distinct as the previous ones because the curvature of deformation decreased rapidly from A to K, so that the web remained almost flat in the vicinity of K. Continuous shifting of the line KA (Fig. 5.9c) diffused the deformation pattern and the actual yield line was approximately identified by light reflection. A rolling deformation along KA would be required to produce a mechanism compatible with the kinematics of the rest of the web. The area in the vicinity of the lower edge of the flange (KL) remained almost undeformed (circle 9 in Fig. 5.9e).

The angle between the web and tension flange along KL remained practically constant due to the deformation of the tension flange (Figs. 5.8b and 5.9b).

The web collapse mechanism is completed by bending along the yield line GK with a representative ellipse 10 in Fig. 5.9e and Table 5.1.

The two halves of the compression flange are getting closer together and in later stages of collapse ($\theta > 40^\circ$ in square sections) the rolling deformation along GA is jammed by the material along BA. Further collapse is then made possible by an increased bending along GK and by the new bending lines ATK and TL in Fig. 5.9b and c. This change of the collapse mechanism does not usually produce a variation in the general strength curve until the two halves of the compression flange contact each other. This point is followed by spreading of the collapse mechanism away from its original volume. New bending hinges are formed at $0.5 \cdot KL$ away from the section GHNK, the webs buckle inwards and the compression

flange outwards, starting a new, "secondary" hinge adjacent to the first one. The secondary hinge did not develop in square sections for $\theta < 45^\circ$.

The tension flange KLMN produces a concave, cylindrical segment deflection, with the two characteristic sections shown in Fig. 5.8b and c. Boundaries of this "depression" create a curve between a rectangle and an irregular ellipse (solid and dotted lines LM and KN in Fig. 5.9f). The major axis of the "ellipse" increases with hinge rotation. The section considered develops a fully plastic moment, so that plastic strains were recorded in the circular grid which was oriented as the ellipses 11 and 12 in Fig. 5.9f. The strains were fairly evenly distributed, so that the effective stretching of the distance KL would be approximately 4%, according to results in Table 5.1. Most of the stretching is produced at the beginning of collapse, and the subsequent deformation is directed inwards in sympathy with the webs moving out (the angle at the common edges KL and MN remains practically constant).

The hinges in rectangular section beams (Fig. 5.7) displayed the same general pattern as the collapse mechanism described above. The only important difference was that the length of the hinge (KL or GBE) varied depending on the section dimensions. The length of the hinge was approximately equal to the depth (KL = GBE = GK) in beams whose width was greater than depth (Fig. 5.11). At the same time the yield lines EF and GH of the compression flange became elliptic making the length of the buckled flange bigger in the middle than along the edges. The maximum distance between the yield line and the middle of the hinge was $(0.4 - 0.5) \cdot GH$, the larger values corresponding to sections closer to a square shape. These hinges allowed more rotation than the square section ones before the development of the secondary hinge. The effective rolling radius was again estimated as $(0.03 - 0.05) \cdot KL$.

The length of hinges was approximately equal to the section width (KL = GBE = GH) in beams whose width was smaller than depth (Fig. 5.11). The flange boundaries EF and GH were straight. Jamming of the rolling deformation and development of the secondary hinge occurred at smaller angles θ than in square section beams. These changes in the collapse mechanism occurred earlier in sections with a smaller width to depth ratio. The effective rolling radius was again proportional to the hinge length, i.e. $(0.03 - 0.05) \cdot KL$.

5.4 THE THEORETICAL BENDING COLLAPSE MECHANISM

Description of the actual collapse mechanism of a square or rectangular section tube indicated the four characteristic phases in the hinge development:

1. Initial phase, with a "bulge" created in the webs, but without rolling deformations;
2. Second phase, with rolling along yield lines GA, AK and their symmetric counterparts;
3. Third phase, initiated by jamming of the rolling deformations and terminated by the creation of the secondary hinge;
4. Fourth phase - the development of the secondary hinge.

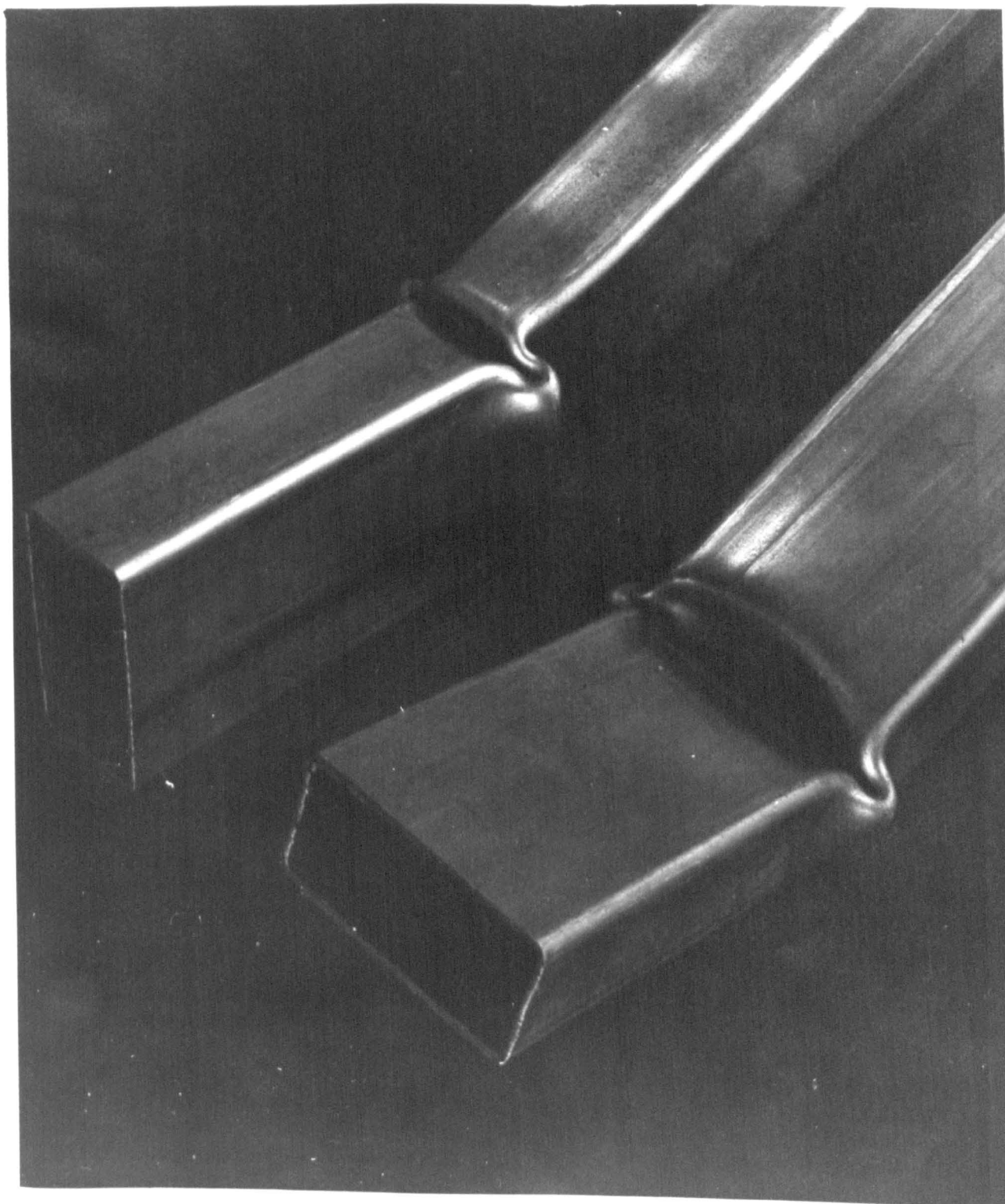


Fig. 5.11

A different hinge mechanism is displayed within each phase of the bending collapse in contrast to the unique mechanism of rectangular tubes in compression (69 - 77). Transition from one to another phase is gradual so that some transient "hybrid" mechanisms are also present. The detailed theoretical modelling of such a behaviour is very complex.

All the mechanisms above are not equally important. The first one lasts through the initial $5 \div 10$ degrees of hinge rotation, depending on section dimensions and shape. The second phase includes the next 20 - 30 degrees, while the third and fourth often occur at angles which are close to or beyond reasonable maximum rotations limited by the preservation of survival space. Experimental evidence reported in Chapter 6 has shown that the third mechanism maintains the character of the strength variation established during the second stage. The experiments of this thesis and other researchers (25, 80) also indicated that the first mechanism produces a monotonic and smooth transition from the point of maximum strength into the second phase, enabling a reasonable interpolation in the theoretical curve. The second mechanism covers the widest range of angles within limits required by practical application. These arguments were used to justify the selection of the second mechanism in the following theoretical analysis.

The actual collapse mechanism described in the previous section includes a complex combination of bending, rolling and in-plane plastic deformations. However, the deforming material is mainly concentrated along the yield lines. The theoretical collapse mechanism is therefore developed assuming that the section walls are inextensible and incompressible and that deformation takes place along yield lines only. Structural continuity should be maintained at the same time, which is very difficult to achieve at any point of the theoretical model. The continuity condition will be considered at some characteristic sections only, thus ensuring that the possible discontinuities at other places are small and without effect on the overall kinematics of the collapse mechanism.

The theoretical analysis will start with the collapse model in Fig. 5.12. Inextensibility of the section walls makes the two rigid "blocks" rotate about yield lines LM and KN through $\theta/2$ to produce a total hinge rotation θ . The collapse mechanism consists of bending deformation along the yield lines EF, GH, BC, GB, BE, HC, CF, AB, CJ, EL, GK, FM, HN, KN, LM and rolling along the lines GA, AE, AK, AL, HJ, JF, JN and JM. The most important deformations take place in the webs, and a cross section of the idealised web collapse mechanism (Fig. 5.12) is shown in Fig. 5.13a. Point B of the compression flange moves down and the edges GB and EB (Fig. 5.12) are "pulling" the adjacent segments of the web which are forced to roll along GA and EA about "frictionless rollers" with a radius r (Fig. 5.13a). The axis of the "roller" passes through the point S and is almost parallel to the line GA.

The conditions determining the position of characteristic points on the section are:

$$1. \text{ Line UD: } z_U = y_U \tan \xi \quad (5.24)$$

$$2. \text{ Line SU: } \frac{y_U}{z_U} = \frac{z_U - z_S}{y_S - y_U} \quad (5.25)$$

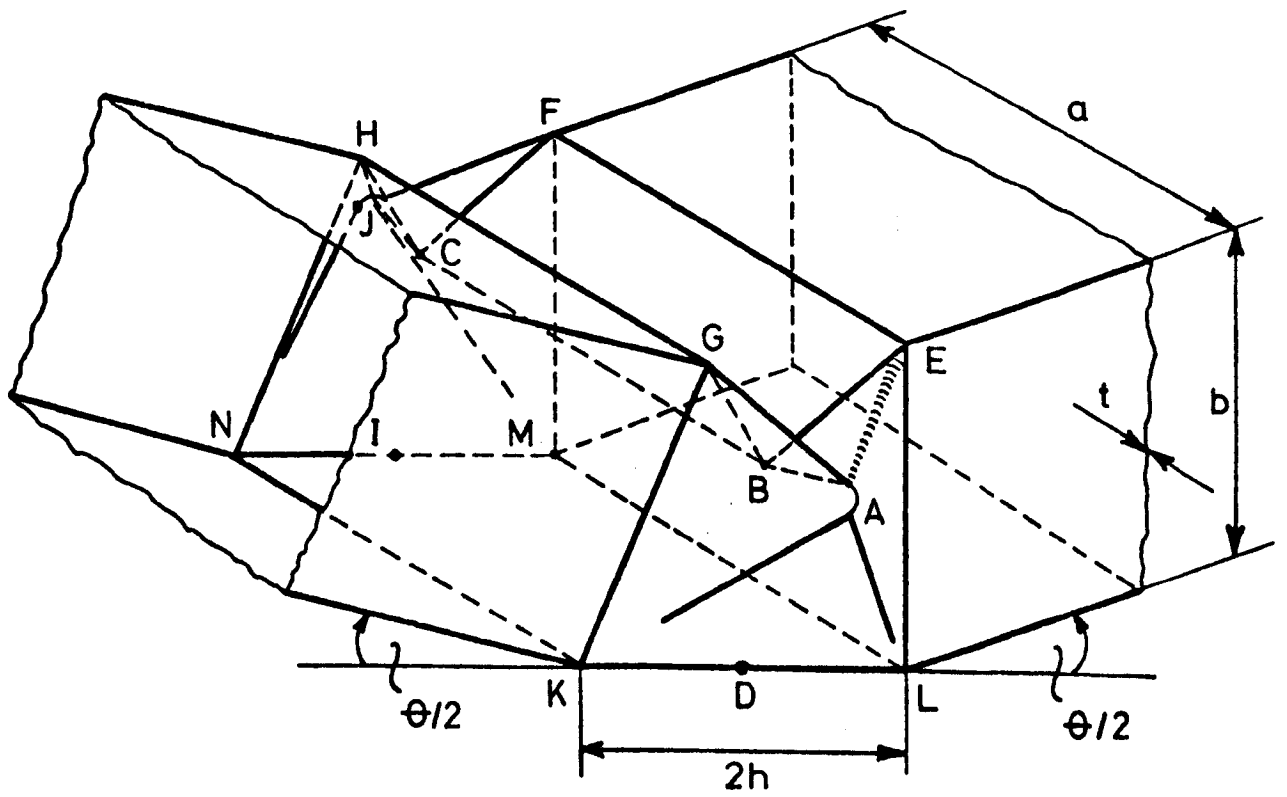


Fig. 5.12

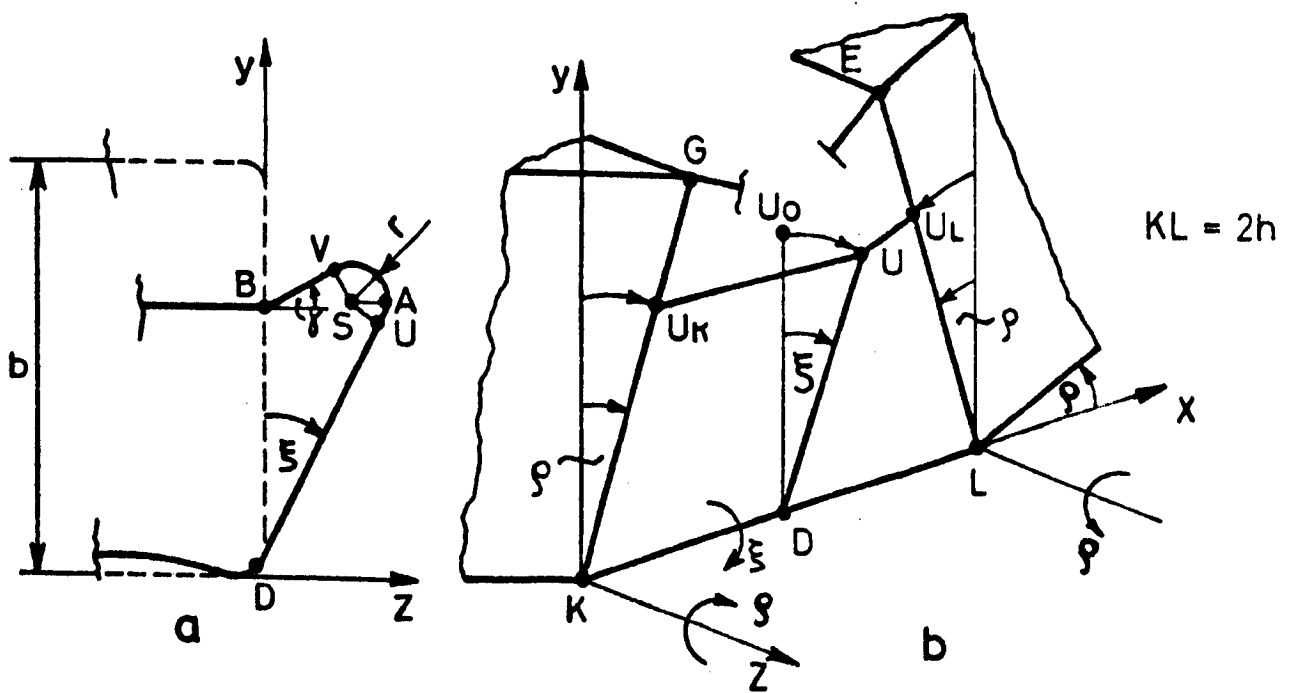


Fig. 5.13

3. Point U is on the circle about S if:

$$(z_U - z_S)^2 + (y_U - y_S)^2 = r^2 \quad (5.26)$$

4. Point V is on the circle about S if:

$$(z_V - z_S)^2 + (y_V - y_S)^2 = r^2 \quad (5.27)$$

5. Radius SV is perpendicular to BV if:

$$\frac{y_V - y_B}{z_V} = \frac{z_S - z_V}{y_V - y_S} \quad (5.28)$$

where y_B can be found from the deformation of the compressed flange - equation (5.34).

6. The length of the section BVAUD must be equal to the depth of the section (b), because of the wall inextensibility condition:

$$b = \sqrt{z_V^2 + (y_V - y_B)^2} + r\left(\frac{\pi}{2} + \xi + \arctan \frac{z_S - z_V}{y_V - y_S}\right) + \sqrt{y_U^2 + z_U^2} \quad (5.29)$$

7. Points U_K , U and U_L in Fig. 5.13b belong to the same longitudinal fibre in the web. The co-ordinates of U_K and U_L are:

$$x_{U_K} = \sqrt{y_U^2 + z_U^2} \sin \rho ; \quad y_{U_K} = \sqrt{y_U^2 + z_U^2} \cos \rho ; \quad \text{where } \rho = \frac{\theta}{2}$$

Neglecting the radii of deformation as in Fig. 5.13b we may write inextensibility condition in the longitudinal direction ($U_K U = h$) in the form (after removing the square roots on both sides):

$$h^2 + z_U^2 = (h - \sqrt{y_U^2 + z_U^2} \sin \rho)^2 + (y_U - \sqrt{y_U^2 + z_U^2} \cos \rho)^2 \quad (5.30)$$

The hinge length (2h) and rolling radius (r) are theoretically unknown. However, even if they are determined experimentally there are still seven unknowns: ξ , x_U , y_U , x_S , y_S , x_V and y_V which can be calculated from (5.24) + (5.30). A numerical solution can be obtained in any particular case, but the aim of the analysis is to produce a simplified solution in an explicit form and some approximations will have to be introduced.

One possibility, supported by experimental evidence, is to assume that $\xi = \rho = \theta/2$, $y_U = y_S$, $z_U = z_S$ (U coincides with A) and that $z_V = z_S$ (Fig. 5.13a). This approximation was used to derive the theoretical $M - \theta$ curve of a square section tube (87) and the result is summarised in Appendix 1. The model gave good results, but it was rather complex, not quite continuous and did not predict the theoretical rolling radius (r)

and the length of the hinge (2h) in rectangular section tubes, so a new attempt was made.

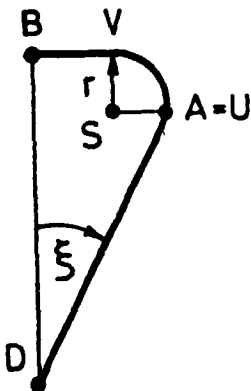


Fig. 5.14

The second approximation is shown in Fig. 5.14. The energy of rolling deformation (W_r) was expressed in terms of the angle of hinge rotation θ and rolling radius r (Appendix 2), following the same principles as in section 5.5. A contribution of the rolling deformation to the total hinge moment was then obtained from:

$$M_r = \frac{dW_r(\theta, r)}{d\theta} = M_r(\theta, r) \quad (5.31)$$

The hinge moment is always at its current minimum, so an attempt was made to derive the theoretical rolling radius from the condition:

$$\frac{dM_r(\theta, r)}{dr} = 0 \quad (5.32)$$

The equation (5.32) had no zeros within limits of the problem considered, but it indicated that the rolling radius tends to be as large as possible.

Minimisation of $W_r(\theta, r)$ with respect to r also showed that the rolling radius tends to be as large as possible.

Inextensibility of the section walls is the limiting factor of the rolling radius, so an attempt was made to derive r as the largest radius that would simultaneously satisfy the continuity conditions (5.29) and (5.30), rearranged to suit Fig. 5.14. A very complex system of non linear equations was obtained, which could not produce a solution in a convenient explicit form. The equations contained the hinge length (h) which was also a theoretically unknown quantity. It was decided therefore to use the experimental results for the rolling radius.

The third and final simplification of the collapse mechanism in Fig. 5.12 is shown in Fig. 5.15. The yield line ABCJ of the new model is straight and the effect of the rolling radius on the overall geometry of the mechanism has been neglected. The first approximation is close to reality because most of the bending along BE, BG, CF and CH takes place in the very beginning of collapse, and the contribution of this deformation to the total energy absorbed was negligible in the first approximation (Appendix 1) of the mechanism in Fig. 5.12. Leaving out the radius also has a relatively small effect on the overall geometry.

Consider the compression flange and web deformation in Fig. 5.16a and b respectively. The actual yield lines GH, BC, and EF (Fig. 5.15) also have some bending radius due to spreading of the plastically deformed zones during deformation. The effect of this bending radius on the overall geometry is small, except in thick walled beams.

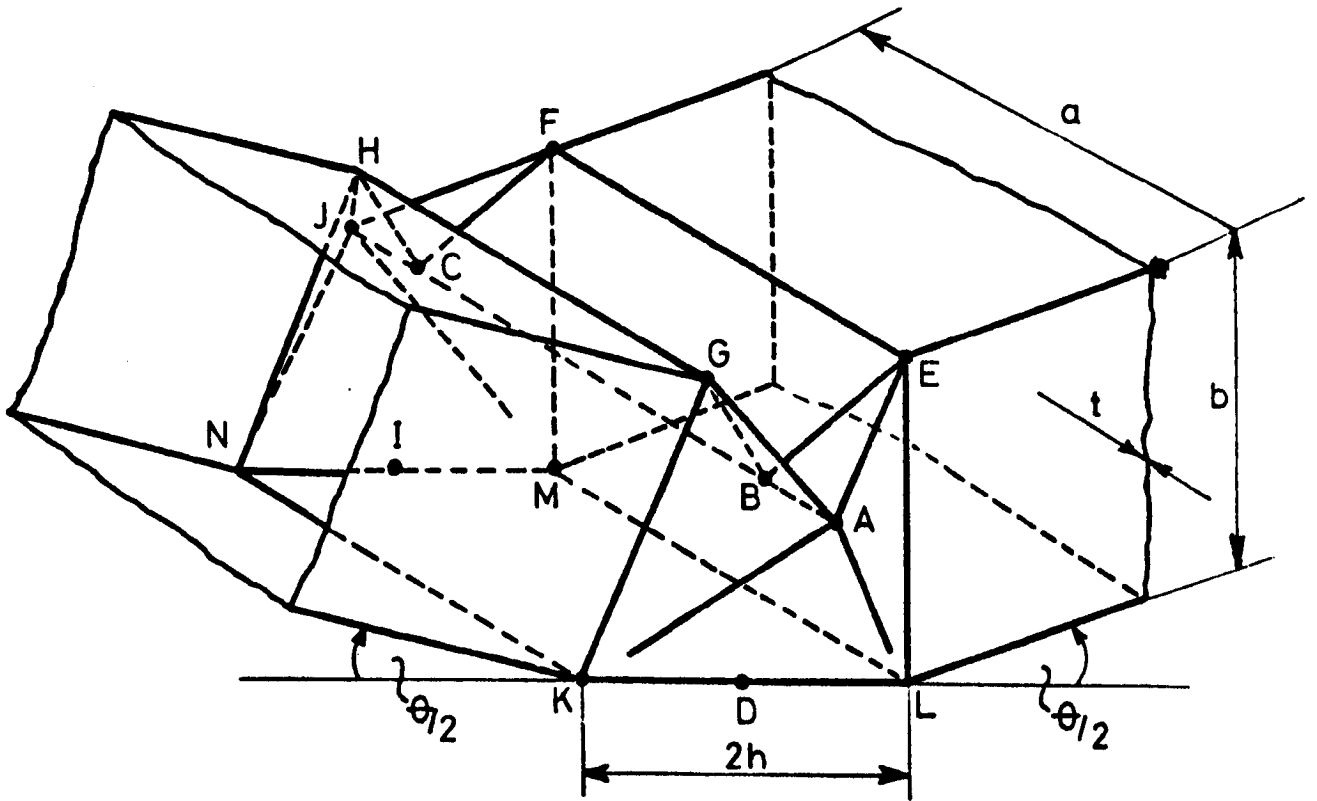


Fig. 5.15

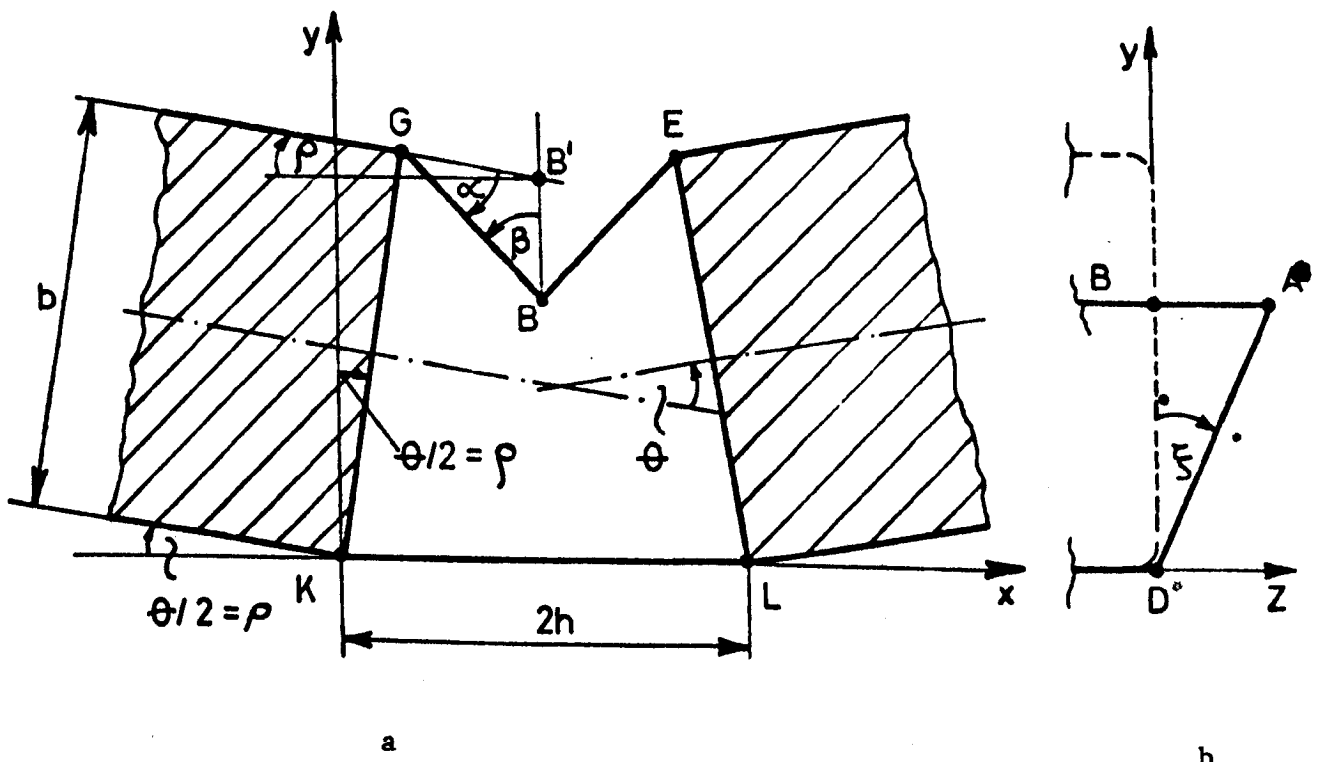


Fig. 5.16

The hinge is symmetric, so only one half will be considered. An angle

$$\rho = \frac{\theta}{2} \quad (5.33)$$

will be introduced (Fig. 5.16) to make the formulae simpler. Co-ordinates of point B in Fig. 5.16 are:

$$x_B = h ; \quad y_B = b \cos \rho - (h - b \sin \rho) \cot \beta ; \quad z_B = 0$$

or, after some rearrangement (with $0 \leq \beta \leq \pi/2$):

$$x_B = h ; \quad y_B = b \cos \rho - \sqrt{b \cdot \sin \rho \cdot (2h - b \sin \rho)} ; \quad z_B = 0 \quad (5.34)$$

The continuity condition (5.29) now becomes:

$$b = z_A + \sqrt{y_A^2 + z_A^2} \quad (5.35)$$

with (Fig. 5.16): $y_A = y_B \quad (5.36)$

From (5.34), (5.35) and (5.36):

$$z_A = b \sin^2 \rho - h \sin \rho + \sqrt{b \sin \rho (2h - b \sin \rho)} \cos \rho \quad (5.37)$$

The continuity condition in the longitudinal direction (5.30) is:

$$h^2 + z_A^2 = (h - \sqrt{y_A^2 + z_A^2} \sin \rho)^2 + (y_A - \sqrt{y_A^2 + z_A^2} \cos \rho)^2 \quad (5.38)$$

Substituting (5.34), (5.36) and (5.37) into (5.38) it can be shown that the continuity conditions (5.35) and (5.38) are met simultaneously for any ratio a/b and for any angle θ only if:

$$h = \frac{a}{2} \quad \text{or} \quad h = \frac{b}{2} \quad (5.39)$$

The actual hinge length of a particular section can be obtained by substituting both values (5.39) into the expression (5.69) for the hinge moment variation, derived in the next section. The correct value for h is the one that gives lower moments or energy absorption. It was concluded in this way that:

$$h = \frac{a}{2} \quad \text{if} \quad a \leq b \quad (5.40)$$

and $h = \frac{b}{2} \quad \text{if} \quad a \geq b$

which is due to a smaller length of the rolling yield line.

The theoretical result (5.40) agrees very well with the experimental evidence (Figs. 5.7 and 5.11) reported in the last two paragraphs of section 5.3. This proves that the idealised collapse mechanism in Fig. 5.15 is realistic and applicable to thin walled rectangular section tubes of an arbitrary width to depth ratio. Continuity condition may also explain why the static and dynamic hinge mechanisms are virtually the same.

5.5 THE THEORETICAL ENERGY ABSORBED IN THE HINGE

5.5.1 The Energy of Plastic Bending and Rolling

The idealised hinge absorbs energy by plastic bending and rolling deformations along the yield lines shown in Fig. 5.15. The energy of plastic deformation absorbed by bending of a constant width sheet about a constant radius r_b (Fig. 5.17a) is:

$$W_b = \int_0^{\psi} m'_p \cdot L \cdot \frac{ds_b}{r_b} = \int_0^{\psi} m'_p L d\psi \quad (5.41)$$

where: m'_p [Nm/m] = fully plastic moment of a unit width of the sheet, which will be discussed in section 5.7,

L [m] = length of the yield line (width of the sheet), and

ψ [rad] = angle of relative rotation between the two sheet segments about the yield line.

The quantity m'_p may vary during deformation, but it is common to assume an average, effective value m_p , so that (5.41) takes a simpler form (69 - 75):

$$W_b = m_p \cdot L \cdot \psi \quad [J] \quad (5.42)$$

If $m_p = \text{const}$, the energy W_b does not depend on the bending radius. Larger bending radii increase the deformed volume of the material, but reduce proportionally the angle of deformation of a unit volume, so that (5.42) applies to any bending radius. However, a smaller bending radius produces larger local deformations along the yield line. In strain-hardening materials this may increase the effective value of m_p relative to the one produced by a larger radius. Extremely small bending radii can cause separation of the material, but this is unlikely to happen in the case considered.

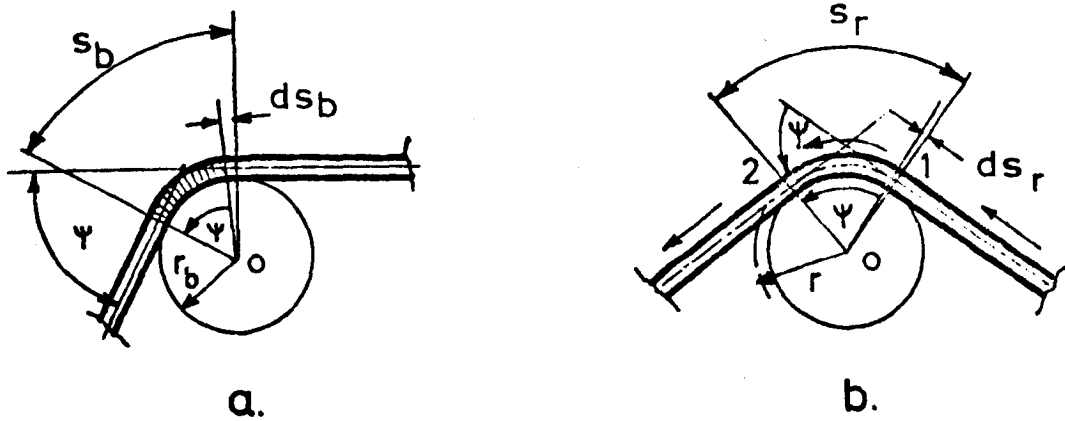


Fig. 5.17

In the case of sheet rolling about a frictionless roller with radius r (Fig. 5.17b) an elementary segment of the sheet length " ds " enters the curvature at point 1, bends through an angle ψ , proceeds "sliding" about the roller and straightens up again at point 2, where it leaves the curvature. The angle ψ can be calculated from Fig. 5.17b as:

$$\psi = \int_0^{s_r} \frac{ds}{r} \quad (5.43)$$

where s_r represents the rolled length.

The plastic deformation takes place twice (at points 1 and 2) and the expression for the energy of rolling a unit width of a sheet is (71, 75):

$$W'_r = 2 \cdot \int_0^{s_r} m_p \frac{ds}{r} = \frac{2m_p}{r} \int_0^{s_r} ds \quad [J/m] \quad (5.44)$$

Rolling deformation may be such that the rolled length s_r varies along the yield line. In such a case it is convenient to express the rolled length as a function of the distance ℓ from one end of the yield line: $s_r = s_r(\ell)$. The total energy absorbed along the whole yield line (L), with $r = \text{const}$, then becomes:

$$W_r = \frac{2m_p}{r} \int_0^L s_r(\ell) \cdot d\ell = \frac{2m_p}{r} \cdot A_r \quad [J] \quad (5.45)$$

where $A_r [m^2] =$ area swept by the yield line during rolling deformation.

Expressions (5.42) and (5.45) will now be used to calculate the energy absorbed by the collapse mechanism in Fig. 5.15.

5.5.2 The Compression Flange

Rotation of the hinge through an angle θ produces an idealised deformation

of the compression flange in Fig. 5.16. The angle $\rho = \theta/2$ (5.33) is used again, and the co-ordinates of point G, corresponding to the hinge rotation θ are:

$$x_G = b \cdot \sin \rho ; \quad y_B = b \cdot \cos \rho \quad (5.46)$$

Hence:

$$\beta = \arcsin \left(\frac{h - x_G}{GB} \right) = \arcsin \left(1 - \frac{b}{h} \sin \rho \right) \quad (5.47)$$

The secondary hinge starts, theoretically, when the two halves of the buckled flange contact each other. From $\beta = 0$ follows $\rho' = \arcsin (h/b)$. If $2h = b$, $\rho' = 30^\circ$ or $\theta_J = 60^\circ$. If $2h < b$, $\theta_J < 60^\circ$, which agrees with observations in the previous section. The effective angle θ_J will be smaller than both values due to the effect of the wall thickness and web deformation, as discussed later in section 6.4.

The angle α of relative rotation of the flange walls along GH can be derived from the triangle GBB' using:

$$\alpha + \beta + \frac{\pi}{2} + \rho = \pi$$

$$\text{hence: } \alpha = \frac{\pi}{2} - \rho - \arcsin \left(1 - \frac{b}{h} \sin \rho \right) \quad (5.48)$$

The energy absorbed along yield lines EF and GH as the hinge rotates through an angle θ can now be calculated from (5.42), (5.48), (5.40) and Fig. 5.16 in a form:

$$W_1 = W_{EF+GH} = 2 m_p a \left[\frac{\pi}{2} - \rho - \arcsin \left(1 - \frac{b}{h} \sin \rho \right) \right] \quad (5.49)$$

The angle of relative rotation along the yield line BC is $(\pi - 2\beta)$ (Fig. 5.16), so that the energy absorbed becomes:

$$W_2 = W_{BC} = m_p a \left[\pi - 2 \arcsin \left(1 - \frac{b}{h} \sin \rho \right) \right] \quad (5.50)$$

5.5.3 The Web

The symmetry of web deformation (Fig. 5.15) makes it sufficient to consider only one half of the web mechanism, i.e. bending along AB, BG, GK and rolling along GA and AK.

The length of the yield line AB is equal to z_A in equation (5.37) and the angle of relative rotation can be seen in Figs. 5.15 and 5.16 as $(\pi - 2\beta)$, where β is known from (5.47). The energy absorbed along AB and CJ becomes:

$$W_3 = W_{AB+CJ} = 2 \cdot m_p \cdot (b \sin^2 \rho - h \sin \rho + \sqrt{b \sin \rho (2h - b \sin \rho)}) \cdot \cos \rho \cdot (\pi - 2 \cdot \arcsin (1 - \frac{b}{h}) \sin \rho) \quad (5.51)$$

with h known from (5.40).

The angle of relative rotation along BG is $\pi/2$ (Fig. 5.15) and the hinge length is h . There are four yield lines under the same conditions, hence:

$$W_4 = W_{BG+BE+CH+CF} = 4 \cdot m_p \cdot h \cdot \frac{\pi}{2} = 2m_p h \pi \quad (5.52)$$

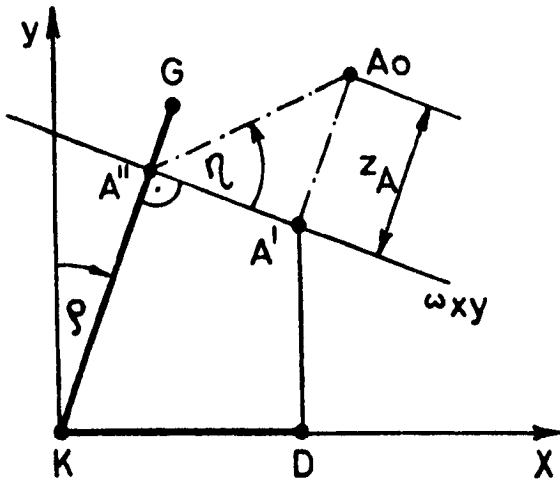


Fig. 5.18

The angle " η " of relative rotation along yield line GK will be determined from Fig. 5.18. Point A' represents the normal projection of point A (Fig. 5.15) on the xy plane of the undeformed web. Point A' coincides with point B in Fig. 5.15. A plane ω , perpendicular to GK and passing through A intersects the xy plane along the straight line ω_{xy} . Line GK lies in the xy plane, therefore the ω plane is perpendicular to xy . Plane ω intersects GK at point A'' . If we now rotate ω about ω_{xy} so that point A falls into the point A_0 in xy , the actual angle η will be:

$$\eta = \arcsin \frac{A'A_0}{A'A''} \quad (5.53)$$

The distance $A'A_0 = z_A$ and can be obtained from (5.37).

Co-ordinates of point A' are the same as of point B (5.34).

Line $A'A''$ is normal to GK and

$$x_{A''} = y_{A''} \tan \rho \quad (5.54)$$

hence:

$$\tan \rho = \frac{y_{A''} - y_{A'}}{h - x_{A''}} = \frac{y_{A''} - y_B}{h - y_{A''} \cdot \tan \rho}$$

or:

$$y_{A''} = \frac{h \tan \rho + b \cos \rho - \sqrt{b \sin \rho (2h - b \sin \rho)}}{1 + \tan^2 \rho} \quad (5.55)$$

The length of the yield line GK is b and there are four of them in the complete mechanism, so:

$$W_5 = W_{GK+EL+HN+FM} = 4 \cdot m_p \cdot b \cdot \arctan \frac{z_A}{\sqrt{(h - x_{A''})^2 + (y_{A''} - y_B)^2}} \quad (5.56)$$

where h, y_B , z_A , $y_{A''}$ and $x_{A''}$ can be obtained from equations (5.40), (5.34), (5.37), (5.55) and (5.54) respectively.

The rolling radius along GA is reasonably constant, so that equation (5.45) may be used. The area swept by the yield line GA is equal to the triangle ABG in Fig. 5.15. There are four such yield lines in the mechanism, hence:

$$W_6 = W_{GA+AE+CH+CF} = 4 \cdot \frac{2m_p}{r} \cdot \frac{h \cdot z_A}{2} = 4m_p \frac{h}{r} z_A \quad (5.57)$$

or, taking z_A from (5.37) and h from (5.40):

$$W_6 = 4m_p \frac{h}{r} (b \sin^2 \rho - h \sin \rho + \sqrt{b \sin \rho (2h - b \sin \rho)}) \cdot \cos \rho \quad (5.58)$$

The actual rolling radius decreases slowly during deformation, and an approximate, empirical variation:

$$r(\theta) = (0.07 - \frac{\theta}{70}) h \quad (5.59)$$

is suggested to fit the experimental results. If θ varies between zero and 40° the expression (5.59) will produce $r = (0.07 \pm 0.06)h$, which falls within the observed range: $r = (0.05 \pm 0.03)KL = (0.1 \pm 0.06)h$, as reported in section 5.3.

Rolling along the yield line KA (Fig. 5.15) takes place with a varying rolling radius. The radius is almost infinite at K (flat web), then decreases rapidly within the lower half of the yield line and then continues decreasing slowly to become approximately equal to the rolling radius of the line GA at point A. Such variation can be approximated by a hyperbolic function:

$$r_{KA} = \frac{KA}{l_k} r \quad (5.60)$$

where l_k is the distance from K along KA, and r is the rolling radius in (5.59).

The rolled length at A is equal to z_A (Fig. 5.15). Assuming a linear variation of the rolled length between K and A:

$$l_r = \frac{l_k}{KA} \cdot z_A \quad (5.61)$$

The energy absorbed along KA becomes:

$$W_{KA} = \int_0^{KA} 2m_p \cdot \frac{l_r}{r_{KA}} \cdot dl_k = 2m_p \int_0^{KA} \frac{l_k}{KA} z_A \cdot \frac{l_k}{KA \cdot r} \cdot dl_k = \frac{2m_p z_A^2 KA}{3r} \quad (5.62)$$

The distance KA is (Fig. 5.15):

$$KA = \sqrt{h^2 + y_B^2 + z_A^2} \quad (5.63)$$

There are four yield lines similar to KA in the mechanism, hence:

$$W_7 = W_{KA+LA+NJ+MJ} = \frac{8}{3} m_p \cdot \frac{z_A}{r} \sqrt{h^2 + y_B^2 + z_A^2} \quad (5.64)$$

where y_B , z_A , h and r are known from (5.34), (5.37), (5.40) and (5.59) respectively.

5.5.4 The Tension Flange

The inextensibility of walls of the idealised mechanism (Fig. 5.15) does not allow concavity to be formed in the tension flange. The only deformation that can take place is bending along yield lines KN, LM, KL and MN. The angle of relative rotation along yield lines KN and LM is $\rho = \theta/2$, and for lines KL and MN the angle $\xi = \arctan(z_A/y_A)$ (Fig. 5.16b) should be used. The energy absorbed becomes:

$$W_8 = W_{KN+LM+KL+MN} = 2 \cdot m_p \cdot (a \cdot \rho + 2h \cdot \arctan \frac{z_A}{y_A}) \quad (5.65)$$

where h, z_A and $y_A = y_B$ are known from (5.40), (5.37) and (5.34) respectively.

A more accurate model of the shallow concave deflection in the tension flange (Fig. 5.8b and c) is shown in Fig. 5.19. It consists of a cylindrical segment of the tension flange cut longitudinally by the webs (sections KL and MN) and at an angle ρ to the cylinder axis by the tension

flanges of the two rigid "blocks" on either side of the hinge (elliptical sections LM and KN).

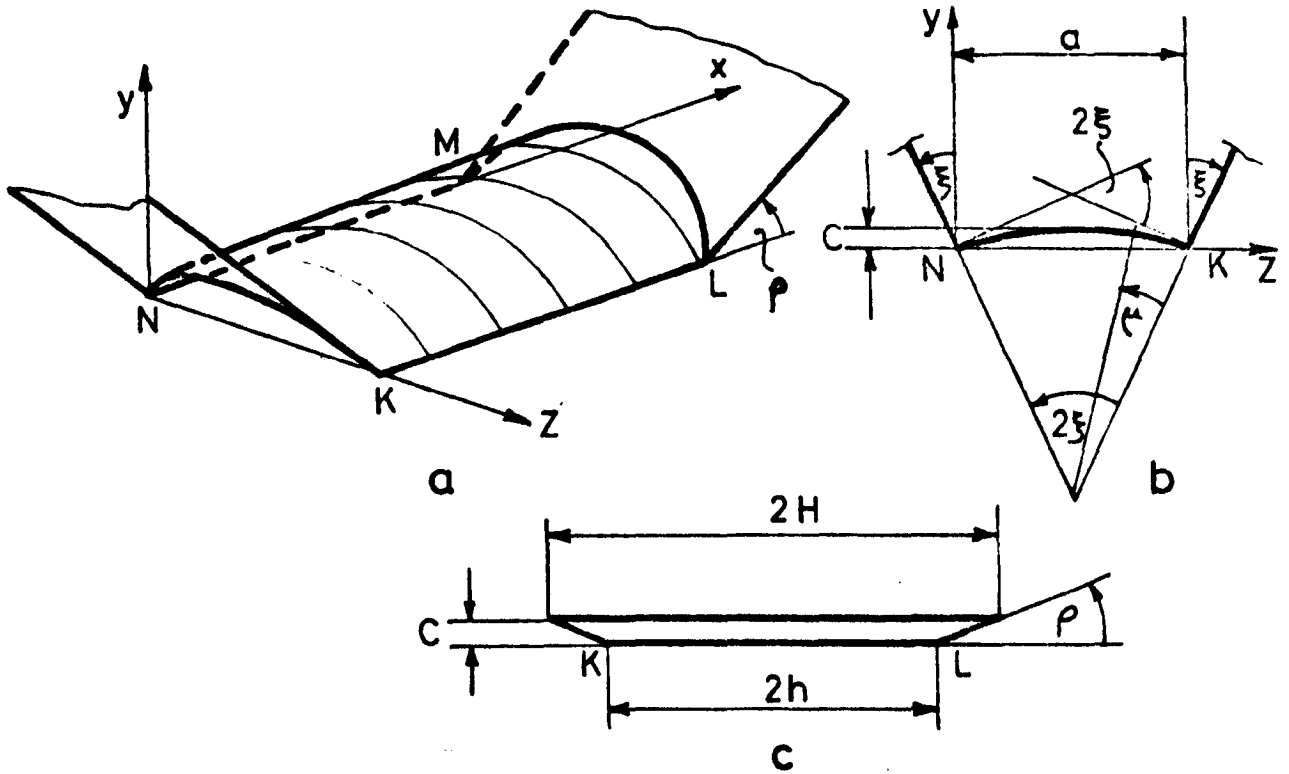


Fig. 5.19

Assuming no deformation along KL and MN, the deformation of the tension flange consists of bending in Fig. 5.19b and rolling along the elliptic boundaries. The concavity depth "C" can be found from the uniquely defined circular arc NK in Fig. 5.19b. This depth can then be used to find the distance 2H from Fig. 5.19c. Both C and H are functions of θ , so that rolling, rather than bending, must take place along the elliptic boundaries.

The angle of bending in Fig. 5.19b is 2ξ , but the bent width l_b varies between $2h$ and $2H$ and can be expressed in terms of the angle " μ " in Fig. 5.19b, because the elliptic sections are uniquely defined. The energy of bending is:

$$W_{sb}^l = m_p \cdot \int_0^{2\xi} l_b(\mu) d\mu \quad (5.66)$$

If $l_b(\mu) = 2h = \text{const}$, equation (5.66) is equal to the second term in (5.65). In most practical cases the distance $2H$ is close to $2h$, so that the bending deformation is well allowed for in the idealised model. The theoretical $2H$ is slightly larger than the actual one because some bending probably takes place along KL and MN.

The rolling deformation is approximated by the first term in (5.65). The experimental rolling radius appears very large (Fig. 5.8c), so that the actual energy absorbed should not be much greater than that absorbed by the bending deformation through an angle ρ , as in (5.65).

The in-plane deformations of the tension flange have been small (Table 5.1) and developed in the initial stages of collapse only. The curvature of the cylindrical deformation had to be met by some lateral deflection of the webs.

It is, therefore, believed that equation (5.65) is adequate for the purpose.

5.5.5. The Total Energy Absorbed

The energy absorbed in the hinge can now be expressed in terms of the angle θ of hinge rotation as a sum:

$$W(\theta) = \sum_{i=1}^8 W_i(\theta) \quad (5.67)$$

where the energies $W_i(\theta)$ are given in equations (5.49), (5.50), (5.51), (5.52), (5.56), (5.57), (5.64) and (5.65) respectively.

However, the theoretical model in Fig. 5.15 has been based on the hinge behaviour during the second stage of collapse only (section 5.4). The strength variation derived from (5.67) will also have to be checked before accepting the theory. The other important problem to be considered now is the effective fully plastic moment of the sheet (m_p) which occurs in all the energy equations.

5.6 THE THEORETICAL VARIATION OF THE HINGE MOMENT

The theoretical variation of the hinge moment $M(\theta)$ can be obtained from the energy equation (5.67) in a form:

$$M(\theta) = \frac{dW(\theta)}{d\theta} \quad (5.68)$$

Derivation of the equation (5.67) is possible, but it produces a formula which is too long and complex for practical application. It is much simpler to replace the differentiation by a finite-difference expression:

$$M(\theta) = \frac{\Delta W(\theta)}{\Delta\theta} = \frac{W(\theta + \Delta\theta) - W(\theta)}{\Delta\theta} \quad (5.69)$$

The difference between (5.68) and (5.69) is negligible for a sufficiently small angle increment $\Delta\theta$. The program used in this thesis has $\Delta\theta = 0.1^\circ = 0.001745$ rad. An assumption of a constant moment within such a small

interval is quite acceptable for practical application.

Expression (5.69) produces a discrete point on the theoretical $M - \theta$ curve. A series of such points can be calculated by assuming a suitable interval of the angle θ separating the adjacent points, and repeating (5.69) for each of them.

The moment $M(\theta)$ must, of course, satisfy the condition:

$$M(\theta) \leq M_{\max} \quad (5.70)$$

where M_{\max} is the maximum bending strength of the section (5.23).

5.7 DETERMINATION OF MATERIAL PARAMETERS

Formulae for maximum strength (5.23), energy absorption (5.67) and moment variation (5.68) include material properties - yield stress (σ_p) and the effective fully plastic moment of the section walls (m_p). All tubes were tested as received, so that both of these parameters may be influenced by several factors which drew little attention in references 69 - 79, dealing with collapse of structural components. These factors will now be considered and reasons for selection of the material properties will be given.

5.7.1 Pure Bending of an Ideally Plastic Sheet

Pure bending of solid beams allows formation of the anti-clastic curvature, producing an almost uniaxial stress state. A plane stress field is obtained if shear is added to the bending stresses. Bending of plates, however, produces a more or less plane stress field only in the vicinity of the free edges (Fig. 5.20a), while a plain strain field (shaded in Fig. 5.20a) prevails over a major area in the middle. The strains in the direction 2 are suppressed by the plate width ($\epsilon_2 = 0$).

The bending yield line is parallel to the axis 2 and the effective fully plastic moment of the sheet depends on the stress σ_{p1} in direction 1 normal to the yield line. Full plasticity of the sheet, represented by the stress distribution in Fig. 5.20b, gives the fully plastic moment per unit width (m_0) in pure bending:

$$m_0 = \sigma_{p1} \cdot \frac{t}{2} \cdot \frac{t}{2} = \frac{\sigma_{p1} t^2}{4} \quad [\text{Nm/m}] \quad (5.71)$$

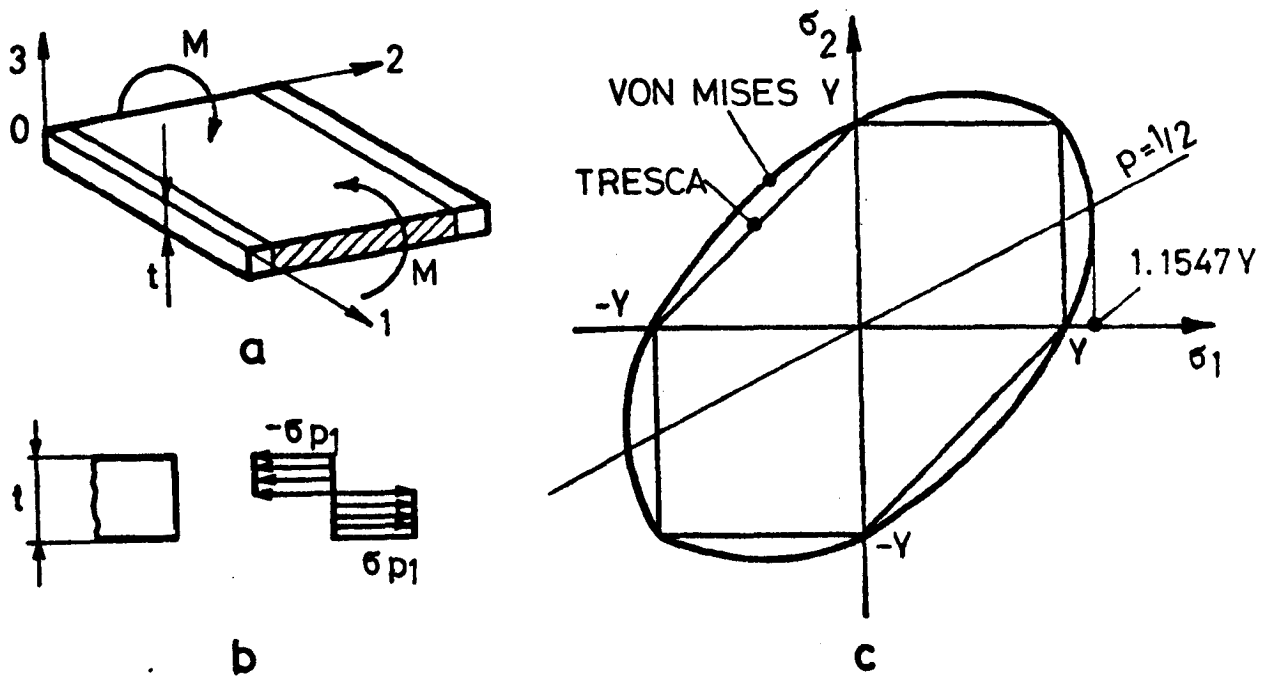


Fig. 5.20

The yield criteria commonly used in practice are due to Tresca (88) and von Mises (89). The Tresca criterion suggests that yielding occurs when the maximum shear stress is equal in magnitude to half the difference between the algebraic maximum and minimum principal stresses. In uniaxial tension:

$$\tau_{\max} = \frac{1}{2} Y \quad (5.72)$$

where Y is the yield stress in uniaxial tension. In the biaxial stress situation, with principal stresses σ_1 and σ_2 :

$$\tau_{\max} = \frac{1}{2} (\sigma_1 - \sigma_2) = \frac{1}{2} \sqrt{\sigma^2 + 4\tau^2} \quad (5.73)$$

and from (5.72) and (5.73) the Tresca yield criterion gives:

$$\sigma^2 + 4\tau^2 = Y^2 \quad (5.74)$$

The yield loci in the $\sigma_1 \sigma_2$ plane (Fig. 5.20c) are represented by a Tresca hexagon. The stress σ_{p1} in the direction 1 (Fig. 5.20b) can be obtained from (5.74) with $\tau = 0$, or from the hexagon in Fig. 5.20c, as

$$\sigma_{plt} = Y \quad (5.75)$$

The von Mises criterion is based on the assumption that the yielding starts when the shear strain energy in 3-dimensional stress system becomes equal to the strain energy causing yielding in uniaxial tension. The appropriate expression is:

$$(\sigma_1 - \sigma_2)^2 + (\sigma_2 - \sigma_3)^2 + (\sigma_1 - \sigma_3)^2 = 2Y^2 \quad (5.76)$$

If the stress σ_3 , normal to the sheet surface is zero, a biaxial stress system is obtained:

$$2\sigma_1 = \sigma + \sqrt{\sigma^2 + 4\tau^2} \quad (5.77)$$

$$2\sigma_2 = \sigma - \sqrt{\sigma^2 + 4\tau^2}$$

and from (5.76) and (5.77)

$$\sigma^2 + 3\tau^2 = Y^2 \quad (5.78)$$

Von Mises criterion produces the ellipse in Fig. 5.20c.

Plastic strain depends on the stress history and can be found by summing the increments following the stress history. If the elastic strains are negligible in comparison with the plastic ones, the ratio of strain increments for a small increment in stress at the stress level $\sigma_1, \sigma_2, \sigma_3$ can be obtained from the Levy-Mises equations:

$$\frac{d\epsilon_1}{\sigma_1'} = \frac{d\epsilon_2}{\sigma_2'} = \frac{d\epsilon_3}{\sigma_3'} \quad (5.79)$$

where $d\epsilon_1, d\epsilon_2$ and $d\epsilon_3$ are the total principal strain increments and the "reduced principal stresses" are:

$$\sigma_1' = \sigma_1 - \bar{\sigma} ; \quad \sigma_2' = \sigma_2 - \bar{\sigma} \quad \text{and} \quad \sigma_3' = \sigma_3 - \bar{\sigma} \quad (5.80)$$

where $\bar{\sigma}$ denotes the mean stress (hydrostatic pressure).

$$\bar{\sigma} = \frac{1}{3} (\sigma_1 + \sigma_2 + \sigma_3) \quad (5.81)$$

In the plate bending case the stress through the thickness $\sigma_3 = 0$ and the strain in 02 direction (Fig. 5.20a) $d\epsilon_2 = 0$. The plate volume remains unchanged during deformation, hence:

$$d\epsilon_1 + d\epsilon_2 = 0 \quad (5.82)$$

From (5.79), (5.80) and (5.82), with $\sigma_3 = 0$ we obtain $\sigma_1' + \sigma_3' = 0$ and:

$$p = \frac{\sigma_2}{\sigma_1} = \frac{1}{2} \quad (5.83)$$

which represents the plain strain condition - straight line in Fig. 5.20c.

Substituting the ratio (5.83) into (5.76), with $\sigma_3 = 0$, we obtain the von Mises yield stress σ_{p1m} , perpendicular to the yield line (Fig. 5.20b) as:

$$\sigma_{p1m} = \frac{2\sqrt{3}}{3} Y = 1.1547 Y \quad (5.84)$$

Comparison of (5.71), (5.75) and (5.84) indicates that the fully plastic moment of an ideally plastic sheet in pure bending may vary by 15%, depending on the selection of the yield criterion.

5.7.2 Effect of the Actual Material Properties

It will be assumed that section walls are not affected by corrosion or fatigue prior to collapse. If intensive, they may lower significantly both the strength and energy absorbing capacity of the hinge by reducing the effective wall thickness and by increasing the tendency of material separation.

The yield stress Y of an ideally plastic material is equal in tension and compression. In cubic crystal materials, such as steel, the assumption is reasonable because the slip deformation can operate equally well in both directions. Ref. 90 states, however, that the compressive yield stress (σ_{pc}) of mild steel is usually 10 + 15% higher than the yield stress in tension (σ_{pt}). The fully plastic moment of the sheet can then be obtained from Fig. 5.20b, assuming no axial force, as:

$$m_0 = \frac{t^2 \sigma_{pc}}{2(1 + \sigma_{pc}/\sigma_{pt})} \quad (5.85)$$

Yielding of the material often takes place before the hinge starts collapsing. Bending along the yield lines produces therefore a reverse plastic deformation in one half of the wall thickness. In many materials this causes the Bauschinger effect (Fig. 5.21) (91), i.e. if the material is plastically deformed in one direction (line OA), subsequent yielding in the opposite direction (point C) will start at a lower stress than if the second loading were applied without pre-stressing. The Bauschinger

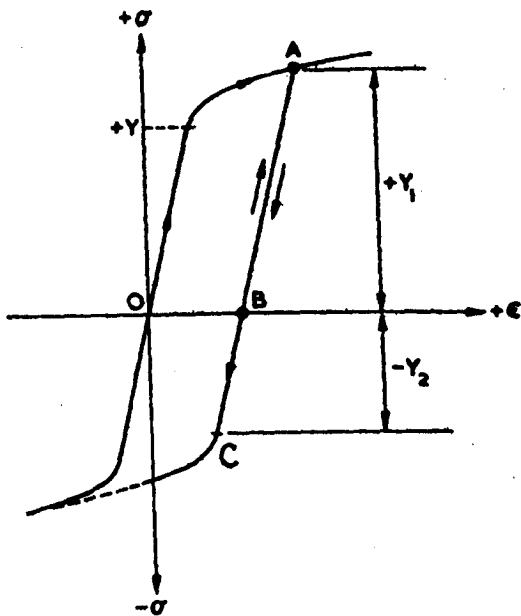


Fig. 5.21

effect vanishes with the increase of the reverse strain (Fig. 5.21), and can be neglected in high strain (Table 5.1) conditions along the yield lines of the hinge collapse mechanism.

Anisotropy due to chemical content or welding in seam welded tubes is not considered. A uniform chemical content can be reasonably assumed within a hinge, and seam welding produces normally a localised increase of the yield stress without a significant overall effect on hinge properties.

However, anisotropy due to crystallographic texture resulting from the deformation during production is common in rolled sheets. Anisotropy can be planar (in the plane of the sheet) and/or normal (through the thickness). The normal anisotropy is sometimes

more pronounced than the planar one and may have greater effect on the wall deformations. This is because resistance to thinning affects yielding of the sheet in a biaxial stress state. These two stress systems differ by hydrostatic tension only, which does not affect yielding. A simple measure of the thinning resistance is the ratio:

$$R = \frac{\epsilon_w}{\epsilon_t} = \frac{\ln(w_0/w)}{\ln(t_0/t)} \quad (5.86)$$

where ϵ_w and ϵ_t are the natural strains in the lateral and normal (through the thickness) directions found by the tension test on a strip, and w_0 , w , t_0 , t are the initial and final width and thickness of the strip respectively.

Hill (39) has extended the von Mises yield criterion to a material texture that is rotationally symmetric about the sheet normal. From his results the yield criterion under a biaxial, in-plane stress system without Bauschinger effect can be written in a form:

$$\sigma_1^2 \left[1 + p^2 - p \left(\frac{2R}{R+1} \right) \right] = Y^2 \quad (5.87)$$

where $p = \sigma_2/\sigma_1$ as in (5.83).

Condition (5.87) is plotted in Fig. 5.22 (92) for several values of R and stress ratios p . Yielding begins as the loading path intersects the appropriate locus. The values $R = 3 + 5$ are often found in hexagonal crystal metals (zinc, magnesium, titanium, etc.), and the more commonly

used structural materials with cubic crystals (steel) have the R values closer to 1. If $R = 1$ material is isotropic and von Mises ellipse is obtained (Figs. 5.20b and 5.22). Directions x, y and z in Fig. 22 correspond to 1, 2 and 3 in Fig. 5.20a.

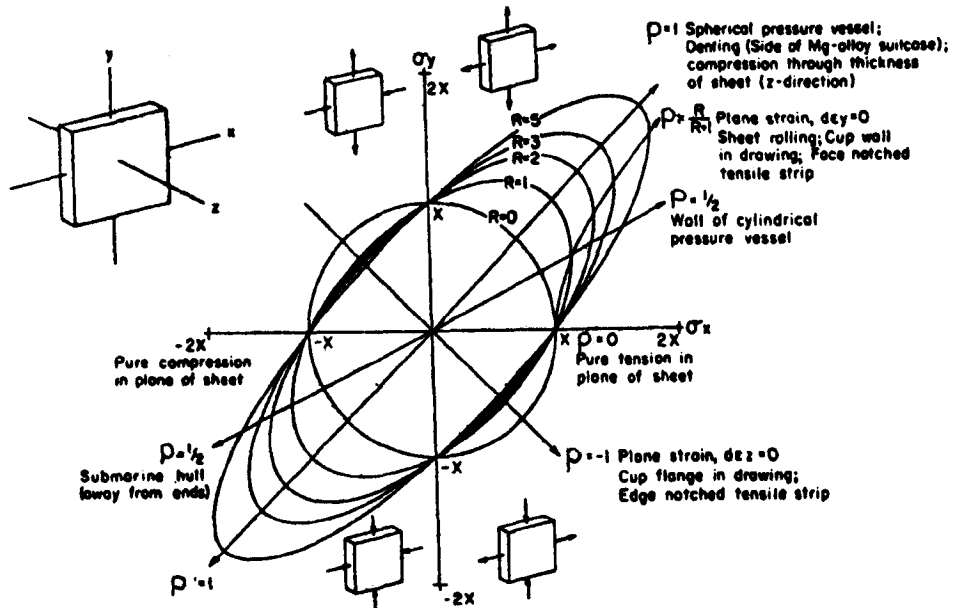


Fig. 5.22 (Ref. 92)

In plane strain deformation (Fig. 5.20a) $de_2 = 0$ and the stress ratio p (5.83) becomes

$$p = \frac{R}{R+1} \quad (5.88)$$

The texture hardening ($R > 1$) or softening ($R < 1$) of a particular sheet should therefore be determined and substituted into (5.87) to obtain more reliable information on the effective yield stress.

In sheets which display both normal and planar anisotropy, the normal anisotropy is given by the average strain ratio R obtained by averaging the value of ratios R measured in different directions with respect to rolling (the term "rolling" refers here to the production method rather than Fig. 5.17). The degree of planar anisotropy is then reflected by the variation ΔR during these measurements.

Strain hardening is another important property of the actual material. A typical nominal stress (σ_0) - engineering strain (e) curve of mild steel obtained by a quasi-static uniaxial tensile test, is shown in Fig. 5.23a. The initial part OABC displayed by an annealed material is usually lost during tube production, so that the stress-strain curves of specimens taken out of the tube walls mostly have the form DCEF. The amount of plastic deformation during production varies depending on the

position on the section. Section corners are subject both to the initial rolling and subsequent bending, so that the material may behave according to curves GHEF, or, say MEF. It will be shown in section 6.3 that large initial plastic deformation may increase the maximum nominal flow stress σ_{pu} above the value obtained by testing a specimen displaying the DCEF stress-strain curve.

Yield stress or hardness variation around the section is shown in Fig. 5.23b. Tabor (93) suggested that the Vicker's Hardness Number (VHN) is proportional to the flow stress at $e \approx 8\%$.

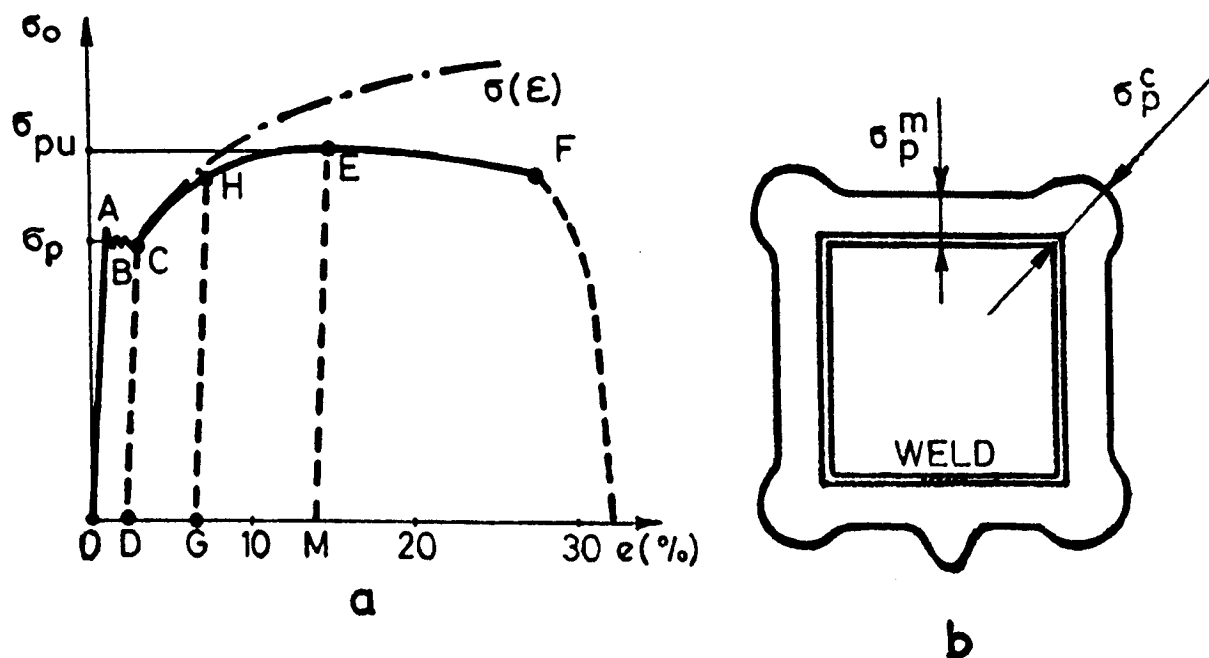


Fig. 5.23

Examination of the Vickers Hardness distribution along the section perimeter of several rectangular section hot rolled tubes (94) indicated that the section corners are usually $20 \pm 25\%$ harder than the "parent material" away from corners or weld. The heat affected zones around the seam welds were $50 - 75\%$ harder than the parent material. However, these zones do not normally spread over a larger width of the wall, so that they do not have a significant effect on the hinge collapse behaviour. The maximum strength of $45 \times 45 \times 2$ mm tubes was 5% greater (2) with the seam weld in the flange rather than web. In the latter case the weld run along the plastic neutral axis and its higher yield stress could not be fully utilised. The weld location had hardly any effect on the energy absorbed during hinge rotation of approximately 15 deg.

Strain hardening due to strain rate ($\dot{\epsilon}$) may become important in a dynamic collapse situation. An extensive review of this phenomenon with a series of empirical formulae and diagrams relating the quasi-static and dynamic yield and flow stresses at room and elevated temperatures is given by Goldsmith (46) and Johnson (47). Quasi-static parameters are usually related to a strain rate of $\dot{\epsilon} \approx 10^{-3}/\text{sec}$, while most of the dynamic testing covered strain rates up to $10^2 - 10^3/\text{sec}$. For example, the

following formula relating the static (σ_p) and dynamic (σ_{pd}) yield stresses was found adequate to fit the experimental results on mild steel tensile specimens (Manjoine, ref. 95) and cantilever beams (Bodner, ref. 96) at the room temperature:

$$\sigma_{pd} = \sigma_p \left[1 + \left(\frac{\dot{\epsilon}}{40.4} \right)^{0.2} \right] \quad (5.89)$$

The ratio σ_{pd}/σ_p increases to almost 3 for $\dot{\epsilon} = 10^3/s$. The ratio between the dynamic and static flow stresses is the smaller, the larger the plastic strain at which the comparison is made. The ultimate stress σ_{pu} (Fig. 5.23) of mild steel at $\dot{\epsilon} = 10^3/sec$ was only 1.48 greater than its static value (94), so that the difference between σ_{pd} and σ_{pud} reduces at higher strain rates.

The comments above refer to testing with a constant strain rate. If the strain rate is suddenly changed from $\dot{\epsilon}_1$ to $\dot{\epsilon}_2$ the flow stresses will shift from the constant $\dot{\epsilon}_1$ curve towards, but not quite to the constant $\dot{\epsilon}_2$ curve originating from $\epsilon = 0$ (47). It can be argued therefore that the effect of strain rate will tend to decrease with reduction of the collapsing speed of the structure.

The strain rate effect will be considered again in Chapter 7 dealing with static and dynamic testing of the bus rings.

Material separation in a hinge is closely preceded by the occurrence of the local instability of plastic deformation (corresponding to necking in the uniaxial tensile test). Instability of plastic deformation in uniaxial and biaxial stress state is well documented (39-41). An empirical exponential function relating the equivalent plastic stresses and strains is introduced to express the instability condition in a suitable mathematical form. However, these results could not be employed here because the actual distribution of stresses and strains in the hinge is unknown. A kinematic (upper bound) approach has been adopted in this analysis, as already explained in the introduction to this chapter.

5.7.3 Effect of Loading Conditions

The previous discussion considered a sheet in pure bending. However, the yield lines of the hinge mechanism are subject to other loads as well. A unit width sheet segment loaded by a bending moment M , membrane force N and shear S is shown in Fig. 5.24a. Loads M and N are normal and S tangential to the yield line.

The presence of membrane force will shift the plastic neutral axis by a distance "d" from the middle plane (Fig. 5.24). Assuming uniform distribution of shear the loads per unit width can be obtained from the equilibrium condition in a form:

$$N = 2\sigma d \quad ; \quad S = \tau t \quad ; \quad M = \frac{\sigma t^2}{4} \left[1 - \left(\frac{2d}{t} \right)^2 \right] \quad (5.90)$$

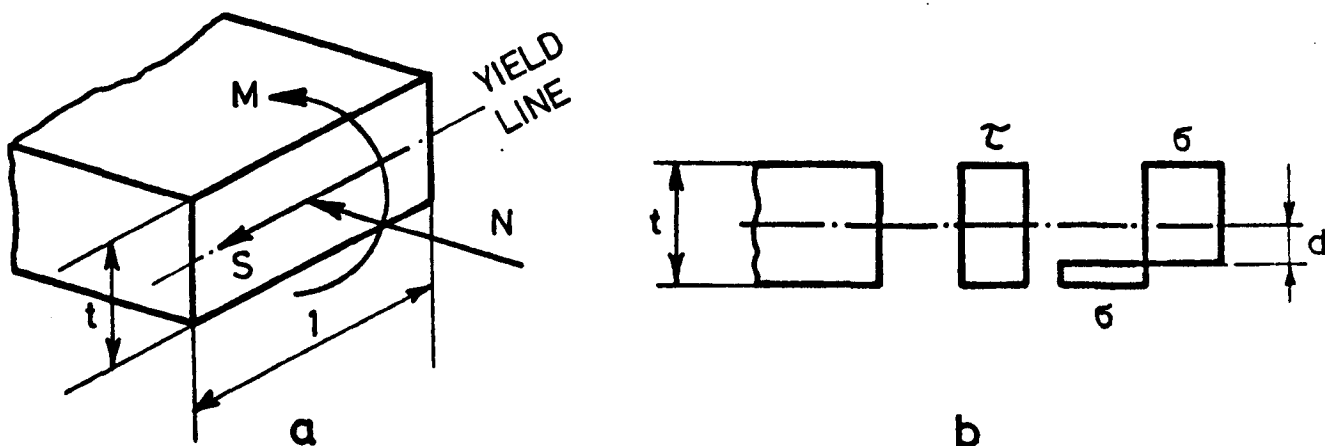


Fig. 5.24

As the section yields the stresses σ and τ from (5.90) satisfy a yield condition. Using the more conservative Tresca criterion (5.74) with (5.90), the loads along the yield line should satisfy:

$$\frac{m_p}{m_o} \left[1 - \left(\frac{S}{S_o} \right)^2 \right]^{\frac{1}{2}} + \left(\frac{N}{N_o} \right)^2 + \left(\frac{S}{S_o} \right)^2 = 1 \quad (5.91)$$

where $m_o = \frac{Yt^2}{4}$ = fully plastic moment in pure bending,

$N_o = Yt$ = pure membrane force making the whole section plastic,

$S_o = \tau_{\max} t =$ (from (5.72)) $= \frac{Yt}{2}$ = pure shear making the whole section plastic

The effective moment m_p along the yield line is generally smaller than the fully plastic value in pure bending m_o . This is not allowed for when applying the kinematic theorem of the limit analysis (section 5.1) in its "pure" form. The internal load distribution is not considered and the theory gives an upper bound solution.

5.7.4 Selection of the Material Parameters

Yield Criterion

The seam welded tube with the circular grid (Fig. 5.8a) was used to measure the normal anisotropy of the material. It was manufactured by hot rolling in the same way as the other tubes tested, so it was considered reasonably representative. A tensile test specimen was cut along the middle of the compression flange (in the direction of rolling), and a square pattern grid was applied to one face. Longitudinal

ϵ_1 and lateral ϵ_w strains were measured after producing an engineering tensile strain of 12%. The elastic strains are negligible and the volume of the specimen is constant, hence

$$\epsilon_1 + \epsilon_w + \epsilon_t = 0 \quad (5.92)$$

and
$$\epsilon_t = -(\epsilon_1 + \epsilon_w) \quad (5.93)$$

The normal strain ϵ_t was calculated from (5.93) and substituted into (5.86) to produce:

$$R = 0.7 \quad (5.94)$$

The ratio is less than one, so that texture softening takes place (Fig. 5.22), reducing the effective yield stress in comparison with the von Mises value (5.84). Substitution of (5.94) into (5.88) and (5.87) gives the effective yield stress in plane strain conditions:

$$\sigma_{1p} = 1.097 Y \quad (5.95)$$

which is less than σ_{1pm} (5.84), but more than σ_{1pt} (5.75). Yield stress and R value could not be measured at an angle to the rolling direction because of the small width of the tube. Yield stress is likely to be less at right angles to the direction of rolling than in the rolling direction itself. The flow stress determining the m_p value is reduced by the other loads acting along the yield line (5.91). It was therefore decided to use the more conservative, Tresca's yield criterion (5.74), (5.75), rather than the von Mises one.

Yield Stress for Calculation of the Maximum Strength

Production induced strain hardening (Fig. 5.23b) does not spread far from the section corners. The effective width at collapse (5.3) occupies at least one half of the compression flange in most structural members. The stress σ_p^m in Fig. 5.23b, equal to the yield stress Y of a specimen taken from the middle of compression flange, should therefore be used in equations (5.23) defining the maximum strength of the beam. If the seam weld is in the middle of the compression flange a specimen should be taken from the parent material away from corners or weld.

Flow Stress for Calculation of the Energy Absorbed

The first phase of hinge collapse (section 5.4) with $0 \leq \theta < 5 \pm 10$ degrees is characterised by high membrane loads along the gradually developing

yield lines. The effect of shear on the effective moment m_p is usually negligible, but the membrane forces may reduce considerably the initial values of m_p , particularly in sections which can develop full plasticity at maximum strength. Section resistance is then provided by in-plane wall deformation and the equation (5.91) reduces to $N = N_0$ with $m_p = 0$. However, buckling of the section wall reduces their membrane load carrying capacity which becomes limited by the bending strength of the material along the yield lines. The membrane load N drops rapidly and the moment m_p gets closer and closer to the pure plastic value m_0 . On the other hand, plastic deformations start to concentrate along the yield lines, producing high local strains to follow the kinematics of the collapse mechanism (Table 5.1). It is therefore argued that strain hardening of the material develops along the yield lines soon after the hinge starts collapsing (the initial part OABC of the stress-strain curve in Fig. 5.23a is lost during tube production).

The idealised mechanism in Fig. 5.15 is based on hinge behaviour during the second stage of collapse (section 5.4). The membrane forces are a lot smaller than initially and strain hardening has reduced the stress variation along the section in Fig. 5.23b. Strain hardening produces a symmetric expansion of the Tresca's hexagon (Fig. 5.20c), but the true stress (σ) - natural strain (ϵ) curve is necessary to describe the material behaviour theoretically. This curve can be easily calculated from the $\sigma_0 - e$ diagram in Fig. 5.23a, but its application requires a reasonably accurate correlation between the strains developed along the yield lines and the angle of hinge rotation. An attempt to derive this relationship was not successful because of difficulties related to the theoretical determination of the varying bending and rolling radii and to the validity of the assumption that the plane wall sections remain planar during plastic deformation. A compromise considered more reliable was therefore introduced.

In most of the tube specimens tested (Chapter 6) the flow stress - engineering strain curve between points H and F (Fig. 5.23) was almost horizontal within a strain region $e = 5 \pm 25\%$. This curve gives lower stresses than the $\sigma - \epsilon$ one, and allows indirectly for the effect of other loads along the yield line (5.91) on the effective value of the flow stress. It is therefore suggested that the upper nominal flow stress σ_{pu} (Fig. 5.23a) be used to calculate the effective plastic moment m_p in equations (5.67) for the energy absorbed. This stress is obtained by tensile test of the parent material away from the section corners and weld.

Utilisation of a constant nominal flow stress rather than the higher and increasing true stress, combined with the omission of some in-plane deformation of the actual collapse mechanism ensuring a complete continuity of the hinge walls, caused the fact that the empirically determined rolling radius (5.59) falls within but tends to the lower bound of the range observed in the actual tubes (section 5.3). Such a selection will also produce higher plastic moments m_p in the initial stages of collapse ($\theta < 5 \pm 10^\circ$), when the membrane forces are still relatively high and the actual collapse mechanism is not truly represented by the theoretical model. However, this phase of collapse can be interpolated between the two theoretically determined parts of the $M - \theta$ curve: the maximum strength and the second stage of hinge collapse.

Practical experience has shown that material properties (σ_p and σ_{pu}) of the actual tubes may vary if specimens are taken from the same location of different sections, or even from different locations of the same section. An example is shown in section 6.3. It is therefore advisable to test several specimens representing a particular range of tubes and use average values of σ_p and σ_{pu} , or to rely on the minimum properties guaranteed by the material specification.

The whole calculation procedure will be checked and summarised in the final form in section 6.5.

6.1 INTRODUCTION

Experimental verification of the theoretical method derived in Chapter 5 was organised in the following stages:

- a. Design of an experimental procedure that would enable the definition of the actual hinge moment - rotation curve;
- b. Determination of the material properties;
- c. Preliminary testing of selected tubes in order to check and modify the theory;
- d. Definition of the final form of the theoretical hinge moment - rotation curve;
- e. Experimental verification of the theory applied to a wide range of rectangular section tubes.

6.2 THE TEST METHOD

Collapse behaviour of a hinge is determined by its collapse mechanism and by the effective fully plastic moments m_p of the section walls along the yield lines. In most frameworks the hinges are subject to a combination of moments and forces but the influence of bending is by far the most significant. Repeatability of hinge mechanisms in several cases of roof collapse described in section 5.3 indicates that other loads had a small effect on the local collapse modes. However, their influence on the effective moment m_p (equation 5.91) has to be borne in mind when designing the experimental procedure for checking the theory.

The simplest form of the yield condition (5.91) is obtained if the hinge is produced by pure bending. The axial and shear forces are eliminated, but the normal membrane forces balancing the external moment still remain. Beam collapse by pure bending was performed by McIvor et al (80,97) using a fairly complex four point loading mechanism installed in a Tinius Olsen Universal Testing Machine. Each specimen was 6 feet long and used wooden internal plugs with rounded ends (Fig. 6.1) to support the cross section at the points of load application and to localise the hinge in the centre of the fixture. An unsupported segment of the length 2.5 times the larger section dimension (D) was left at the centre of each span. If the hinge occurs near or at the centre this clearance is sufficient since the length of the primary hinge is equal to the smaller section dimension, as shown by equation (5.40).

The assembly in Fig. 6.1 does not seem to control the exact position of the hinge, and it is likely that the failure will not occur in the centre but near the end of the wooden plug. This argument is supported by the author's experience with a similar arrangement described in Fig. 6.2. The probable eccentricity of the hinge is small in comparison

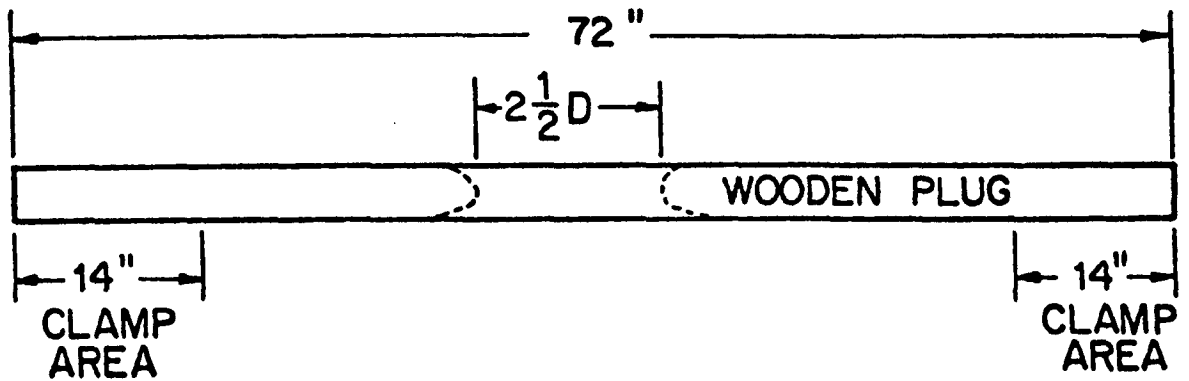


Fig. 6.1

with the span, but interaction between the hinge mechanism and the plug may take place. This could have caused some disagreement between the results for large angles of rotation reported here and in ref. 97.

A simple four point loading fixture mounted on the Denison Universal Testing Machine (Fig. 6.2) has been tried in order to produce pure bending between the inner points of load application. The end supports were mounted on the fixed part of the machine, while the central load F was applied by the movable assembly and divided equally by a channel section ram. The beam was reinforced by two sets of plates bolted together (shaded in Fig. 6.2), leaving a clearance in the middle, similar to the one between the plugs in Fig. 6.1.

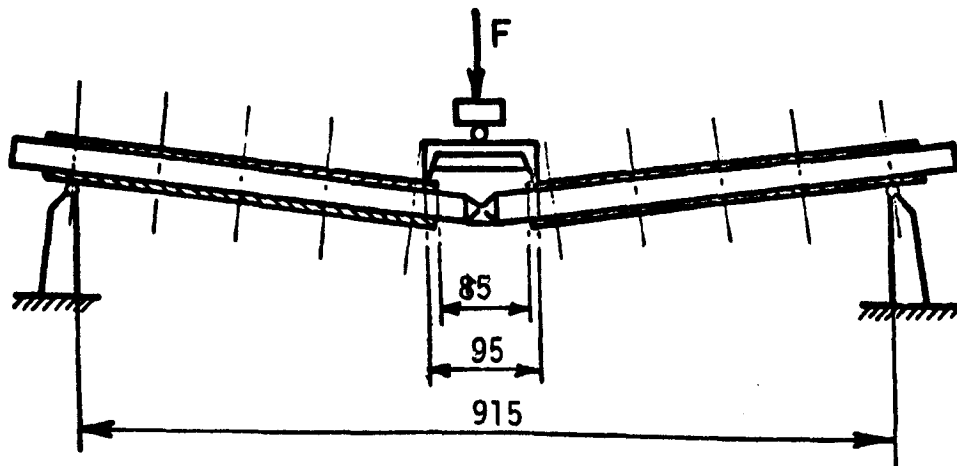


Fig. 6.2

The beam tested by the rig in Fig. 6.2 started buckling at a section adjacent to the end of the reinforcement plate. Load was released, bolts slackened and the buckle shifted to the middle between the plates. The test was restarted and the beam continued collapsing in the middle. However, at the hinge rotation of approximately 20° the arrangement became unstable with the ram tilting and sliding. The moment - rotation curve was the same as obtained by the simpler method described below (Figs. 6.3 and 6.12) and this test procedure was abandoned.

Shear and axial forces have a fairly small effect on the total stresses in most practical cases of framework elastic and plastic behaviour. It was therefore decided to design a cantilever bending rig which was simpler to produce and operate and which could control the hinge position and enable a reasonably accurate measurement of the hinge moment and rotation. The basic layout of the rig is shown in Fig. 6.3 and the actual arrangement using the already existing main components is in Fig. 6.4.

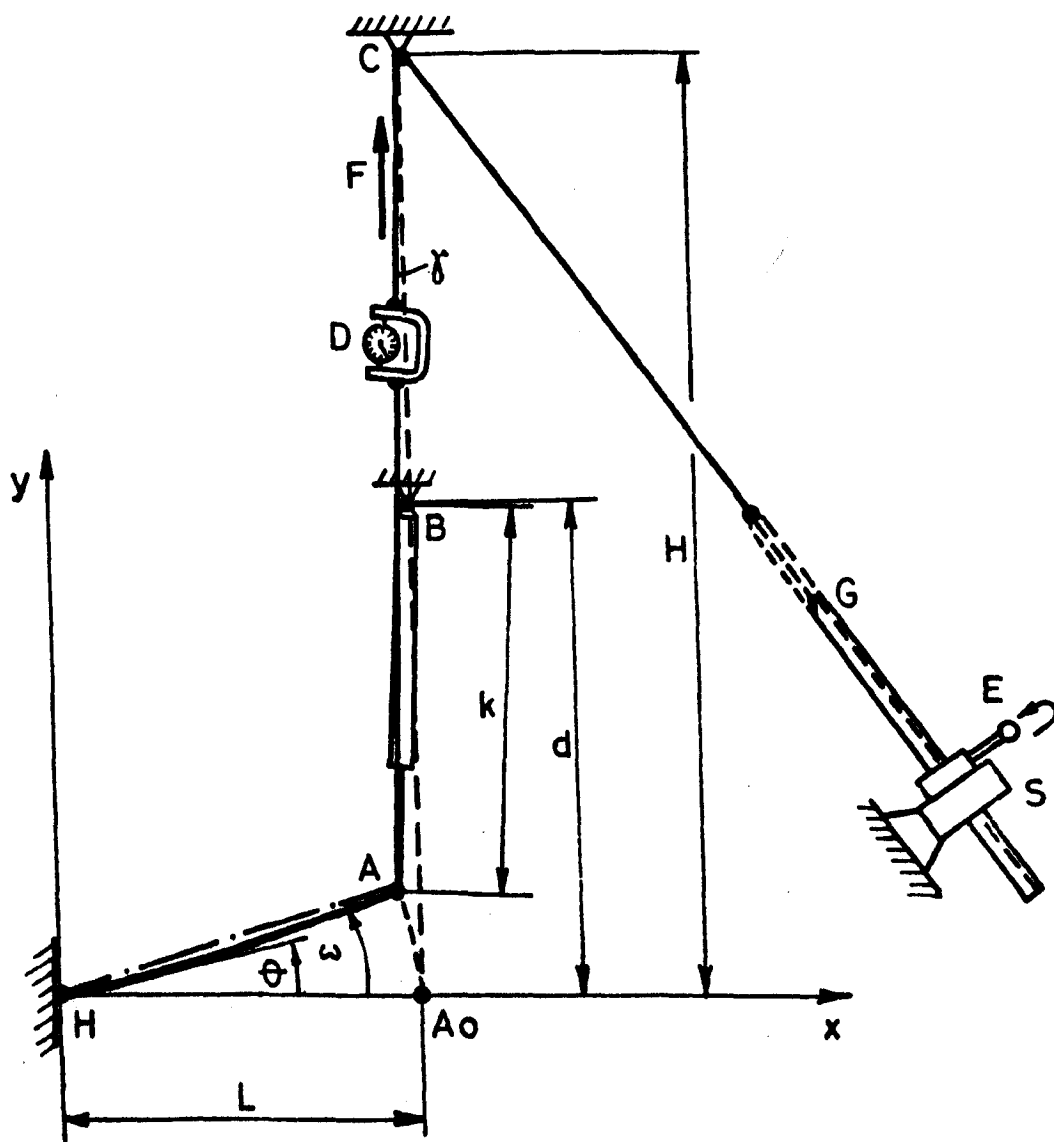


Fig. 6.3

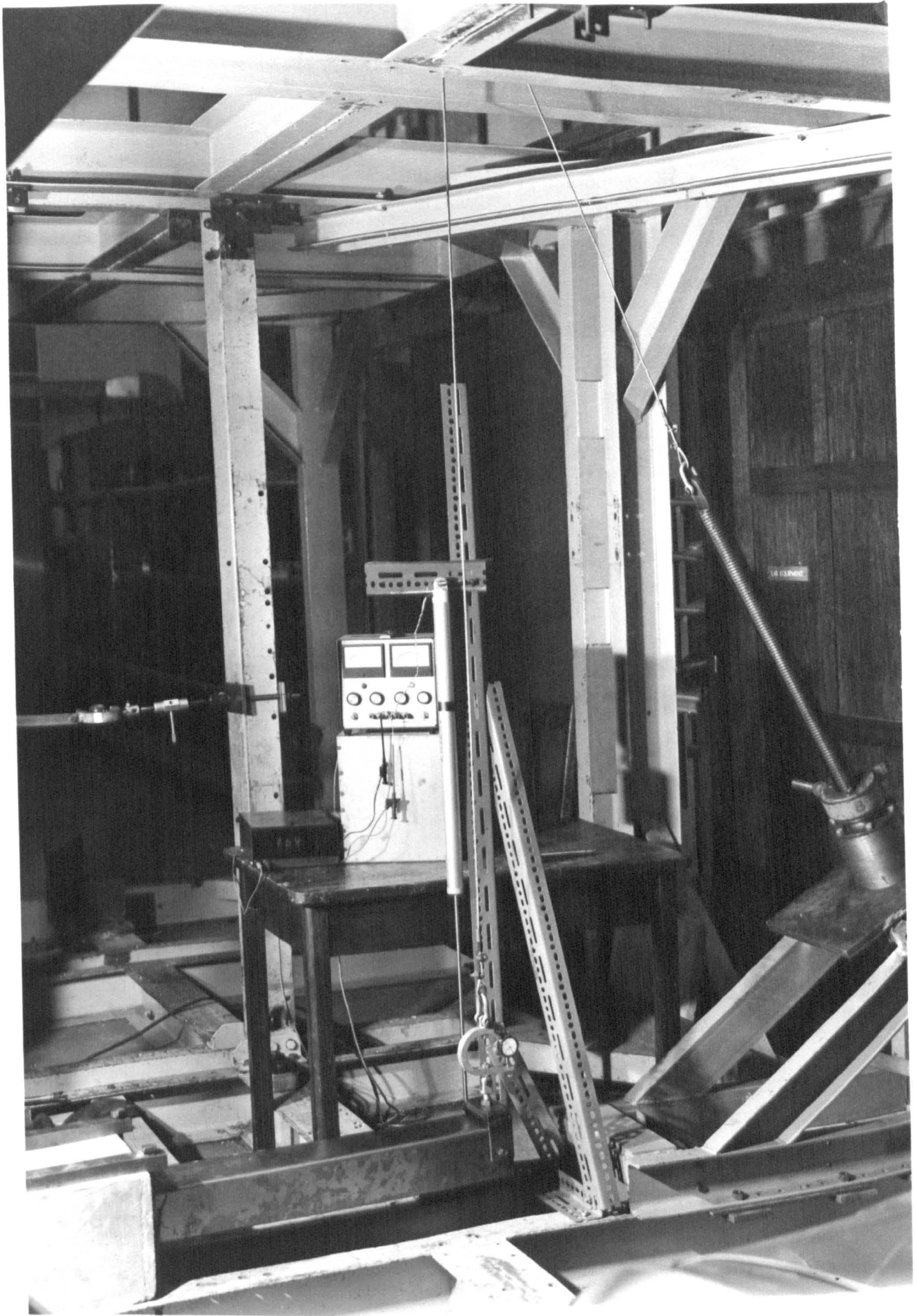


Fig. 6.4

Cantilever HA is fixed at the end H and loaded at the free end A via a cable A₀DC. The cable is wound around the fixed pulley C and connected to a long screw G passing through a fixed support S. The screw cannot rotate because it has a longitudinal groove sliding along a cam in the support S. Pulling of the cable is performed by turning the threaded disc E attached to the support S. Force in the cable is measured by a dynamometer D.

The cantilever is horizontal before the test while the cable A₀DC is vertical. The distance k between points A and B is measured by a potentiometer AB, whose end B is fixed in space so that A₀B is also vertical.

The beam length (L) is measured between the centre of the hinge H and the point of load application A. The hinge length 2h (equation 5.40) was always small in comparison with L and the elastic curvature had a negligible effect on L. It was assumed therefore that point A rotates about H along a circular path A₀A in the vertical plane, hence:

$$x_A^2 + y_A^2 = L^2 \quad (6.1)$$

The distance (k) between A and B is measured, and the co-ordinates of B are known constants $x_B = L$ and $y_B = d$, so that:

$$k^2 = (L - x_A)^2 + (d - y_A)^2 \quad (6.2)$$

Co-ordinates of point A can be obtained from (6.1) and (6.2) in the form:

$$x_A = \frac{L \cdot (d^2 + 2L^2 - k^2) + \sqrt{L^2 (d^2 + 2L^2 - k^2)^2 + [4d^2 L^2 - (d^2 + 2L^2 - k^2)^2] (L^2 + d^2)}}{2(L^2 + d^2)} \quad (6.3a)$$

and

$$y_A = \sqrt{L^2 - x_A^2} \quad (6.3b)$$

The angle ω between HA₀ and the straight line HA (Fig. 6.3) is:

$$\omega = \arctan \frac{y_A}{x_A} \quad (6.4)$$

Co-ordinates of point C are constant and known: $x_C = L$ and $y_C = H$. Angle γ between the cable AC and vertical A₀C is therefore:

$$\gamma = \text{arc tan} \frac{L - x_A}{H - y_A} \quad (6.5)$$

where x_A and y_A are found from (6.3).

Cable AC remained almost vertical during the tests. The actual dimensions of the test arrangement were: $L \approx 700$ mm and $H \approx 2250$ mm, while the angle ω was increased up to maximum 45° . Substitution of these data into (6.4), (6.3b) and (6.5) produces a maximum angle γ of only $\gamma_{\text{max}} = 6.7^\circ$. In the initial stages of collapse, with $\omega < 15^\circ$, the angle γ is less than 0.9° .

Force F , measured by the dynamometer D , is directed from A to C , hence the moment at the hinge becomes (Fig. 6.3):

$$M = F (x_A \cos \gamma - y_A \sin \gamma) \quad (6.6)$$

A typical load (F) - deflection (y_A) test curve is shown in Fig. 6.5a. The initial part 0-8-1 is linear - elastic with the first non-linearities occurring at point 1, as already discussed in Chapter 4 (Fig. 4.1). After a fairly short elastic-plastic segment 1-2 the beam reaches its maximum strength at point 2. Unloading from point 2 may follow any path parallel to 0-1 within the area 0-1-2-6-0. If full plasticity takes place at 2, the unloading curve will be 2-6. Further increase of y_A produces a hinge and the load F starts dropping off along the line 2-3.

The hinge rotation angle θ is related to plastic deformations only, so that elastic deflection of point A should be subtracted from its total displacement. Elastic deflection is due to elastic deformation of the beam, support and hinge itself. The first two effects are represented by the initial slope 0-1 of the load-deflection curve in Fig. 6.5. All the three effects can be estimated from the final unloading curve 4-5. The hinge effect on the final stiffness is demonstrated by the finishing, non linear part of the unloading curve due to residual stresses (compare with curve 2-3' in Fig. 4.2). The effect of hinge on the beam stiffness is negligible as long as the beam is substantially loaded, assuming, of course, that the hinge is small in comparison with the beam length.

The hinge is assumed to start rotating from point 2, where the beam develops its maximum strength. The program CRASHD assumes, theoretically, that the hinge starts collapsing at point 7 (Fig. 6.5) rather than 2 because of the section shape factor equal to unity, but the difference becomes negligible as θ increases.

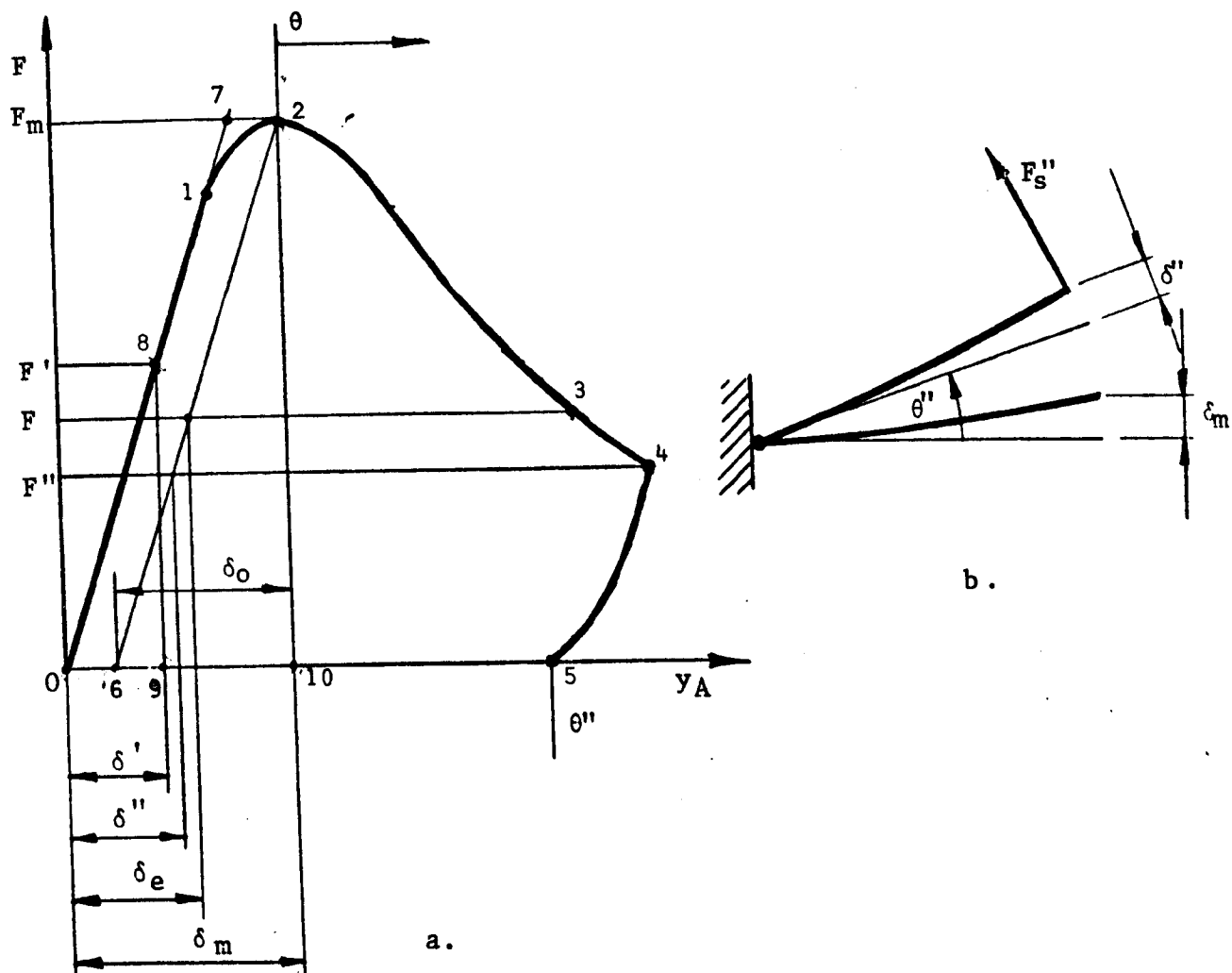


Fig. 6.5

Most of the tubes tested developed fully plastic moments, so that the elastic unloading path 2-6 could be assumed. A force F , corresponding to any point 3 on the load-deflection curve, produces an elastic-partially plastic deflection of point A equal to δ_e in Fig. 6.5. This deflection determines the difference between the angles θ and ω , so that:

$$\theta = \omega - \arctan \frac{\delta_e}{L} \approx \omega - \arcsin \frac{\delta_e}{L} \tag{6.7}$$

Deflection δ_e can be calculated by selecting an experimentally determined force $F' \approx (0.5 + 0.7) F_m$ and the appropriate elastic deflection δ' (Fig. 6.5). Triangles 0-8-9-0 and 6-2-10-6 are similar, hence:

$$\frac{F'}{\delta'} = \frac{F_m}{\delta_m - \delta_o} \tag{6.8}$$

The unknown deflection increment δ_o can now be expressed in terms of the experimentally determined quantities in the form:

$$\delta_o = \delta_m - \frac{F}{F'} \delta' \quad (6.9)$$

and the required deflection δ_e becomes (Fig. 6.5):

$$\delta_e = \delta_m - \delta_o + \frac{F}{F_m} \delta_o = \delta_m - \delta_o \left(\frac{F}{F_m} - 1 \right) \quad (6.10)$$

Elimination of δ_o from (6.9) and (6.10) gives:

$$\delta_e = \delta_m - \frac{F_m - F}{F'} \delta' \quad (6.11)$$

Combining equations (6.4), (6.7) and (6.11) the angle of hinge rotation becomes finally:

$$\theta = \theta(F) = \arctan \frac{y_A}{x_A} - \arctan \left[\frac{F' \delta_m - (F_m - F) \delta'}{F' L} \right] \quad (6.12)$$

where x_A and y_A are known from (6.3) and F' , δ' , F_m , δ_m and L are experimentally determined constants.

Deflection δ_e is affected by shear force F_s , so that (6.12) is less accurate at larger angles θ . However, this inaccuracy can be safely ignored since δ_e decreases with the hinge moment and the plastic deflection also becomes much greater than δ_e . The second, correction term in (6.12) reduces very much in comparison with the first one (ω).

Discrete points on the hinge moment - rotation curve can thus be calculated by measuring the constant lengths L , d and H , variable distance k (Fig. 6.3) and the force in the cable F . Moment is given by (6.6) and rotation by (6.12). The accuracy of (6.12) could be checked after each test by measuring the hinge rotation angle due to the remaining plastic deformations. The agreement was always within 5%.

The shear force F_s in the beam:

$$F_s = \frac{M}{L} = F (\cos \gamma \cos \omega - \sin \gamma \sin \omega) \quad (6.13)$$

is equal to F at the beginning of collapse and reduces during hinge rotation to $F_s'' = 0.62F$ at the end of a typical test ($\omega_{\max} = 45^\circ$, $\gamma_{\max} = 6.7^\circ$).

The beam is also subject to an axial, tensile force F_a :

$$F_a = F (\cos \gamma \sin \omega + \sin \gamma \cos \omega) \quad (6.14)$$

which can also be expressed using (6.13) and (6.14) in the form:

$$F_a = \frac{M \cos \gamma \sin \omega + \sin \gamma \cos \omega}{L \cos \gamma \cos \omega - \sin \gamma \sin \omega} \quad (6.15)$$

The axial force is zero at the beginning of collapse and increases to $F_a = 1.27 (M/L)$ for $\omega_{\max} = 45^\circ$ and $\gamma_{\max} = 6.7^\circ$.

Both of these effects are considered in sections 6.4 and 6.6.

6.3 DETERMINATION OF MATERIAL PROPERTIES

All the tubes were tested as received, i.e. without annealing treatment, in order to bring the analysis closer to a real life situation. The tubes were hot rolled and seam welded if not stated otherwise.

The effect of the actual material properties on the maximum strength and energy absorption of a hinge was discussed in the previous chapter. Quantitative assessment of the resistance to thinning and hardness distribution was also made in section 5.7. Material properties to be determined now are the nominal stress-engineering strain curves.

The stress-strain curves were obtained by quasi-static tensile tests on standard, $\frac{1}{2}$ in wide specimens cut out of the section walls. All the specimens were cut only in the direction of tube rolling because section dimensions did not allow testing of material properties in any other direction. The strain rate was approximately $3.3 \cdot 10^{-3}$ /sec in some and $1.67 \cdot 10^{-3}$ /sec in other specimens. Both values can be considered as quasi-static, giving almost identical results.

Specimens were taken so that they consisted of the parent material away from section corners or welds, in order to reduce or eliminate the additional effects of the initial plastic deformation and heat developed during tube manufacture. Plastic pre-straining has a greater effect on yield than on the flow stress. This is illustrated by the $\sigma_0 - e$ diagrams in Fig. 6.6 obtained by testing three specimens taken from the same $45 \times 47 \times 0.86$ mm tube (no. 19, Table 6.1 in Section 6.6) hand made from a hot rolled sheet. The corresponding curves and specimen locations are marked by the same number. Curves 1 and 2 display the initial yielding without strain-hardening, while greater plastic deformation of specimen 3 eliminated this initial segment of the stress-strain curve.

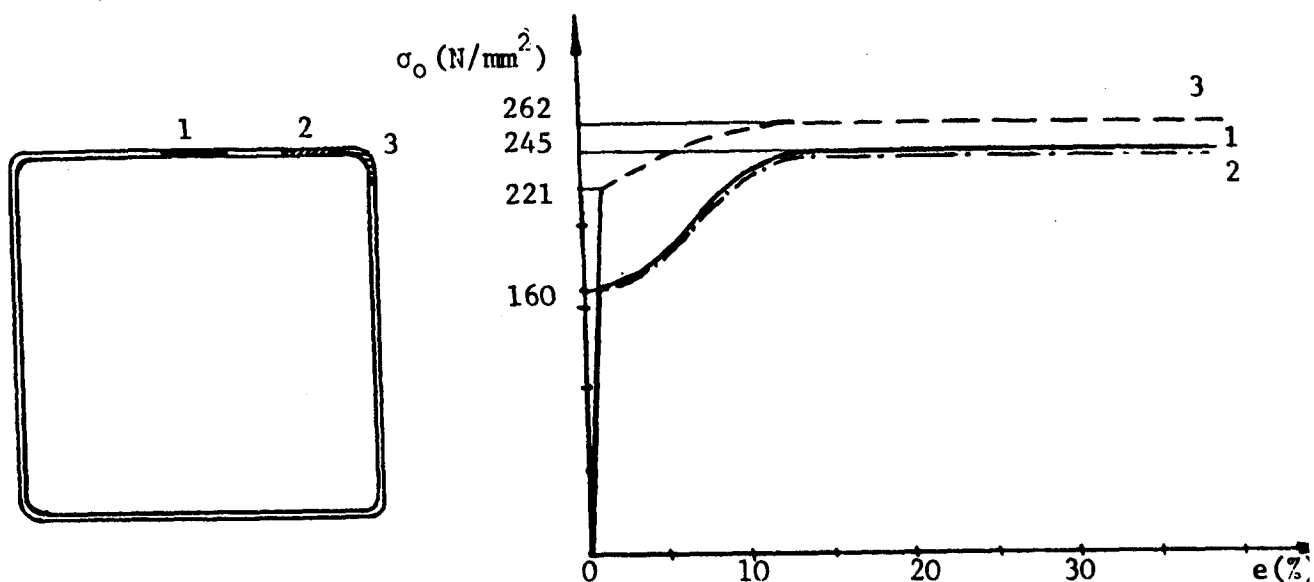


Fig. 6.6

Variation of both the yield and flow stresses with plastic pre-straining makes it desirable to test several specimens of each representative section. One can still only hope that the effective properties within the hinge will be close to an average value. A fairly wide range of tubes was prepared for testing and production of a large number of specimens was not easy to achieve. It was therefore decided to test one tensile test specimen per typical section, expecting that the other results for the parent material of the same tube would be very similar. This expectation was based on previous experience (2, 94) which indicated that nominally identical properties did not actually differ by more than 5-10%. The stress-strain curves are attached to the appropriate hinge moment rotation diagrams appearing later in this chapter and the original copies are given in the Appendix 3.

In a practical design situation it is advisable to use the minimum properties guaranteed by the material specification.

Variation of material properties and section geometry in the actual tubes requires testing of several nominally identical beams in order to establish repeatability of experimental results.

6.4 PRELIMINARY TESTS AND THEORY MODIFICATION

Preliminary tests were organised in order to check and modify the theory and establish the details of the experimental procedure.

The first test was performed on a hand made tube with the following section dimensions $a = 100$ mm, $b = 103$ mm, $t = 0.81$ mm, (section no. 18 in Table 6.1), corner radius before deformation $r \approx 4$ mm. The nominal stress-engineering strain curves of the tube material taken from different

locations on one section are shown in Fig. 6.9.

One end of the tube was cast into a 300 x 300 x 220 mm concrete block (Fig. 6.4) in order to produce an adequate built-in end of a relatively weak section. (An earlier attempt to fix the end of this beam using a wooden plug supporting the section from inside, while clamping the end between the two rigid plates was unsatisfactory. It was very difficult to produce a fit between the plug and the tube that would support the section exactly, i.e. provide a sufficiently stiff support without initial tube deformation.) The tube was imbedded in concrete to the same level both outside and inside the section. The block was then bolted firmly to the sturdy floor beam of the "cathedral" rig (Fig. 6.4), so that the flange welded in the middle was in tension during the test.

The test arrangement was described in section 6.2 (Figs. 6.3 and 6.4). Distance between the point of load application A and the concrete surface at the built in end was $L_1 = 725$ mm, and the other relevant dimensions in Fig. 6.3 were $d = 1100$ mm and $H = 2220$ mm.

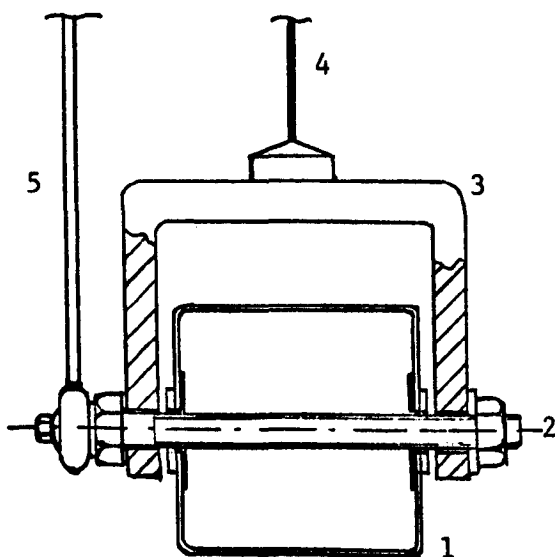


Fig. 6.7

Force F was applied to the end of cantilever 1 (Fig. 6.7) via a 12 mm diameter bolt 2, passing loosely through 12.7 diameter holes in the locally reinforced webs of the beam. The holes were drilled so that the beam and bolt axes could be close to one another. The bolt was also passing through 12.7 mm diameter holes in the external "wishbone"-shaped bracket (3). Cable 4 was attached to the middle of the bracket and adjusted before the test so that the cable axis passed approximately through the middle of the beam. The bracket 3 could rotate freely about the bolt 2, but relative translation was not possible

after the test had started. The end (5) of potentiometer AB (Fig. 6.3) was attached to the end of bolt 2 (Fig. 6.7) so that it could rotate about but not translate with respect to the bolt. The other end of the potentiometer was fixed to a dexion framework (Fig. 6.4).

A horse-shoe dynamometer with a full range of 1000 lb ≈ 4450 N was used to measure the force in the cable. Instrument calibration was carried out on a Denison universal machine. The dynamometer displayed a linear load-deflection curve with a rate of 13.4 N/division up to a maximum load of 3000 N. Two more calibrations were done after the load exceeded 70% of the nominal maximum. After the first "overloading" the rate was 13.16 N/division, and remained at this figure until the end of the testing program.

The distance k in Fig. 6.3 was measured by a linear potentiometer (Penny & Giles, D, LP.21B/85/5/18"/18K) with a maximum travel of 18 ins = 457 mm. Calibration was adjusted by the supply voltage to 1 in/V = 25.4 mm/V, so that the minimum resolution of the reading was 0.254 mm. This was quite adequate for measuring large displacements of the cantilever end.

The test was prepared by loading the beam by an initial force of about $10 \div 20\text{N}$ to remove the gap between the bolt and holes. After putting down the reading on the potentiometer, the load was increased slowly to approximately 30% of the estimated maximum in order to eliminate any possible loose connections and check whether the instruments are working correctly. The load was then reduced back to the initial $10 \div 20\text{N}$ and the potentiometer reading was always either the same or very near (less than one mm) to the initial value. This situation was considered as the datum for the collapse test.

The actual collapse test started with load increments of about $10 \div 15\%$ of the maximum expected. The disc E in Fig. 6.3 was rotated manually at a rate of approximately $60\text{-}120^\circ/\text{sec}$, producing the speed of the cantilever tip of $\approx 1.5 \div 3 \text{ mm/sec}$. After one step of $60\text{-}120^\circ$ rotation the disc lever was swung back and a new disc rotation step was added until the required load increment was finalised. The load (F) and potentiometer (k) readings were recorded 15 - 30 secs after stopping the load incrementation. This time was sufficient for stabilising the elastic deformations. The elastic creep did not alter the potentiometer reading, but the load was dropping by $\approx 1 \div 2\%$ of the value it had at the end of the current load increment. The load increment was reduced as the beam reaction became non linear in order to determine the maximum strength more accurately.

Displacement increments had to be applied after the beam started collapsing. The initial steps were small, giving $\Delta\theta = 0.3 \div 0.5^\circ$ until the angle of hinge rotation was approximately 3° . This was necessary due to an abrupt drop off of the hinge resistance (Fig. 6.9). Displacement steps were increased gradually to produce $\Delta\theta = 1 \div 2.5^\circ$ at $\theta > 20^\circ$, as the strength variation became much less. More time was necessary for the plastic deformations to stabilise reasonably. Experience with this and subsequent tests indicated that 1 + 3 mins was sufficient to eliminate the "primary creep", i.e. to let the internal stresses stabilise. The appropriate load drop was $3 \div 5\%$ of the value reached at the end of the current displacement increment. Larger drops, but still within the above range, occurred at higher loads and after larger displacement steps.

The compression flange started buckling shortly before the maximum strength was developed. The wave-length of the buckles was approximately equal to the width of the flange (Fig. 6.8a), which agrees well with the theory of elastic buckling. The "inwards" buckle, starting at $\approx 0.5a$ from the concrete block continued collapsing, producing a typical hinge failure as in Fig. 5.7. The effective distance between the centre of the hinge and point of load application was therefore $L_2 \approx 625 \text{ mm}$ (Fig. 6.8b).

The measured values of F and k were then used following the procedure described in section 6.2 to calculate a series of discrete points on the experimental hinge moment (M) - rotation (θ) curve in Fig. 6.9. The

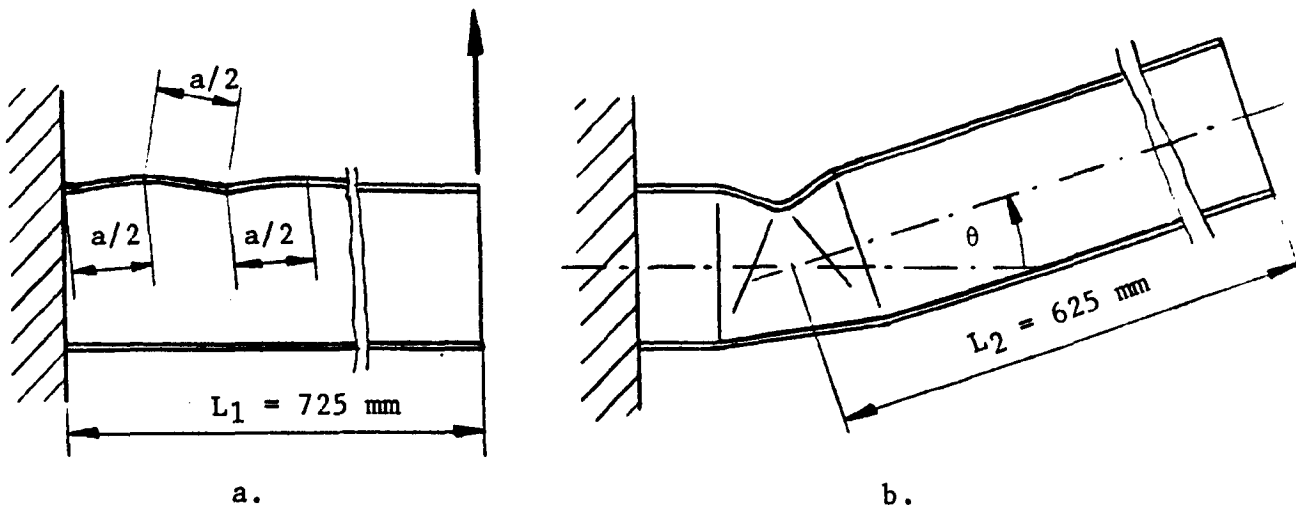


Fig. 6.8

maximum moment with respect to the hinge axis was $M_{m,e} = 1450 \text{ Nm}$, while the moment at the very root of the cantilever $M'_{m,e}$ was $M'_{m,e} = 1680 \text{ Nm}$. The lower value $M_{m,e}$ should be taken because it corresponds to the section which collapsed eventually. A very rapid drop in resistance in the initial stage of hinge rotation was followed by a slow further decrease after $\theta = 15^\circ$ (Fig. 6.9). The strength of the beam at $\theta = 10^\circ$ was only 22% of the maximum value. The same behaviour was displayed by two more similar beams reported in the next section. Beams like these are not used in bus bodies, but they illustrate well the argument regarding the legal maximum load requirement put forward at the end of section 1.3.

The two solid lines in Fig. 6.9 represent the theoretical $M - \theta$ curves calculated following the procedure outlined in Chapter 5. The theoretical maximum strength, calculated using equations (5.23) with $\sigma_p = 161 \text{ N/mm}^2$, was $M_{m,t} = 1360 \text{ Nm}$. This represents 94% of the actual maximum strength $M_{m,e} = 1450 \text{ Nm}$. The agreement is very good, particularly in the light of the fact that the critical buckling stress of the compression flange ($\sigma_{cr} = 67 \text{ N/mm}^2$) was only 42% of the yield stress σ_p .

The top theoretical curve (A) in Fig. 6.9 was obtained using equations (5.67) and (5.69) with $\sigma_{pu} = 253 \text{ N/mm}^2$, and it served as a basis for the empirical definition of the rolling radius in the equation (5.59), Chapter 5. The reasons why the theory overestimates the hinge strength in the initial phase of collapse have already been established in the following form:

- a. The theoretical hinge mechanism does not reflect the actual collapse mechanism of the first phase and represents therefore an incorrect upper bound solution;
- b. The membrane forces reducing the assumed fully plastic moment of the section walls are greatest in the first stage of hinge collapse;

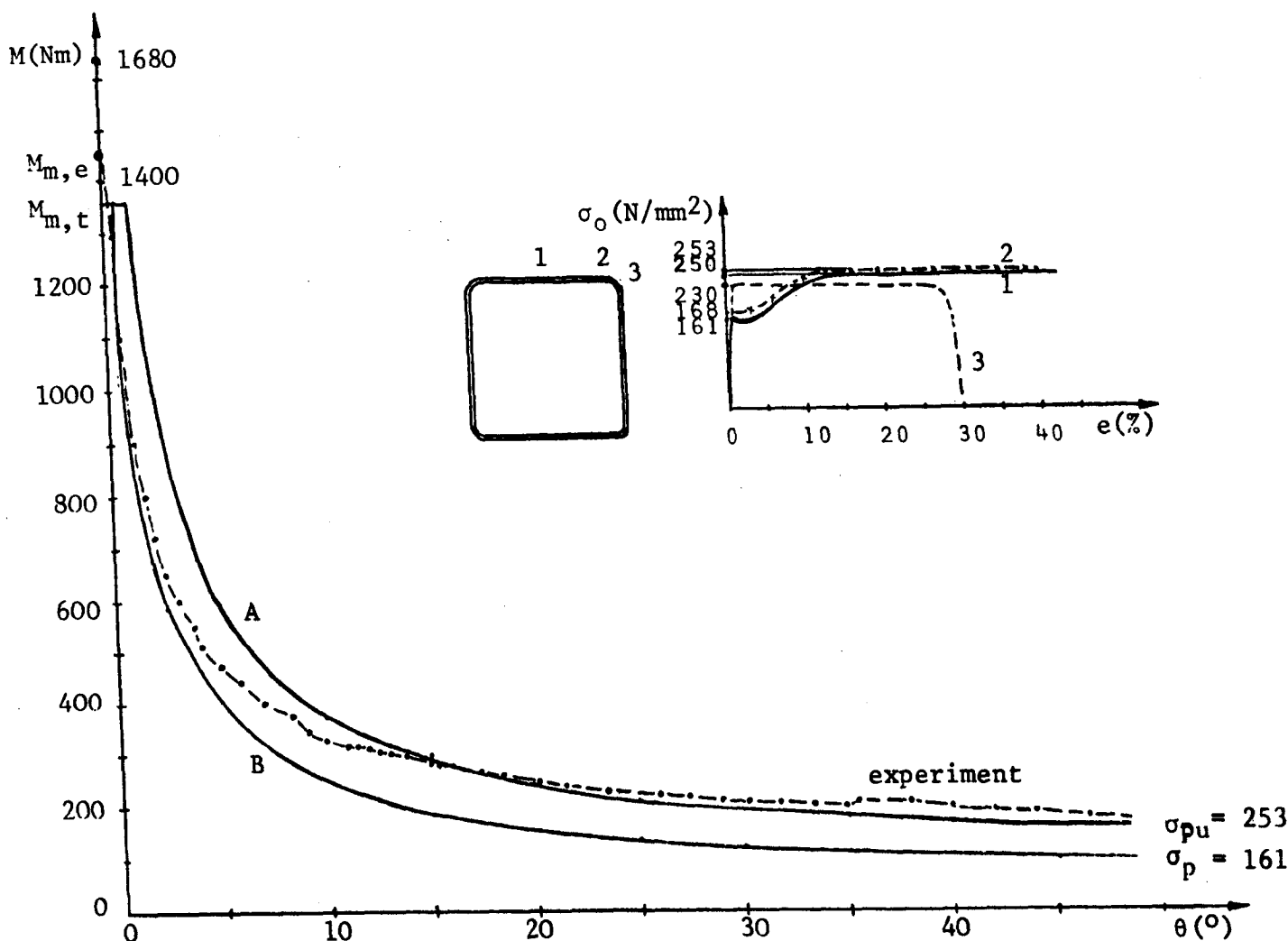


Fig. 6.9

- c. Strain hardening of the material does not occur immediately after the hinge starts collapsing;
- d. The initial rolling radius is larger than its theoretical substitute.

The lower theoretical curve (B) in Fig. 6.9 was calculated with $\sigma_{pu} = \sigma_p = 161 \text{ N/mm}^2$. The actual strength is slightly underestimated in the initial stages of collapse, but the disagreement becomes greater as the collapse progresses. This result indicates that the actual and theoretical mechanisms of this tube get reasonably close together soon after the hinge starts collapsing. The increased underestimate of the actual hinge performance at larger angles θ may be attributed mainly to the lack of the strain hardening effect.

Two more tests on similar tubes are discussed in section 6.6.

This example has shown that some adjustment of the theoretical $M - \theta$ curve will be necessary in the first stage of hinge collapse if the maximum nominal flow stress σ_{pu} is to be used in the energy equations.

The maximum shear force F_s developed in each web at the beginning of test was

$$F_{sm} = \frac{M_m}{2L_2} = \frac{1450}{2 \cdot 0.625} = 1160 \text{ N} \quad (6.16)$$

Assuming a constant shear in the relatively thin and deep webs the maximum shear stress at the beginning of collapse was:

$$\tau_{max} = \frac{F_{sm}}{bt} = \frac{1160}{103 \cdot 0.81} = 13.9 \text{ N/mm}^2 \quad (6.17)$$

The ratio $(S/S_0)^2$ in the yield criterion equation (5.91), with $\tau_p = 0.5\sigma_p = 0.5 \cdot 161 = 80.5 \text{ N/mm}^2$, becomes $(S/S_0)^2 = 0.03$ and has a negligible effect on the ratio m_p/m_0 .

The axial force was maximum at the end of collapse. Substituting the known relevant data into equation (6.15) $F_{am} = 422.5 \text{ N}$ is obtained. The corresponding axial stress over the whole section was:

$$\sigma_{am} \approx \frac{F_{am}}{\text{Area}} = \frac{F_{am}}{2(a+b)t} = \frac{422.5}{2(100+103) \cdot 0.81} \approx 1.2 \text{ N/mm}^2 \quad (6.18)$$

and the ratio $(N/N_0)^2$ in (5.91) is negligibly small, i.e. 0.00005.

The second set of preliminary tests were carried out on three tubes with section dimensions 38.4 x 38.4 x 1.6 mm, and with beam welds in tension flanges. The sections were stable enough to allow clamping the end of cantilever (Fig. 6.10-1) between the two 12 mm thick steel plates 2, 3 bolted to the I section floor beam of the rig 4. The four $\frac{1}{2}$ in diameter bolts 5 could not interfere with the hinge mechanism at any stage of collapse. The bolts were tightened before the test so that they did not allow lifting of the cantilever end by the maximum shear force. This was checked by putting a sheet of paper under the beam covering slightly more area than the hinge itself. An attempt was made not to subject the section to an unnecessarily high compressive load, but that was judged by an arbitrary "feel" rather than by a more reliable and measurable indicator.

It is believed that local prestressing did not have a significant effect on the hinge behaviour. The elastic critical stress of the compression flange was 4.7 times higher than the yield stress, so that local stability could not have been grossly affected by the actual distributed compressive

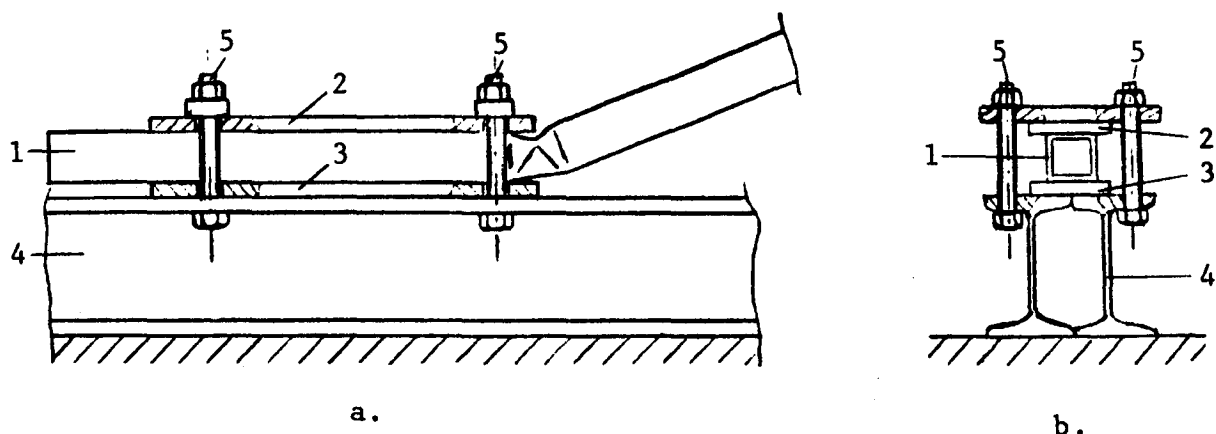


Fig. 6.10

load. The agreement between the actual and theoretical maximum strengths was very good indeed (Fig. 6.11). The compression flanges buckled inwards at the edge of the top plate 2, lost contact with it and the hinge was free to collapse naturally. The tests were stopped, however, at $\theta \approx 5^\circ$ in order to release the load and move the top plate 2 away from the hinge so that it made no contact with the opposite half of the buckled flange (on the right side of the hinge in Fig. 6.10a). All beams continued collapsing at the original hinge with a very good continuity between the original and extended load deflection curves.

All the other details regarding the test arrangement, procedure and data processing were the same as described earlier in this section. The experimental moment-rotation curves are shown as dotted lines in Fig. 6.11. The specimen used to obtain the stress-strain diagram in the same figure was taken from the tube with a circular grid applied to it as discussed in section 5.3. The $M - \theta$ curve of this beam is marked with crosses in Fig. 6.11, while the other two beams showed the repeatability of the test results.

The maximum theoretical strength was equal to the fully-plastic moment M_p , given by the equation (5.20). Using $\sigma_p = 374 \text{ N/mm}^2$ (Fig. 6.11), the maximum strength was $M_p = 1216 \text{ Nm}$, which agreed perfectly with the measured $M_{pt} = 1224 \text{ Nm}$. The strength of the other two beams was also close, i.e. 1202 and 1259 Nm.

The theory developed in Chapter 5, with $\sigma_{pu} = 390 \text{ N/mm}^2$, predicts the hinge moment variation represented by the solid line M_m ATB in Fig. 6.11. Over-estimate of the hinge performance within the first stage of collapse is caused by effects already mentioned in the discussion of the first preliminary test (Fig. 6.9). It is therefore suggested that the initial hinge behaviour is approximated by a linear moment $M_i(\theta)$ variation:

$$M_i(\theta) = M_m - \frac{\theta}{\theta_T} (M_m - M_T), \text{ for } \theta < \theta_T \quad (6.19)$$

where M_m is the theoretical maximum strength and M_T is the moment calculated by the theory for an angle θ_T at which transition from the

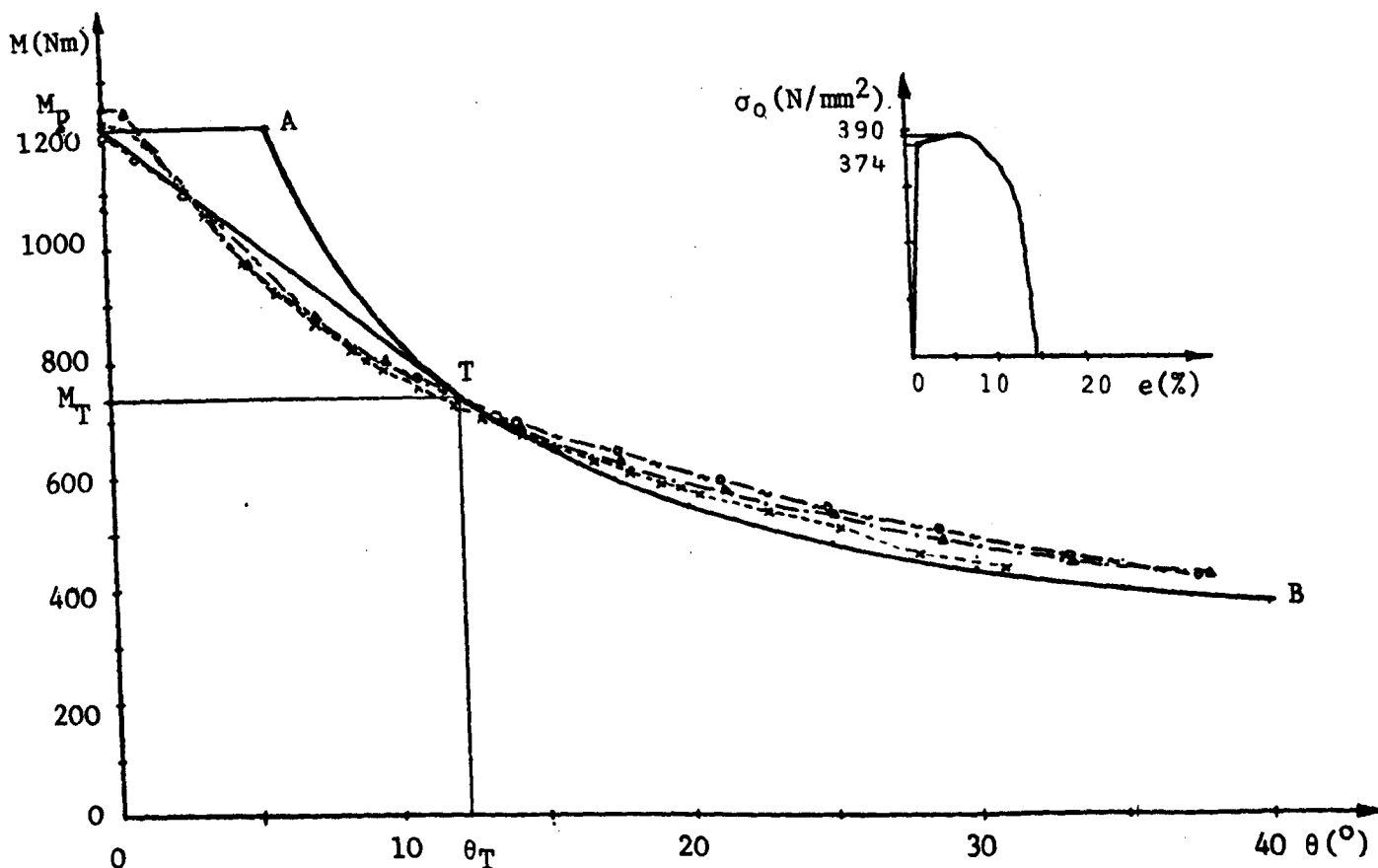


Fig. 6.11

linear segment to the original curve takes place. The angle θ_T is defined by minimising the theoretical energy absorbed, i.e. by minimising the area under the theoretical $M - \theta$ curve. This means that the linear and non-linear parts should be tangent to one another at point T.

The theoretical curve employing the yield stress $\sigma_p = 374 \text{ N/mm}^2$ gives better agreement in the initial stage and reduces the transition angle, but underestimates the hinge performance at larger angles of rotation.

The maximum stresses due to shear and axial forces, calculated by equations (6.13), (6.15), (6.17) and (6.18) were: $\tau_{\max} = 14.6 \text{ N/mm}^2$ (at $\theta = 0^\circ$) and $\sigma_{\text{am}} = 2.4 \text{ N/mm}^2$ (at $\theta = 38^\circ$). The appropriate ratios $(S/S_0)^2 = 0.006$ and $(N/N_0)^2 = 0.00004$ can be neglected in the yield criterion equation (5.91).

The last preliminary tests were carried out on three $25.4 \times 50.8 \times 1.25 \text{ mm}$ section tubes with seam welds in one of the webs (section no. 24 in Table 6.1). (Material properties in Fig. 6.12 were obtained using a specimen taken from the middle of the other web.) Two tubes were tested as

cantilevers using the procedure described already. The experimental $M - \theta$ curves are marked by dots and triangles in Fig. 6.12. Closing of the flange buckle at $\theta \approx 25^\circ$ initiated the third and fourth phase of collapse producing a gradual increase in the hinge strength.

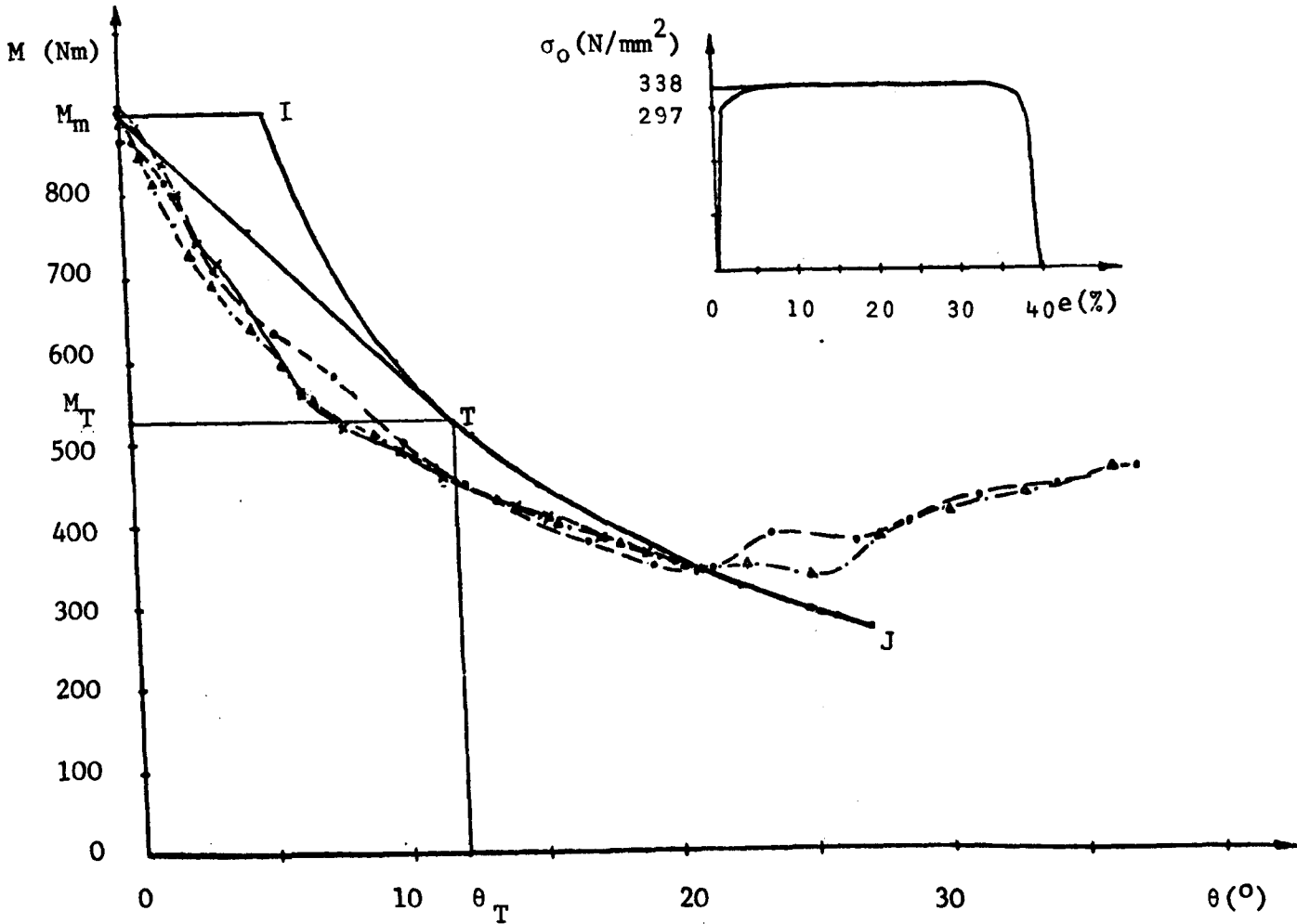


Fig. 6.12

The curve marked by crosses in Fig. 6.12 was obtained by testing the simply supported beam (Fig. 6.2) mentioned at the beginning of section 6.2. The hinge was subject to pure bending and the experimental procedure and data processing were based on the same principles as in the cantilever tests. Coincidence of the three curves supports the argument that shear and axial forces in cantilever tests have a negligible effect on both the collapse mode and yield condition (5.91).

The theoretical $M - \theta$ curve employing $\sigma_p = 297 \text{ N/mm}^2$ and $\sigma_{pu} = 338 \text{ N/mm}^2$ (Fig. 6.12) is represented by the solid line M_mITJ . Minimisation of the theoretical energy with the assumption (6.19) produces the final theoretical curve M_mTJ .

It was mentioned in section 5.5.2 that jamming of the primary hinge and onset of the secondary one occur earlier in "deep" sections with $a < b$. The theoretical mechanism does not allow for the effects causing

the recovery of strength after $\theta = 25^\circ$ (Fig. 6.12). "Jamming" of the theoretical collapse mechanism occurs when the angle β in Fig. 5.16 and equation (5.47) becomes zero, and the calculation breaks down. This occurred at $\theta_J = 30^\circ$ in Fig. 6.12, which is more than 25° due to the neglected effect of the wall thickness and accumulation of material along the yield line BA (Fig. 5.15) of the collapse mechanism.

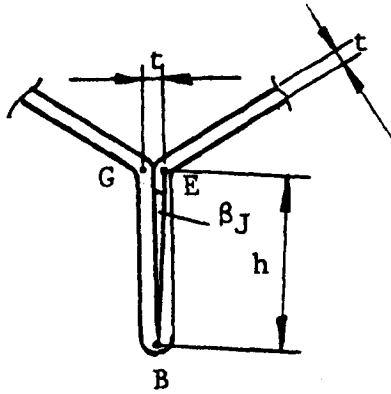


Fig. 6.13

A theoretical contact between the two halves of the compression flange is made when the distance between points G and E of the collapse mechanism (Fig. 5.15) is equal to the wall thickness (Fig. 6.13). The appropriate angle β_J is:

$$\beta_J = \arcsin \frac{t}{2h} \quad (6.20)$$

The angle of hinge "jamming" θ_J can be determined from the equation (5.47) and (6.20) in the form:

$$\theta_J = 2 \arcsin \left(\frac{h - 0.5t}{b} \right) \quad (6.21)$$

There is little information on the hinge behaviour after jamming. Experimental investigations reported later in this chapter gave a fairly wide scatter of results in this region, caused by extensive plastic straining and some material separation. These results were used to establish an approximate relation for the moment variation after hinge jamming, as shown in the next section.

6.5 THE FINAL PROCEDURE TO CALCULATE THE THEORETICAL MOMENT - ROTATION CURVE

The final procedure to calculate the theoretical hinge moment-rotation curve is based on the theory developed in Chapter 5 and on the experimental evidence gathered from the preliminary tests. The theory applies to uniaxial bending collapse of mild steel rectangular or square section tubes.

6.5.1 Input Data

Input data are:

1. flange width "a";
2. depth of the tube "b";
3. wall thickness "t", assumed constant within the hinge;
4. yield stress of the material " σ_p ", obtained as described in sections 5.7.4 and 6.3;
5. the maximum nominal flow stress of the material " σ_{pu} ", obtained as described in sections 5.7.4 and 6.3;
6. Young's modulus of the material "E" - a standard value $E \approx 208000 \text{ N/mm}^2$ for mild steel may be used in all practical applications;

7. the maximum angle of hinge rotation " θ_{end} ";
8. the hinge rotation step " θ_s " between the adjacent calculated points on the $M - \theta$ curve.

All the input data are shown in Fig. 6.14: section dimensions of tubes bent about the axes $x - x$ (a), stresses σ_p and σ_{pu} in the quasi-static nominal stress-engineering strain curve (b) and maximum rotation θ_{end} with the calculation step θ_s in the hinge moment-rotation diagram (c).

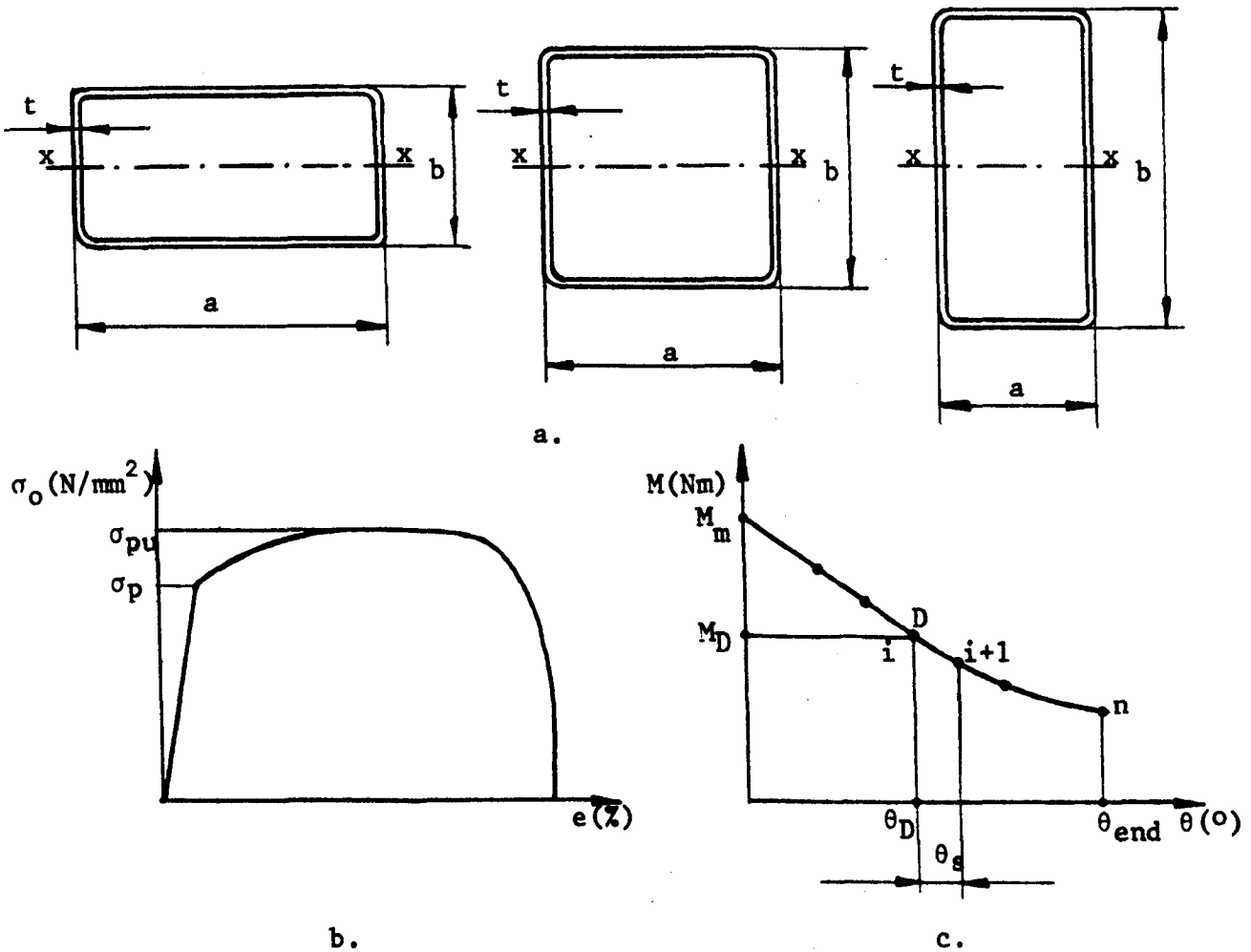


Fig. 6.14

The data above enable calculation of the quasi-static moment-rotation curve. Dynamic conditions considered in Chapters 2 and 3 do not alter the kinematics of the hinge collapse mechanism, so that the same model can be employed allowing for the strain rate effect on material properties. An example of dynamic collapse will be given in Chapter 7.

6.5.2 The maximum Bending Strength

The maximum bending strength M_m is calculated in the following sequence explained in section 5.2.

The critical stress σ_{cr} of the compression flange is:

$$\sigma_{cr} = 0.9E \left(5.23 + 0.16 \frac{a}{b} \right) \left(\frac{t}{a} \right)^2 \quad (6.22)$$

giving the appropriate effective flange width a_e at the onset of collapse:

$$a_e = a \left(0.7 \frac{\sigma_{cr}}{\sigma_p} + 0.3 \right) \quad (6.23)$$

with $a_e = a$ if $\sigma_{cr} \geq \sigma_p$.

The maximum strength M_m depends upon the stability of section walls, measured by the ratio σ_{cr}/σ_p , i.e.

if $\sigma_{cr} \leq \sigma_p$:

$$M_{max} = M'_m = \sigma_p t b^2 \left[\frac{2a + b + a_e \left(3 \frac{a}{b} + 2 \right)}{3(a + b)} \right] \quad (6.24)$$

if $\sigma_{cr} > 3\sigma_p$:

$$M_{max} = M_p = \sigma_p t [a(b - t) + 0.5(b - 2t)^2] \quad (6.25)$$

and, finally, if $\sigma_p < \sigma_{cr} \leq 3\sigma_p$, a moment

$$M'_p = \sigma_p t b \left(a + \frac{b}{3} \right) \quad (6.26)$$

is defined first, and the maximum strength becomes:

$$M_{max} = M'_p + (M_p - M'_p) \frac{\sigma_{cr} - \sigma_p}{2\sigma_p} \quad (6.27)$$

6.5.3 Hinge Dimensions

Hinge dimensions are: width "a", depth "b" and the theoretical half length "h" is

$$h = \frac{a}{2}, \text{ if } a \leq b \quad (6.28)$$

$$h = \frac{b}{2}, \text{ if } a \geq b$$

6.5.4 The Basic Moment - Rotation Curve

The basic moment-rotation curve is defined for the angles of hinge rotation between zero and the "angle of jamming" θ_J :

$$\theta_J = 2 \arcsin \left(\frac{h-0.5t}{b} \right) \quad (6.29)$$

Given an angle θ_D , a discrete point D on the basic moment-rotation curve is defined by calculating first the geometrical parameters of the theoretical collapse mechanism in Fig. 5.15:

$$\rho = \frac{\theta_D}{2} \quad (6.30)$$

$$y_A = y_B = b \cos \rho - \sqrt{b \sin \rho (2h-b \sin \rho)} \quad (6.31)$$

$$z_A = b \sin^2 \rho - h \sin \rho + \sqrt{b \sin \rho (2h-b \sin \rho)} \cdot \cos \rho \quad (6.32)$$

$$\beta = \arcsin \left(1 - \frac{b}{h} \sin \rho \right) \quad (6.33)$$

$$y_{A''} = \frac{h \tan \rho + b \cos \rho - \sqrt{b \sin \rho (2h-b \sin \rho)}}{1 + \tan^2 \rho} \quad (6.34)$$

$$x_{A''} = y_{A''} \cdot \tan \rho \quad (6.35)$$

The empirical expression for the rolling radius r is:

$$r = \left(0.07 - \frac{\theta_D}{70} \right) h = \left(0.07 - \frac{\rho}{35} \right) h \quad (6.36)$$

and the fully plastic moment per unit length of the yield line is given by:

$$m_p = \frac{\sigma_{pu} \cdot t^2}{4} \quad (6.37)$$

The energy absorbed as the hinge rotates through $\theta_D = 2\rho$ can now be expressed (from equation (5.67) in the form:

$$\begin{aligned}
 W(\theta_D) = m_p [& a(\pi-2\rho-2\beta) + a(\pi-2\beta) + 2z_A (\pi-2\beta) + \\
 & + 2h\pi + 4b \arctan \left(\frac{z_A}{\sqrt{(h-x_{A''})^2 + (y_{A''}-y_A)^2}} \right) + 4 \frac{h}{r} z_A + \\
 & + \frac{8z_A}{3r} \sqrt{h^2+y_A^2+z_A^2} + 2(ap+2h \arctan \frac{z_A}{y_A})] \quad (6.38)
 \end{aligned}$$

or, after some rearranging, the final expression is:

$$\begin{aligned}
 W(\theta_D) = 0.5 \sigma_{put}^2 [& a(\pi-2\beta) + 2b \arctan \left(\frac{z_A}{\sqrt{(h-x_{A''})^2 + (y_{A''}-y_A)^2}} \right) + \\
 & + h(\pi+2 \arctan \left(\frac{z_A}{y_A} \right)) + 2 \frac{z_A}{r} \left(h + \frac{2}{3} \sqrt{h^2+y_A^2+z_A^2} \right)] \quad (6.39)
 \end{aligned}$$

Equation (6.39) represents a product between the maximum nominal flow stress σ_{pu} and a factor depending entirely on the section geometry. The first three products in the square brackets represent contribution of bending along the yield lines, while the last term corresponds to the rolling deformation of the webs.

The angle θ_D should now be varied by a small but finite increment $\Delta\theta$ within which the hinge moment M_D may be assumed constant. A negative variation $\Delta\theta = -0.00174533 \text{ rad} = -0.1^\circ$ was used in this work to enable the definition of the moment M_J at the "jamming" point θ_J , which would not be possible with a positive $\Delta\theta$. The difference in results with small $\Delta\theta$ is negligible, whatever the sign of the increment is.

The new angle:

$$\theta'_D = \theta_D + \Delta\theta_D = \theta_D - 0.00174533 \quad (6.40)$$

is now used in equations (6.30) to (6.39) enabling the definition of the appropriate difference in the two energies:

$$\Delta W(\theta_D) = W(\theta_D) - W(\theta_D + \Delta\theta_D) = W(\theta'_D) - W(\theta_D) \quad (6.41)$$

The moment M_D can now be expressed in the form:

$$M_D(\theta_D) = \frac{\Delta W(\theta_D)}{\Delta \theta_D} = \frac{W(\theta'_D) - W(\theta_D)}{\theta'_D - \theta_D} \quad (6.42)$$

with an additional condition:

$$M_D \leq M_m \quad (6.43)$$

The basic theoretical curve $ABDJ$ in Fig. 6.15 is produced by calculating a set of discrete points starting from $M_1 = M(\theta_1) = M(\theta_s)$. The next one corresponds to $\theta_2 = \theta_1 + \theta_s$, and then $\theta_3 = \theta_2 + \theta_s$ e.t.c. until the last, n -th step makes $\theta_n \geq \theta_J$ or $\theta_n \geq \theta_{end}$, what ever happens first. The last moment M_J or M_{end} is then determined by putting $\theta_n = \theta_J$ or $\theta_n = \theta_{end}$. The latter case with $\theta_{end} < \theta_J$ is common in sections where $a \geq b$ because they usually have $\theta_J > 50^\circ$. Situation with $\theta_J < \theta_{end}$ (Fig. 6.15) is more general and appears particularly in "deep" beams with $a < b$.

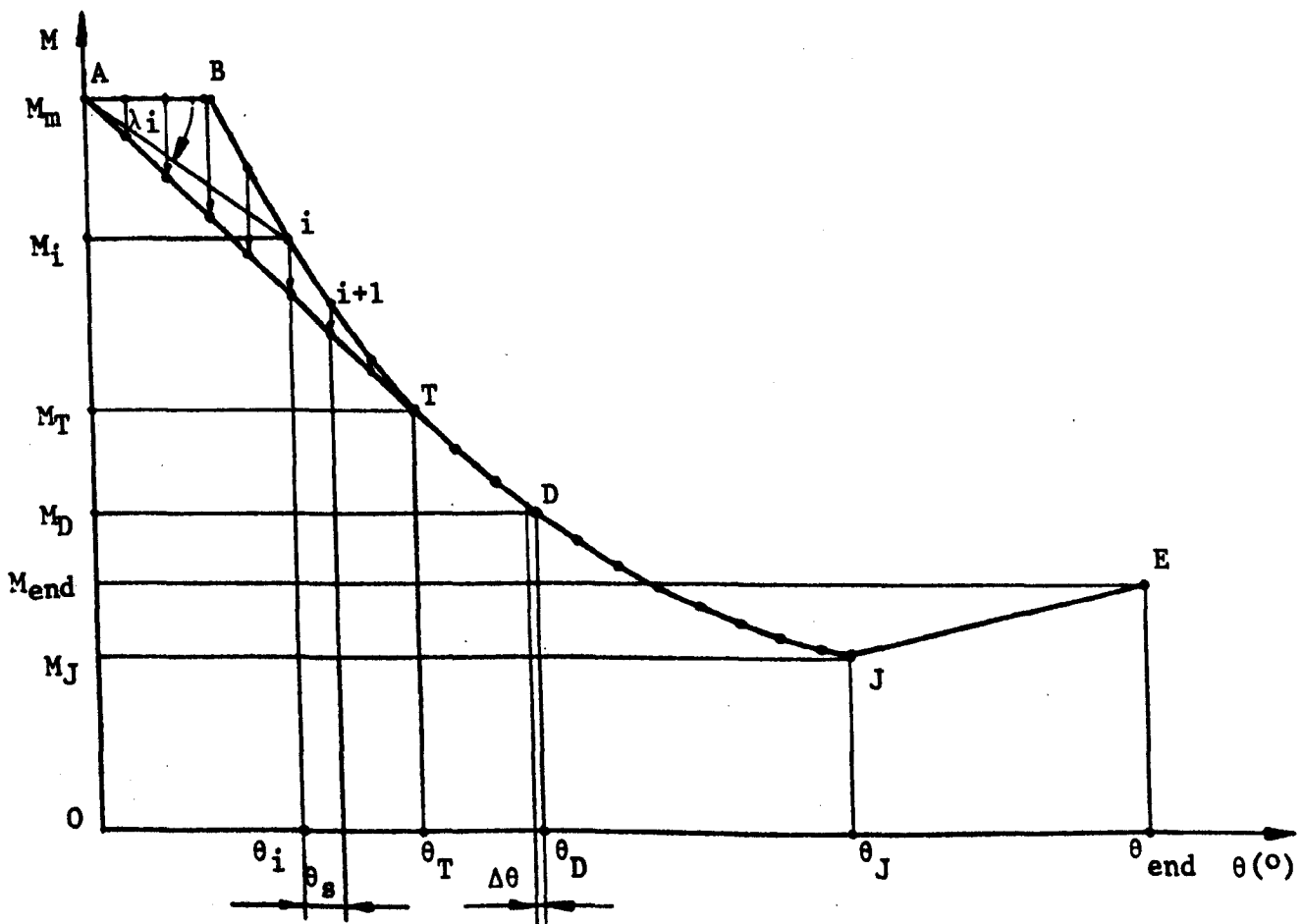


Fig. 6.15

6.5.5 The Modified Moment-Rotation Curve

Modification of the basic moment-rotation curve is required in the first stage of hinge collapse and also for bending collapse beyond the angle of jamming θ_J (Fig. 6.15). Reasons for both adjustments are given in section 6.4.

The initial linear interpolating segment AT (Fig. 6.15) is determined by the condition that the energy absorbed at the hinge, i.e. the area under the M- θ curve, is minimum. This condition is met if the segment AT is tangent to the basic M- θ curve. The basic curve is not given in an explicit form, so that an iterative numerical process would be necessary to determine the "transition angle" θ_T (Fig. 6.15) very accurately.

A sufficiently accurate position of the transition point T can be obtained in a much simpler way if the step θ_g between the calculated discrete points on the basic curve is reasonably small, say $\theta_g = 1^\circ$. It is possible to define an angle λ_i (Fig. 6.15), corresponding to the i-th point on the basic curve, such that $\tan \lambda_i$ is proportional to the ratio $(M_m - M_i) / \theta_i$. An approximate position of point T can now be found from the condition that the angle λ_T is bigger than any other λ_i where $i = 1, 2, \dots, n-1, n$. The search is made starting with $i = 1$ and point T is placed at the first discrete point calculated as in section 6.5.4 satisfying:

$$\frac{M_m - M_i}{\theta_i} > \frac{M_m - M_{i+1}}{\theta_{i+1}} \quad ; \quad (\theta_i = \theta_T) \quad (6.44)$$

The transition angle θ_T has thus been determined and the moment variation along the segment AT can be expressed in the form:

$$M_{AT}(\theta) = M_m - \frac{\theta}{\theta_T} (M_m - M_T) \quad ; \quad (6.45)$$

The points on the basic curve with $0 \leq \theta_i \leq \theta_T$ are therefore shifted to the new position on the AT line.

It is important to note that the original theory may be applied successfully to a wider range of angles than between θ_T and θ_J (Fig. 6.15). The difference between the original M- θ curve and the interpolating line AT is usually small for angles greater than $5 + 10^\circ$, depending on the section geometry. However, the modification introduced here has two important advantages:

- a. it reduces or eliminates the theoretical overestimate of the hinge performance during the initial stages of collapse, and minimises the theoretical results regarding the strength and energy absorption;

- b. it gives a smooth transition between the two segments of the theoretical M-θ diagram - a property which is desirable when incorporating this theory into the program CRASHD.

Experimental results reported in the next section have indicated that a reasonable approximation of the actual moment increase after jamming can be obtained by the following empirical function:

$$M_{JE} = M(\theta_J) + 1.4 (M_{\max} - M(\theta_J)) \cdot (\theta - \theta_J); \theta \geq \theta_J \quad (6.46)$$

The last equation applies only after the hinge has already rotated through a large angle. Structural elements that should absorb energy by bending are not likely to have a/b < 0.5 because otherwise the difference in strengths about two axes becomes too great and collapse may easily take place about the "weaker" axis. In most practical cases the angle of jamming θ_J will be close to 30°.

The expression for the theoretical energy absorbed W_{mod} (θ), following the modifications above, becomes

if 0 < θ ≤ θ_T:

$$W_{\text{mod}}(\theta) = \frac{1}{2} [M_{\max} + M_{AT}(\theta)] \theta = \frac{1}{2} [M_{\max} (2 - \frac{\theta}{\theta_T}) + \frac{\theta}{\theta_T} M(\theta_T)] \theta \quad (6.47)$$

if θ_T < θ ≤ θ_J:

$$W_{\text{mod}}(\theta) = \frac{1}{2} [M_{\max} + M(\theta_T)] \theta_T + W(\theta) - W(\theta_T) \quad (6.48)$$

and if θ_J < θ ≤ θ_{end}, using Fig. 6.15,:

$$W_{\text{mod}}(\theta) = \frac{1}{2} [M_{\max} + M(\theta_T)] \theta_T + W(\theta_J) - W(\theta_T) + \frac{1}{2} [2M(\theta_J) + 1.4 (M_{\max} - M(\theta_J)) \cdot (\theta - \theta_J)] (\theta - \theta_J) \quad (6.49)$$

All quantities M(θ) and W(θ) in (6.47) ÷ (6.49) are calculated using the basic theory.

6.6 COMPARISON BETWEEN THE THEORETICAL AND EXPERIMENTAL RESULTS FOR VARIOUS TUBULAR SECTIONS

6.6.1 Introductory Remarks

The theory was checked against results of 56 quasi-static cantilever bending tests which were conducted in the same way as the preliminary experiments described in section 6.4. Beams with $a/t > 100$ were cast in concrete while others were clamped as shown in Fig. 6.10. The tubes were arranged with seam welds in tension flanges, but in some rectangular sections the welds had to be in the webs.

The aspect ratio a/b ranged between 3.0 and 0.33 and the compression flange width to thickness ratio a/t varied between 128 and 9.14. Structural members used in bus bodies had $a/t \leq 40.6$. All the section dimensions with characteristic ratios and material properties are listed in Table 6.1.

The wall thickness t was taken by averaging the thickness measured in the middle of each side of the section. It was noticed that it varied usually within $\pm 3\%$ of the nominal value, with some exceptions of $\pm 5\%$. Equation (6.39) gives the energy and moment proportional to the square of thickness. This is not quite true, since the equation has been modified, but the variation of wall thickness may still produce scatter of experimental data. Material properties may also vary, so it was decided to check the repeatability of experimental results by testing more than one tube per section. Three tubes per section were tested in 13 cases and the general repeatability of results remained within $\pm 5\%$ of the average values, with somewhat larger scatter in section number 12. The hand-made tubes 10, 11 and 18 were similar, but their geometry was not consistent enough to be treated as a single section. The scatter was also small in 3 cases where two tubes per section were tested. The 8 remaining standard sections were manufactured in the same way as the others and they were represented by a single test per section.

The test results are shown as dotted lines connecting the discrete measured points in Figs. 6.16-6.42. The solid curves in the same figures represent the theoretical hinge moment (M) - rotation (θ) curves. Bending took place about axes indicated in the small section drawings. The nominal stress-engineering strain curves of the tube material are attached to the M - θ diagrams, while the original curves can be found in Appendix 3.

The effect of shear and axial forces on the yield condition (5.91) was negligible in all cases. The characteristic ratios $(S/S_o)^2$ and $(N/N_o)^2$ were similar to those calculated in section 6.4.

A comparison between the energies absorbed by bending a beam and a flat sheet of the same material whose width and thickness correspond to the respective circumference and wall thickness of the section was made again as in Chapter 4. In thin walled tube no. 18 with $a/t = 123$ the energy absorbed at $\theta = 40^\circ$ was 223 J (Table 6.2) while the sheet can absorb only 11.7 J, which is almost 20 times less. In the thick walled tube 23 the sheet would absorb almost 16 times less energy than the beam, which again indicates the advantage of beams as energy absorbers over sheets when subject to bending.

Table 6.1

Section Number	a [mm]	b [mm]	t [mm]	σ_p [N/mm ²]	σ_{pu} [N/mm ²]	$\frac{a}{b}$	$\frac{a}{t}$
1	45	15	1.30	277	308	3.0	34.6
2	50.8	25.4	1.25	297	338	2.0	40.6
3	50.8	25.4	1.44	283	297	2.0	35.3
4	38	19	1.26	290	326	2.0	30.2
5	54	28.5	1.60	267	300	1.9	33.8
6	45.2	29.3	3.25	463	463	1.54	13.9
7	38.1	25.4	1.62	352	363	1.5	23.5
8	50.8	38.1	1.26	253	284	1.33	40.3
9	50.8	38.4	1.6	380	430	1.33	31.8
10	104	87	0.813	161	250	1.2	128
11	103	99	0.813	161	250	1.04	127
12	44.4	44.4	1.6	313	348	1.0	27.8
13	38.4	38.4	1.6	374	390	1.0	24
14*	45	45	1.94	340	416	1.0	23.2
15	45	45	2.15	324	360	1.0	20.9
16	25.4	25.4	1.48	329	353	1.0	17.5
17	25.4	25.4	2.0	418	418	1.0	12.7
18	100	103	0.813	161	250	0.97	123
19	45	47	0.86	160	245	0.96	52.3
20	38.4	50.8	1.6	380	430	0.756	24
21	38.1	50.8	1.26	253	284	0.75	30.2
22	38.1	50.8	1.67	308	351	0.75	22.8
23	29.3	45.2	3.25	463	463	0.66	9.14
24	25.4	50.8	1.25	297	338	0.5	20.3
25	25.4	50.8	1.44	283	297	0.5	17.6
26	19	38	1.26	290	326	0.5	15.1
27	15	45	1.3	277	308	0.33	11.5

* Section with "re-entrant" flange (third from the right in the middle print of Fig. 5.7).

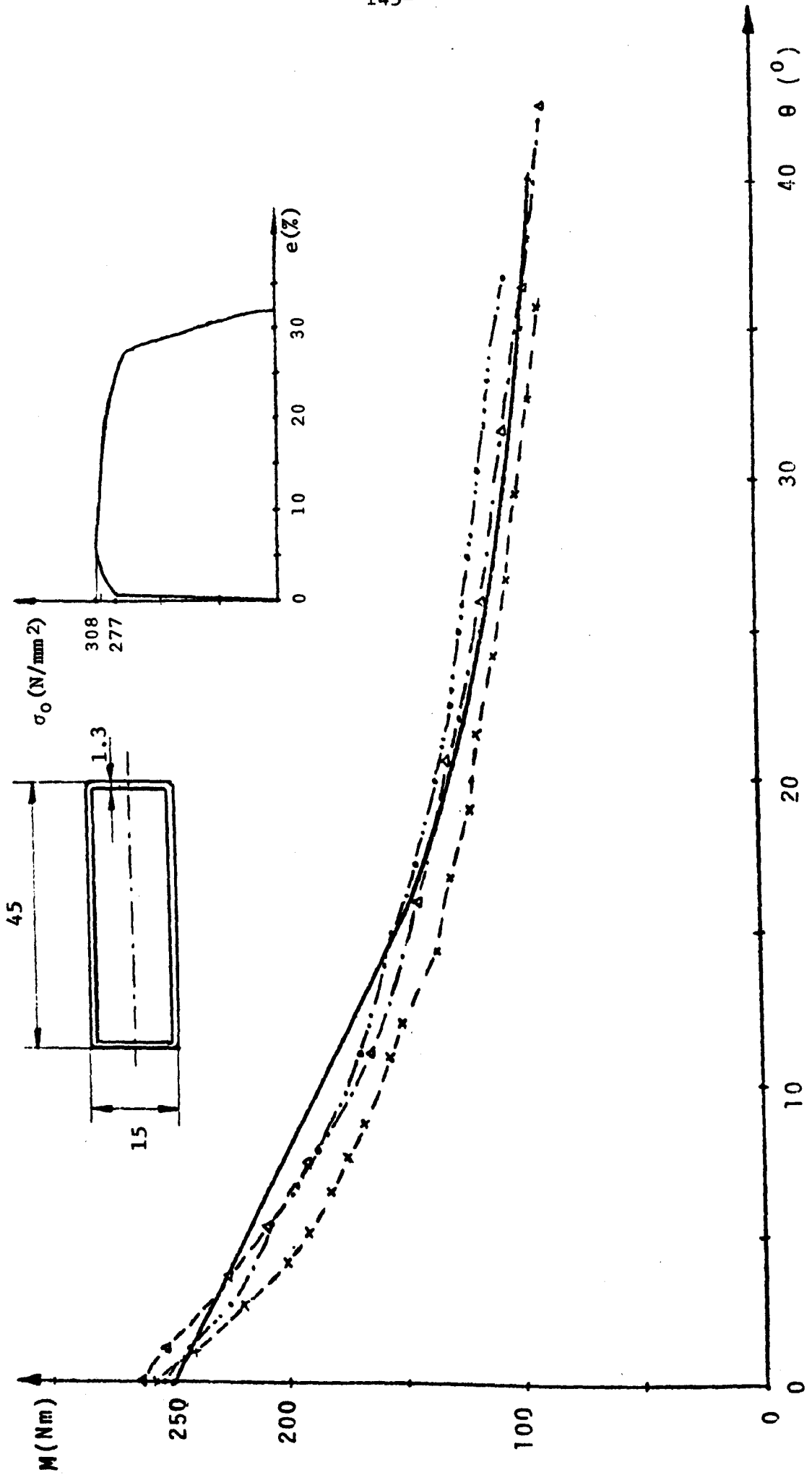


Fig. 6.16 - SECTION I

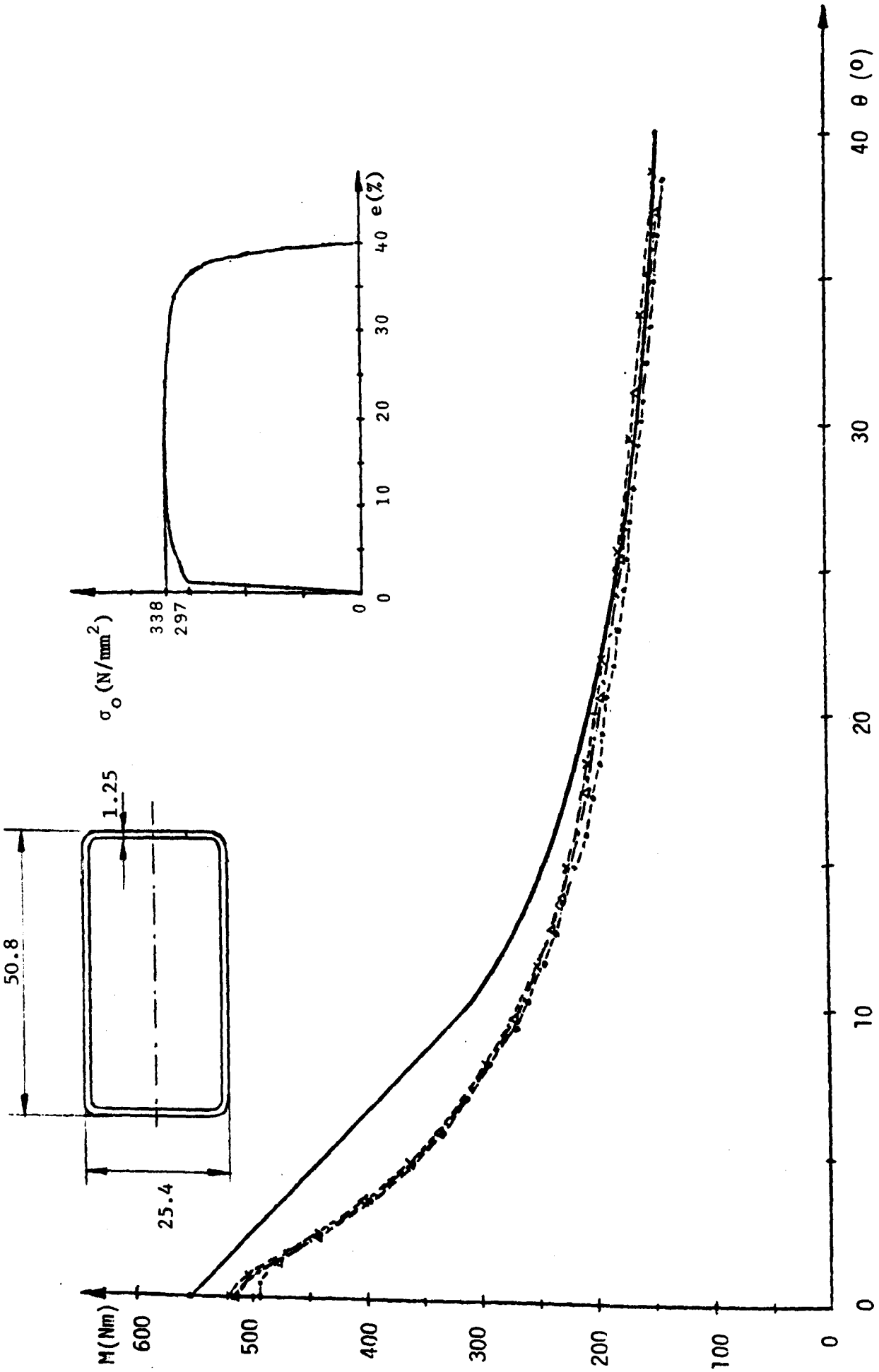


Fig. 6.17 - SECTION 2

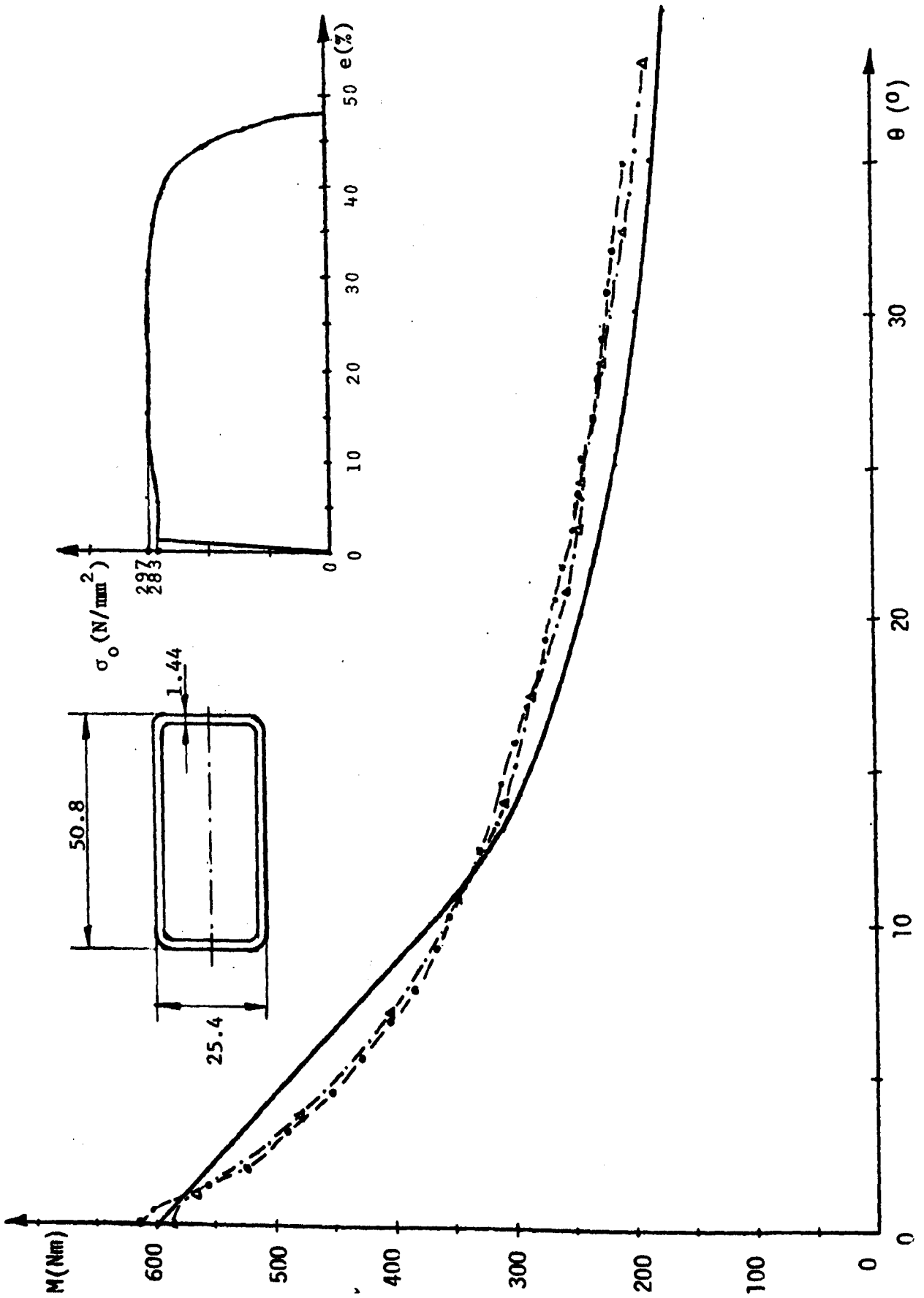


Fig. 6.18 - SECTION 3

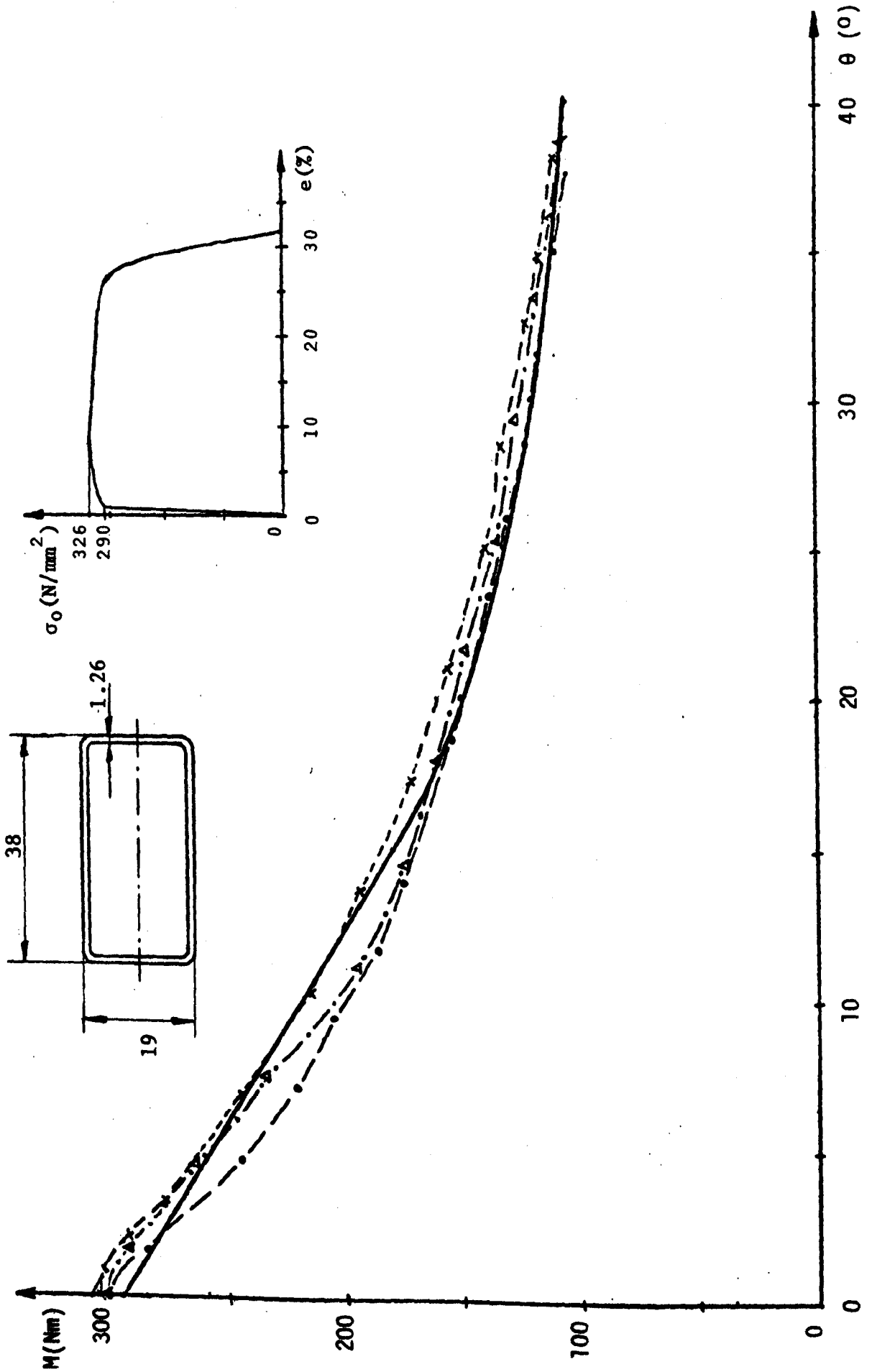


Fig. 6.19 - SECTION 4

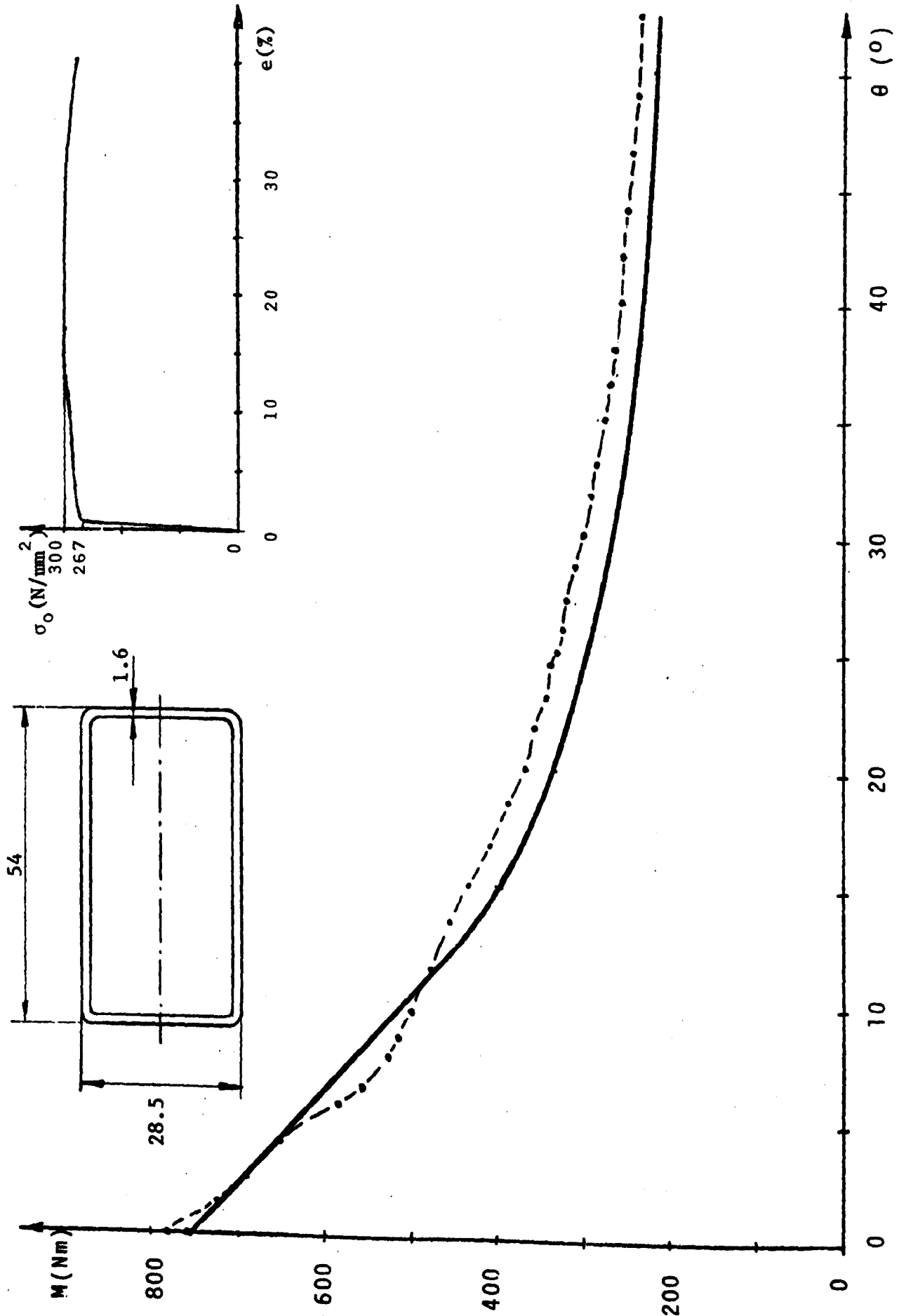


Fig. 6.20 - SECTION 5

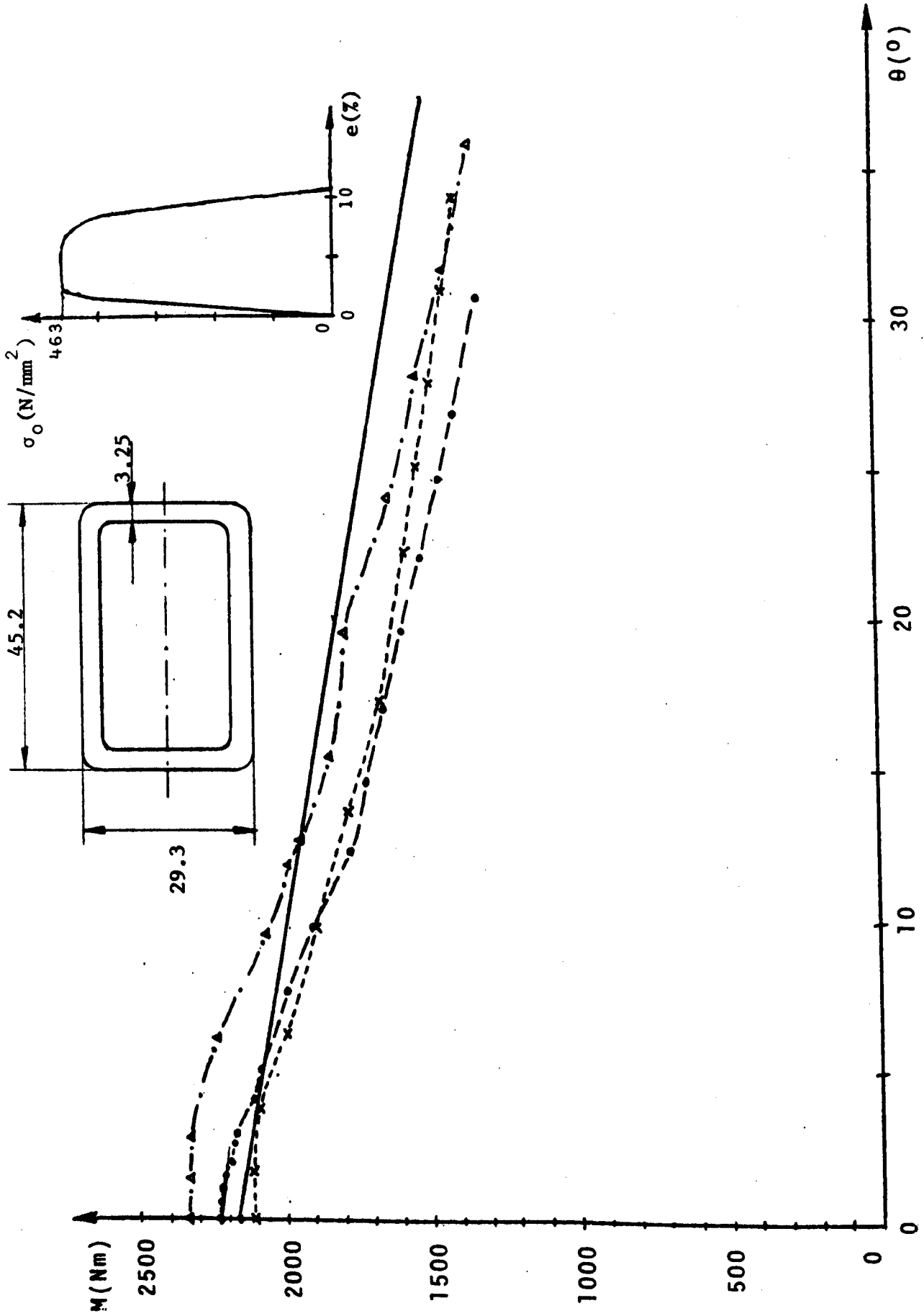


Fig. 6.21 - SECTION 6

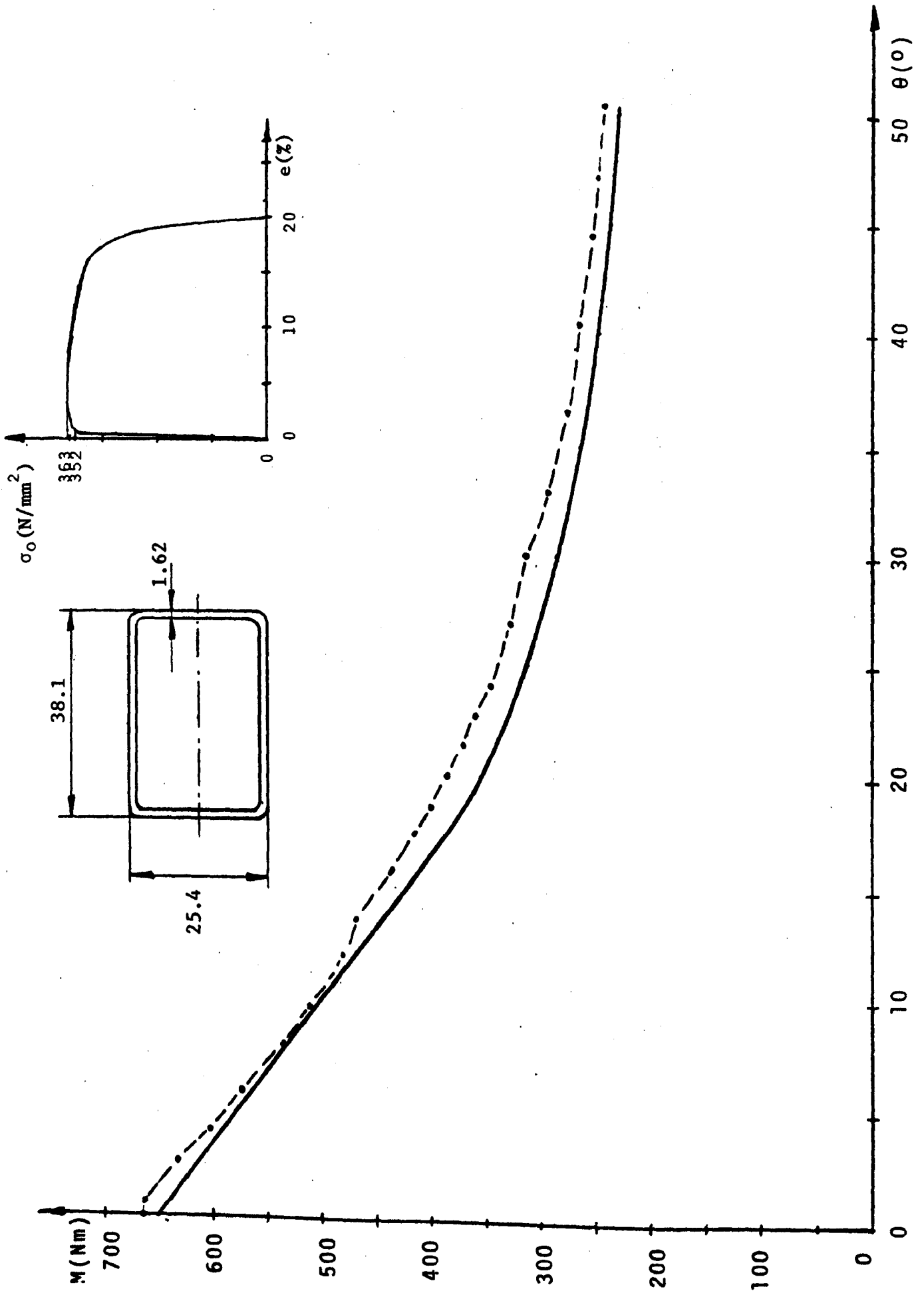


Fig. 6.22 - SECTION 7

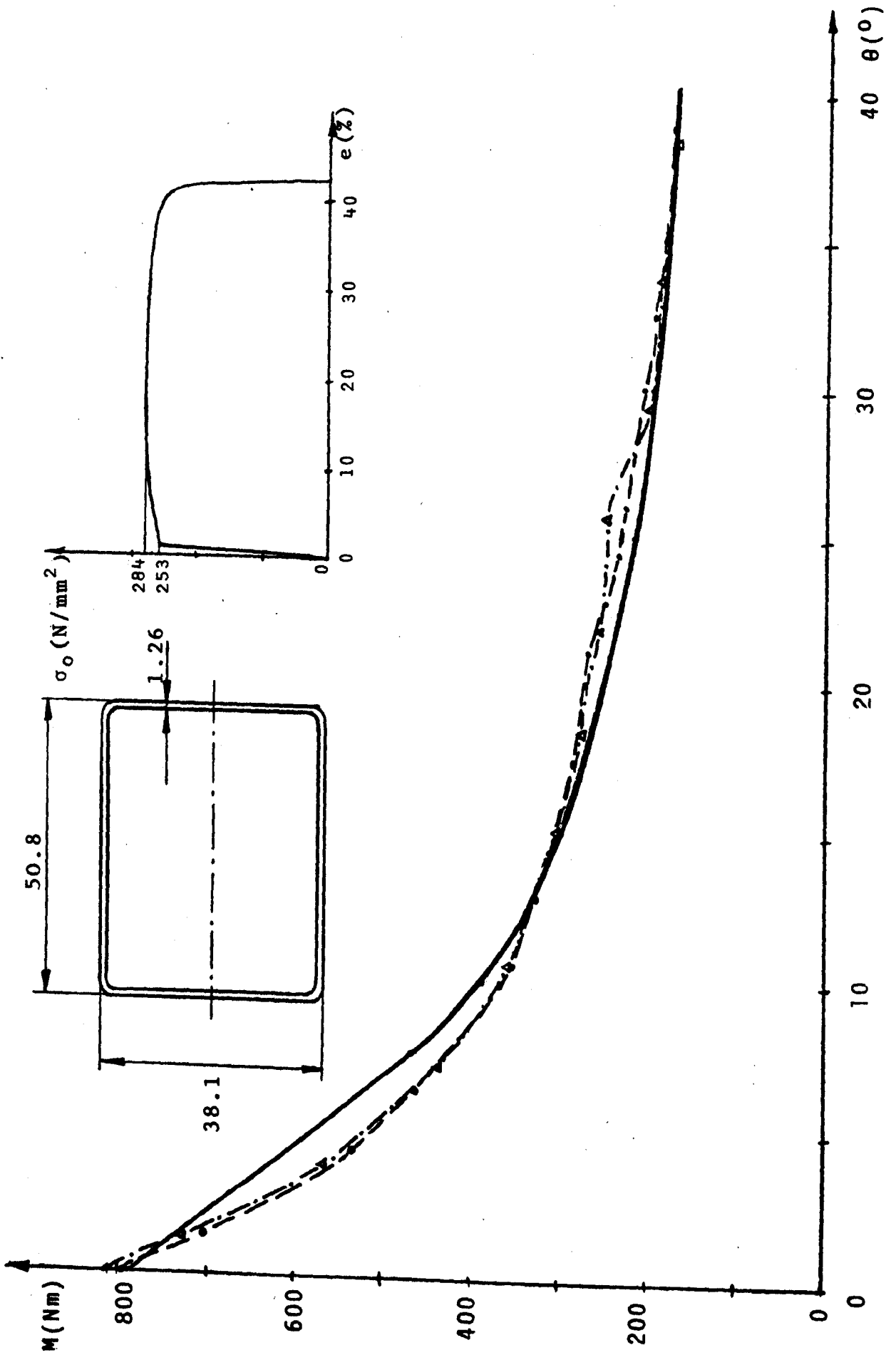


Fig. 6.23 - SECTION 8

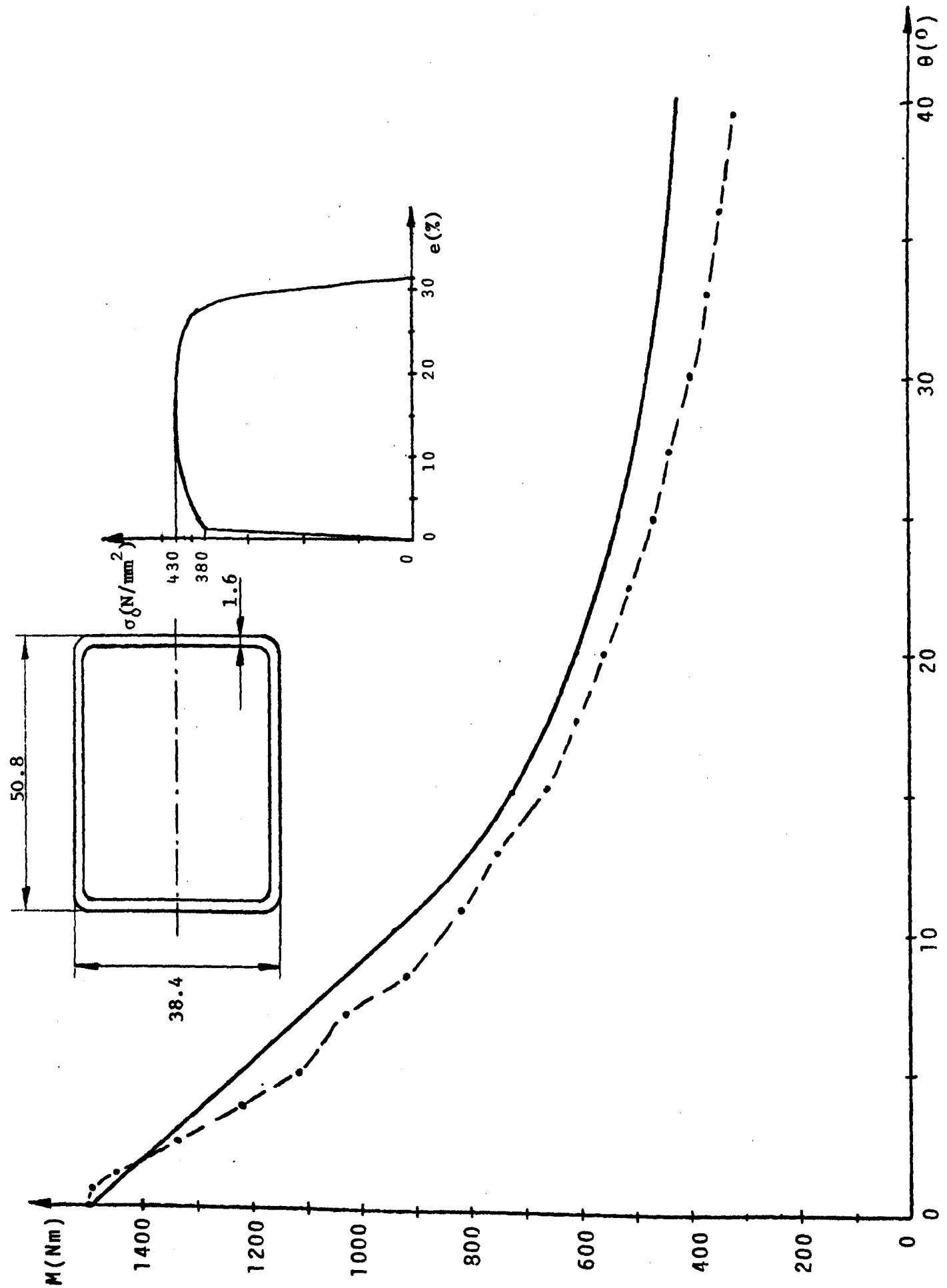


Fig. 6.24 - SECTION 9

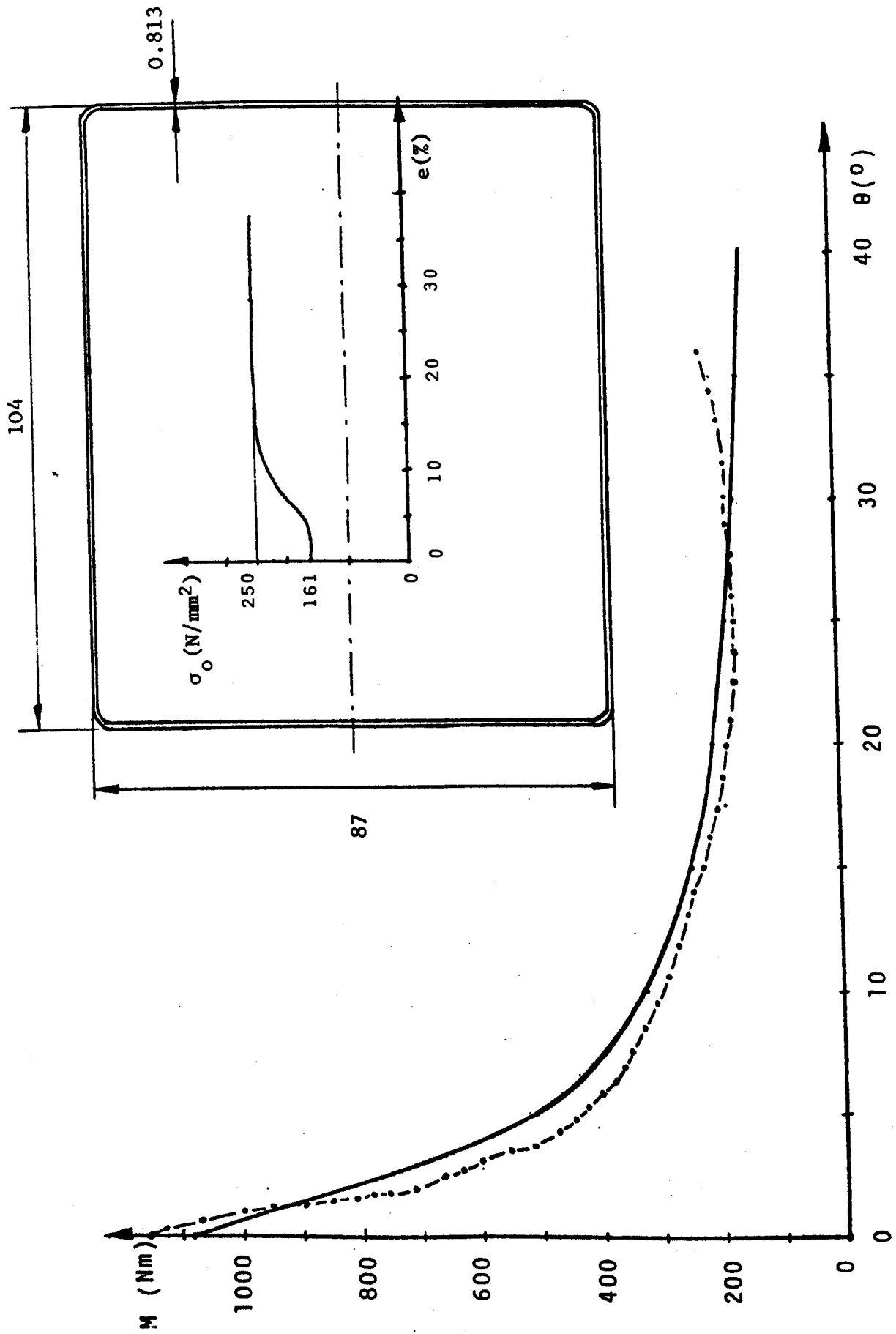


Fig. 6.25 - SECTION 10.

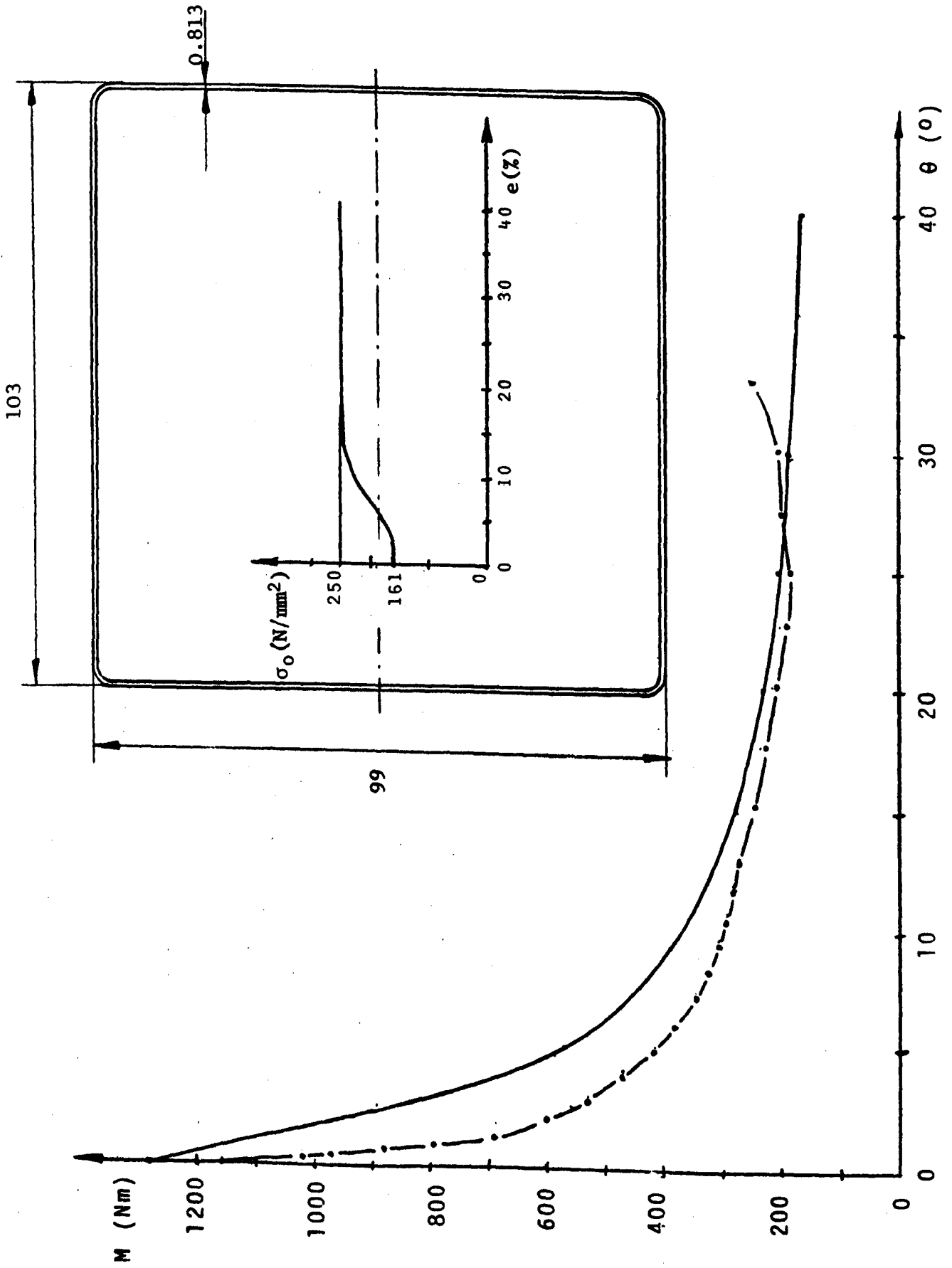


Fig. 6.26 - SECTION 11

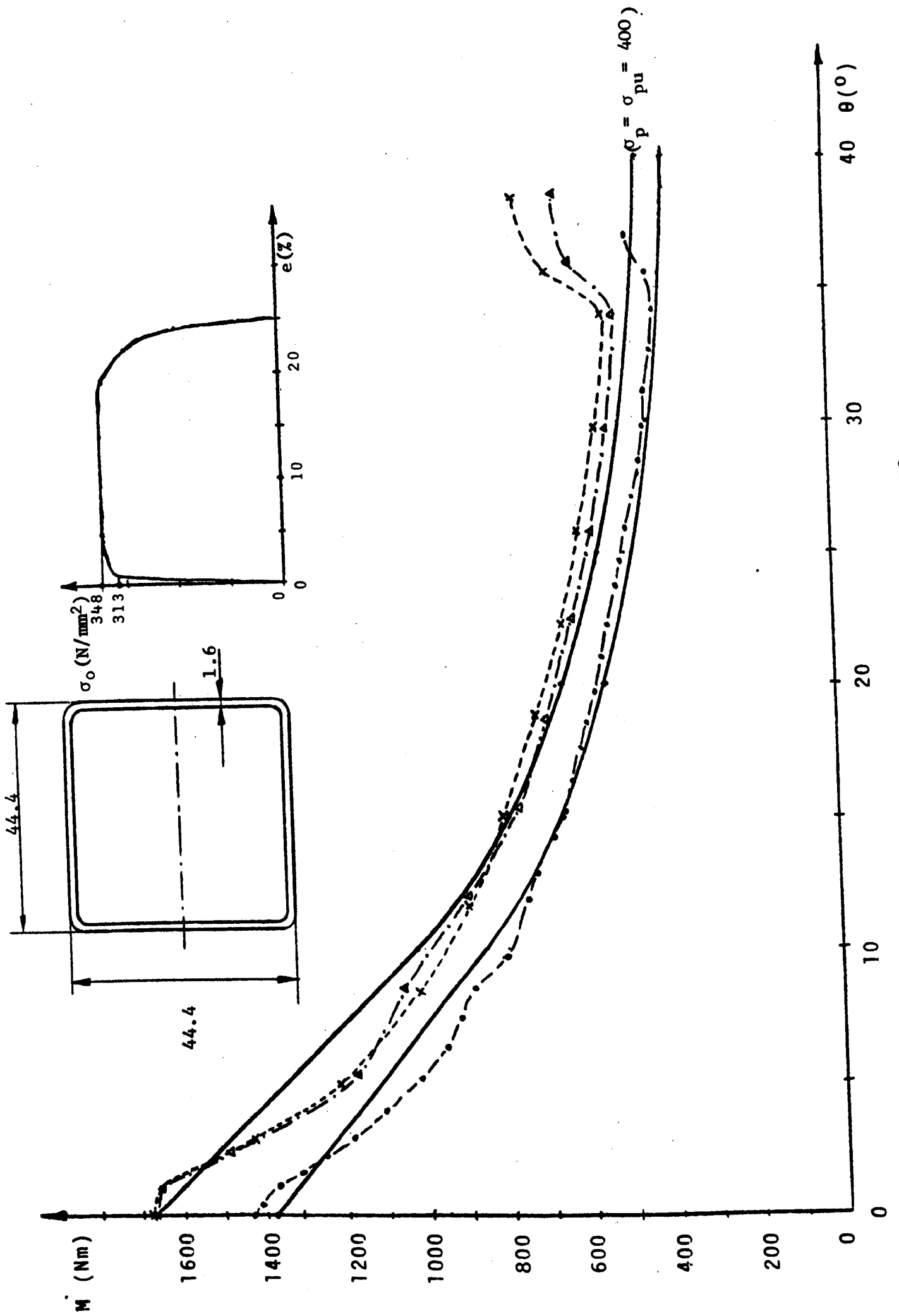


Fig. 6.27 - SECTION 12

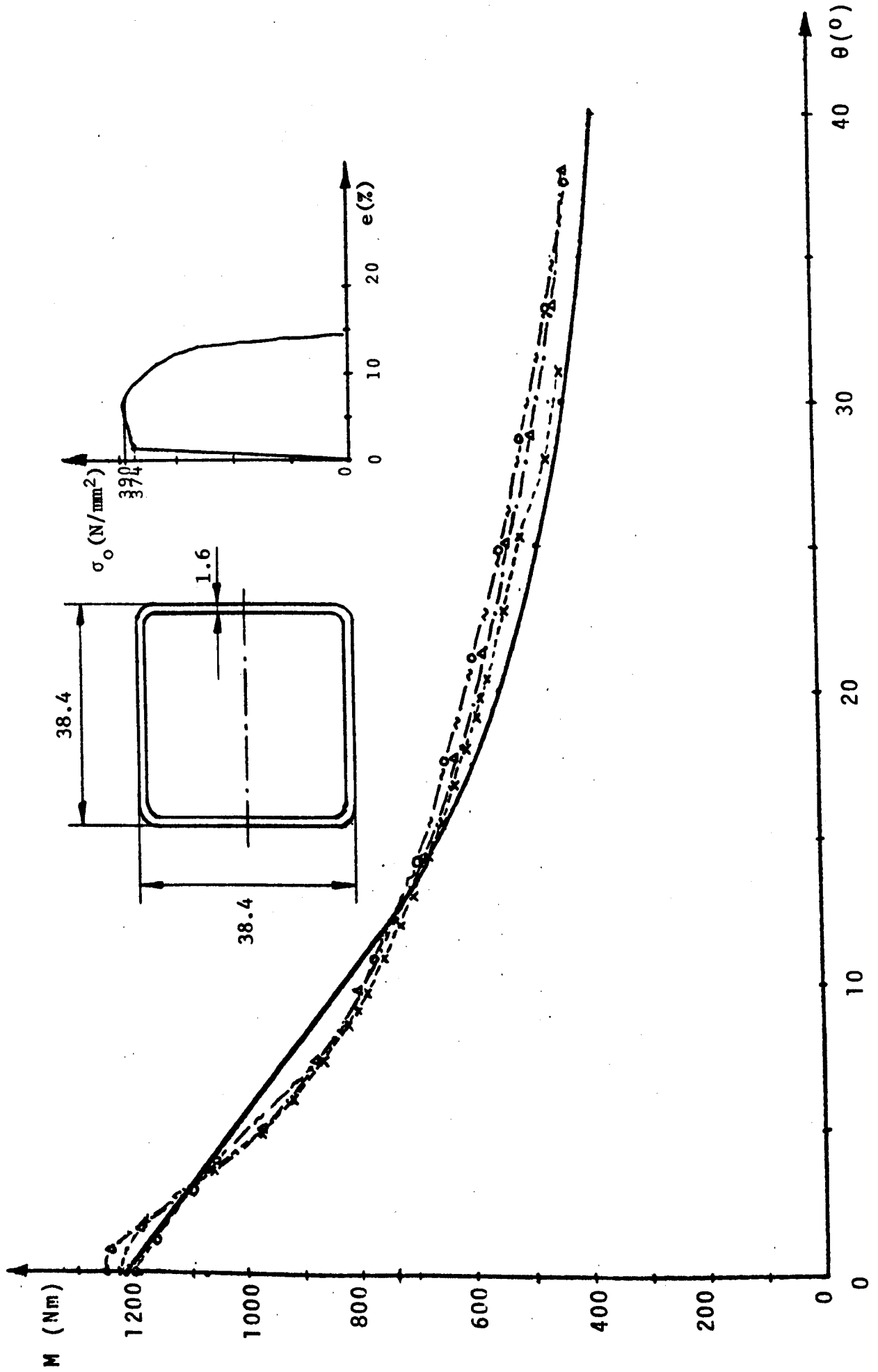


Fig. 6.28 - SECTION 13

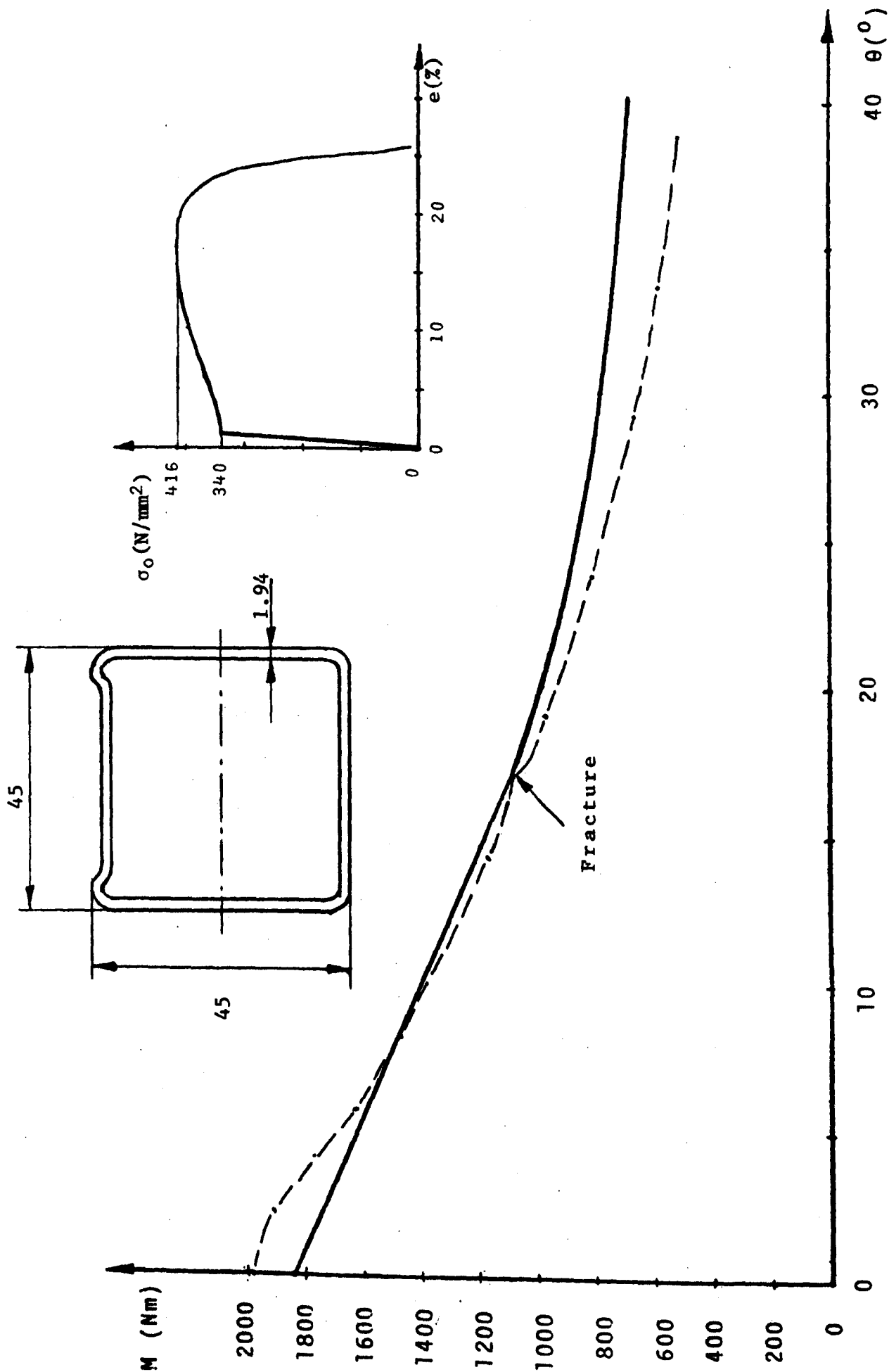


Fig. 6.29 - SECTION 14

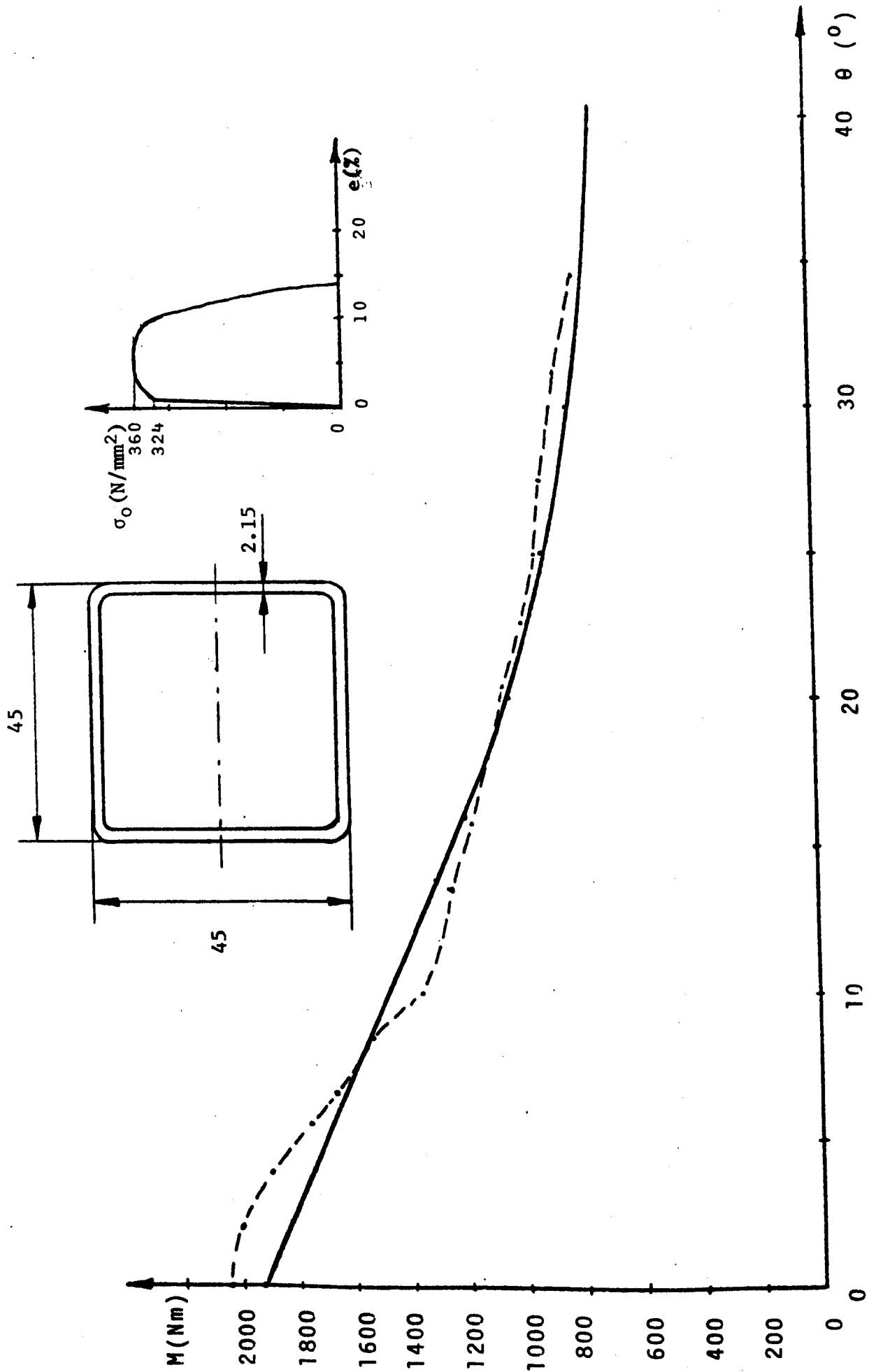


Fig. 6.30 - SECTION 15

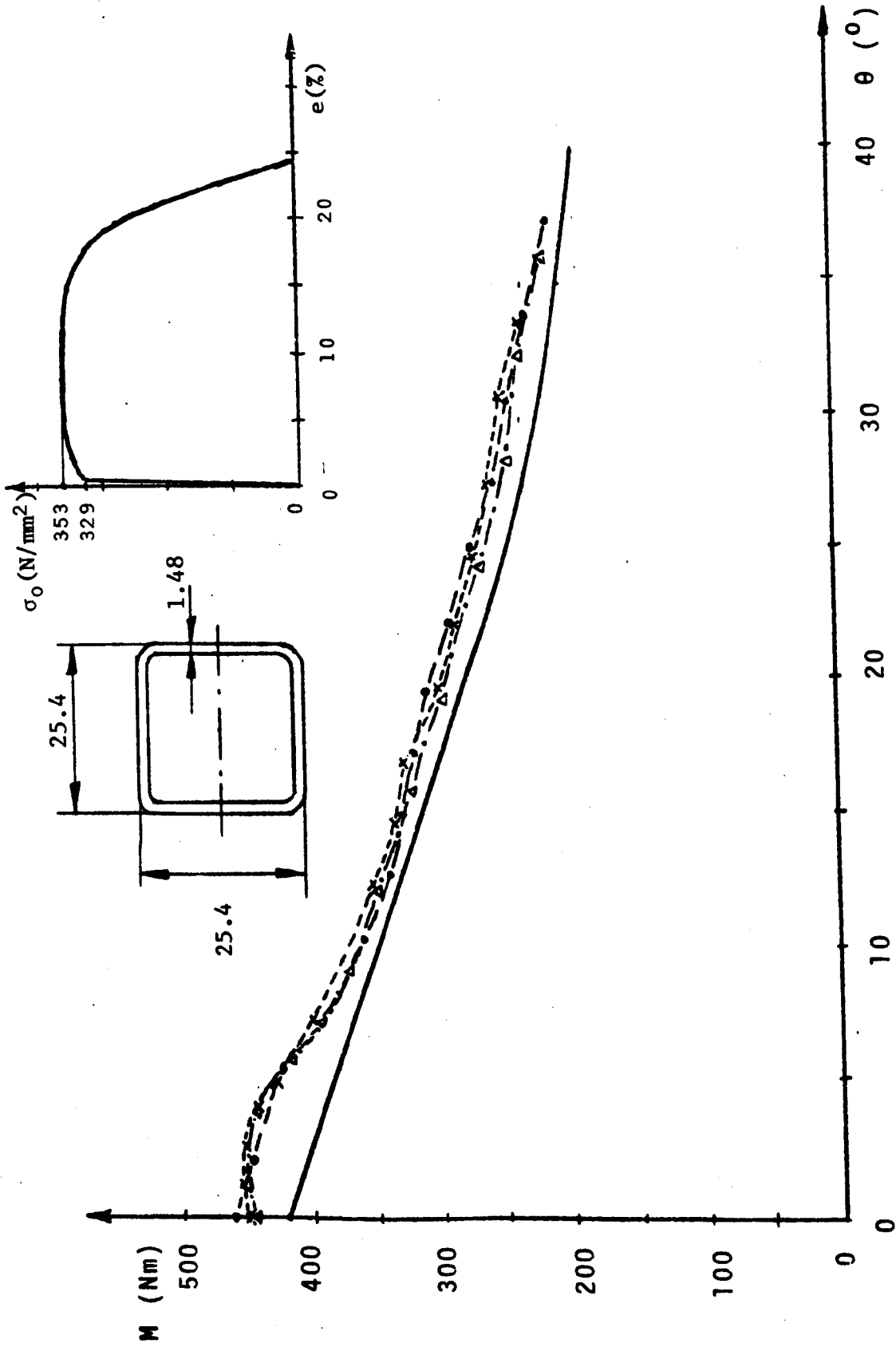


Fig. 6.31 - SECTION 16

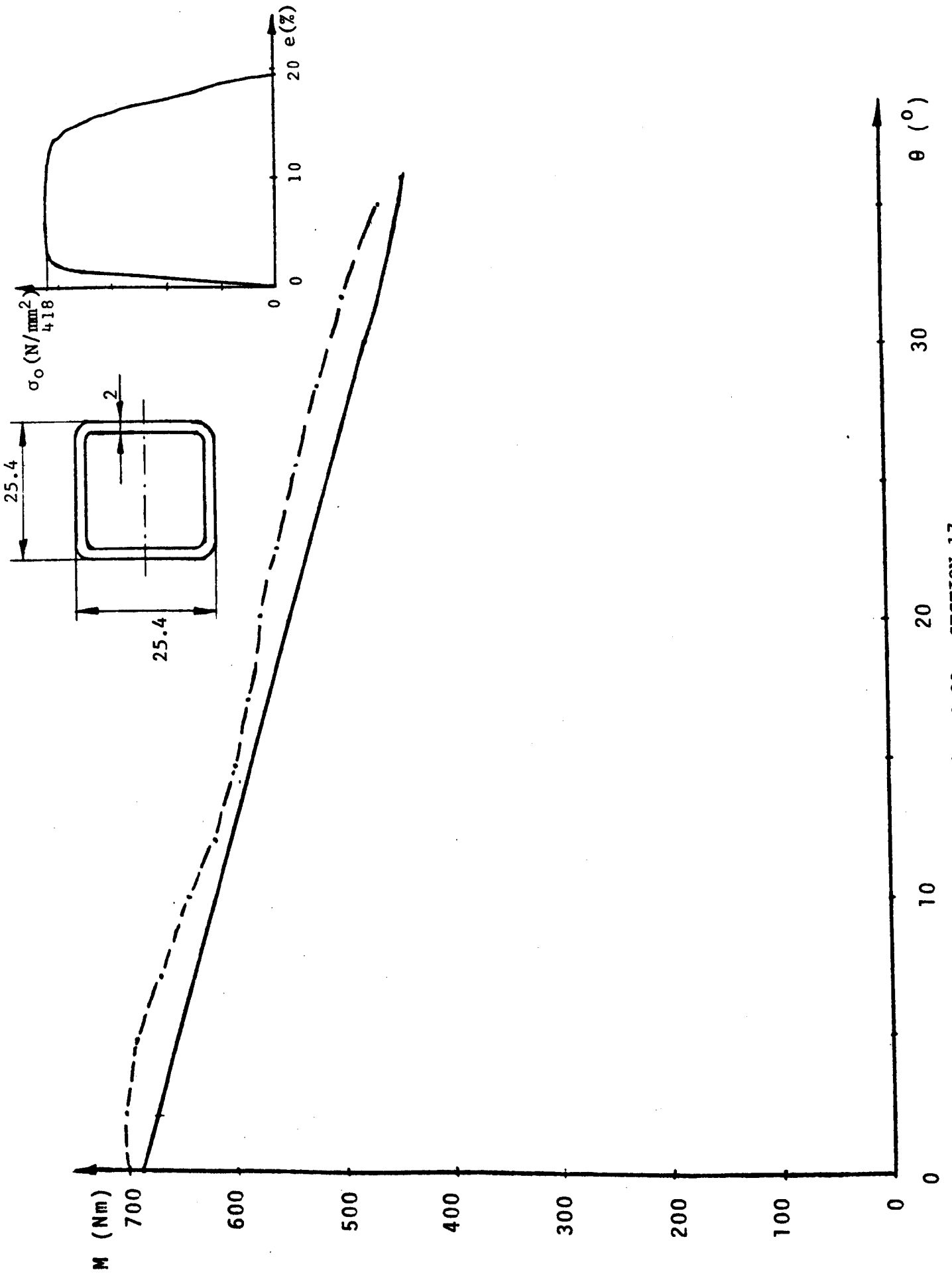


Fig. 6.32 - SECTION 17

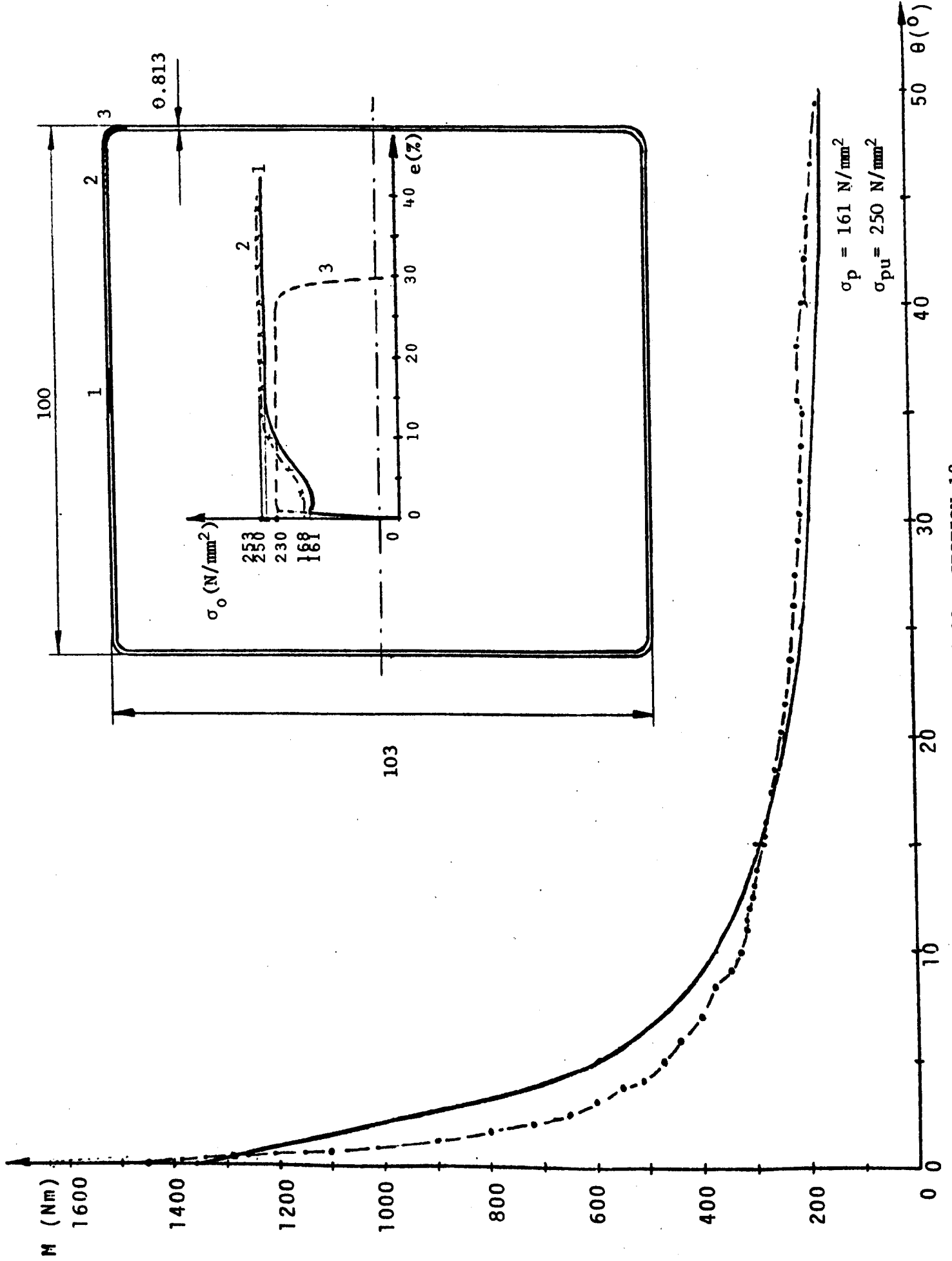


Fig. 6.33 - SECTION 18

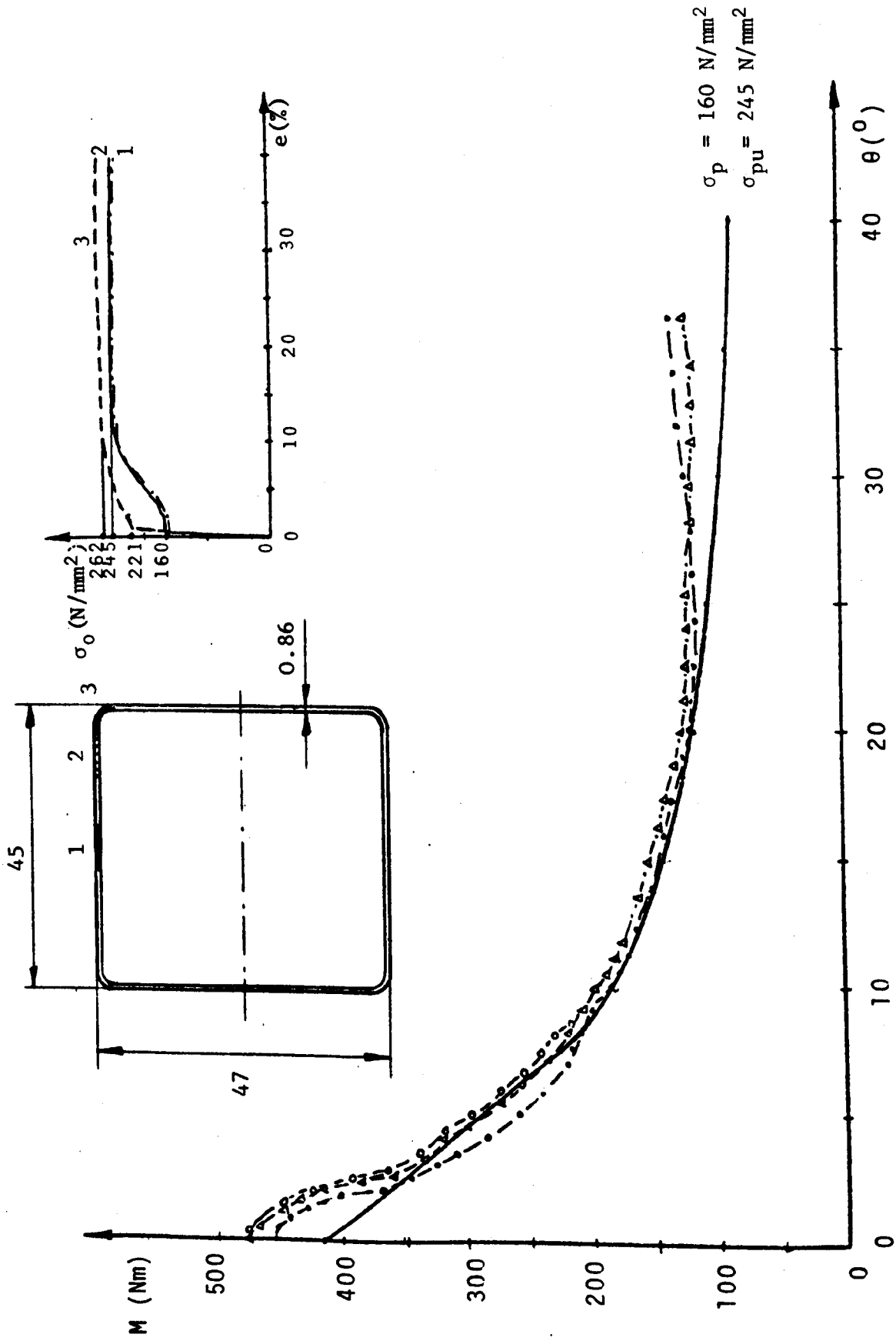


Fig. 6.34 - SECTION 19

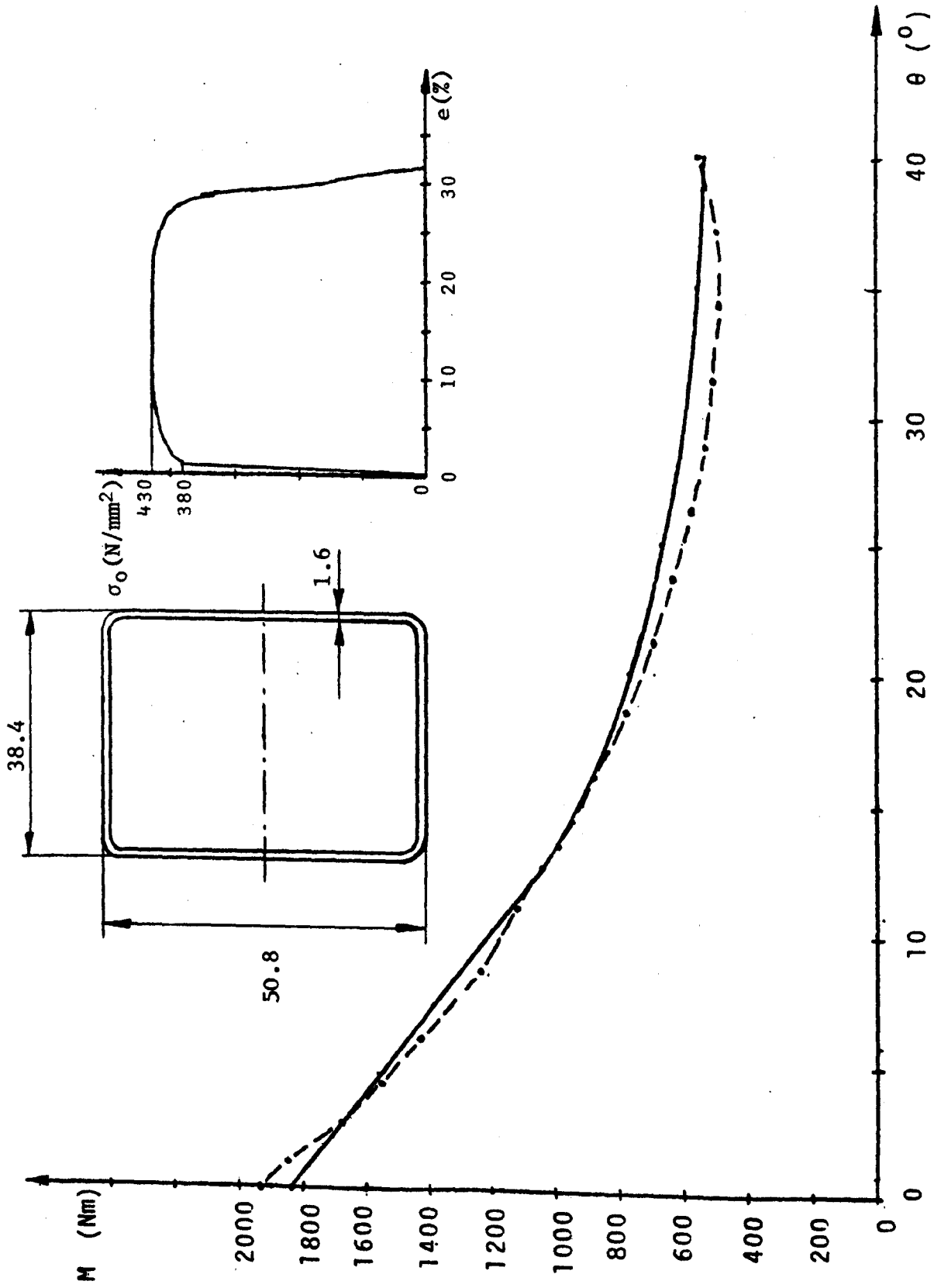


Fig. 6.35 - SECTION 20

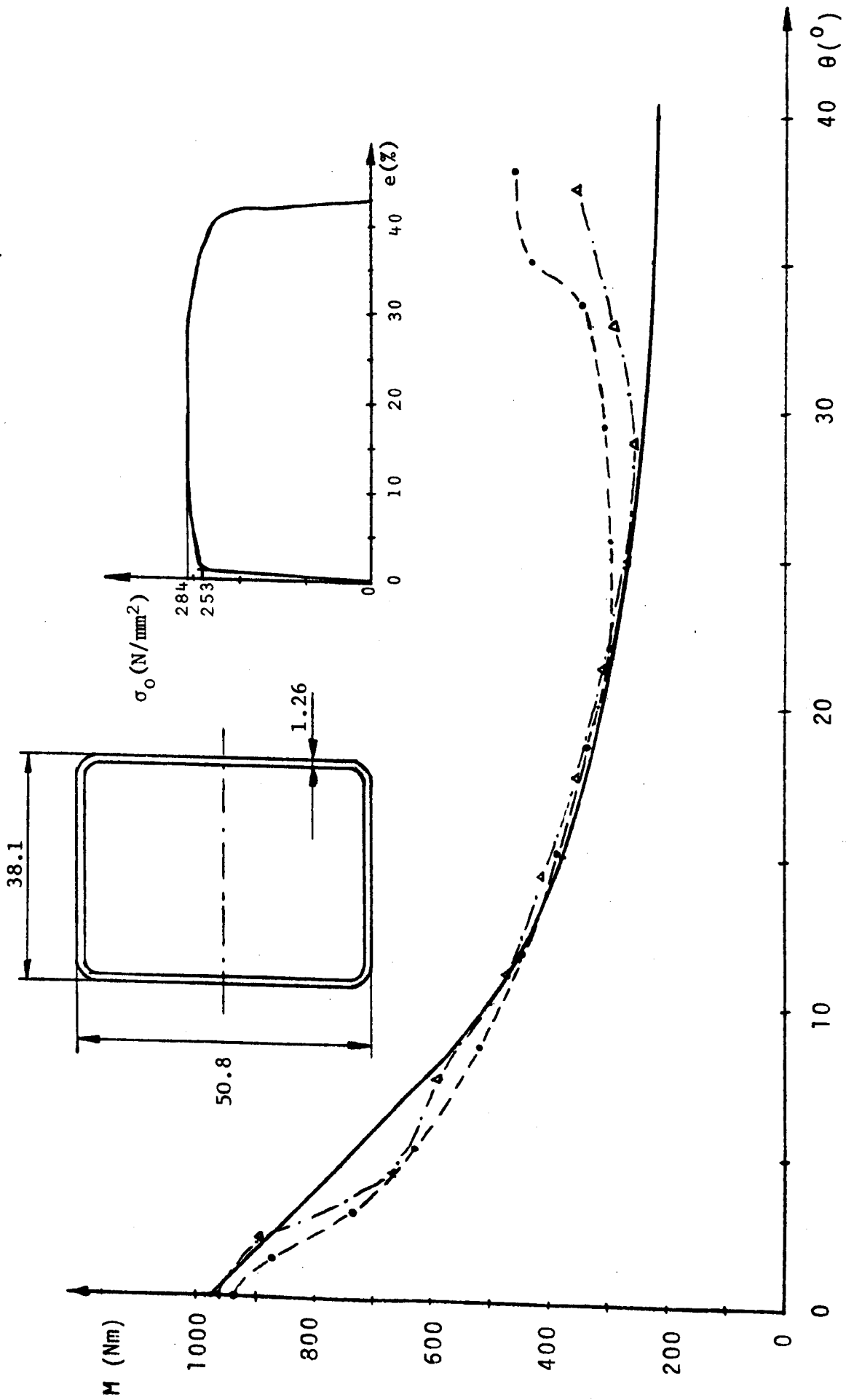


Fig. 6.36 - SECTION 21

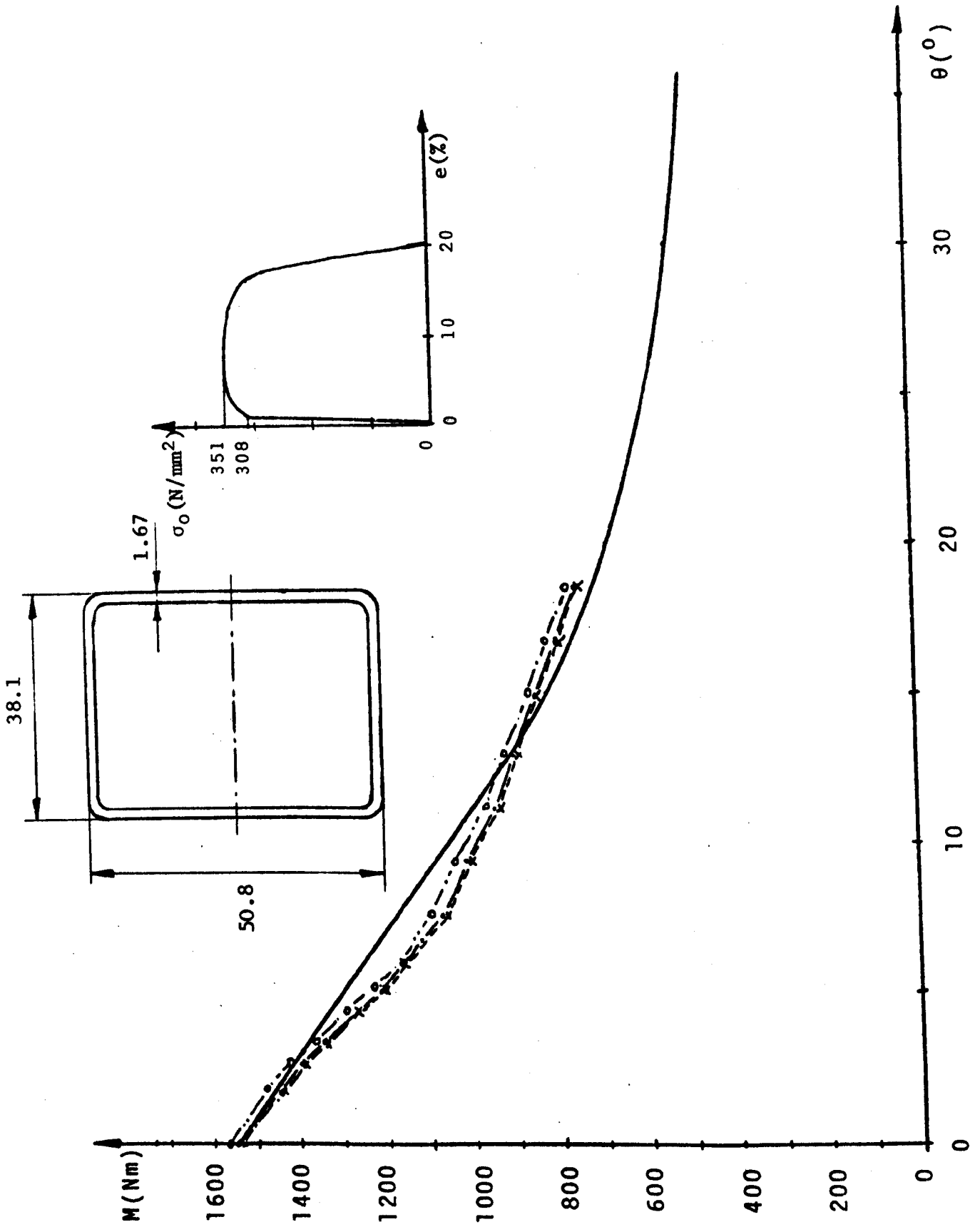


Fig. 6.37 - SECTION 22

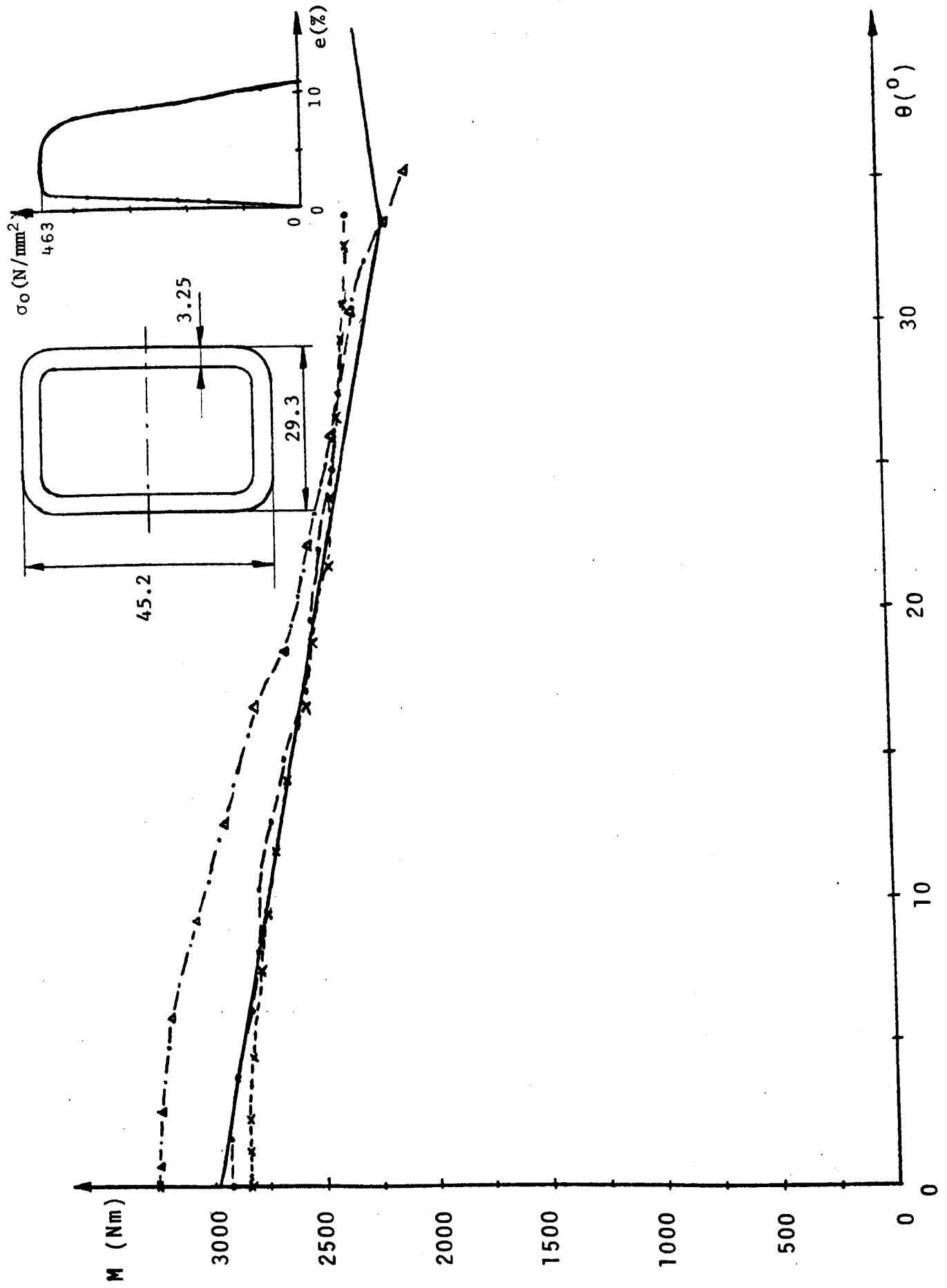


Fig. 6.38 - SECTION 23

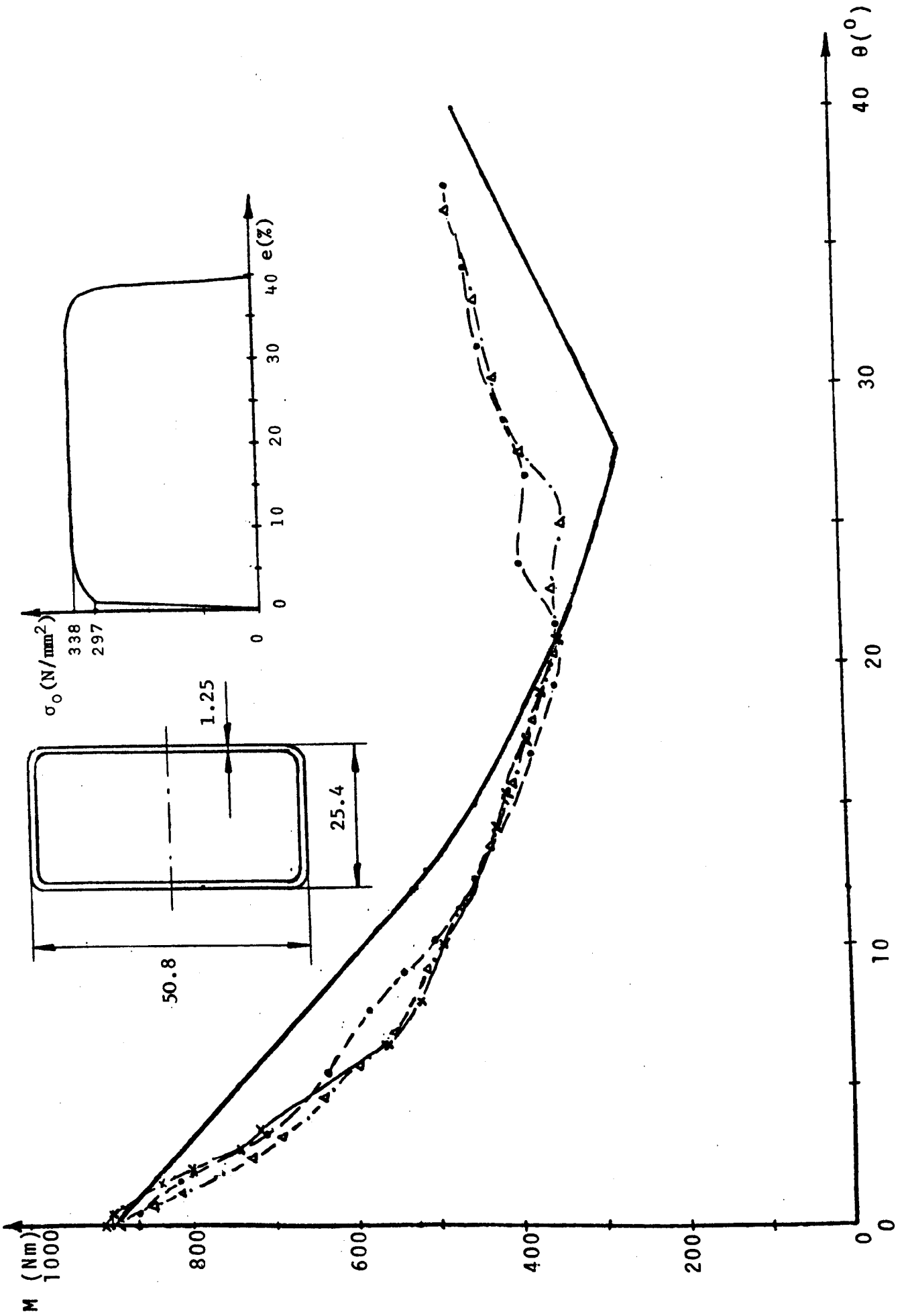


Fig. 6.39 - SECTION 24

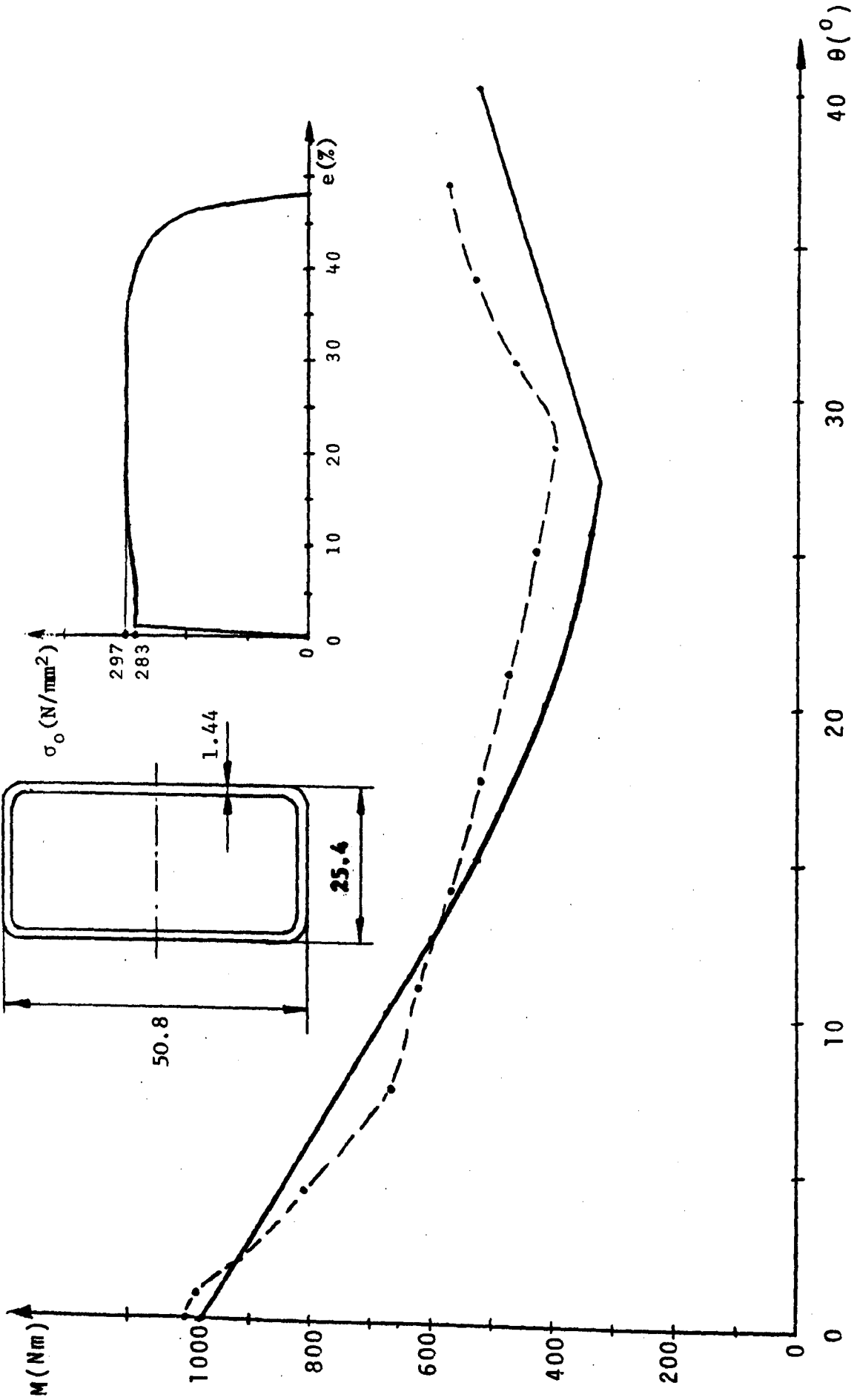


Fig. 6.40 - SECTION 25

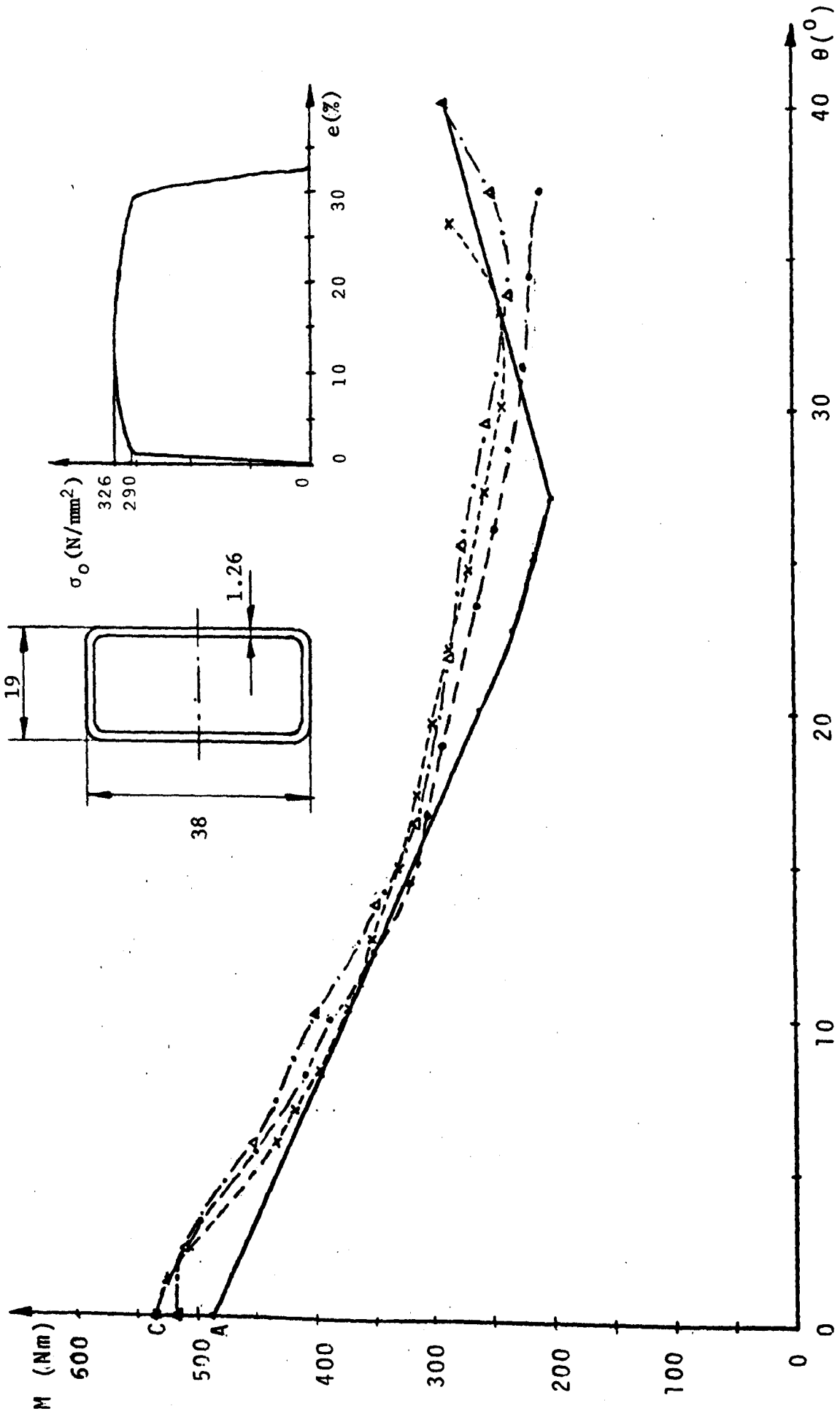


Fig. 6.41 - SECTION 26

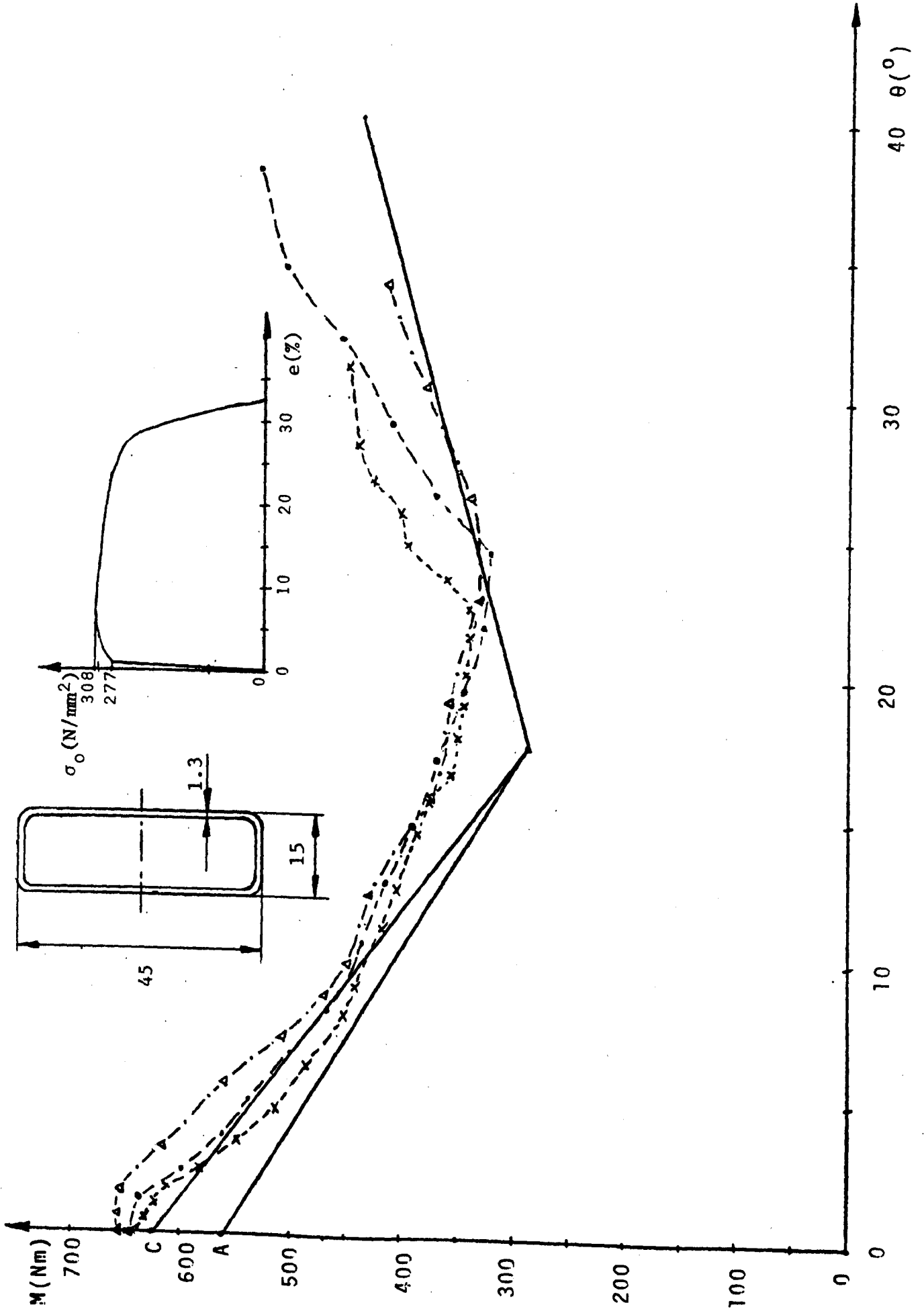


Fig. 6.42 - SECTION 27

In order to provide a quantitative assessment of the agreement between the theoretical and experimental results the hinge moments and energies absorbed were compared at 0, 10, 20, 30 and 40 degrees of rotation. Experimental results were taken as average values of the tests on a particular section. If the theory predicts a reasonably accurate maximum strength, then the energy absorbed may also be used as a convenient indicator of the agreement between the theoretical and experimental variation over a range of angles θ . The energies cannot be read easily from the diagrams, and are listed in Table 6.2. The maximum angle of hinge rotation did not reach 40° in some tests. An approximate experimental quantity was used in cases where a reasonable estimate could be made - numbers in parenthesis in Table 6.2, otherwise the spaces are left blank.

Each of the 27 section types in Table 6.1 was considered as one separate case, and the frequency of various ratios (R) between the theoretical and experimental results is shown by histograms in Fig. 6.43 which are obtained from the table of the Appendix 4. The left column in Fig. 6.43 corresponds to the moments and the right one to the energies absorbed.

6.6.2 The Maximum Strength Prediction

In 90% of the cases the theoretical maximum strength was within $\pm 10\%$ of the experimental results (Fig. 6.43). Such a good agreement may be partly due to the fact that most of the tubes developed fully plastic moments, but even the ones which buckled elastically (sections 10, 11, 18) gave agreement within less than 10%.

Underestimates that occurred in sections 26 and 27 (points A in Figs. 6.41 and 6.42) can be explained by the fact that the narrow flanges were strain-hardened by the manufacturing process, while the parent material in the middle of the webs used for the tensile tests was in the vicinity of the plastic neutral axis. If σ_{pu} is used to calculate M_{max} a much better agreement (points C in both figures) is obtained. A similar argument explains the good agreement for the same tubes bent about their weaker axes (Figs. 6.16 and 6.19). Some underestimate also occurred in sections which strain-harden rapidly (Figs. 6.30 and 6.31), or have a lot of pre-straining in the compression flange (Fig. 6.29). The case in Fig. 6.34 is more difficult to explain.

Overestimate in section 2 (Fig. 6.17) is probably due to a more than average yield and maximum strength of the tensile test specimen, as will be explained in the next section on the energy absorption. A similar tendency was present in sections 8 and 21 where 8% variation in material properties was observed (Appendix 3).

The maximum overestimate of 10.8% (section 11 in Fig. 6.26) was probably due to the rather irregular geometry of that tube.

A good agreement was obtained for tube 12 (Fig. 6.27), but the two other nominally identical specimens in the same diagram were considerably stronger. Their material properties were not tested, and the assumed values $\sigma_p = \sigma_{pu} = 400 \text{ N/mm}^2$ gave a good agreement, but were not further considered in the current analysis. The same results are also listed in the Table of the Appendix 4.

Table 6.2

The Experimental and Theoretical Energies Absorbed in Hinges*

θ [deg]	10		20		30		40	
Section Number	W_{exp} [J]	W_{th} [J]	W_{exp} [J]	W_{th} [J]	W_{exp} [J]	W_{th} [J]	W_{exp} [J]	W_{th} [J]
1	36	38	61	65	81	85	98	102
2	65	76	105	119	133	151	159	178
3	80	85	133	135	175	172	208	203
4	45	45	75	76	99	99	118	119
5	108	110	183	180	240	231	288	274
6	368	362	675	694	938	995	(1170)**	1263
7	101	101	178	174	236	229	284	275
8	93	107	145	162	187	202	214	236
9	198	213	318	340	398	433	457	511
10	93	102	135	146	166	178	201	205
11	83	116	127	166	163	202	-	232
12	186	196	298	313	379	398	(471)	470
13	170	178	288	291	378	374	(451)	443
14	286	282	482	487	616	638	716	765
15	307	296	510	512	677	674	(817)	809
16	73	67	130	121	177	163	214	198
17	117	114	218	216	315	305	-	381
18	100	121	147	173	188	210	223	241
19	52	50	75	76	97	94	(119)	109
20	260	264	423	428	537	546	611	643
21	120	126	186	194	230	242	(293)	282
22	219	226	368	372	-	476	-	562
23	508	498	980	953	1392	1364	-	1749
24	114	130	185	208	248	261	(325)	328
25	136	144	234	235	307	297	(397)	373
26	81	75	138	130	183	168	(225)	213
27	94	84	160	142	222	200	(300)	271

* Numbers are rounded off to the nearest integer.

** Numbers in parentheses indicate estimated values.

HINGE MOMENT

$$R = \frac{\text{Theoretical result}}{\text{Experimental result}}$$

ENERGY ABSORBED

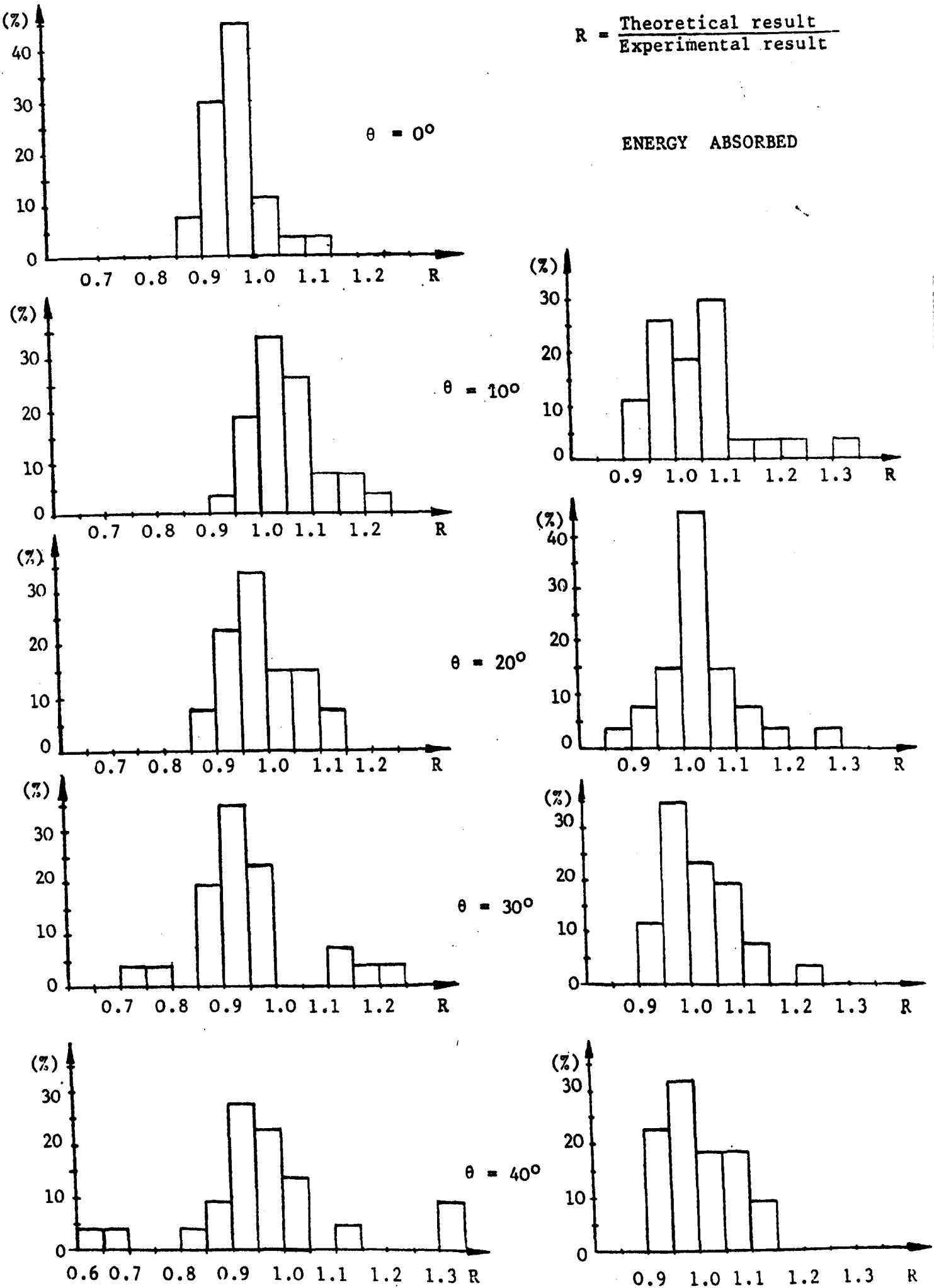


Fig. 6.43

6.6.3 Prediction of the Moment Variation and Energy Absorbed

The theory gave a very good qualitative and quantitative prediction of the moment variation for the whole range of tubes tested, and that includes such different cases as, for example, sections 18 (Fig. 6.33) and 23 (Fig. 6.38). This is particularly important since all the theoretical results are based on a common calculation procedure.

The theory has some tendency to overestimate the load carrying capacity and energy absorption of beams within the first 10° of hinge rotation, for reasons explained in section 6.4. However, this overestimate was generally within 10% (Fig. 6.43) and the main exceptions were the very thin walled, handmade tubes 11 and 18 (Figs. 6.26 and 6.33). The disagreement in these tubes was probably due to a relatively slow but extensive strain-hardening which developed fully after $\theta = 10^\circ$ (compare with Fig. 6.9). Geometry imperfections could have contributed as well, because the agreement for section 10 (Fig. 6.25) was much better. All these three sections make very poor energy absorbers in bending, and the theory shows that clearly.

The other overestimates of more than 10% occurring in one tube type bent about both axes (sections 2 (Fig. 6.17) and 24 (Fig. 6.39)) are likely caused by the fact that the appropriate tensile test specimen was stronger than average. A similar reason may have contributed to the overestimate in section 9 (Fig. 6.24).

The agreement between the theoretical and experimental moment variation during the second stage of hinge collapse was generally within 10% (Fig. 6.43). Extensive material separation on one side of section 14 (Fig. 6.29) may have caused somewhat lower hinge strength after $\theta=17^\circ$.

The theory underestimates moments when θ is less than but close to the angle of hinge jamming θ_j (sections 21, 24 + 27), but the angle θ_j is predicted reasonably well (Figs. 6.39 + 6.42). The empirical function (6.46), describing the strength increase during development of the secondary hinge, is not equally successful in all sections and tends to be conservative. Change of collapse mechanism at the end of second phase of hinge collapse is the main reason why the accuracy of the method becomes somewhat less at $\theta > \theta_j$ (Fig. 6.43).

The agreement between the theoretical and experimental energies absorbed after the first stage of collapse is generally within 10 + 15% (Fig. 6.43). The initial small overestimate was often cancelled by subsequent underestimate and that improved the general accuracy of prediction.

6.6.4 A Comment on the Accuracy of the Theory Presented

The accuracy of a theoretical method can be assessed in relative or absolute terms. Relatively speaking, the theory of hinge behaviour presented in this thesis is acceptable because it produces reasonable agreement with experiments and because a better theory does not seem to be currently available.

The accuracy required in absolute terms depends on various circumstances regarding the structure whose collapse characteristics are being

investigated. The accuracy of the method presented should be considered allowing for:

- a. Production tolerances regarding material properties;
- b. Tolerances regarding the manufacturing process of the structure itself;
- c. Level to which the structure is idealised by the finite element model;
- d. Reserve of strength and energy absorbing capacity required.

Production tolerances for the basic material and components are directly related to their price, and it is unlikely that any major changes in this respect may be expected in the near future. In the author's experience, relative variation of σ_p and σ_{pu} in the parent materials of nominally identical standard tubes may easily be as high as 10%. Local differences may be even greater, but they have less effect on the average hinge behaviour, provided that no significant material separation occurs.

Structures are generally manufactured by putting components together and the strength of joints becomes therefore a very significant factor affecting the collapse performance. Bearing in mind the possible variations in properties of most man-made vehicle structures, it is important to design joints which would be stronger than the beams they are connecting under any circumstances.

The theory of hinge behaviour will be combined with the CRASHD program and the final results will be also affected by the level of the finite element idealisation of the actual structure and by the accuracy obtainable by the program (see sections 3.4 and 7.4). The theory would be particularly useful in the early stages of design, when it can provide very important guidelines rather than exact estimate of the final collapse performance. In any case it is desirable to make the safety structures as simple as possible because simplicity often implies better controllability and reliability.

Reserve of strength and energy absorbing capacity of a collapsing structure involves a "factor of ignorance" which should allow for most of the uncertainties of the design process. It should be bigger in structures which may be subject to a greater variety of loading conditions and also in those which have a higher relative responsibility in providing passive safety (in some cases a part of this responsibility is taken by other auxiliary devices such as safety belts).

Although further refinements of the theory are possible, the author believes that the calculation presented already provides sufficient accuracy for application within the framework described above. The use of minimum guaranteed material properties usually contains a "factor of safety" against any significant overestimate of the actual collapse performance. Should a necessity arise, the easiest way of making the theory more conservative is to increase the coefficient 0.07 in equation (6.36) to 0.075 or, say, 0.08.

7.1 INTRODUCTION

The theory of hinge behaviour, developed and verified earlier in the thesis, can be used

- a. to optimise section dimensions from the safety point of view;
- b. to provide the hinge characteristics required by the CRASHD program for the collapse analysis of structural frameworks.

This gives an opportunity to predict the collapse behaviour of frameworks composed of rectangular or square section tubes entirely theoretically, i.e. without testing any of the structural components, and also to minimise the weight of the structure meeting some safety criteria.

The theory is still limited to cases where beams collapse in uniaxial bending, but it is believed that the principles used in this work can be extended to the more general situation of biaxial bending as well.

7.2 OPTIMISATION OF SECTION DIMENSIONS FROM THE SAFETY POINT OF VIEW

Optimisation of a vehicle structure has to allow for various functional tasks, manufacturing problems, economic reasons, etc. However, the passive safety requirements should be, ideally, met by the lightest possible structures.

The safety criteria may concern any one or all of the following:

- a. maximum strength;
- b. energy absorbed during a given hinge rotation;
- c. strength remaining after a given hinge rotation.

Tubes with smaller ratio a/b are "deeper" and offer higher collapse characteristics for the same section area. However, too small ratio a/b may make the tube too weak in bending about the other principal axis and small variations in the direction of the external load may produce an unexpected collapse mode with much less resistance. The minimum ratio a/b depends therefore on the variety of impact loading conditions and on other design requirements. A square section tube may be necessary in some places in spite of the fact that this shape does not provide an optimum performance when bent about one axis.

Although the theory does not give a direct answer to the design of the lightest section meeting a specific safety requirement, an accurate result can be obtained by formulating the problem as one of constrained optimisation. The way to organise this iterative calculation is as follows:

1. Design criteria are specified;
2. Material is selected, i.e. σ_p and σ_{pu} are assumed;

3. Constraints concerning the section geometry are given, e.g.:
 $a = k \cdot b$, t_{\min} , a_{\max} , etc.;
4. Theoretical hinge moment - rotation curve is used in an iterative numerical process producing a square or rectangular section of minimum area, satisfying criteria 1 and constraints 2 and 3 above.

Mathematical interpretation of the problem yields the following equations:

The objective function to be minimised is:

$$\text{Area} = 2t [a + (b - 2t)], \quad (7.1)$$

subject to the geometry constraint:

$$a = k \cdot b \quad (7.2)$$

and constraint(s) governed by one or more of the following safety criteria:

$$M_{\max} \geq SMAX \quad (7.3)$$

$$W(WTH) \geq ENER \quad (7.4)$$

$$M(WTH) \geq STREN \quad (7.5)$$

where SMAX, ENER and STREN are, respectively, the specified values of the maximum strength, energy absorbed and remaining strength after a given hinge rotation WTH.

The most economical manner of solving a particular optimisation problem may require different approaches and three possibilities are given below.

The first method combines information supplied by the computer with a graphical procedure presented in Fig. 7.1. Assume, for example, that a designer wants to obtain the lightest square section tube ($k = 1$ in (7.2)) made of the same material as tube 13 in Table 6.1 and Fig. 6.28, and with the following safety criteria: $SMAX = 1216 \text{ Nm}$ (Fig. 6.28), $ENER = 150 \text{ J}$ and $STREN = 150 \text{ Nm}$ at $WTH = 30^\circ$.

The shape of the section is assumed, so that the area (7.1) becomes a function of two variables only: a and t . It is therefore possible to plot the constant area curves in the $a - t$ system in Fig. 7.1. The section area is represented by the surface starting from the a and t axes and the constant area curves are the contour lines of this surface.

The program OPT1 is now used to define the safety constraint boundaries I, II and III in Fig. 7.1. Discrete points on curve I are calculated by taking arbitrary dimensions a and finding the appropriate values of t (and areas), satisfying the safety constraint (7.3). This is achieved by employing a relatively inexpensive to use standard NAG library subroutine CO5AAF for finding the zero of an arbitrary continuous function. Sections below curve I cannot meet the condition of $M_{\max} = 1216 \text{ Nm}$. Curves II and

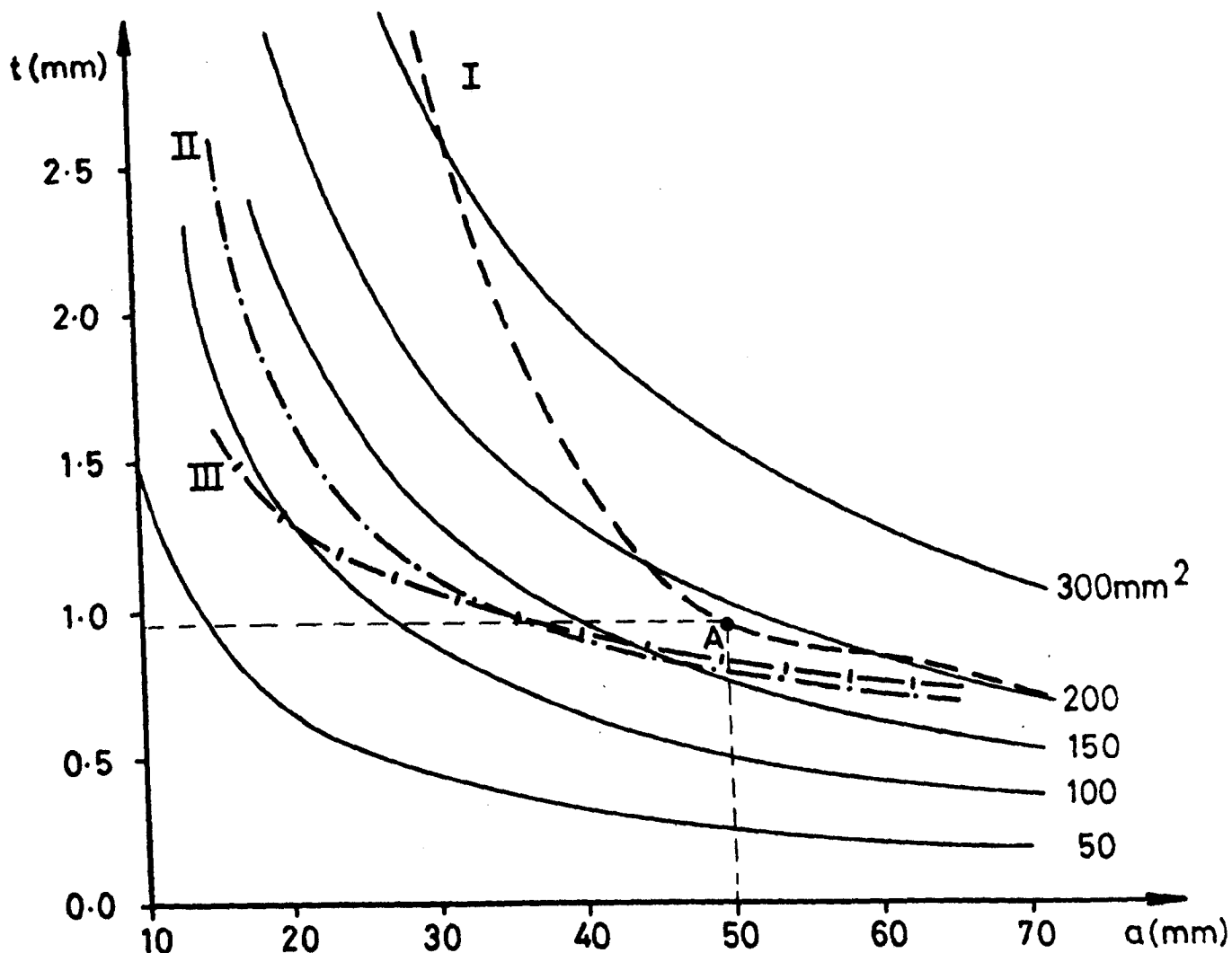


Fig. 7.1

III are obtained in a similar way by using the energy or remaining strength conditions, respectively.

The lightest section meeting all the safety criteria corresponds to the lowest point on the area - surface which does not fall below any of the boundary curves I, II or III. This point is in the vicinity of the point A in Fig. 7.1 with $a = b = 50$ mm, $t = 0.974$ mm and $A = 191.09$ mm². The exact value is difficult to determine because the boundary I and constant area curves are almost parallel in the most interesting region. However, the accuracy of this semi-graphical method is sufficient if the section is to be selected from the range of the available standard dimensions. The nearest, metric size section would be 50 x 50 x 1 mm with an area of 196 mm, which is 17% lighter than section 13 in Table 6.1 of the same shape, material and maximum strength.

The second program (OPT2) minimises the area of the section if only one of the three possible safety criteria (7.3) to (7.5) is specified. It starts from an arbitrary point above the appropriate boundary curve (Fig. 7.1) and solves equations (7.1), (7.2) and one of the safety

criteria for the unknown dimensions a , b and t , i.e. finds the intersection between the given constant area curve and the appropriate boundary line nearest to the guessed solution. The program uses the standard NAG library subroutine COSNAF for solving a system of n equations in n unknowns. The area is then reduced, new point calculated, etc., so that the solution moves along the boundary line to the minimum area point. Calculation stops when the current area falls below the actual minimum and no real solution for section dimensions can be found. The accuracy is controlled by the area reduction coefficient used in the last iteration. Program OPT2 produced the following solution to the example in Fig. 7.1: $a = b = 50.139$ mm and $t = 0.97$ mm, giving 19% weight reduction in comparison with section 13 in table 6.1. The last reduction was 1%, so that the lightest possible section cannot save 20% of the weight of section 13.

The third program (OPT3) minimises the area (7.1) of the section if any one, two or all three safety criteria (7.3) to (7.5) are to be used. The current version of the program uses the geometry constraint (7.2), but other forms of geometry constraints can be included very easily. No derivatives of the constraint functions (7.3) to (7.5) with respect to a and t can be provided, so that the NAG library subroutine EO4UAF for a non-linear constrained optimisation is used. Optimisation with respect to one or two safety criteria only is achieved by giving a relatively small value to the safety parameter(s) which are unimportant. Accuracy is controlled by the appropriate parameters in EO4UAF.

Consider a case allowing for all the three safety criteria, and let all of them correspond to section 13 (Tables 6.1 and 6.2 and Fig. 6.28): $k = 1$, $\sigma_p = 374$ N/mm², $\sigma_{pu} = 390$ N/mm², $S_{MAX} = 1216$ Nm, $WTW = 300$, $ENER(WTW) = 374$ J and $STREN(WTW) = 430$ Nm. These figures are rounded off, but a minimum weight section should still be very close to section 13. Program OPT1 has produced the three boundary curves I, II and III in Fig. 7.2 which intersect at a common point A defining almost exactly the actual dimensions of section 13: $a = b = 38.4$ mm and $t = 1.6$ mm. Solution obtained by the program OPT3 was: $a = b = 38.26$ mm and $t = 1.613$ mm, which is also very close to section 13 and gives an area increase of 0.3% only.

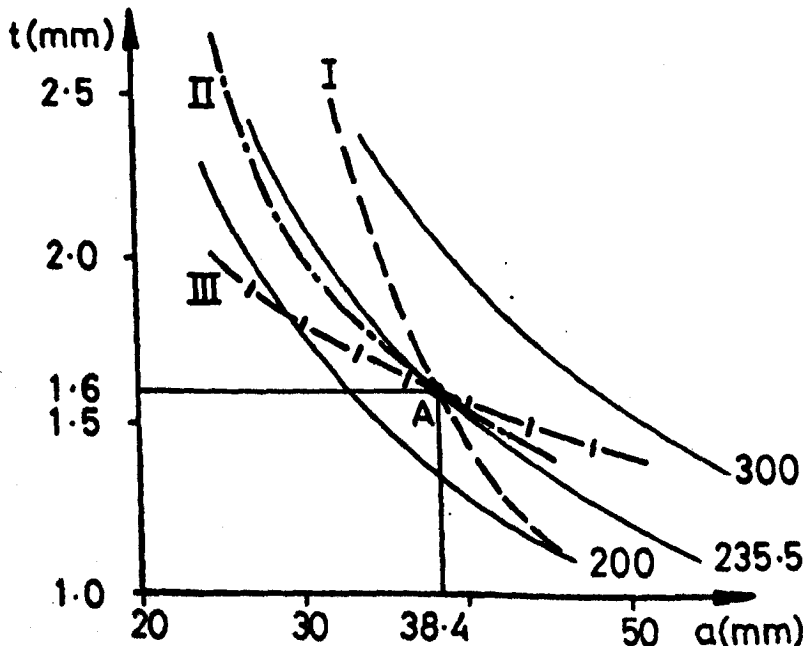


Fig. 7.2

Program OPT3 is most general and does not require any graphical aid. It is, however, by far more expensive to use than OPT1 or OPT2 and is also more sensitive to numerical ill-conditioning. Scaling of variables, objective (7.1) and constraint functions (7.3) to (7.5) has been undertaken in OPT3, but this could not always eliminate ill-conditioning during the first run on a particular problem. For example, solution to the optimisation problem in Fig. 7.2 was obtained quickly because the minimum point A is well defined by the intersection of boundary curves I and III. The minimum in Fig. 7.1 is very "flat" because the boundary curve I is almost parallel to the constant area lines in the "critical area". The results of the two monitored trial runs indicated, according to the NAG manual, that "progress has been made" but further adjustment of the appropriate parameters was necessary. This manual is an essential aid when using the program OPT3.

Further reduction in weight of section 13 could be achieved by assuming a smaller ratio a/b . For example, if $k = 0.5$, the maximum strength of 1216 Nm can be obtained (solution by OPT2) by a section with $a = 36.468$ mm, $b = 72.875$ mm and $t = 0.73$ mm. This section is 33% lighter than 13, but has a very rapid moment drop off undesirable in energy absorbing components.

Weight minimisation allowing for the maximum strength only tends to produce tubes with relatively thinner walls (bigger a/t ratio) than if energy absorbed and/or remaining strength are specified. Reduction of the wall thickness in the first case is limited by the flange stability and the theory allows for that effect. It should be borne in mind, however, that maximum bending strength of thin walled tubes may be reduced very much by a local dent, produced by an impact prior to bending collapse (e.g. waist rail or cant rail hitting the ground). Thicker walled tubes are less sensitive to the effect of initial deformations.

The optimisation presented here refers to rectangular or square section tubes only. Further improvements may be possible by using other shapes, multicell tubes, section fillings (e.g. as in Fig. 4.4a), or even joints that would act as better energy absorbers. However, these possibilities fall beyond the scope of this thesis.

7.3 COMBINATION OF THE THEORY OF HINGE BEHAVIOUR WITH THE PROGRAM CRASHD

A detailed description of the program CRASHD can be found in ref. 23 and some basic information was given in Chapters 1 and 3 of this thesis. The program increments external loads or displacements in prescribed steps until either the maximum strength or the maximum desired deflection is reached. An elastic calculation within each step is performed using the current structural stiffness matrix assembled of the normal and geometric stiffness matrices of the beam elements. The overall stiffness matrix is updated after each step to allow for the change in geometry and occurrence of plastic hinges which are inserted at those beam ends where local, internal loads violate a predetermined failure criterion. If a hinge maintains its moment during collapse, insertion of a pin-joint (i.e. transformation of the appropriate element stiffness matrix) is accompanied by the addition of fully plastic moments M_p and associated shear forces Q_p to the corresponding elements of the internal load vector. The load-displacement equation of a beam in local co-ordinates becomes:

$$\{p\} = [K] \cdot \{d\} + \{Q\} \quad (7.6)$$

where $\{p\}$ and $\{d\}$ are the beam end loads and displacements respectively;
 $[K]$ is the updated stiffness matrix of the element after a hinge
 has been inserted at one or both of its ends;
 $\{Q\}$ is the constant additional load vector containing M_p and Q_p
 loads.

Matrix $[K]$ is used in the updated overall stiffness matrix in the usual way and vector $\{Q\}$ is added, after transformation into global co-ordinates, to the vector of external loads. Elements of vector(s) $\{Q\}$ are internal loads and their sum in global system can create no extra, unbalanced external load (occurrence of brittle fractures is different in this respect (23), but does not fall within the scope of this thesis).

The new system of equations, including the updated stiffness matrix and load vector, is then solved to give the increments of node displacements and external reactions. Displacement increments are used to calculate the increments of internal loads which are then added to the previous ones and the cumulative values of external reactions and internal loads are obtained. A new search for hinges is made, new stiffness matrix is assembled, etc., until the final state is reached. In this way the program does not allow for the possibility of elastic unloading in a previously plastic zone as loading progresses. It is reasonable to expect, however, that the main hinges determining the eventual collapse mode of the structure continue to rotate during the entire collapse process and do not unload elastically.

The moment drop-off characteristic of thin walled members is reproduced by replacing the pin-joint at a hinge by a rotary spring which exhibits the same drop characteristic or negative stiffness as the beam itself. Such a "compound beam element" with a rotary spring at the end 2 is shown in Fig. 7.3a and the $M-\theta$ curve that it should produce in Fig. 7.3b.

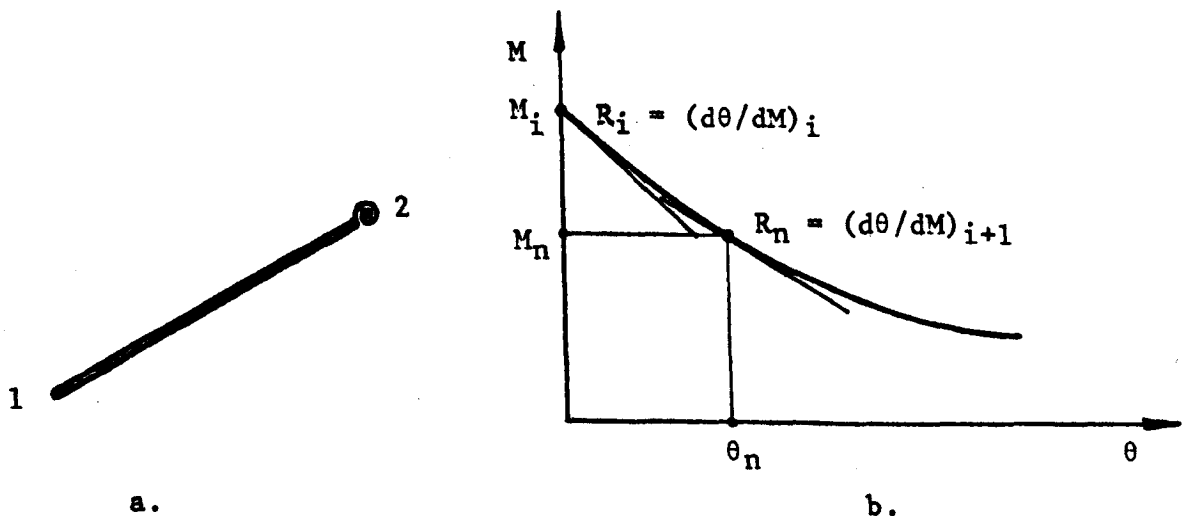


Fig. 7.3

The stiffness matrix of a compound beam element is derived using the approach suggested by Livesley (98). If the stiffness matrix of the

beam is separated into sub-matrices corresponding to ends 1 and 2, so that

$$\begin{Bmatrix} P_1 \\ P_2 \end{Bmatrix} = \begin{bmatrix} K_{11} & K_{12} \\ K_{21} & K_{22} \end{bmatrix} \cdot \begin{Bmatrix} \delta_1 \\ \delta_2 \end{Bmatrix} \quad (7.7)$$

it can be shown (98) that sub-matrices K_{11} , K_{12} and K_{21} can be expressed in terms of K_{22} using a known "equilibrium matrix" $[H]$ which is a function of the beam length. This has been used by Livesley to derive the stiffness matrix of a beam with finite stiffness joints. Miles (23) has employed the same principle to derive the sub-matrix K_{22} of the "compound beam" considered here in the form:

- If the springs are at both ends of the beam:

$$K_{22} = \begin{bmatrix} \frac{1}{\frac{L}{AE} + \frac{1}{K_1} + \frac{1}{K_2}} & 0 & 0 \\ 0 & \frac{\frac{L}{EI} + R_1 + R_2}{Z_3} & -\frac{(\frac{L^2}{2EI} + LR_1)}{Z_3} \\ 0 & \frac{\frac{L^2}{2EI} + LR_1}{Z_3} & \frac{\frac{L^3 R_1}{3EI} + L^2 R_1}{Z_3} \end{bmatrix} \quad (7.8)$$

where: E , A , I and L are the Young's modulus, section area, moment of inertia and beam length respectively;

$R_1 = (d\theta/dM)_1$ = flexibility of the spring at end 1;

$R_2 = (d\theta/dM)_2$ = flexibility of the spring at end 2;

$Z_3 = (L^3/3EI + L^2 R_1)(L/EI + R_1 + R_2) - (L^2/2EI + LR_1)^2$

K_1, K_2 = axial stiffness of springs at end 1 and 2 respectively.

Experimental evidence has shown that the effect of K_1 and K_2 can be simulated by multiplying the axial stiffness term AE/L of the beam by 0.04 if the spring occurs at one end or by 0.02 if the springs are attached to both ends of the beam.

Matrices K_{22} , similar to (7.8) can be derived (23) for cases where springs are attached to either end 1 or end 2 of the compound beam.

Let the hinge with a spring be introduced at a node after the i -th increment of calculation. The initial value of the spring flexibility (R_1 or R_2) will be proportional to the slope of the $M-\theta$ curve at $\theta=0$ (Fig. 7.3). At the end of the $i+1$ st step the moment at the same place will be $M_n = M_{i+1} < M_i$ (Fig. 7.3). The new value of R for the $n+1$ step is calculated in the following manner: the program calls subroutine "COIL" which uses the moment $M_n = M_{i+1}$ to find the appropriate θ_n from the known relationship $M_n = M(\theta_n)$. The angle θ_n is then used in subroutine "REAL FUNCTION CURV (THETA)" to calculate the tangent to the $M-\theta$ curve at the

point $\theta = \theta_n$, which is inversely proportional to R_n . The $n + 1$ st step of calculation is performed with the new $R = R_n$ in the stiffness matrix of the compound element considered.

In the original version of the program CRASHD the $M - \theta$ curve (Fig. 7.3) was defined as an exponential function (equation (1.4) in Chapter 1):

$$M(\theta) = A + Be^{-c\theta} \quad (7.9)$$

where constants A , B and c were selected to approximate the experimental $M - \theta$ curve obtained by bending collapse tests similar to those described in Chapter 6. The tests reported in (23) did not exceed $\theta \approx 10 + 15^\circ$ and did not allow for the further moment drop off and occurrence of the secondary hinge. Both the angle θ and spring flexibility could be obtained directly from or after differentiation of the equation (7.9).

The new subroutines "COIL" and "CURV" make use of the theoretical $M - \theta$ curve in the form summarised in section 6.4. The input data to the program are the usual parameters required for the elastic analysis, section dimensions a , b , t and material properties σ_p and σ_{pu} . The hinge is initiated after the local moment exceeds the maximum strength M_{max} calculated as in section 6.4. Some overshoot of M_{max} is inevitable so that the program follows actually the dotted, rather than solid curve in Fig. 7.4. This overshoot is negligible if the load or displacement increments are made sufficiently small. Subroutines COIL and CURV are then called to calculate the initial value of the spring flexibility R_i . Both subroutines in their current forms assume an angle step $\theta_s = 1^\circ$ and determine the characteristic points T, J and E on the theoretical $M - \theta$ curve (Fig. 7.4) as described in section 6.4.

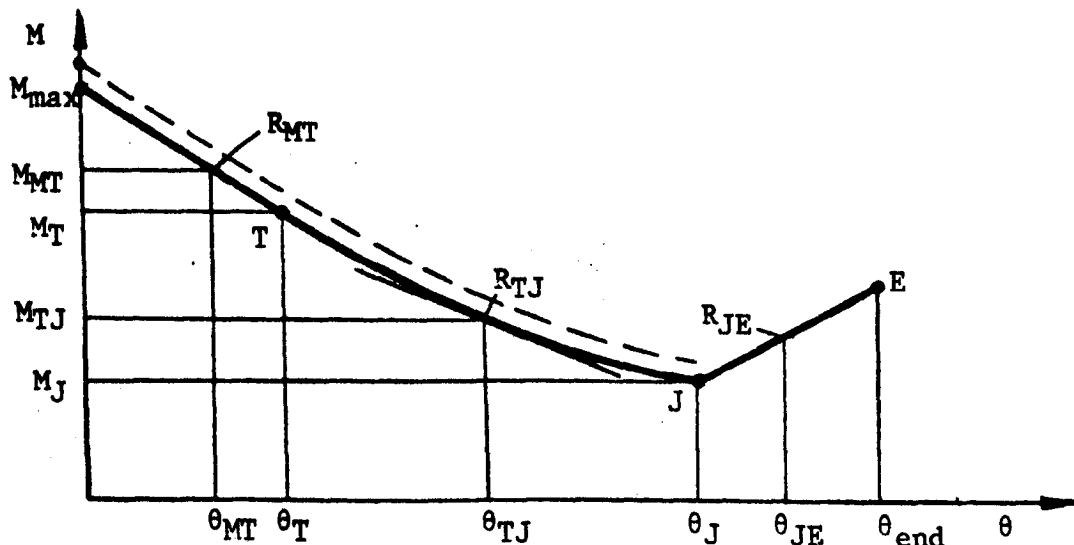


Fig. 7.4

The initial angle θ is set to zero after the first call of subroutine COIL, and the new subroutine CURV produces the initial value of the spring flexibility:

$$R_i = R_{MT} = \frac{d\theta}{dM} = \frac{\theta_T}{M_T - M_{max}} = - \frac{\theta_T}{M_{max} - M_T} \quad (7.10)$$

This is used in assembling the new stiffness matrix, so that the next calculated moment becomes less than M_{max} . If the new moment is still greater than M_T , the angle θ_{MT} is determined from:

$$\theta_{MT} = \frac{M_{max} - M}{M_{max} - M_T} \cdot \theta_T \quad (7.11)$$

and subroutine CURV produces the same flexibility as in (7.10).

If the new moment satisfies $M_J < M < M_T$ (Fig. 7.4), the appropriate angle θ_{TJ} is calculated from the basic theoretical $M - \theta$ curve by an iterative numerical process employing the standard NAG library subroutine C05AAF. This angle is then fed into the subroutine CURV which calculates the hinge moments $M_1 = M(\theta_1) = M(\theta_{TJ})$ and $M_2 = M(\theta_2) = M(\theta_{TJ} + 0.1^\circ)$ in the usual manner. The spring flexibility is then determined as:

$$R_{MT} = \frac{\Delta\theta}{\Delta M} = \frac{0.1 \cdot \pi}{180 \cdot (M_2 - M_1)} = - \frac{0.1 \cdot \pi}{180 (M_1 - M_2)} \quad (7.12)$$

At some stage of collapse the angle M , calculated in the main body of the program may fall below the minimum hinge moment M_J corresponding to the angle of hinge jamming θ_J (Fig. 7.4). When that happens the hinge angle is set to an arbitrary value between θ_J and θ_{end} and a "jamming indicator" JIND changes its initial value set at the beginning of calculation. This diverts the calculation of the spring flexibility in subroutine CURV and produces the new, positive, value corresponding to the empirical equation (6.46):

$$R_{JE} = \frac{\Delta\theta}{\Delta M} = \frac{\theta_{end} - \theta_J}{M_{end} - M_J} \quad (7.13)$$

The last equation may, of course, be different, depending on the type of function $M_{JE}(\theta)$ describing the behaviour of the secondary hinge. If a non-linear function is taken, the appropriate angle θ_{JE} would have to be found exactly after assuming the first θ_{JE} close, but greater than θ_J . The jamming indicator would switch the subroutine COIL to the new function $M_{JE}(\theta)$. In this way the new version of the program CRASHD can allow for the complete theoretical $M - \theta$ curve, including the strength increase following the onset of the secondary hinge.

7.4 THEORETICAL PREDICTION OF THE LOAD-DEFLECTION CURVES IN BEAM TESTS

Various possibilities of the CRASHD program described in ref. 23 are not compiled in a single program, but scattered over several specialised versions. The version used in this thesis included the exponential moment drop-off curve and the results it had originally produced were reported in refs. 23 and 25. These results concerned hinge rotation angles of maximum $10 - 15^\circ$. The theoretical $M - \theta$ curve was incorporated into

this version, as described in the previous section, and the program was tested against experimental results (Chapter 6) which covered hinge rotation angles of more than $35 + 40^\circ$. Application to such large deformations revealed that the original program did not allow for the "strain stiffening" effect* at large deformations which will be described below (this effect was negligible for rotation angles of $10 - 15^\circ$, but became important in the examples shown in this thesis). It was discovered much later that the strain stiffening effect was included in a separate plane frame version of the program dealing with brittle fractures only.

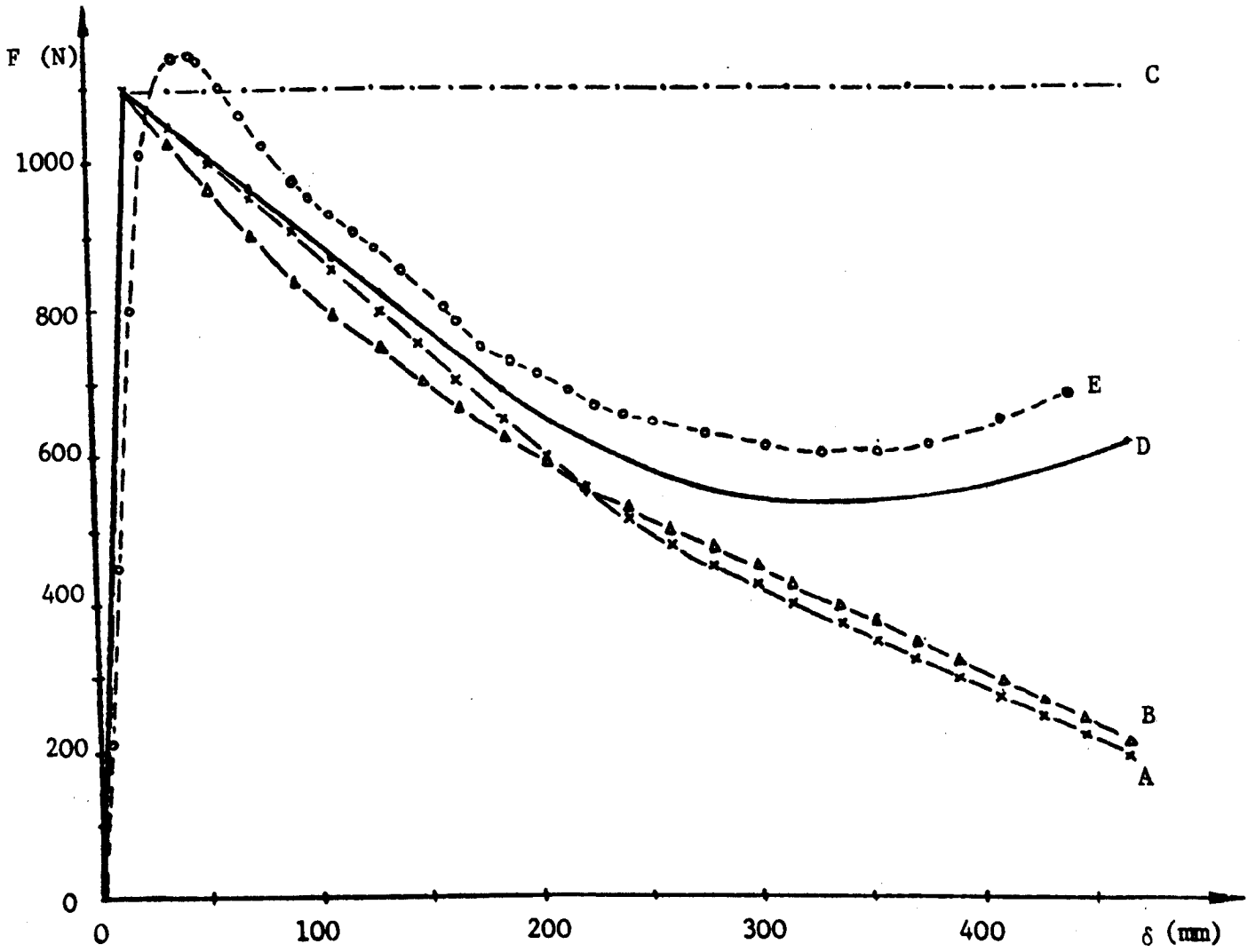
The strain stiffening effect in cantilever beams represents a non-linear effect of large deformations on the effective lateral load at the free end. It has been studied within elastic range by Bisshopp et al (99) and Frisch-Fay (100). In collapse analysis it appears as the moment arm reduction during rotation about a hinge at the built in end on the end load. If the hinge moment is constant, the end load must increase gradually to allow for the shortening of the moment arm (Fig. 7.5b).

The dotted line E (Fig. 7.5a) represents the experimental force (F) - vertical deflection (δ) of the cantilever with section no. 7 (Tables 6.1, 6.2 and Fig. 6.22). Displacement increments δ_s (Fig. 7.5b) were applied in the global Y direction and program (not allowing for strain stiffening) produced the cumulative reaction F represented by the curve A in Fig. 7.5a. Curves E and A agree well up to $\delta \approx 160$ mm, corresponding to $\theta \approx 15^\circ$, but the agreement deteriorates as the hinge collapses further and becomes very poor for $\delta > 300$ mm ($\theta > 30\%$). Modelling the beam by 1, 2, 3 or 4 elements had very little effect on curve A. The theoretical M - θ curve (Fig. 6.22) was approximated by the exponential equation (7.9) with $A = 200000$ Nm, $B = 456660$ Nm and $c = 3$, and the original version of the program gave curve B in Fig. 7.5a. Good agreement between curves A and B indicated that the new subroutines CURV and COIL (section 7.3) were working properly.

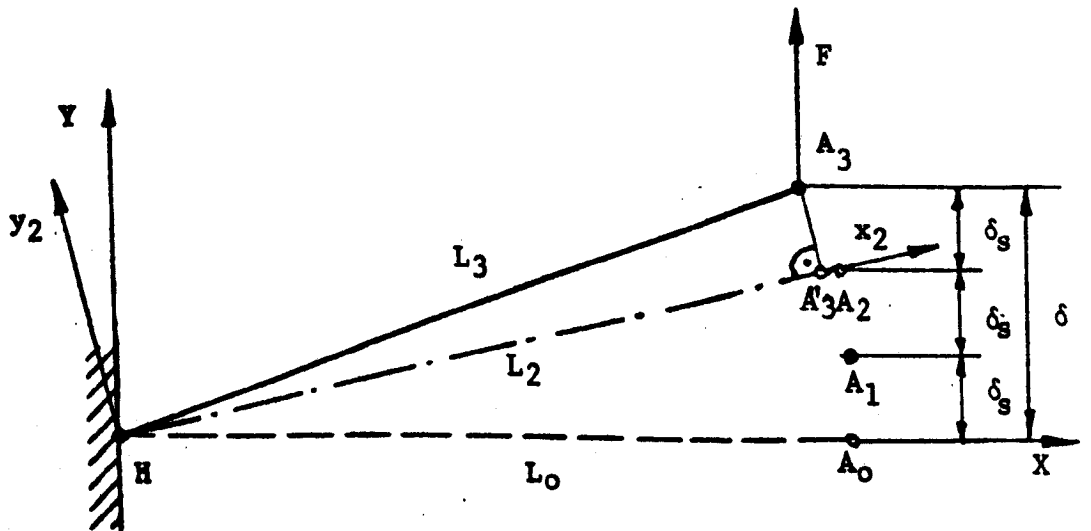
Assume now that no hinge occurs after the first displacement increment δ_s of the end A in Fig. 7.5b. The calculated vertical reaction in +Y direction is F_1 , and the next δ_s is applied to an inclined beam HA_1 . The second reaction increment F_{2s} is also directed upwards, the total reaction becomes $F_2 = F_1 + F_{2s}$ and an axial tension equal to the projection of F_{2s} on the direction HA_1 will be produced in the cantilever. The same tendency continues until a hinge is introduced at H.

If a hinge with constant moment M_p is introduced at H the structure becomes a mechanism rotating freely about H, but the moment M_p and associated shear Q_p are maintained in the cumulative vector of internal loads. Subsequent increments of vertical displacement cannot produce any increments of external reaction (the beam offers no resistance) and hence the cumulative reaction F (curve C in Fig. 7.5a) and internal loads remain constant. The program did not, however, project the constant shear forces Q_p on the global axes in order to allow for the increase in reaction F due to the shortening of the moment arm with respect to hinge H (strain stiffening effect). There was no change in axial load either.

* The term "strain stiffening" was used in ref. 23, paragraph iii, page 31 and Fig. 2.4.



a.



b.

Fig. 7.5

A rotary spring simulating the moment drop-off curve displays a negative rotational stiffness (7.10) or (7.12), so that the increment of the external reaction F_s points in the negative direction of the global Y axis. This F_s has a projection on the current HA line pointing towards H, so that, in the absence of strain stiffening, the initial tension in the beam turns gradually into compression as the collapse progresses. This is also the reason why the cumulative reaction (curve A in Fig. 7.5a) falls much below its actual value at larger angles θ .

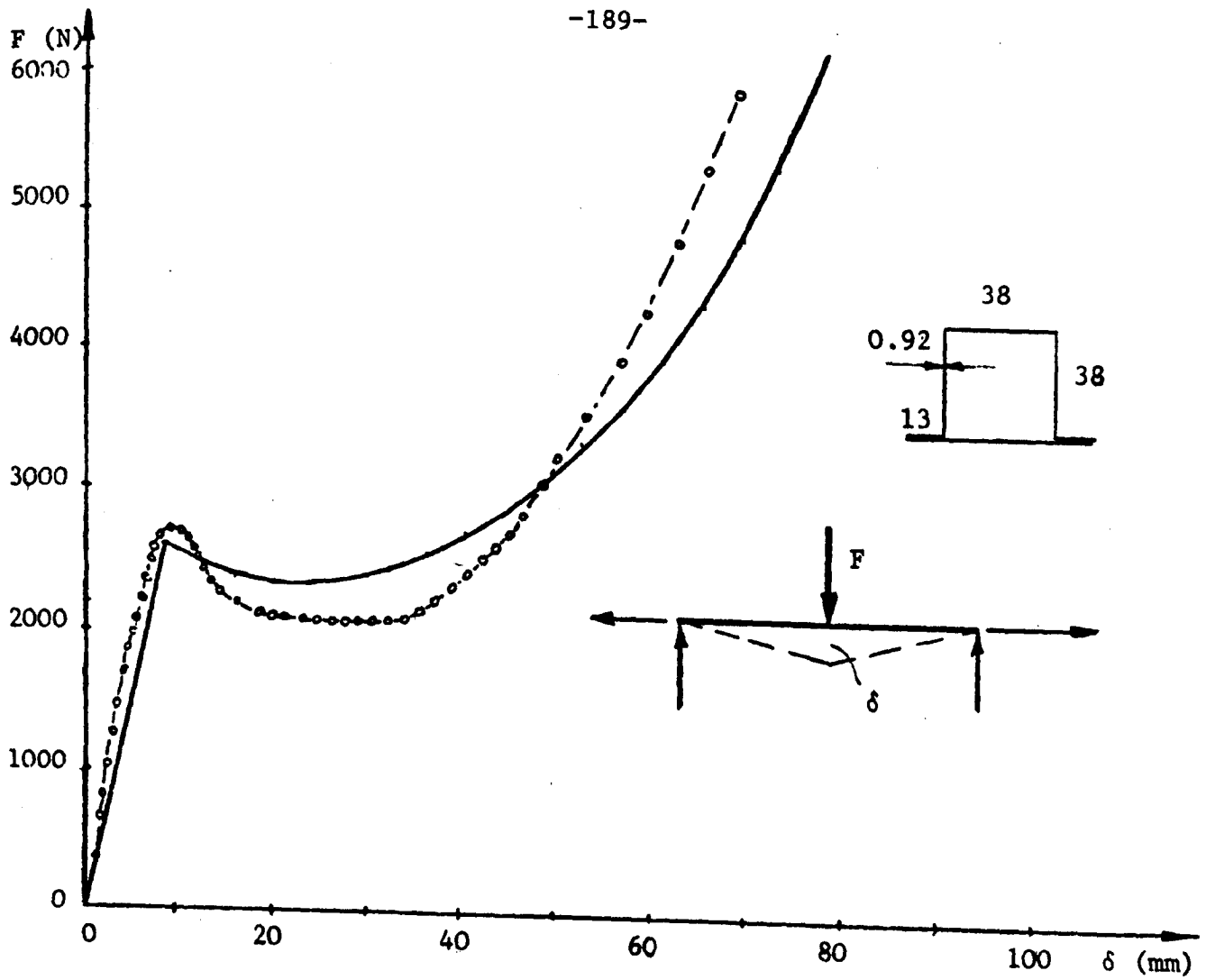
Fortunately, the hinge rotation increment θ_s is controlled by the vertical, specified displacement δ_s . The changes in the beam length due to the inaccurate calculation of the axial load are negligible in comparison with the total length, so that point A moves almost exactly (although "inside" rather than "outside") along a circle about H. The results for θ_s , cumulative θ , the appropriate spring stiffness R, (negative) hinge moment increment M_s and cumulative hinge moment M are therefore almost unaffected by strain stiffening. It was therefore possible to use the updated hinge moment and the current global X co-ordinate of end A (or angle θ - as explained in section 7.3) to calculate the actual vertical cumulative reaction F - curve D in Fig. 7.5a.

The new theoretical curve D allows for the strain stiffening effect and follows the experimental diagram E with a quite reasonable accuracy (Fig. 7.5a). Curves A and D are very close to one another for $\theta < 15^\circ$ ($\delta < 150\text{mm}$) and this may be the reason why strain stiffening was not included earlier into this particular version of the program. The sharp peak of the theoretical curve D is due to the assumption that the shape factor of the section is equal to unity.

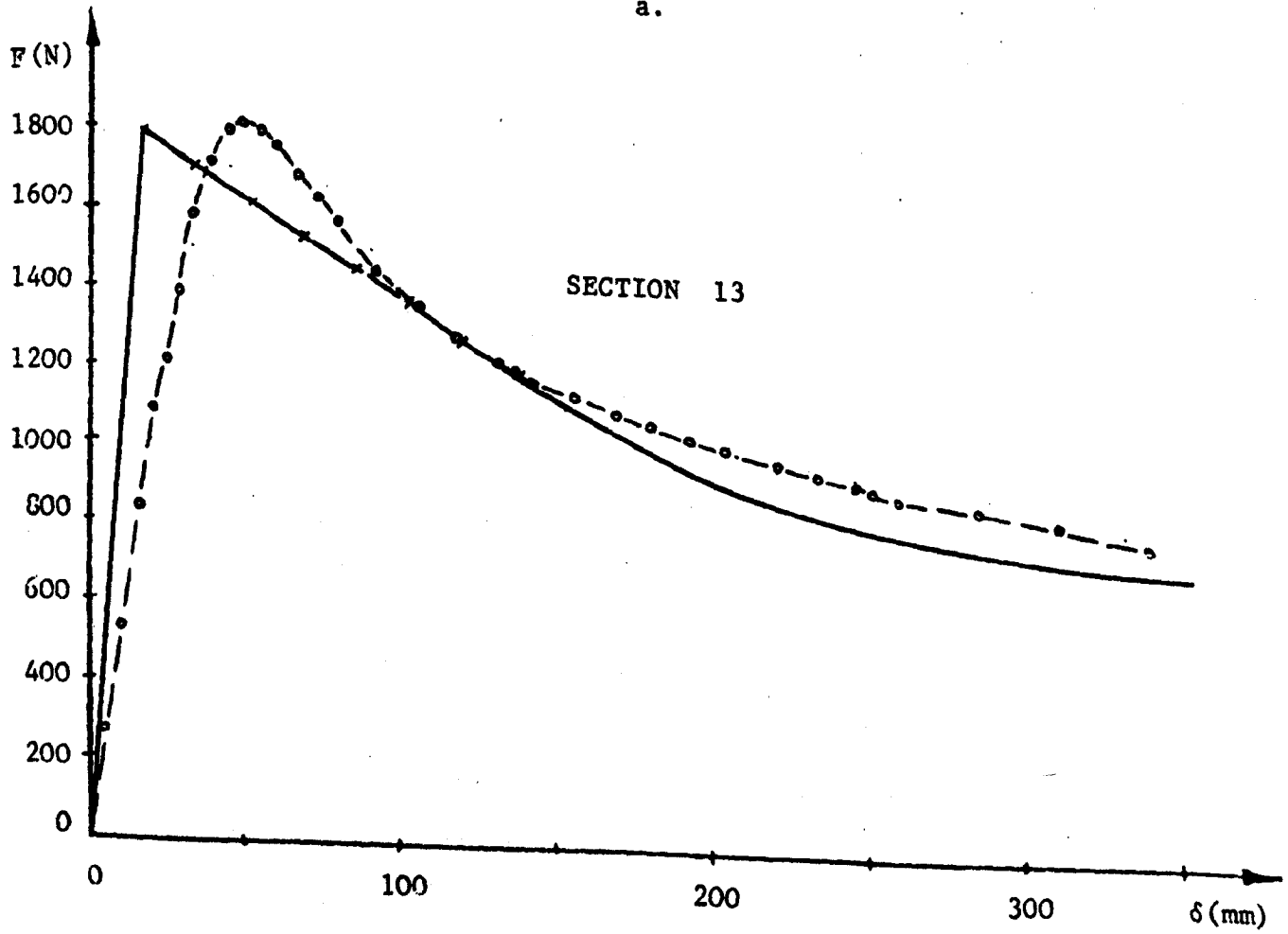
It should be noted, however, that the strain stiffening effect due to catenary action in axially restrained beams is well taken care of by the program in its present form. Catenary action develops at relatively small lateral deflections and hinge rotations due to axial restraints not present in the cantilever example. Bending collapse of a simply supported, axially restrained, closed top hat section beam, loaded in the middle is shown in Fig. 7.6a. The experimental, dotted line is reproduced from Fig. 4.26 of ref. 23. The actual material properties were not known and the stress $\sigma_p = \sigma_{pu}$ was chosen to give the maximum strength obtained by a cantilever test (23). The point of load application moved in vertical direction only (Fig. 7.6a) and the theoretical solid line in Fig. 7.6a was produced directly by the program.

Theoretical and experimental load-deflection curves of cantilever 13 (Fig. 5.8a) are shown in Fig. 7.6b. The actual stiffness was less than the theoretical one (non-rigid support?) and if the stiffnesses are made equal, then the F - δ curves become very similar to the M - θ diagrams in Fig. 6.28.

Figs. 7.7 and 7.8 depict the extreme cases of the cantilever testing program. A rapid load drop off of the very thin walled section 18 (Fig. 7.7a) and a slow decrease in section 23 (Fig. 7.7b) are both well predicted by the theory. The load increase after $\delta \approx 340$ mm is due to introduction of equation (7.13) after $\theta > \theta_j$. Results for cantilever 1 with $a/b = 3$ are shown in Fig. 7.8a, while cantilever 27 with $a/b = 0.33$ gave the curves in Fig. 7.8b. The load increase after $\delta \approx 225$ mm is also caused by (7.13) after the theory predicted jamming of the hinge.



a.



b.

Fig. 7.6

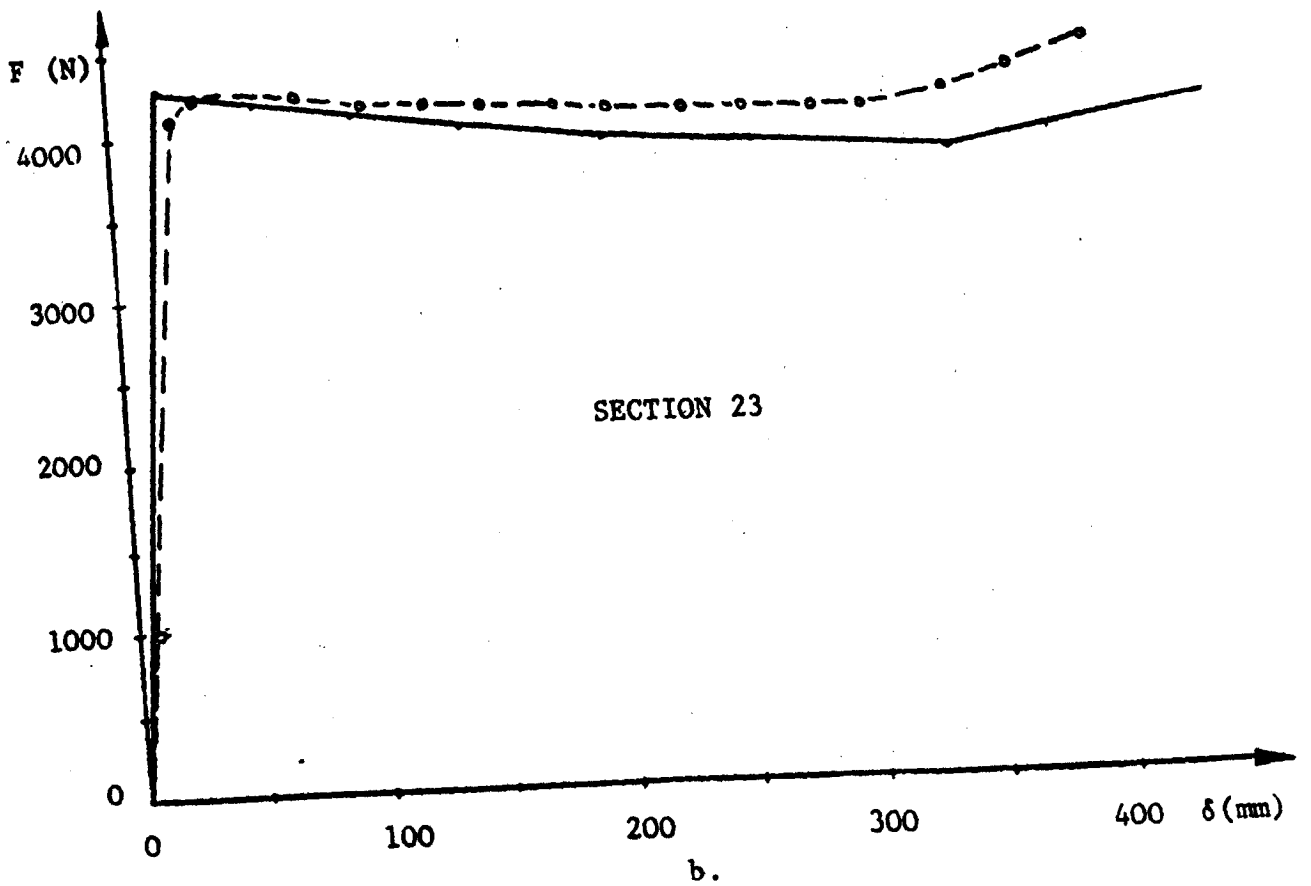
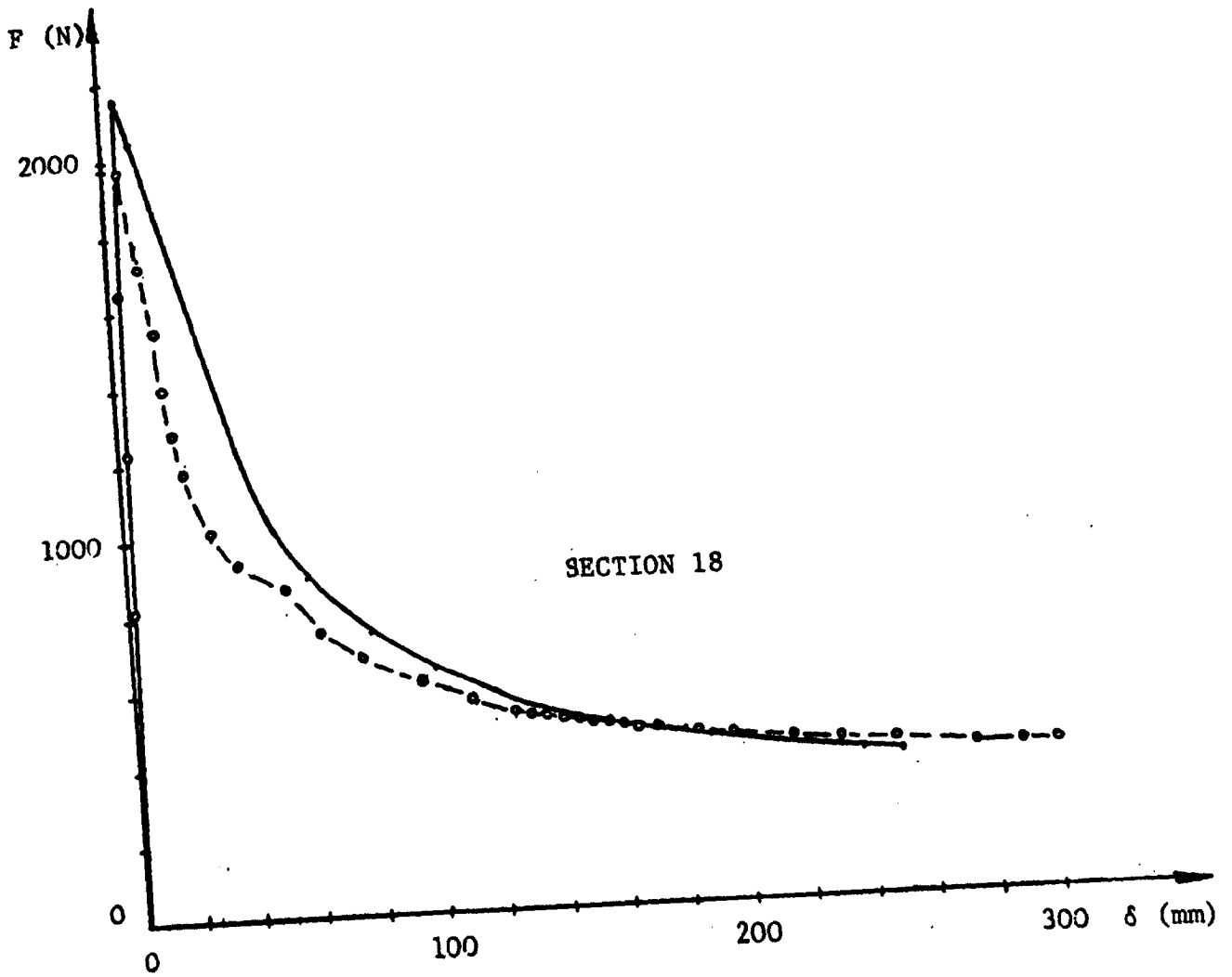
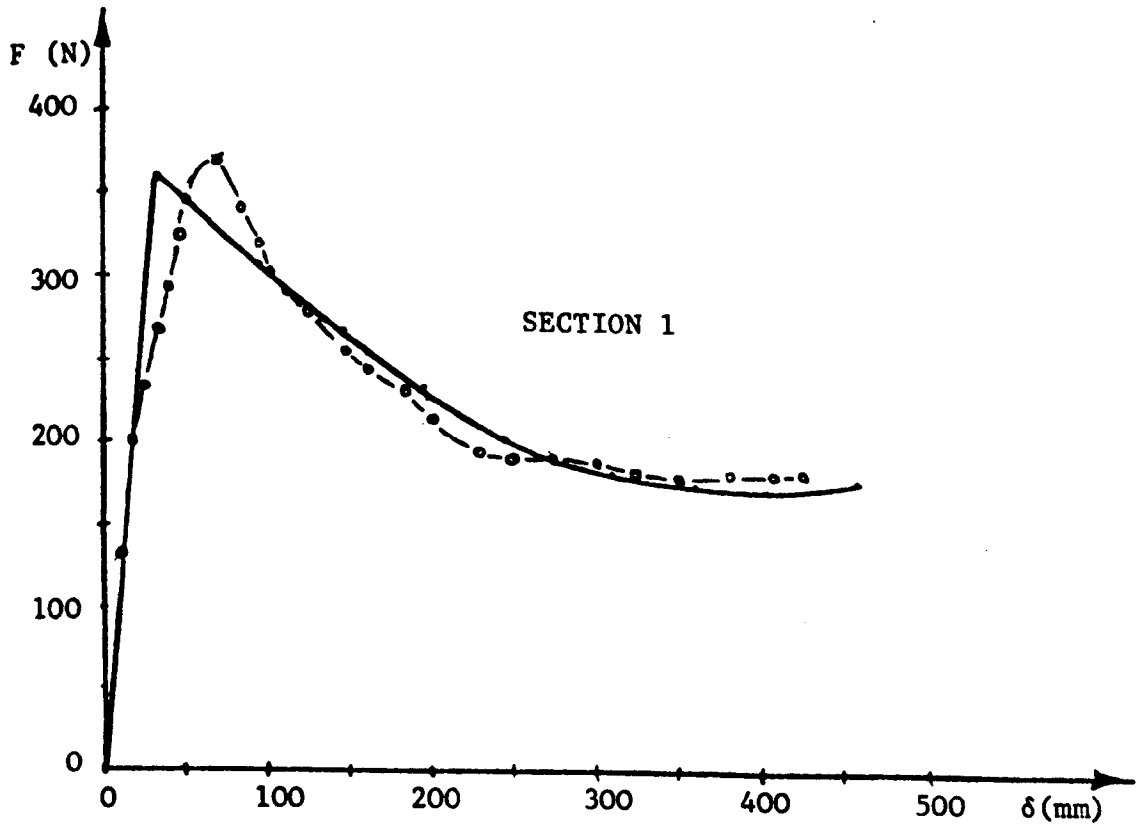
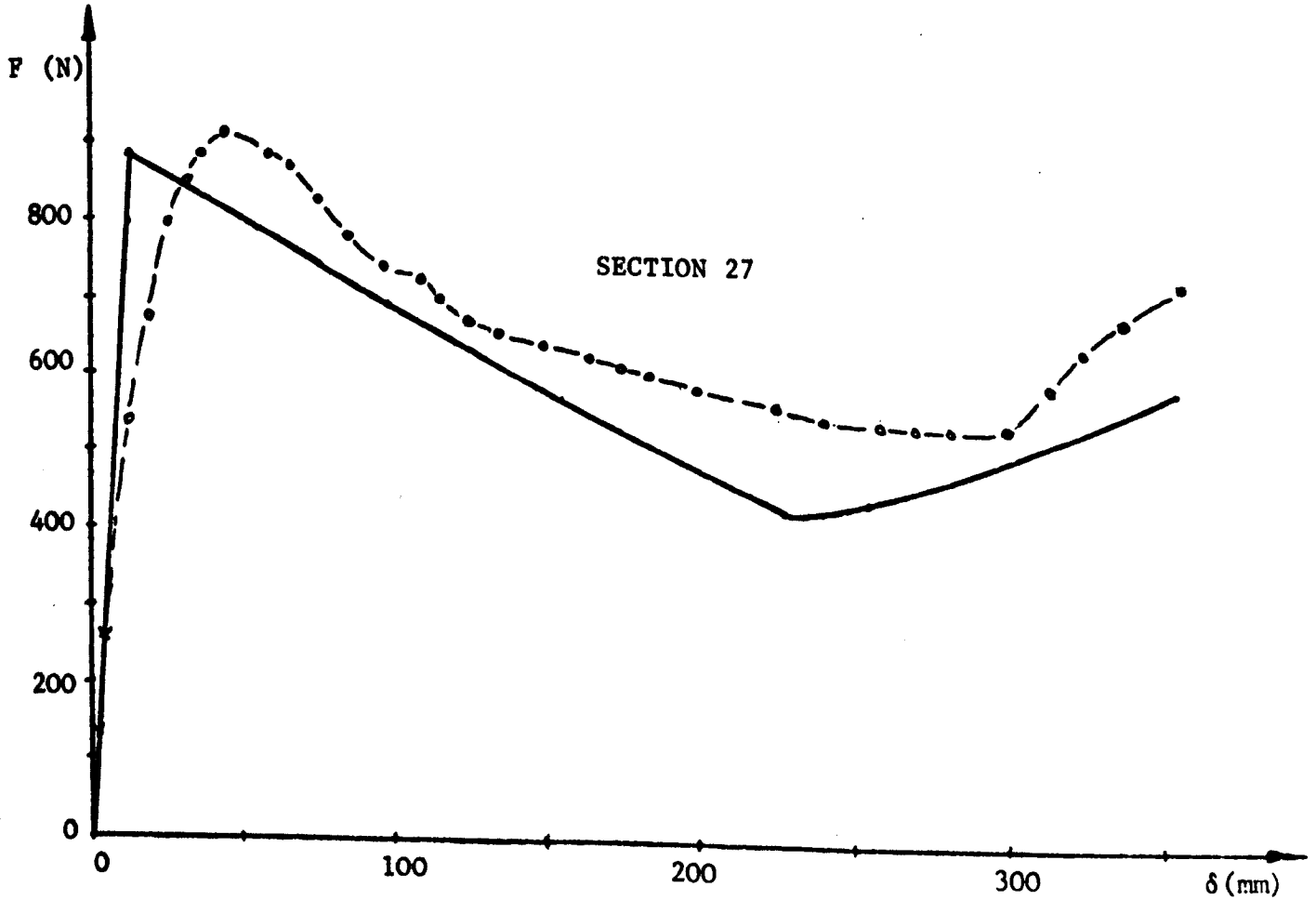


Fig. 7.7



a.



b.

Fig. 7.8

7.5 THEORETICAL PREDICTION OF THE BUS RING COLLAPSE BEHAVIOUR

A part of the bus ring collapse testing program carried out in the School of Automotive Studies (1,2) dealt with rings composed of square or rectangular section beams. Material separation at joints occurred in some of these structures with a significant effect in their load-deflection curves and energy absorbing properties.

The test apparatus was designed to enable static or dynamic testing of a variety of bus rings. The test rings were arranged horizontally and fixed to a support block "B" (Fig. 7.9) at the points where the cross member is attached to the chassis frame. Static or dynamic loads in the ring plane were applied to one cant rail joint at 30° to the floor beam. A lateral restraint was applied to the loaded side at the waist rail level (Fig. 7.9). The restraining device consisted of a cantilever beam mounted on a torsion bar and provided the spring stiffness of approximately 200 N/mm - similar to the experimentally determined lateral stiffness of "typical" bus seats. This stiffness is greater than the limiting theoretical value of 150 N/mm (Fig. 3.3 - Chapter 3) and collapse modes "C" (Fig. 2.1) were always produced. This test arrangement provides a safety margin in some buses and is closer to the actual behaviour in others (Chapter 2).

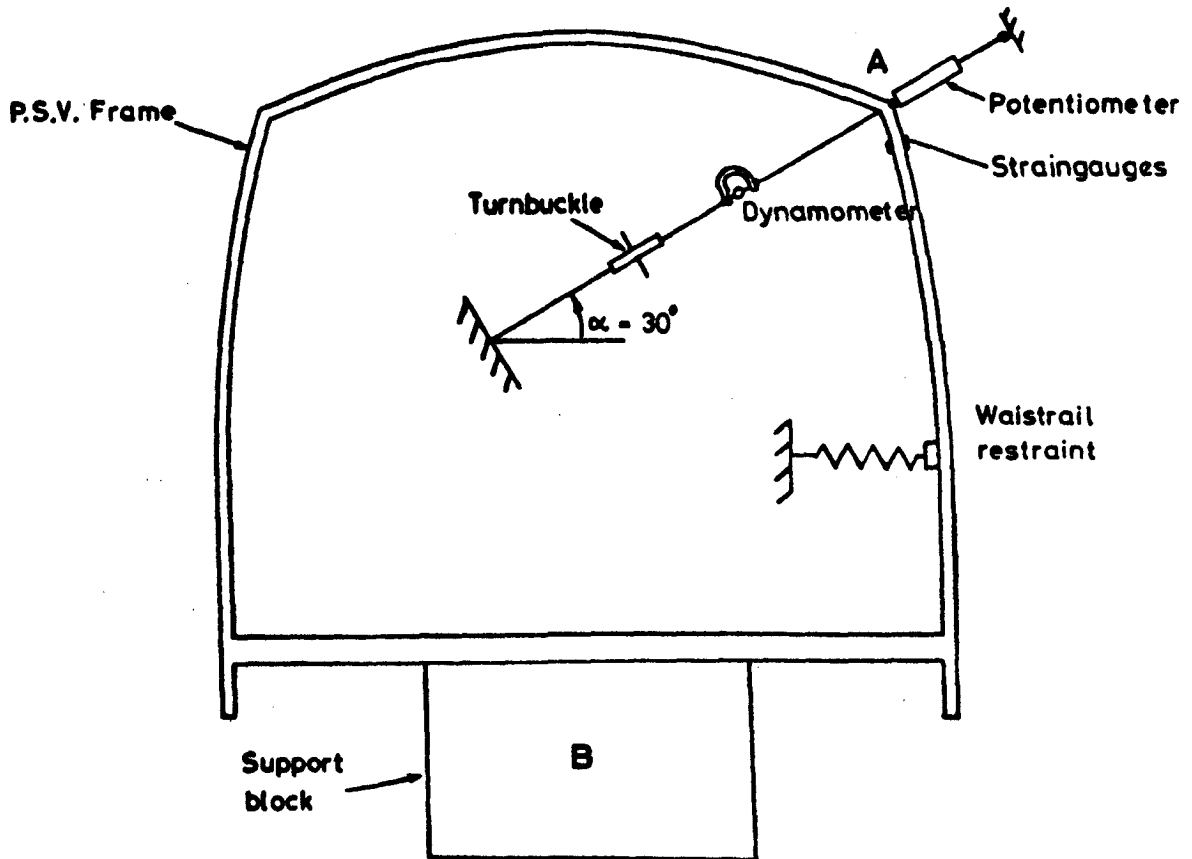


Fig. 7.9

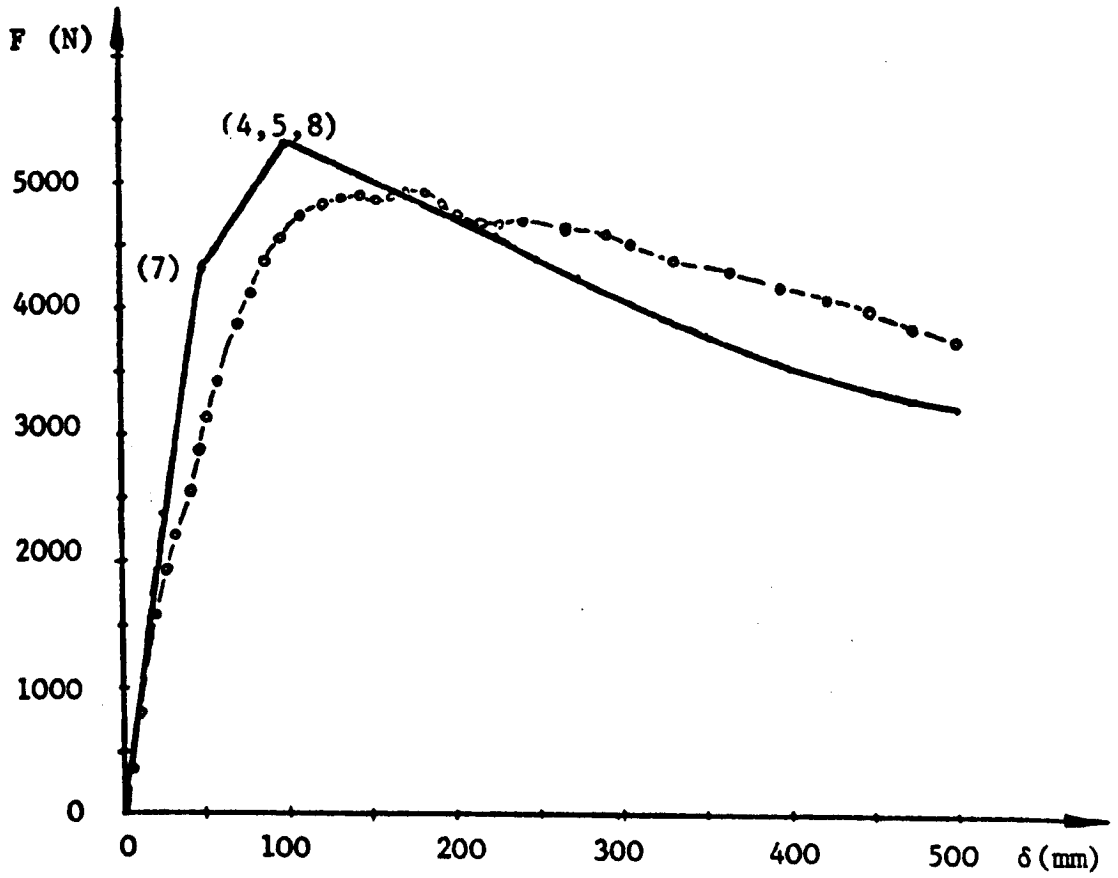
Quasi-static increments of loads or displacements were applied using a turnbuckle (Fig. 7.9) and measured by a horseshoe dynamometer. Variation of angle α (Fig. 7.9) was small during the test. Displacements along the direction of load were measured by a linear potentiometer. Two strain gauges were applied to the pillar flanges near the loaded cant rail joint.

Quasi-static collapse test of a mild steel ring which had no material separation in joints produced collapse mode and load (F) - deflection (δ) curve shown dotted in Fig. 7.10a. Pillars were made of 45 x 45 x 2 mm tube, 38.1 x 50.8 x 1.67 mm section was used for the roof member and the floor beam dimensions were 50 x 70 x 3 mm. Pillars and roof member were welded continuously to the tubular cant rail and the pillar to floor beam joints were bolted.

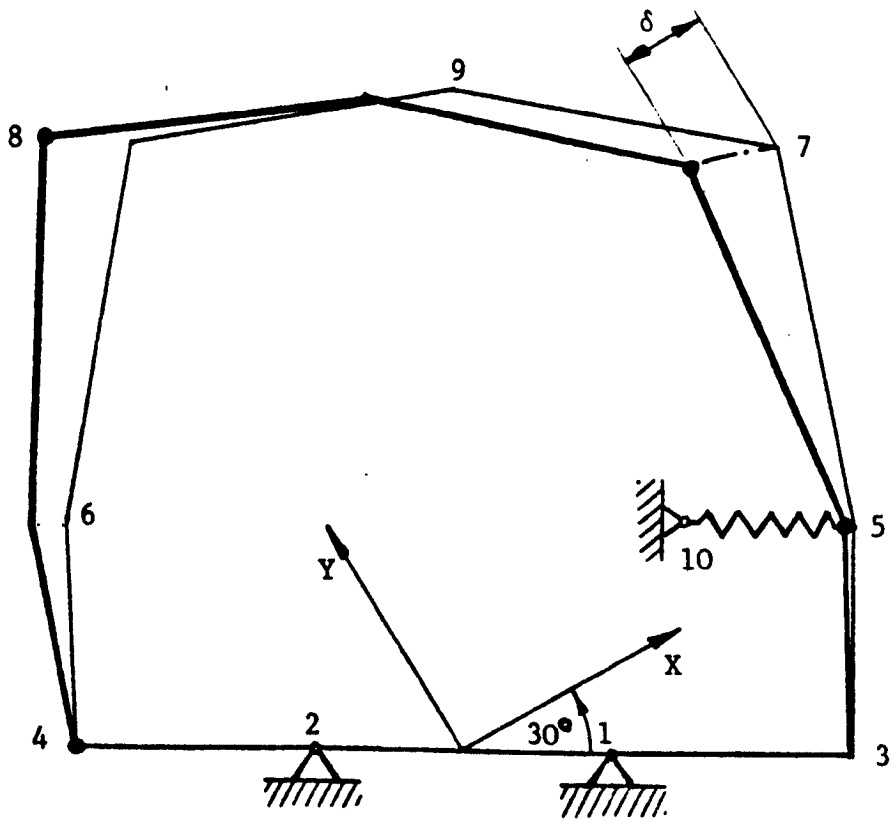
The finite element model of the ring (Fig. 7.10b) was restrained in translation at nodes 1 and 2. The fictitious beam 5-10 had an axial stiffness of 200 N/mm and a very low bending stiffness in order to avoid the step in the bending moment diagram. Material properties of the parent material of the section walls were (2) $\sigma_p = 310 \text{ N/mm}^2$ and $\sigma_{pu} = 350 \text{ N/mm}^2$. Global axes X and Y have been rotated through 30° (Fig. 7.10b) for reasons explained at the end of section 3.3 (Fig. 3.1c). Displacement increments of $\delta_s = 25 \text{ mm}$ were applied to node 7 in -X direction, while the other degrees of freedom have been set free. The theoretical F- δ curve, representing the cumulative reaction at node 7, calculated directly by the program is shown in Fig. 10a and the predicted collapse mode in Fig. 7.10b. The maximum hinge rotation of 15° occurred at node 7 at $\delta = 500 \text{ mm}$.

The theoretical and experimental collapse modes are identical (Fig. 7.10). The theory overestimated the maximum strength by 8% which was largely caused by the overshoot of the local load carrying capacities of hinges. The first "kink" in the theoretical F- δ curve is due to the occurrence of hinge at node 7, and all the three other hinges at 4, 5 and 8 were inserted after the step $\delta = 75$ to 100 mm. Less overshoot of the local strength, separate introduction of all hinges and better agreement between the theoretical and experimental curve for $F > 4000 \text{ N}$ would have been obtained with a smaller δ_s , or even better, with a facility to scale the loads so that a single hinge is introduced within one calculation step (see section 3.4.6). Cant rail joints were subject to some elastic and permanent deformations and this is the most probable reason why the experimental F- δ curve departed from the theoretical one before the ring started collapsing. The beam end conditions prior to collapse can be specified either as fixed or pinned, without the possibility of allowing for a finite-stiffness joint. Shifting the theoretical maximum to $\delta = 150 \text{ mm}$ would give a much better agreement between the experimental and theoretical load drop off curves. Although the joint deformations were relatively small, they allowed less hinge rotation in beams for the same deflection and the load drop off was slightly lower than the theory predicted.

The example in Fig. 7.11 is similar to the one in Fig. 7.10. The first attempt (curve 1) had to be stopped because the loading apparatus seized up. During the second loading the ring stiffness remained at a constant



a.



b.

Fig. 7.10

level (curve 2) right up to the maximum load, and the agreement with the theoretical $F-\delta$ curve before collapse is better. However, at $\delta=120$ mm material separation took place near the weld at the loaded corner, followed by a sudden drop of resistance. The stresses in the pillar flanges near the loaded corner changed direction after fracture because of redistribution of internal loads (contraflexure in the pillar changed into a cantilever-type moment distribution between the cant rail and waist rail). Some permanent deformation was left in the ring after the first test, so it may be more correct to use curve 3 obtained from 1 and 2. The theoretical curve was obtained using the guaranteed material properties $\sigma_p = 350 \text{ N/mm}^2$ and $\sigma_{pu} = 430 \text{ N/mm}^2$, taken from ref. 101.

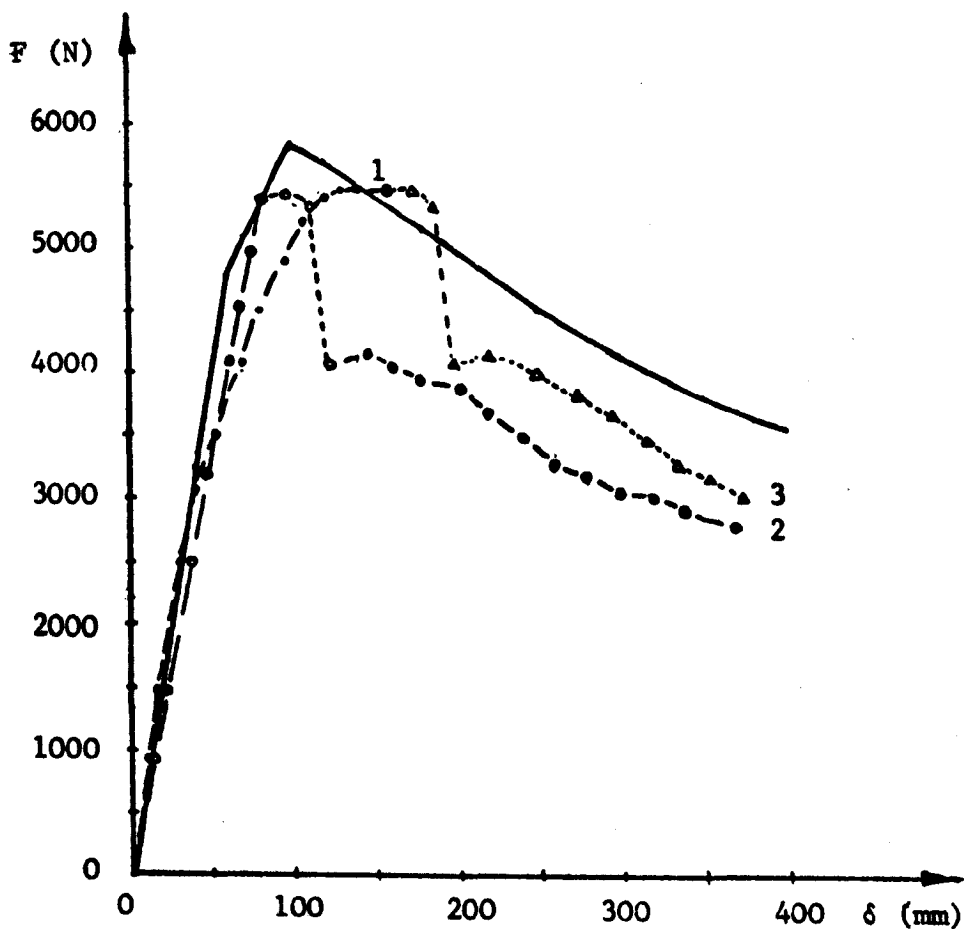


Fig. 7.11

Impact tests were carried out with the same ring mounting, but the load was applied by means of a pendulum (Fig. 7.12). The nose of the pendulum was shaped so that the contact with the ring was always at the cant rail joint. The pendulum was released from a position 1.0m above the impact point, providing an impact speed of 4.6 m/s. The energy input was estimated to be between 3.2 and 3.4 kJ (the calculated figure for the original design was ≈ 3.4 kJ, but the pendulum nose became lighter after being adjusted for bus ring tests).

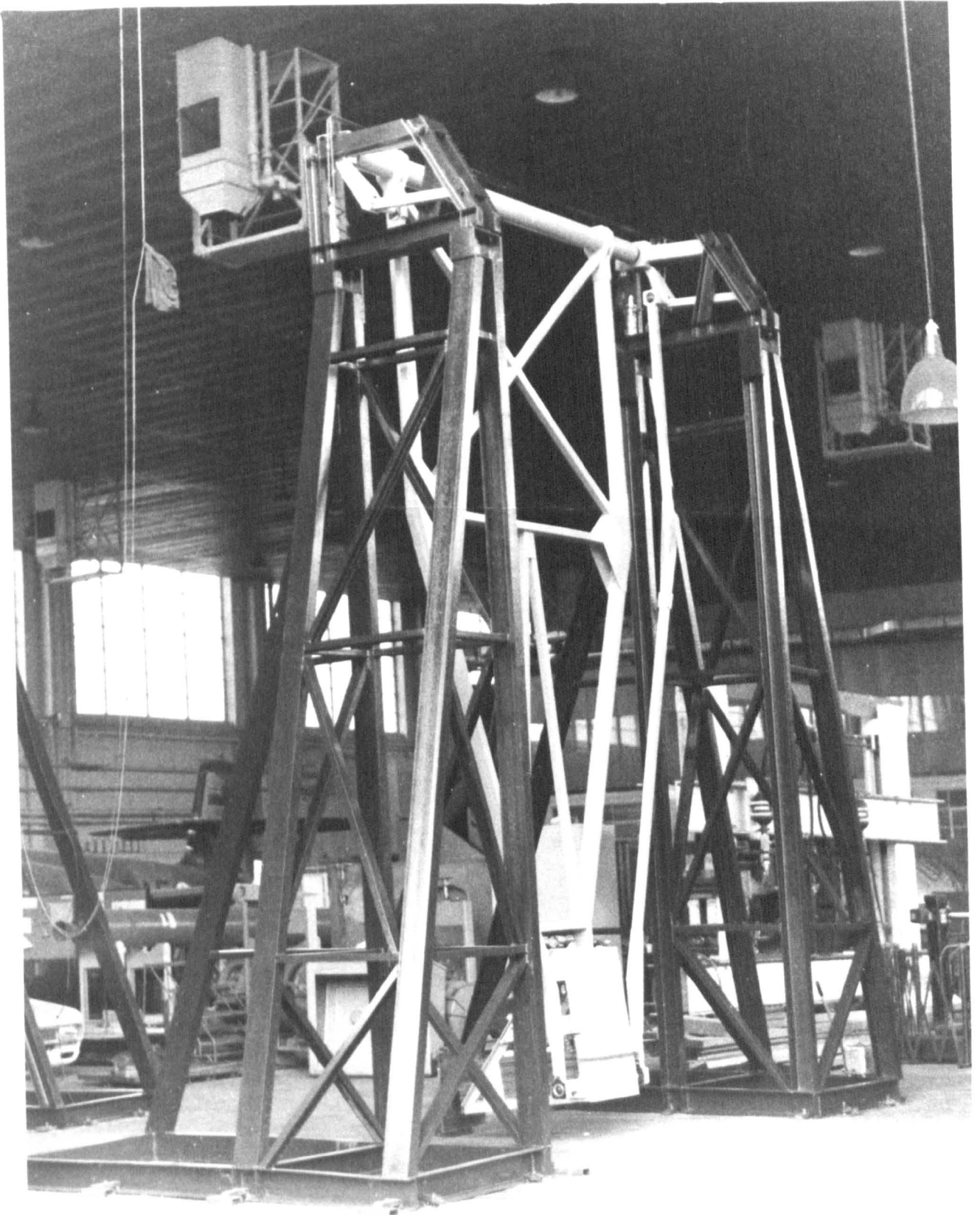


Fig. 7.12

Parameters recorded during impact tests were:

1. Velocity of the pendulum immediately before impact, measured by two photocells 10" apart, whose light beams were interrupted by a pointer attached to the pendulum;
2. Longitudinal deceleration of the pendulum nose;
3. Impact force measured by a strain gauge force transducer;
4. Strain rate in the ring material, measured by 2 strain gauges applied to the pillar flanges near the impact point;
5. Deflections of the ring were measured using a checker-board background and each test was recorded by a high-speed film camera.

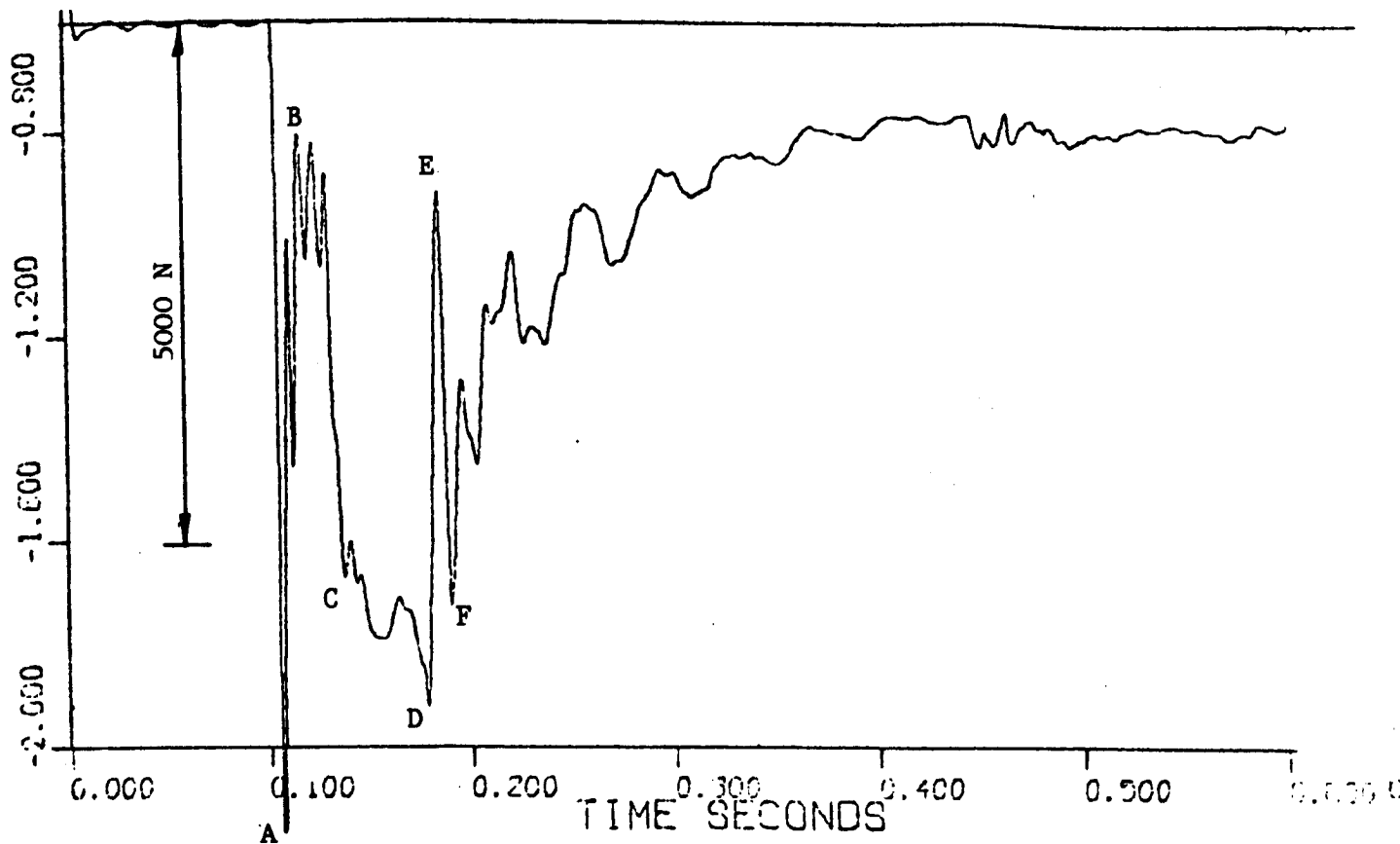
The first four data were digitised by an analogue to digital converter and a scanner which sampled the analogue signals 4800 times a second. Analogue data were also recorded on magnetic tape and a Perifile recorder which digitised the signals and stored them on a cartridge.

A ring very similar to the one in Fig. 7.10 with $\sigma_p = 340 \text{ N/mm}^2$ and $\sigma_{pu} = 416 \text{ N/mm}^2$ was impacted at a speed of 4.66 m/s and the collapse mode was the same as in static conditions, but the permanent deflection of the loaded cant rail was 940 mm. Material separation occurred near the welded joint of the loaded cant rail (Fig. 4.4c), while "typical" hinge failures (Fig. 5.6b) were observed in points 4, 5 and 8 (Fig. 7.10b). The impact force variation and strain rate in the ring material are relevant in the current analysis and these signals are presented in Fig. 7.13. Frequencies above 100Hz have been filtered out to eliminate noise and structural "ringing".

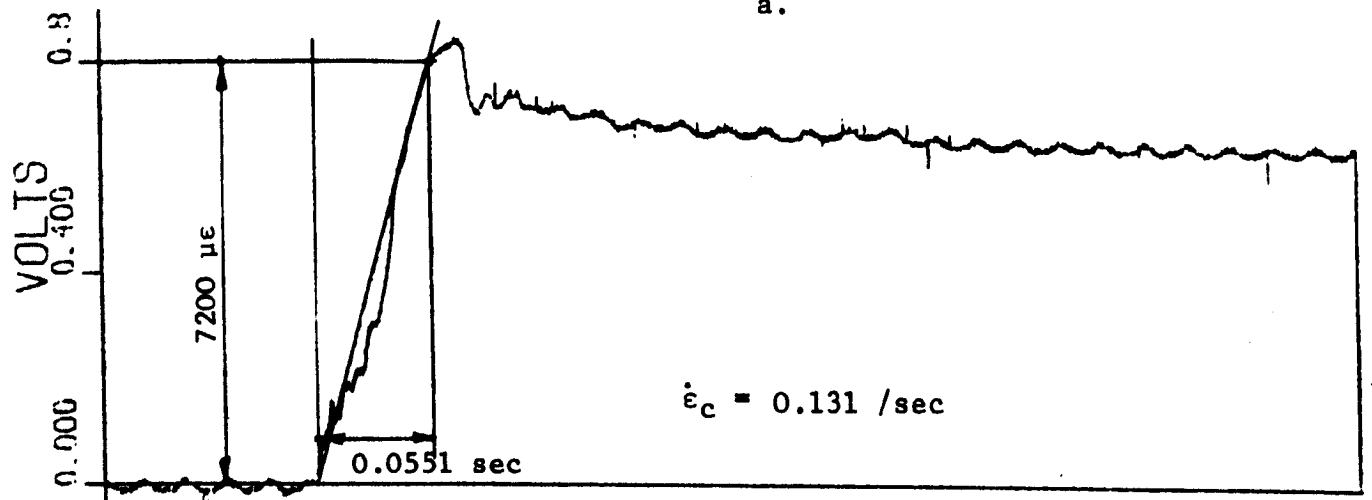
Inertia forces had a significant effect on the initial, peak force A (Fig. 13a), but much less influence on the second load increase between points C and D. The instance of joint fracture corresponds either to point A or D. The tendency of the ring to bounce away from the pendulum after the impact could have contributed to the load drop in the area of point B (the failure in Fig. 4.4c represents a "ductile" fracture caused by concentrated plastic straining and a similar joint separation in another ring (Fig. 7.11) occurred at an effective deflection of 190 mm, which is almost in the middle between points C and D in Fig. 14b). The load decrease after point F follows a fairly regular pattern.

The strain gauge signals from the compression (Fig. 7.13b) and tension (Fig. 7.13c) flanges of the pillar near the impacted corner were used mainly to determine the approximate strain rate. The gauges used were not designed to measure plastic strains so that the post-impact readings are probably inaccurate. The average strain rate was determined using the estimated average straight lines (Fig. 7.13b and c) and the values obtained were $\dot{\epsilon}_c = 0.131/\text{sec}$ (compression) and $\dot{\epsilon}_t = 0.203/\text{sec}$ (tension).

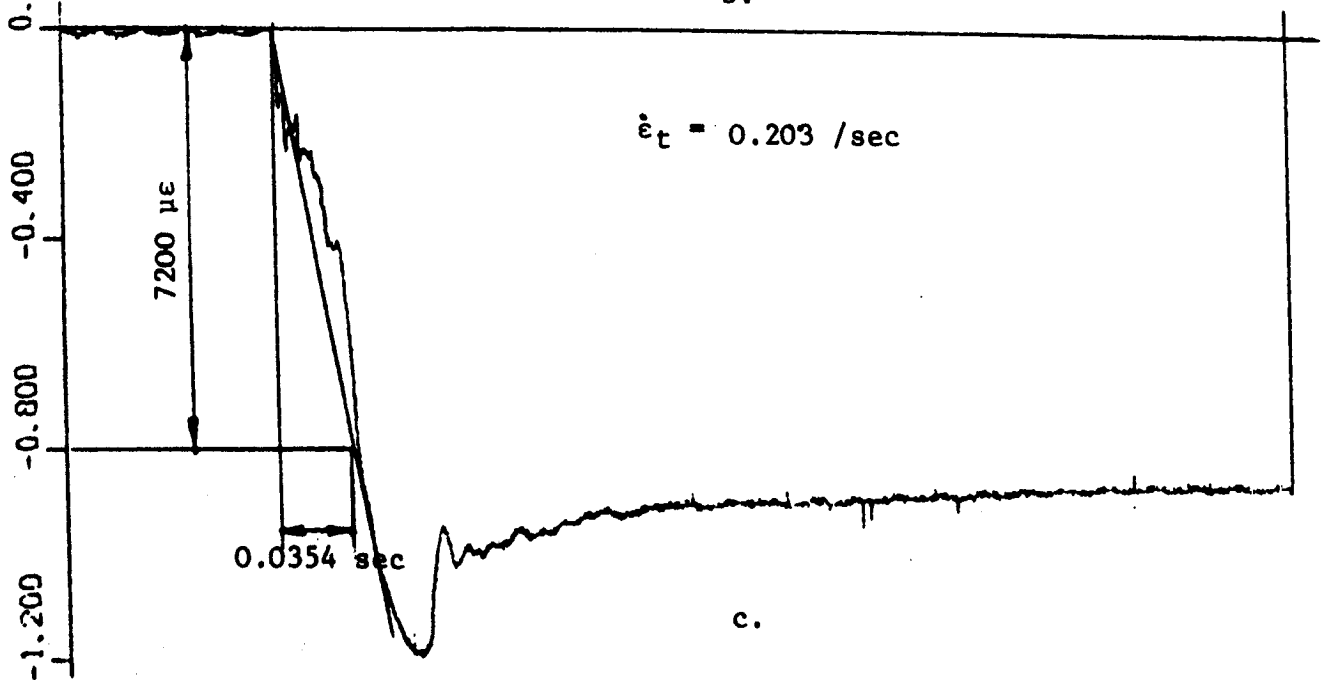
The high speed film record was used to produce the variation of the dynamic deflection of the load application point (δ_d) in time (t) (Fig. 7.14a), where time is measured from the first contact between the pendulum and ring. The maximum deflection during test was approximately 1075 mm, while 940 mm of permanent deformation was left after the test. The δ_d -t curve in Fig. 7.14a was combined with F-t relationship in Fig. 7.13a and the resulting load (F_d) - deflection (δ_d) diagram is shown in Fig. 7.14b.



a.

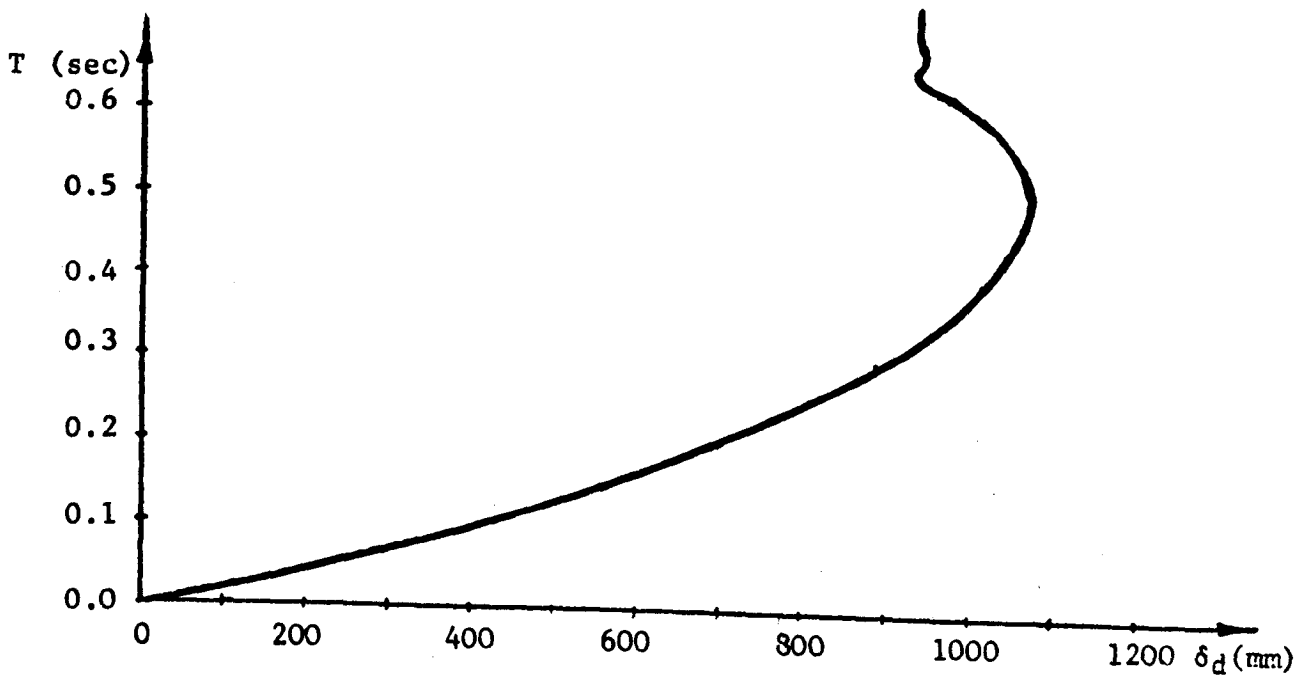


b.

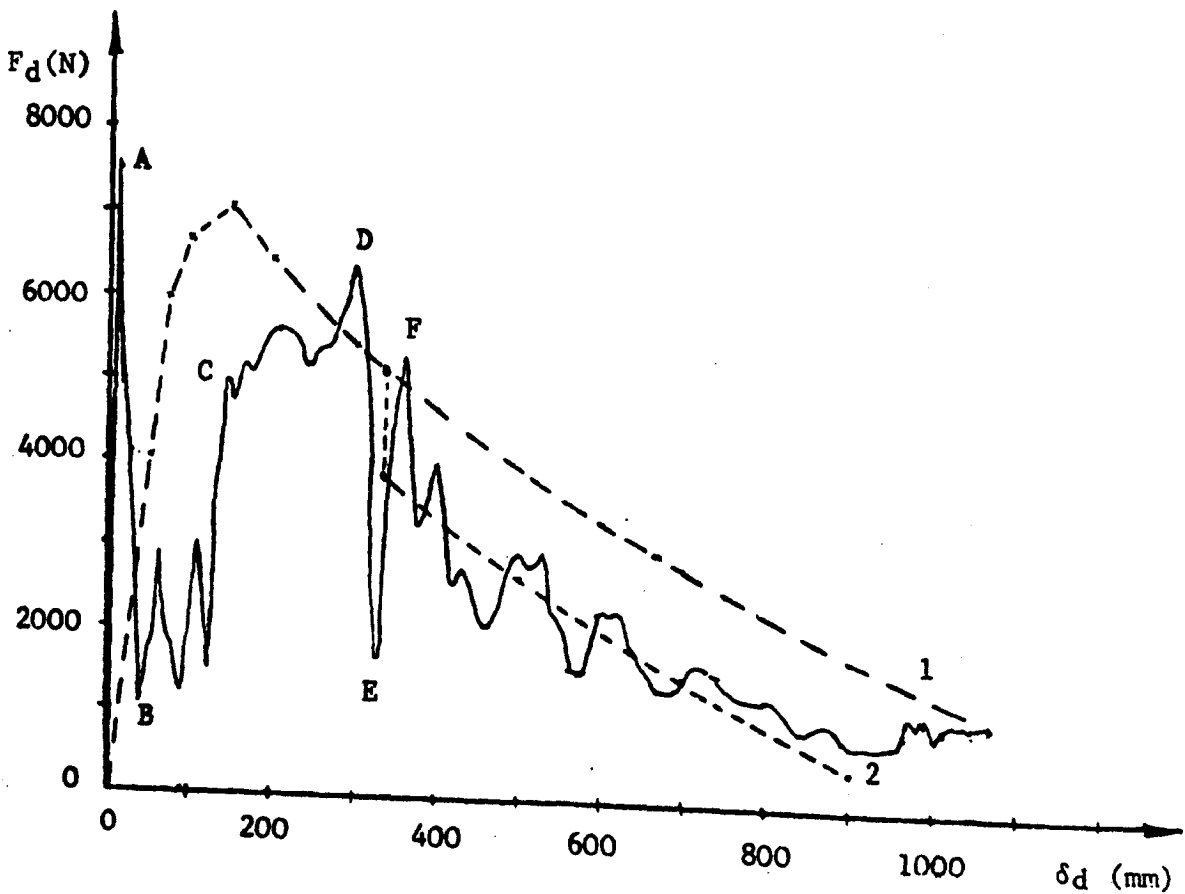


c.

Fig. 7.13



a.



b.

Fig. 7.14

Integration of the area under the $F_d-\delta_d$ curve in Fig. 14b gives the energy of 2.79 kJ absorbed by elastic and plastic deformation until the structure reaches its maximum deflection of 1075 mm. The estimated gain in the potential energy of the pendulum as it swings laterally through 1075 mm was 0.389 kJ, so that the energy dissipated in other ways (vibration of the ring and rig, friction, etc.) ranges between 0.02 and 0.22 kJ. The agreement between the estimated energy of the pendulum and the result from Fig. 14b is very good, bearing in mind the accuracy of measurement and, in particular, the problems of producing the $F_d-\delta_d$ curve in Fig. 7.14b.

The above impact test, although closest to the work presented in this thesis, was not quite adequate for comparison with theory because of the material separation (Fig. 4.4c) at the loaded joint. It is still interesting to see what collapse mode and energy absorption the theory predicts (the highly fluctuating dynamic loads cannot be allowed for in this quasi-static analysis).

The approximate strain rate at the loaded joint was calculated starting from the moment at node 7 (Fig. 7.10b) which is developed after an initial displacement $\delta_1 = 25$ mm is applied along the -X global axis. The section modulus of the pillar (Z) is also known, so that the strain (ϵ) in the pillar flanges near the node 7 is:

$$\epsilon_7 = \frac{\sigma_7}{E} = \frac{M_7}{ZE} = \frac{787886}{4782 \cdot 208000} = 0.00079212 \quad (7.14)$$

The impact speed remains virtually constant during the first 25 mm of deflection and the time for developing the strain (7.14) is:

$$t = \frac{25}{4660} = 0.0053648 \text{ sec} \quad (7.15)$$

The theoretical strain rate

$$\dot{\epsilon} = \frac{0.00079212}{0.0053648} = 0.14765/\text{sec} \quad (7.16)$$

agrees very well with the experimental values in Fig. 7.13b and c.

It is, of course, arguable whether the strain rate measured or calculated near the impacted cant rail applies to other hinges of the collapse mechanism (here-nodes 4, 5 and 8). The stress levels after 25 mm deflection at node 7 are similar in all hinge points, although the stress wave propagation through the structure may have an additional effect on the strain rate distribution. However, it is sufficient in practice to find the order of magnitude rather than exact value of strain rate and for that purpose the above method is adequate. It was also mentioned in section 5.7.2 that the strain rate reduces during collapse and this has some, although not very significant, effect of the flow stress σ_{pu} .

Various references (46, 47, 95, 96) quote experimental results giving different increases in the yield or maximum flow stress for the strain rate (7.16) or the corresponding time to yield. The strain rate factors

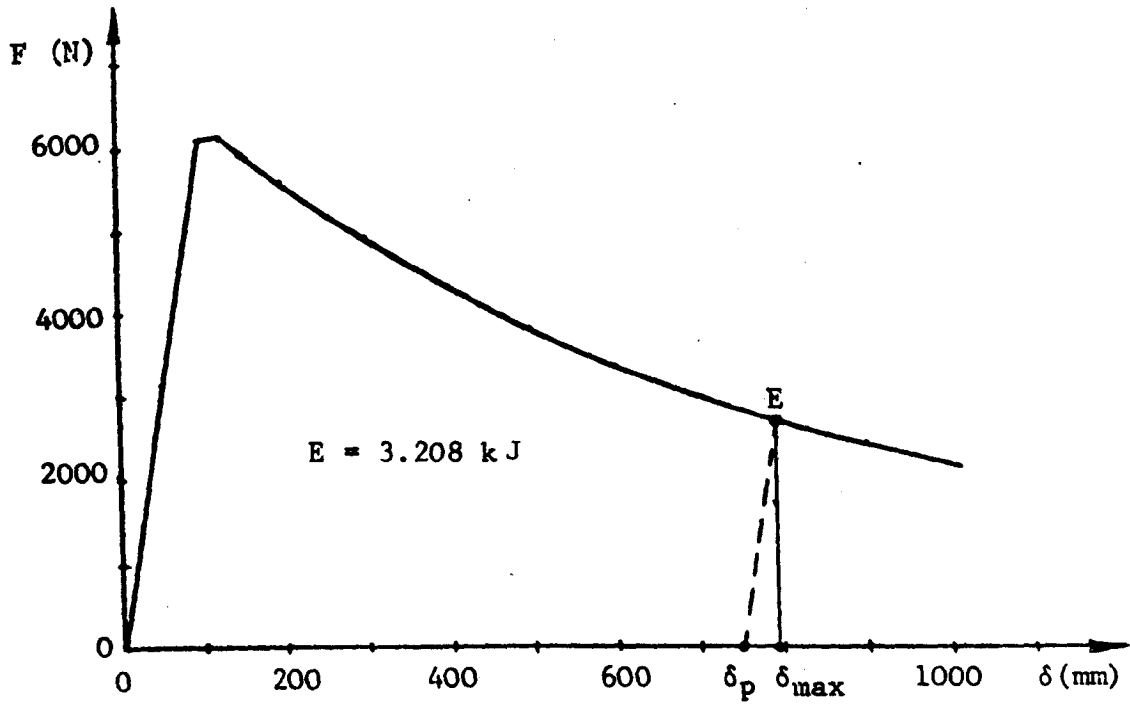
range between 1.226 for σ_p and 1.08 for σ_{pu} (ref 95) and 1.32 (formula 5.89). The probable reason for such a scatter is that the tests were made with mild steels of different properties. For example, ref. 95 deals with annealed mild steel specimens with the static σ_p/σ_{pu} ratio of 0.59 while the same ratio in the current example is $340/417 = 0.815$. This would indicate that the second correction factor is probably greater than 1.08.

The theory predicted a correct collapse mechanism with hinges at 4, 5, 7 and 8 and the more conservative strain rate factors gave the curve 1 in Fig. 7.14b. One of the four hinges in the actual structure became ineffective at point A or D (Fig. 7.14b) so that the theory overestimates the actual collapse performance of the structure. The same type of failure has reduced abruptly the strength of a similar ring by approximately 1300N (Fig. 7.11). If the same load is deducted from the theoretical curve in Fig. 14b starting from deflection at point E, the agreement between the theory (curve 2) and experiment becomes much better.

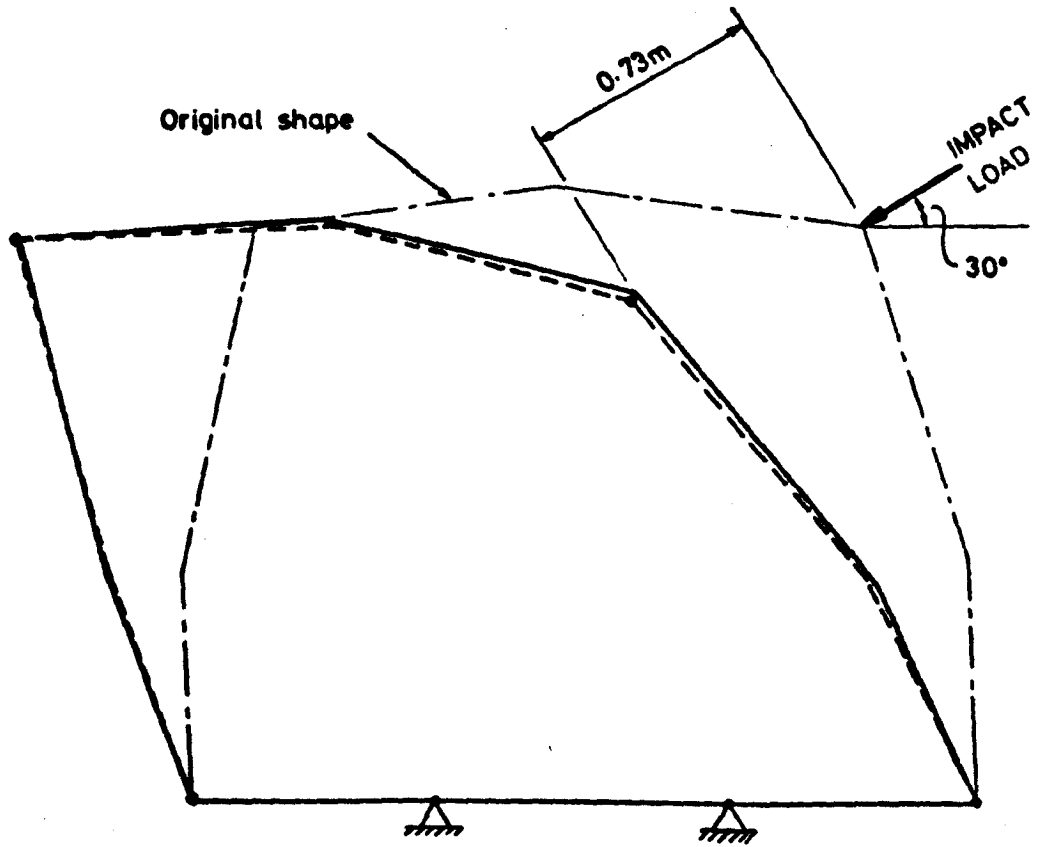
Equating the area under the theoretical curve 1 in Fig. 7.14b to the area under the experimental $F_d-\delta_d$ curve up to the point $\delta_{max} = 1075$ mm (Fig. 7.14a) (the energy absorbed is 2.79 kJ), the theoretical maximum deflection becomes 790mm. Similarly, the permanent theoretical deflection is 700mm rather than 940mm (Fig. 7.14a), which is mainly due to the fracture not allowed for by the theory. The energy in the fictitious spring at $\delta = 700$ mm is negligible.

An early test of a similar ring, but of different material, without waist rail restraint and without high speed film record or force and strain rate reading, did not cause joint fractures (2) and the permanent deflection after the test was 730mm. The theoretical strain rate was 0.1155/sec and formula (5.89) gave a strain rate factors of 1.31. If both $\sigma_p = 310$ N/mm² and $\sigma_{pu} = 351$ N/mm² are multiplied by 1.31 the appropriate theoretical permanent deflection δ_p becomes approximately 750mm. This result was obtained by finding a deflection δ_{max} such that the area under the theoretical $F-\delta$ curve (Fig. 7.15a) gives an energy (3.208 kJ) equal to $3.4 - \Delta E$, where $\Delta E = 0.192$ kJ represents the gain in the potential energy of the pendulum as it swings through δ_{max} from the impact point (the agreement is even better if ΔE is increased to allow for other losses). Permanent deflection was then determined approximately as the intersection between the δ axis and a line through the point E, parallel to the elastic part of the $F-\delta$ curve. Comparison between the experimental (solid line) and the theoretical (dotted) final deflected shapes is given in Fig. 7.15b.

The theoretical results presented in sections 7.2 and 7.4 can be used to minimise the weight of rings satisfying some safety criteria. The $F-\delta$ diagram of the complete ring should always be produced because section optimisation in section 7.2 affects elastic stiffness of the structure as well. Too low stiffness may leave insufficient room for development of plastic deformation before the structure starts intruding into the specified survival space. It should be also borne in mind that the engineering theory of bending tends to overestimate the stiffness of thinner walled components, and that the assumption of rigid joints is not quite true in real structures.



a.



IMPACT ENERGY 3.4 kJ

----- Computed

————— Actual

b.

Fig. 7.15

7.6 APPLICATION OF THE THEORY TO THE ROLL OVER ANALYSIS OF THE COMPLETE COACH

The theoretical collapse mode and maximum strength of a typical British coach in a roll over has been determined in Chapter 3 (Fig. 3.13). It was mentioned, however, that the maximum strength was somewhat over-estimated due to a relatively large displacement increment and the assumption of constant hinge moments. Both of these effects can now be allowed for by considering a "typical" ring restrained at both waist rails by fictitious springs (Fig. 3.3a). The size of the structure allows the use of smaller displacement increments without a high cost penalty, so that the overshoot of the local load-carrying capacity will be much reduced. The moment reduction during hinge rotation can also be included as described in sections 7.3 to 7.5.

The load-deflection curve for rings B to F (Fig. 3.13) collapsing in mode "A" (Fig. 2.1) has been determined by assuming the stiffness of both fictitious springs in Fig. 3.3a $c = 200$ N/mm. This value is higher than the "critical" one of 150 N/mm (Fig. 3.3) and also gives the lateral stiffness of ring close to the "cumulative" stiffness of the bus body, i.e. the waist rail nodes move laterally approximately as much as those in the middle of the vehicle. The ring collapsed in mode "A" with a maximum strength of 6913N at $\delta = 125$ mm. The fact that all the rings in the actual structure do not collapse quite simultaneously has a very small effect on the cumulative results.

Ring A was analysed using the nearside fictitious spring stiffness of 20 N/mm and leaving the other one at 200 N/mm. The ring collapsed in mode "B" as it should have done and the maximum strength was 6286N also at $\delta = 125$ mm (the local strength overshoot was slightly higher in this case and a figure of 6000N would be more realistic).

The cumulative quasi-static load-deflection curve of the complete body is represented by the line R' in Fig. 3.14 and by the line R_s in Fig. 7.16.

The impact speed of the cant rail of a "typical" bus rolling on flat ground with zero initial angular velocity about the nearside wheels is approximately 4.16 m/s (section 3.2), which is very close to the impact speed of the pendulum during ring tests. This result is very approximate, but gives the right order of magnitude required to estimate the strain rate effect on material properties. Using the more conservative values of strain rate coefficients 1.226 for σ_p and 1.08 for σ_{pu} (section 7.5) and repeating the above procedure the new, "dynamic" load deflection curve R_{d1} in Fig. 7.16 is obtained. The energy absorbed after $\delta = 175$ mm is 7.15 kJ which represents an increase of 10% with respect to the static value. The other extreme value of the strain rate coefficient of 1.3 for both σ_p and σ_{pu} gives the curve R_{d2} in Fig. 7.16 with an energy of 8.31 kJ at $\delta = 175$ mm (28% higher than the static value). The difference between R_{d1} and R_{d2} increases with deflection due to the much higher strain hardening effect of R_{d2}.

The important safety parameters in a PSV roll over are the energy absorbed before the structure starts intruding into the specified survival space and the strength of the deformed structure subject to vertical, distributed roof loading (section 1.2). Combination of the Hungarian survival space proposal in Fig. 1.1b with the PSV structure in Fig. 3.5 gives the allowed deflection of the impacted cant rail of $\delta_{max} \approx 240$ mm (Fig. 7.17a) at any time during roll over. This figure refers to a coach with high back seats and more deflection (≈ 300 mm) is allowed if the seat backs are lower.

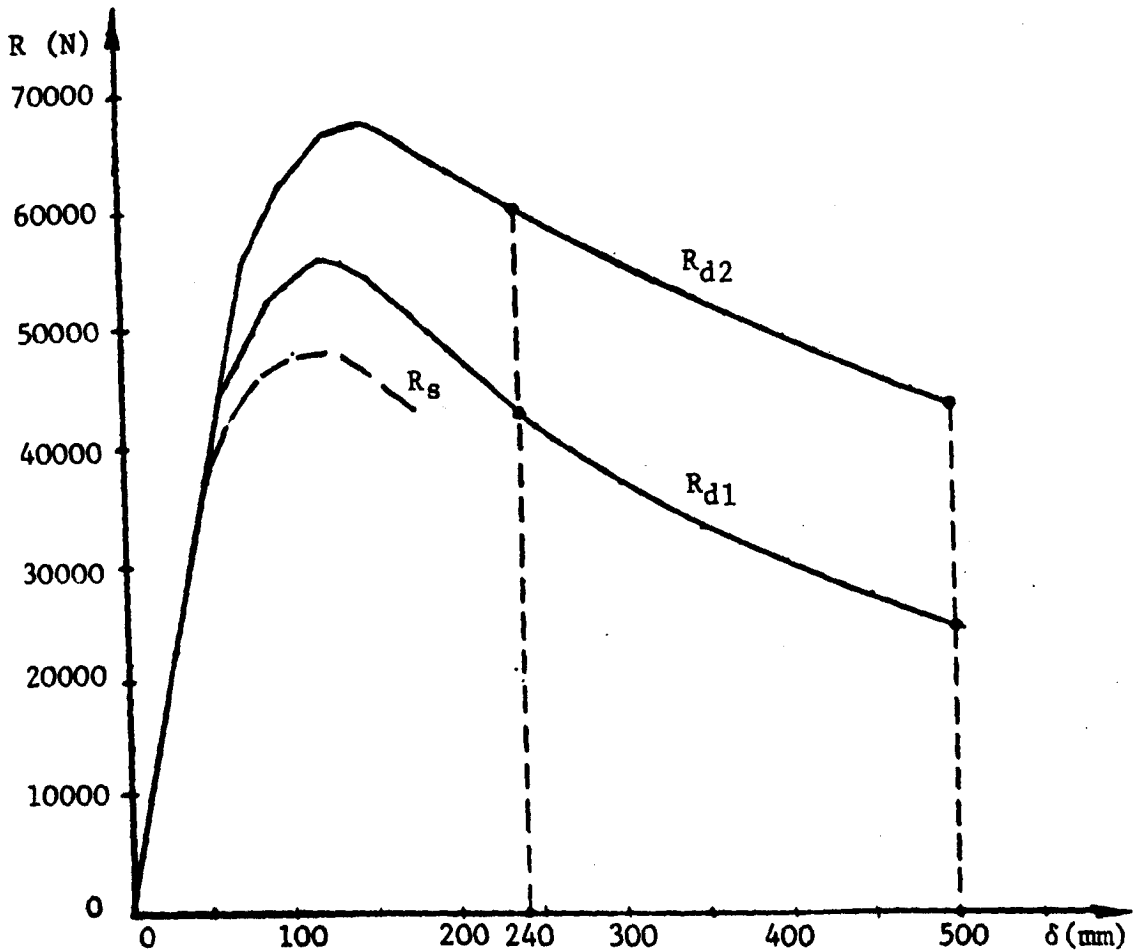
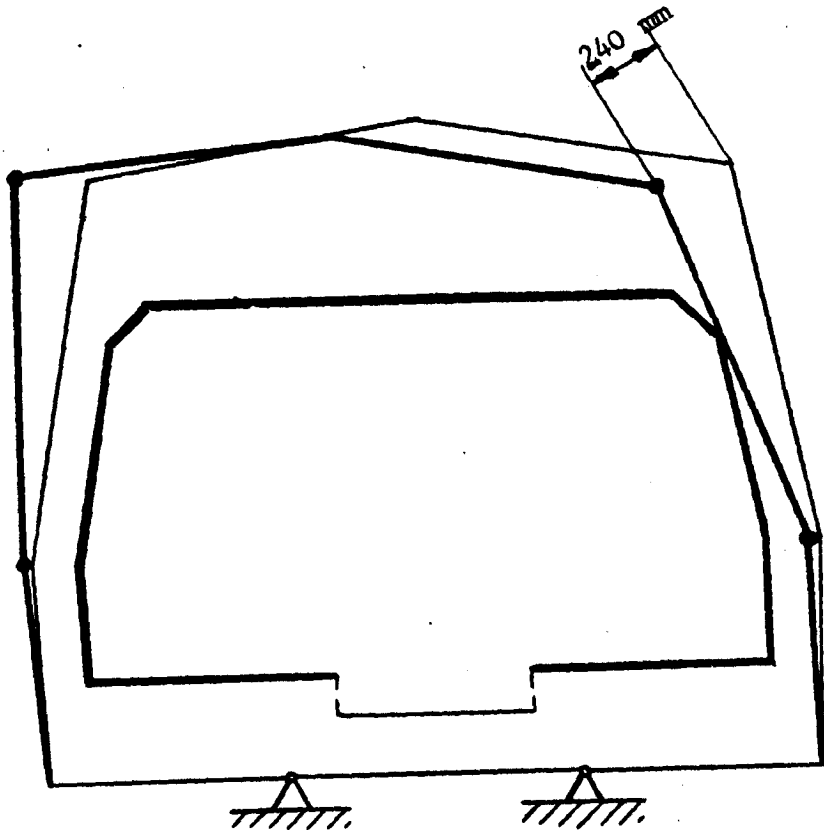


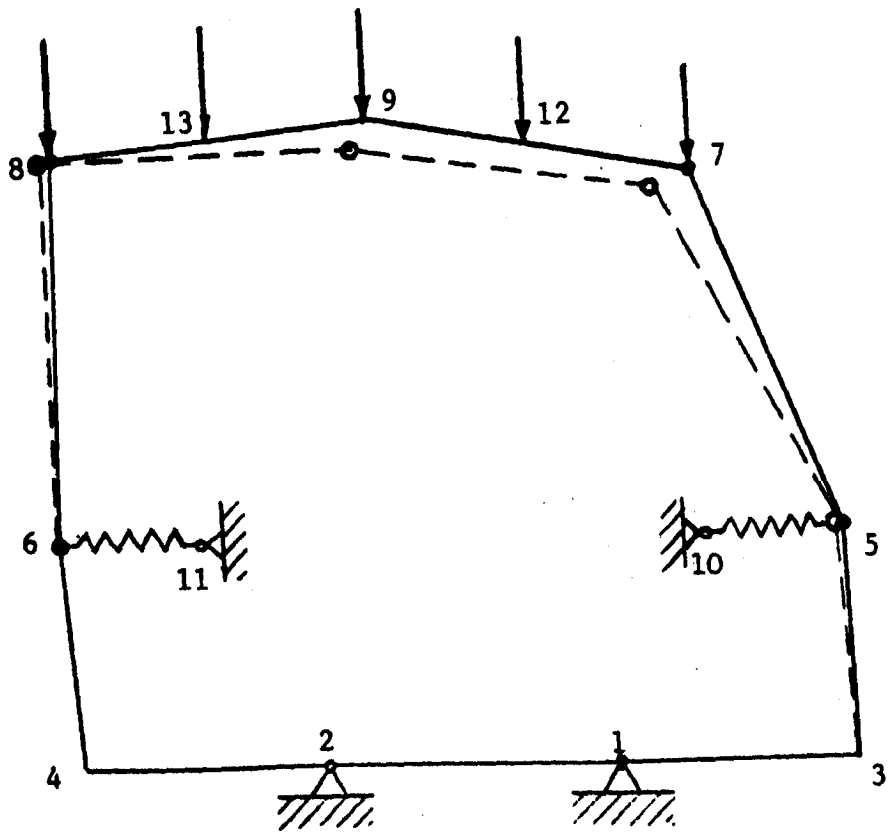
Fig. 7.16

The more conservative curve R_{d1} in Fig. 7.16 gives 10.1 kNm of energy absorbed as the structure deflects through 240 mm, while the area under curve R_{d2} corresponds to the energy of 12.31 kJ . If deflection of 500 mm is allowed (Figs. 7.16 and 7.17a) the theoretical energy absorbed varies between 18.3 kJ (R_{d1}) and 25.4 kJ (R_{d2}). No reversal of elastic deformations is assumed to take place because the coach usually finishes on its roof (section 2.2).

An estimate of the maximum static vertical load that a deformed roof structure can support is now obtained by applying a uniformly distributed load to the roof member of the deformed ring in Fig. 7.17b (displacements should not be applied in this case because the ring would become over-constrained). A uniformly distributed load is usually represented by concentrated forces and the appropriate fixed-end moments for each loaded beam. The fixed end moments would be negligible except at the cant rail nodes 7 and 8 which have the load on one side only. However, incrementation of such an external moment is possible only until a plastic hinge is inserted at the same node. The current program CRASHD does not have a facility to stop moment incrementation under such circumstances and calculation goes wrong after occurrence of a hinge at 7 or 8. Two more nodes 12 and 13 were therefore used in the roof member (Fig. 7.17b). Each



a.



b.

Fig. 7.17

of the five vertical forces represents the appropriate segment of the distributed load and the neglected end moments at 7 and 8 are reduced to values which have little effect on the maximum strength of the ring.

The deflected shape of the structure is known from the results of the first calculation regarding the oblique load at the cant rail (Fig. 7.17b). Node co-ordinates after, say $\delta = 240$ mm (Fig. 7.17a) define the initial geometry for the vertical loading case. Since four hinges at nodes 5, 6, 7 and 8 have already been inserted and rotated, the current local strength at these points is equal to the appropriate internal moments after the step $\delta = 240$ mm in the first calculation. The strain rate effect is greatly reduced, so that only the more conservative result of 8% increase in σ_{pu} is used. It would be safer, still, to use the static values for σ_p and σ_{pu} , but a new "static" collapse run with oblique cant rail loading would be required to determine the remaining hinge strength. Local strength at non-collapsed nodes should have the static value.

The maximum distributed load that a ring can support after $\delta = 240$ mm is, theoretically, 11.5 kN. The load carrying capacity of ring A (Fig. 3.13) is also close, so that the maximum load that the roof can support is 80.5 kN. This collapse mechanism had hinges at nodes 5, 7, 8 and 9 (Fig. 7.17b). The absence of a hinge at node 6 agrees with the relatively small rotation at the offside waist rail hinges observed in accidents (Fig. 2.2), but the hinges between the cant rails were usually confined to structures with local weak points (Figs. 2.2c and 2.3a).

The theoretical roof strength in vertical direction after $\delta = 500$ mm drops to 56 kN, with the same collapse mechanism as after $\delta = 240$ mm.

The above values for the energy absorbed could not be compared with any experimental results, but they are not satisfactory in the light of the energy absorption requirement obtained in ref. 2. The roof strength is also insufficient to support the weight of the vehicle considered. Reserve of roof strength is necessary to allow for some inevitable increase in the static loads as the vehicle rolls on its roof and for non uniform distribution of weight on rings and on each roof member. A complete collapse of the roof structure may be caused by a load even lower than the above figures if the rings start collapsing one after the other due to local overloading.

This section closes the loop initiated in Chapters 2 and 3 of the thesis. The accident survey indicated the relevant characteristics of the collapse behaviour of PSV structures in real roll over accidents, while the rest of the thesis demonstrated a method enabling a designer to predict this behaviour in very early stages of design. The method is based entirely on the usual design data and allows for both the overall and local effects on the collapse performance of the complete vehicle body.

CHAPTER 8

CONCLUSIONS AND RECOMMENDATIONS FOR FURTHER WORK

8.1 CONCLUSIONS

8.1.1 Chapter 1 BUS ROLL OVER SAFETY AND THE ASSOCIATED ANALYTICAL PROBLEMS

Roll over accidents of public service vehicles (PSV) are very dangerous because they directly expose a large number of people to a severe structural deformation of the entire passenger compartment. They are not rare either - twenty one roll overs in Britain have been investigated within a period of the last three years. The relevance of the problem has also been recognised in other countries and there are proposals for more comprehensive international safety legislation. The present PSV safety regulations fail to take into account the most important lateral component of the roof loading and also disregard the structural behaviour after collapse is initiated.

Loading conditions in accidents are substantially different from those arising in normal service. Local failures in framework-type vehicle bodies are caused almost exclusively by bending moments reaching the local load carrying capacity of components. These failures have a role similar to hinges in mechanisms and the overall collapse starts when the number and distribution of these hinges turn the structure into a collapse mechanism. Most of the deformation energy is then absorbed by the material concentrated in hinges.

Structural design for safety should produce vehicle bodies that collapse in a reasonably controllable manner, absorb a sufficient amount of energy without intruding into the survival space and without developing fatal retardations. In the case of roll over, the deformed roof structure should also support the vehicle weight without collapsing into the survival space.

Capability of a vehicle to meet roll over safety requirements depends on its general collapse mode, the energy absorbing capacity of deforming components and on the load carrying capacity of the deformed structure.

The classical collapse analysis was introduced by civil engineers mainly to determine the maximum strength of structures. Application to vehicle body design requires, however, the investigation not only of the overall collapse mode and maximum strength, but also the performance of a structure after it starts collapsing. The first attempts at dealing with roll over protective cabs in earth moving machines and agricultural tractors were still based largely on the classical approach, but with the gradual introduction of geometric non-linearities due to large structural deformations. Later application to cars demanded inclusion of the component stability and some dynamic effects at higher impact speeds.

An outstanding quality of the Cranfield Structural High Deformation Program (CRASHD) is the ability to allow for various hinge moment-rotation characteristics of thin walled components generally applied in vehicle design.

Investigation into the roll over performance of PSV bodies was mainly experimental. Theoretical analysis was confined either to simplified hand calculations applied to well established collapse modes, or to a basically elastic finite element approach.

Most of the theoretical investigations on structural components have been aimed at finding the maximum strength of stable section beams under various loading conditions. The onset of elastic buckling in thin walled beams is also fairly well documented, but only a few papers were found dealing with the determination of the maximum bending strength of such elements. Theoretical research into the collapse behaviour of structural components is very recent and dedicated entirely to the axial or lateral compression. There is still little information on bending collapse of beams and it is based entirely on experimental evidence. This is rather surprising since bending collapse represents the most common collapse mode.

A survey of the published works has, therefore, indicated an apparent lack of information in the following areas:

1. Behaviour of PSV structures in actual roll over accidents;
2. The real collapse analysis of a PSV structure in a roll over situation has not been undertaken;
3. The very relevant bending collapse of rectangular and square section tubes has not been treated theoretically and the amount of experimental evidence is still very limited.

8.1.2 Chapter 2 GENERAL CHARACTERISTICS OF PSV STRUCTURAL PERFORMANCE IN ACTUAL ROLL OVER SITUATIONS

Human error is a major cause of roll over accidents, but in at least 14% of all cases the direct cause was a severe brake failure. The effect of telmar retarders on slippery roads should be examined.

The presence or otherwise of lateral force on the roof structure serves as a distinct criterion for classification of roll over accidents. Accidents with little or no lateral force (roll on side only or "flip overs") usually caused far less damage. It is also more severe if the first impact with a significant lateral component is applied to the cant rail rather than waist rail.

The most frequent accident type is roll over on to the roof on level and relatively even ground or from a moderately elevated road (approximately 1m height difference). Vehicles have generally lost most of their longitudinal speed before the roll over started.

Overall collapse modes depend on roll over dynamics, configuration of the ground and on structural properties of the body. The strengthening effect of glazing in the longitudinal direction might have been important in cases where fore and aft speed of a rolling vehicle was initially present. Collapse is governed by the behaviour of the rings enclosing the passenger compartment.

The roof structures collapsed in an almost pure lateral "lozenging" mode, but with a variety of possible hinge locations. Collapse modes were

affected by the distribution of strength around the rings and also by the side structure below the waist rail and by the seats. Seats have often supported the weight of the overturned bus at least on one side, thus preserving some survival space.

Collapse modes with hinges at the waist rails and cant rails produce maximum hinge rotation before the structure starts intruding into the survival space. This increases the maximum strength and energy absorbing capacity of the structure, but may have a negative effect on the strength remaining after deformation. A comparison of performance of different structures cannot be based, therefore, entirely on the overall collapse mode.

Joint fractures occurred in all accidents, but were particularly common in composite structures. They can drastically reduce the hinge strength and energy absorption since the load carrying potential of the beams they are connecting is not used. A similar effect was produced by beam failures with material separation. The main causes of these failures were stress or strain concentration and inadequate joining methods. Although continuous welding in all metal structures generally provided stronger joints, particularly in simpler designs with more direct load transfer, material separation next to the weld was observed on several occasions.

Local buckling with little or no material separation occurred in steel and aluminium tubes with very repeatable collapse mechanisms. Reduction of hinge strength with rotation is usually much less severe than with fractures, but the assumption of constant hinge moment during complete collapse would not be applicable in this case either.

Driver and passengers stand a much better chance of survival if they are retained within the passenger compartment and if sufficient survival space is preserved during the course of the whole accident. The safest area is between the seats below head rests, but some survival space is also necessary above the head rests.

8.1.3 Chapter 3 THEORETICAL DETERMINATION OF THE OVERALL COLLAPSE MODE OF A TYPICAL BRITISH COACH IN A ROLL OVER

Various collapse modes of PSV structures in roll over accidents had a different effect on passenger safety. It is therefore very desirable to develop a theoretical method of predicting the collapse performance of a particular structure with reasonable accuracy and during relatively early stages of design. The approach suggested in this thesis is based on the application of the program CRASHD for the collapse analysis of structural frameworks.

Application of a quasi-static incremental calculation procedure to an essentially dynamic collapse process is justified by the relatively low speed (less than 10 m/sec) with which the cant rail impacts the ground, by the experimental evidence gathered during static and dynamic tests of bus rings and by the fact that a great majority of the bus mass is distributed away from the load application area and the collapse mechanism itself.

Experiments on rings displayed the same local and overall collapse modes in both static and dynamic conditions. The only exception was an increased

tendency of joint fracture in one design, but the general assumption of the analysis is that the joints are stronger than the beams they are connecting. Although this may not be true in the actual structure, the theory defines very well the loading conditions of all the important joints, so that the actual body can be checked for joint strength and redesigned if necessary.

Displacement increments were applied to the nearside cant rail of the theoretical model, such that the reaction acts at 30° to the floor cross members of the rings. This is justified by the facts that the collapse mechanism is created in early stages of a "typical" roll over accident under the influence of lateral loads, that the displacements can be incremented even after complete collapse of some parts of the body, and that a constant angle of load application may be accepted for laboratory tests of the roll over performance.

Some decisions common in structural modelling for elastic analysis are not adequate to represent the effects arising during collapse. This is particularly true when estimating the influence of panels or other beams ignored in the model on the effective elastic and plastic section properties of elements used in the idealisation. Fictitious spring elements with axial and bending stiffness, attached laterally to the waist rail nodes were therefore used to model the restraining effect of the adjacent side structure on a particular ring. It was shown numerically that variation of this restraining effect may be used to control the ring collapse mode.

A "typical British coach" was used in the example calculation. The internal load distribution within elastic range was determined using a detailed finite element model composed of 556 beams and 145 membrane plates with 400 nodes and 2328 degrees of freedom. The main load paths ran through the rings and the stiffness of the structure increased gradually towards the rear end containing the large box of the luggage compartment.

The elastic model was also used to investigate the effect of rings which have incomplete floor members on the general load distribution, particularly from the collapse point of view. Such rings are used in places where space has to be provided between the chassis side members to accommodate the engine and transmission. The analysis has shown that the effect of such rings is small as long as their number is kept to a minimum (here 2 out of 7 plus two bulkheads) and the other rings are complete. This conclusion agrees with evidence compiled during accident investigation.

The collapse model was much cruder than the elastic one (106 beams and 60 nodes) since it may include only a part of the complete assembly which will envelope the correct collapse mechanism. Properties of the fictitious springs were adjusted to reproduce the bending moment diagrams in rings of the elastic model under identical loading conditions.

The collapse calculation identified an overall collapse mode with hinges at the waist and cant rail nodes, except for the ring next to the entrance door which had one hinge at the floor level in the nearside pillar. It was also found that the second, third and fourth ring from the front were very highly stressed at the floor level as well - some hinges occurred, but without altering the final collapse mode. This means that the

structure is close to a state from which various collapse modes may originate and care must be taken when selecting the side structure components to keep the collapse mechanism under control.

The maximum calculated strength of the structure was reduced by approximately 17% to allow for some overshoot of the local strength of various hinges due to a fixed displacement increment and for the theoretical reduction in the moment of rotating hinges as derived in Chapters 5, 6 and 7.

8.1.4 Chapter 4 BENDING COLLAPSE CHARACTERISTICS OF VEHICLE STRUCTURAL COMPONENTS

Collapse analysis of vehicle structures introduces a number of problems not common in the classical collapse analysis. These are mainly due to the variety of building methods, use of thin walled components and often complex properties of structural joints. All these factors become particularly important if not only the initial strength, but also the behaviour of the collapsing structure, energy absorbed and remaining strength are required.

The very important structural properties: stiffness, strength and energy absorption are often confused in the discussion of the collapse behaviour of a vehicle structure. These three represent entirely different quantities and are not necessarily proportional to one another.

Stiffness is an elastic property relating the increment of external load with the appropriate increment of deflection. Vehicle structural components often display a lower stiffness than the section area and second moments of area give in the engineering theory of bending. The overall stiffness of a structure may be greatly reduced by the elastic stiffness of its joints. Elastic deflections before the collapse is initiated are usually small in comparison with total deformations, so that stiffness rarely represents an important collapse characteristic. This is, however, not so if the elastic deflections are of the same order of magnitude as the total allowed deflection specified, say, by the safety legislation.

Strength of a structure represents its load carrying capacity and depends on the collapse mechanism and hinge properties. The maximum strength is usually achieved at the very beginning of collapse, followed by a gradual decrease controlled by the moment-rotation characteristics of hinges. In special cases where tension builds up during collapse (e.g. door intrusion) the strength may start increasing after initial collapse.

Energy absorbed by the collapsing structure also depends on the collapse mechanism and hinge properties and is proportional to the area under the load-deflection diagram. Energy absorbing capacity of beams in bending is much greater than that of the sheets of the same area.

Static values of the stiffness, strength and energy absorbing capacity are increased under impact loads due to inertia and strain rate effects, unless fractures occur.

Local buckling of thin walled sections reduces the initial strength of the hinge. At the same time it releases the tension parts of the section

from excessive straining, which may prevent catastrophic collapse with material separation in some cases.

Welding at joints may produce annealed zones near the weld with a lower yield stress than the surrounding material. If the structure is subject to large deflections, the strain concentration in these areas may cause an early material separation followed by an abrupt drop in the hinge strength.

8.1.5 Chapter 5 BENDING COLLAPSE OF RECTANGULAR OR SQUARE SECTION TUBES

Rectangular or square section tubes are widely used in structural frameworks and they almost always collapse in bending. Uniaxial bending collapse was evident in all PSV accidents and also in crush testing of other vehicles. The theoretical analysis was aimed at the determination of the maximum strength, strength variation with hinge rotation and energy absorbed during rotation up to angles of $30 \div 45^\circ$. The hinges are assumed to collapse freely under the effect of internal loads only, i.e. no external restraints or loads are applied directly to the hinge mechanism. The assumption is fair for most practical cases of structural collapse.

The maximum bending strength of a tube is equal to or less than the fully plastic moment, depending on the stability of the section walls. The effects of stability and initial geometry imperfections have been allowed for by using results of refs. 66 and 68 and extending them to the rectangular or square closed sections. If the compression flange buckles before collapse is initiated the loads are redistributed to its edges reducing the "effective width" of the flange. Collapse starts and maximum strength is developed when the effective width of the section goes plastic. The fully plastic moments may be safely assumed only if the critical elastic stress of the flange is approximately three times greater than the yield stress of the material. This is due to the possible geometric imperfections affecting stability of the flange.

The theoretical analysis of the hinge collapse behaviour was based on the kinematically admissible set of displacements (collapse mechanism) relating the "internal" deformations along the yield lines to the externally applied displacement-angle of hinge rotation. This approach is known in the limit analysis to produce the upper bound solution to the current hinge strength.

The actual collapse mechanisms in rectangular or square section tubes display a common form. A detailed analysis, supported by a continuous strain pattern in the circular grid applied to the beam surface, revealed that most of the plastic deformation takes place along the characteristic yield lines of the collapse mechanism. A continuation of bending and rolling deformation along yield lines is necessary to maintain the continuity of the hinge walls within the hinge. The term "rolling" does not refer to the manufacturing process but to bending and unbending about a "frictionless" roller. Four characteristic phases in the hinge development were observed. The second stage, between the onset and jamming of the rolling deformation covered the widest range of rotation angles and provided the basis for development of the theoretical model.

The theoretical collapse mechanism was composed of the most significant components of the actual one. A more detailed modelling was rejected on the following grounds: only a small improvement in accuracy could be obtained using a much more complex calculation, and even then fairly crude assumptions in the detail kinematics would have to be made. The mechanism is symmetric about two planes and includes bending about 19 and rolling along 8 yield lines. Inextensible section walls were assumed and the hinge length was accurately predicted using the continuity condition in the two most important sections.

An attempt was made to find a theoretical value of the rolling radius as well. Minimisation of the hinge moment and energy absorbed indicated that the rolling radius tends to be as large as possible. Inextensibility of the section walls was then used again to find the largest radius that would satisfy the continuity conditions, but this resulted in a complex system of non-linear equations which could not produce a solution in a convenient explicit form. An empirical variation of the rolling radius within experimentally established limits was therefore used in the final calculation.

Having established the relationship between the deformations along the yield lines and the angle of hinge rotation, it was possible to use the yield line theory and calculate the energy absorbed by the hinge as it rotates through an arbitrary angle. The theoretical variation of the hinge moment with rotation was then obtained by taking the ratio between finite increments of the energy and appropriate angle at several discrete points. Differentiation of the energy equation with respect to the hinge angle was not used to avoid very long and clumsy expressions.

Formulae for the maximum strength, energy absorbed and moment variation include the material yield stress (σ_p) and the effective fully plastic moment of the section walls (m_p), so that the appropriate values should be selected. The stress state along the yield lines is very complex, but it is reasonable to assume a plain strain field since the section walls may be treated as bent plates. The membrane and shear forces contribute to the yield criterion and reduce the effective fully plastic moment (m_p) in comparison with its value in pure bending (m_0). Even if one assumes an ideally plastic material a 15% difference in the effective yield stress is obtained by using the Tresca or von Mises yield criterion. The actual material often displays some variation of the yield stress in tension and compression, strain hardening, Bauschinger effect and various forms of anisotropy. Anisotropy due to crystallographic texture is often met in rolled sheets and resistance to thinning may have a significant effect on yielding. Strain hardening during tube production gives a very non-uniform distribution of the yield stress along the section perimeter with higher values near the corners. The strain rate effect should also be allowed for under impact conditions.

The more conservative Tresca yield criterion was finally adopted because texture softening was measured in a representative specimen, yield stress at right angles to the direction of rolling during manufacture is usually lower than in the rolling direction itself and internal membrane and shear forces reduce the flow stress determining m_p .

The maximum strength calculation uses the yield stress obtained by uniaxial tension test of a specimen taken from the "parent material" of the section, away from corners or welds.

A reasonably accurate assessment of the strain hardening effect requires the definition of the strain variation along the yield lines in terms of the angle of hinge rotation. An attempt to derive this relationship was not successful because of difficulties related to the theoretical determination of the varying bending and rolling radii and to the inadequacy of the assumption that plane wall sections remain planar during extensive plastic deformation. It was again apparent that a major complication of the theoretical model would still be bound to fairly crude assumptions regarding the detailed strain distribution. A compromise considered more reliable was therefore introduced.

In most specimens tested the maximum nominal flow stress σ_{pu} was virtually constant over an engineering strain region $e = 5 \div 25\%$. The local strains are concentrated along the yield lines, so that they must develop fairly fast with hinge rotation. At the same time the relative effect of the membrane and shear forces on the effective fully plastic moment of the section walls drops rapidly. It was therefore decided to use the maximum nominal flow stress to calculate m_p in the energy and hinge moment equation. The test should also be performed on specimens taken from the tube wall away from corners or weld. Nominally identical specimens may display a variation of properties which are usually within $\pm 5\%$ of the average value, but it is still advisable to test more than one specimen.

Selection of the nominal yield and maximum flow stresses in the theoretical analysis has a great advantage because these are the characteristics usually given in the material specification. Nominal guaranteed properties should be used since they usually provide some safety margin.

8.1.6 Chapter 6

EXPERIMENTAL VERIFICATION OF THE THEORY

The theory was checked against test results obtained by bending rectangular and square section mild steel cantilevers of various dimensions. This test method is simple to perform, enables a good control of the hinge position, free development of the collapse mechanism and a reasonably accurate measurement of the hinge moment and angle of rotation. The effect of shear and axial forces in the beam on the collapse mechanism and yield condition of the material is negligible in reasonably long cantilevers (here $\approx 700\text{mm}$), which was also demonstrated by a comparison with a four point loading beam test with the hinge subject to pure bending.

The initial load increments were followed by displacement increments after the beam started collapsing. The lateral force and the distance between the tip of the cantilever and a fixed point in space were measured after each increment. These data were combined with other relevant rig dimensions to produce a series of discrete points on the hinge moment (M)-rotation (θ) curve. The hinge starts rotating when the beam achieves its maximum strength and the angle θ was calculated allowing for plastic deformations only.

Several preliminary tests confirmed the expectation that the basic theory, developed in Chapter 5, overestimates the hinge strength within the first $5 \div 10^\circ$ of rotation. This was due to the difference between the actual and theoretical hinge mechanisms in the beginning of collapse (section 5.5), to the effect of the initially high membrane forces on

the fully plastic moment of the section walls, to the gradual rather than sudden strain hardening of the material and to the fact that the initial rolling radius is larger than its theoretical substitute. A linear initial moment decrease starting from the theoretical maximum strength was therefore assumed with a condition that the theoretical energy absorbed at a hinge is minimum. The interpolating linear segment is therefore tangent to the basic $M-\theta$ curve.

Jamming of the hinge mechanism occurs when the two sides of the buckle in the compression flange contact each other. This also means the onset of the "secondary" hinge displaying an increase in the moment with further rotation. The theory predicts well the angle of jamming, but the subsequent increase in moment is simulated by an empirical function.

The complete calculation of the theoretical $M-\theta$ curve has been presented in section 6.5. The input data are the section dimensions: width "a", depth "b" and thickness "t" and material properties: yield stress " σ_p " and maximum nominal flow stress (often called maximum strength) " σ_{pu} ". The same formulae are used for any section dimensions or material properties.

The test program included 56 tests on 27 different sections. The aspect ratio a/b ranged between 3.0 and 0.33 and a/t ratio varied between 128 and 9.14. Structural members used in PSV bodies had $a/t \leq 40.6$. The maximum hinge rotation angles were generally close to 40° .

The agreement between the theoretical and experimental results can be assessed from the diagrams in Fig. 6.43. In a great majority of cases the difference between the theory and experiments was less than 10% for both moments at various angles and the appropriate values of the energies absorbed. A good agreement was obtained over the whole range of the test specimens which displayed a great variety of moment reduction curves.

Although further refinements of the theory are possible, the author believes that the theory already provides sufficient accuracy for practical application. This view is supported by the fact that other sources of inaccuracy also occur in mathematical modelling of vehicle structures, i.e. production tolerances regarding material properties and manufacture of the complete structure, the level to which the structure is idealised by a finite-element model and limitations of the computer program used for the collapse analysis.

8.1.7 Chapter 7

APPLICATION OF THE THEORY OF HINGE BEHAVIOUR

The theory of hinge behaviour can be used to optimise rectangular or square section tubes from the safety point of view and to provide the hinge characteristics required by the CRASHD program for the collapse analysis of complete structural frameworks. This gives an opportunity to predict the collapse behaviour of frameworks entirely theoretically, i.e. without testing any of the structural components and also to minimise the weight of the structure meeting some safety criteria.

Section Optimisation

Optimisation of section dimensions is organised as a constrained optimisation problem. The safety criteria that a tube should meet include

some or all of the following: maximum strength, energy absorbed after a given hinge rotation and hinge strength after a given rotation. Material properties (σ_p and σ_{pu}) are also selected, as well as constraints regarding the section geometry. Geometry constraints are necessary for either design and production reasons, or to avoid the application of sections with too low a/b ratio which would be too weak about their other principal axis. The theoretical hinge moment-rotation curve is then used in an iterative numerical process producing a rectangular or square section of minimum area, satisfying the safety criteria and other constraints.

Three different optimisation programs have been written in order to solve a particular optimisation problem in a most economical manner. The first one provides data for plotting boundaries based on the safety criteria and the minimum area section is then determined graphically. The second program minimises the area of the section if only one safety criterion is specified at a time. The result is produced directly in a numerical form. The third option is to use the routine which deals with any combination of the safety requirements and makes use of a standard, but complex and fairly expensive to use NAG library routine for solving problems of non linear, constrained optimisation. Although most advanced, the last program is not always the most economic and also may suffer from numerical ill-conditioning if the area function has a nearly "flat" minimum.

Combination of the Theory with the CRASHD Program

The hinge moment drop off with rotation is allowed for in the CRASHD program by the use of "compound" beam elements which have a negative-stiffness rotary spring attached to the collapsed end(s). The theoretical moment-rotation curve is incorporated into the program, so that it produces automatically the current value of the spring stiffness at the beginning of every new step of calculation. The moment increase after hinge jamming is also taken into account. A very good agreement between the theoretical and experimental load-deflection curves was obtained for the whole range of cantilever tests in Chapter 6.

Bus Ring Collapse Behaviour

Static and dynamic collapse tests were performed on four coach rings composed of rectangular or square section mild steel tubes, and the results were compared with the theoretical prediction. All the rings were fixed at the floor member mounts and loaded obliquely at one cant rail. The theory predicted a correct collapse mode in all four cases and a very good agreement was obtained for the maximum strength of the rings subject to quasi-static loading. The slope of the theoretical load-deflection curve after static collapse has been initiated and the energy absorbed agreed well with the experimental data. A fracture occurred at the loaded joint of one ring causing a sudden and significant drop of resistance not allowed for by the theory. It was also noted that the experimental load-deflection curve starts departing from the theoretical one after the initial load exceeds approximately 50% of the maximum strength. The theoretical stiffness before collapse becomes therefore higher than the actual one, mainly due to some elastic-plastic deformations in the ring joints. This effect may become important if the elastic deformations are of the same order of magnitude as the maximum allowable ones.

The highly fluctuating dynamic loads produced by a pendulum impact applied obliquely to one cant rail cannot be predicted by the quasi-static approach. However, since the overall and local collapse modes are the same in static and dynamic conditions, it is possible to use the strain rate effect on material properties and obtain a theoretical estimate of permanent deflections of the ring after impact. A very good agreement between the theoretical and experimental strain rate values during impact was achieved, but a fairly wide scatter of the appropriate strain rate factors was found in various references. Material separation took place at the impacted joint of one ring, so that a fully adequate comparison with theory could not be made. An accurate prediction of the permanent deflections was obtained in the second case (without fractures) when using the higher extreme values of the strain rate coefficients.

Application to the Collapse Analysis of the Complete Coach

The theoretical collapse mode of a typical British coach in a roll over has been determined in Chapter 3. These results were used in the last section of the thesis to produce a more realistic full load-deflection curve up to a lateral roof deflection of $\delta = 500\text{mm}$, allowing for the theoretical hinge characteristics. The cumulative reaction of the whole structure was obtained as a sum of the individual ring reactions. Two curves with the lower and upper bound strain rate coefficients were produced.

The theoretical energies absorbed by the structure before it starts encroaching on the survival space suggested by Hungarian authors ($\delta = 240\text{mm}$) and after $\delta = 500\text{mm}$ were lower than the requirements of ref. 2.

The maximum roof strength of an overturned bus was also determined as a sum of results obtained for each individual ring. The calculation used a deformed structure ($\delta = 240\text{mm}$ and $\delta = 500\text{mm}$) whose current hinge strength was reduced to allow for the rotation that had already taken place during the cant rail impact. Vertical, concentrated forces simulating the uniformly distributed load on the roof member were used. The theoretical roof strength was insufficient to support the weight of the vehicle, particularly under realistic conditions of non uniform load distribution.

In this way the thesis demonstrates a method enabling a designer to predict the collapse behaviour of the PSV structure in a typical roll over accident or test. The method is based entirely on the usual design data (general layout, section dimensions and material properties) and allows for both the overall and local effects on the collapse performance of the complete vehicle body.

8.2 RECOMMENDATIONS FOR FURTHER WORK

Most of the problems discussed in the thesis are open-ended, so that many different topics could be proposed for further investigation. A selection of the more important ones has been made and these are listed below:

1. Investigation into the collapse behaviour of PSV structures in the actual roll over accidents should be continued mainly because a great proportion of the current evidence refers to relatively old designs which are being gradually abandoned or greatly improved. It would be particularly important to monitor the performance of the future PSV's incorporating various roll over safety features and assess their value in practice.
2. Collapse analysis presented in Chapters 3 and 7 provides information on the potential performance of the structure subject to the condition that all the main structural joints remain intact. It also defines very well the loads acting at each of those joints. The next step in the design process is to concentrate on the relevant details and make them strong enough. Investigation into the strength of joints represents therefore a very important continuation of the present work.

There is, however, an even more interesting and challenging possibility regarding the joints. The above concept treats them as load carrying elements, while the energy absorption is left to the beams. It should not be too difficult, say by various reinforcements and brackets, to raise the joint strength above the required level. There may be a possibility though to exchange the roles of the beams and joints, i.e. to design joints that would be slightly weaker than the beams, but act as better energy absorbers. This would enable, at least in theory, the use of lighter beams (see section 7.2) which would be designed to meet the maximum strength rather than energy absorption requirement.

3. Separate collapse models may be developed for the initial phase of hinge collapse and for the period after jamming. Although these contributions would have an academic value, it is considered much more important to investigate the collapse behaviour of rectangular and square section tubes when subject to biaxial bending. There are two basic directions to follow.

One possibility is to use the compound beam concept of the program CRASHD and try to determine the rotary spring stiffness under biaxial bending. The author believes that the approach similar to the one displayed in this thesis could be used to solve this more complex situation. Even the approximate estimate of the reduction of the two principal moments, without introduction of normality condition at the hinge, would be of great practical value. The theoretical results regarding the uniaxial bending cases could possibly be employed, but this suggestion would have to be supported by experimental evidence.

The other option is to combine the theoretical hinge behaviour in uniaxial bending with the approach demonstrated in refs. 80 and 81. The theoretical moment-rotation curve would be used to determine the scaling parameters α_2 and α_3 (equation 1.5 in section 1.4.2.3) for the bending components of the total collapse load. Development of the theoretical model for the tube collapse in pure torsion would then enable an entirely theoretical analysis of frameworks under arbitrary loading conditions.

4. In some cases of structural collapse, i.e. simply supported beam loaded in the middle, the hinge is directly exposed to the external load, so that external interference with the local section stability or collapse mechanism may take place. This effect will probably vary depending on how thin walled the beam is and how is the load introduced. Further investigation in this area may also provide useful results.
5. The most immediate action to improve the program CRASHD in its present form would be to incorporate the various possibilities into a single, general routine. This refers particularly to the "strain stiffening" effect which does not currently exist in the version dealing with the moment drop off hinge characteristics. It would be beneficial to include the scaling of externally applied displacements or loads, so that the hinges occur in the natural sequence without overshooting the local strengths.

The current efforts to include dynamic collapse analysis of frameworks in the program are also extremely valuable.

6. The section optimisation programs developed in this thesis refer to square or rectangular section tubes only. Further improvements may be possible by using other shapes, multi-cell tubes or various section fillings.

REFERENCES

1. Kecman D., Miles J.C., Sadeghi M.M., Tidbury G.H.: Investigation of PSV Roll Over Safety; Conf. The Design, Construction and Operation of PSV's; IMechE and SAS, Cranfield 1977.
2. SAS Structural Design Group: Reports to the DoT on the PSV Roll Over Research, SAS, 1975-78
3. Matolcsy M.: Bus Research and Development at AUTOKUT Research Institute, Hungary, source as 1 above.
4. Adams A., Khadilkar L., Pauls L., Rup W.: Development of a Unitized School Bus; Report DOT HS-802005 to the US Dept. of Transportation, 1976.
5. Ryabichinski A.I., Ilinski E.V., Fotin R.K.: Testing of the Bus Roll Over Safety, Proc. of the G.K.S.B., L'vov, 1972 (in Russian).
6. Barr H.F.: Automotive Safety in Review, SAE paper 700247.
7. Wilson R.A.: A Review of Vehicle Impact Testing: How it Began and What is Being Done, SAE paper 700403.
8. Klose G.L.: Engineering Basics of Roll Over Protective Structures; SAE paper 690569.
9. Steinbruegge G.W.: Energy Analysis of Side Upsets with a Large Deflection Tractor Cab, Am. Soc. of Agricult. Engineers, paper 75-1549, 1975.
10. Macarus W.P.: Design and Testing of Rollover Protective Structures in Accordance with SAE J395; SAE paper 710509.
11. Wetjen R.D.: Testing ROPS and FOPS for Safety Compliance; SAE paper 760689.
12. Ashburner J.E.: Aspects of the Design and Testing of Tractor Safety Frames; IMechE paper 202/75.
13. Srivastava A.K., Rehkugler G.E., Masemore B.J.: Similitude Modelling for ROPS Overturn Tests; Am. Soc. of Agricult. Engineers, paper 76-1524, 1976.
14. Cobb L.J.: ROPS Force and Energy Absorption from Simulated Overturn Analysis; SAE paper 760691.
15. Yeh R.E., Huang Y., Johnson E.: An Analytical Procedure for the Support of ROPS Design, SAE paper 760690.
16. Pistler R.A.: Computer Analysis of Roll over Protective Structures, Soc. for Exp. Stress Analysis, Spring Meeting, May 1975.
17. Easter R.G.: Analytical Prediction of ROPS Static Elastic-Plastic Behaviour, Soc. for Exp. Stress Analysis, Spring Meeting, May 1975.
18. Thompson J.E.: Vehicle Crush Prediction Using Finite Element Techniques SAE paper 730157.

19. Saczalski K., Park K.: An Interactive Hybrid Technique for Crashworthy Design of Complex Vehicular Structural Systems; SAE paper 740327.
20. Kirioka K., Hotta Y., Saji H.: Elasto-Plastic Analysis of Automobile Body Structure by the Finite Element Method; SAE paper 740039.
21. Przemieniecki I.S.: Discrete Element Methods for Stability Analysis of Complex Structures; Aeron. J., 72, 1968.
22. Kajio Y., Hagiwara I.: Non-Linear Analysis of a Car Body Structure; SAE paper 760022.
- 23. Miles J.C.: The Application of Finite Element Methods to Vehicle Collapse Analysis; PhD thesis, Cranfield Institute of Technology, 1977.
24. Wardill G.A.: Small Computer Procedures as Tools for Structural Designers, I.Mech.E./A.S.A.E. Conf. "Body Engineering", Proc. I.Mech.E. Vol 184 pt 3M, 1969-70.
- 25. Miles J.C.: The Determination of Collapse Load and Energy Absorbing Properties of Thin Walled Beam Structures Using Matrix Methods of Analysis; Int. J. Mech. Sci., Vol 18, 1976.
- ✓ 26. Miles J.C., Wardill G.A.: Analysis and Design of a Fire Engine Safety Cab using Finite Element Methods; I.Mech.E. paper Vol 191 29/77.
- ✓ 27. Miles J.C., Kecman D.: Application of the finite element method to the roof crush and door intrusion analysis of a passenger car, paper considered for one of the SAE meetings in 1979.
28. Rumph W.C.: Static Load Test Code for School Bus Body Structures, SAE Report No. 650717.
29. Severy D.M., Brink H.M., Baird J.D.: School Bus Passenger Protection, SAE Paper 670040.
30. Lundstrom L.C., Kelly A.H., La Belle D.J.: Crash Research for Vehicle Safety, SAE paper 831A.
31. Voith A.: Investigation into the Roll Over Safety of Bus Superstructures 6th Meeting of Bus Experts, Budapest 1975. (In German).
32. Voith A.: Proposals for Bus Roof Strength with regard to Roll Over; Conf. "Science and Motor Vehicles 77", JUMV., Belgrade 1977 (in German).
33. Matolcsy M.: Constructional Problems of Buses from the Viewpoint of Frontal Collisions; Conf. "Science & Motor Vehicles 77", JUMV., Belgrade 1977.
34. McHugh J., Tidbury G.H.: The Design of Touring Coach Bodywork for Safety, I.Mech.E. paper C200/73, Conf. "Vehicle Safety Legislation - Its Engineering and Social Implications", I.Mech.E./S.A.S., 1973.
35. Tidbury G.H.: Roof Strength of Public Service Vehicles, S.A.S., 1975 (unpublished).

36. Tidbury G.H., Miles J.C.: Collapse Analysis of Automotive Structures Using Finite Element Techniques, Cong. FISITA, Tokyo, 1976.
37. Snoad M.: The Simulation of the Dynamic Rollover Loads in a Bus Ring by Means of a Scale Model, MSc thesis, S.A.S., C.I.T., 1975.
38. Robinson C.R.: The Development of a Model Bus Ring Rollover Test Rig, MSc. Thesis, S.A.S., C.I.T., 1975.
39. Hill R.: Mathematical Theory of Plasticity, Calendar Press, Oxford 1950.
40. Nadai A.: Theory of Flow and Fracture of Solids, Vol II, McGraw Hill, 1963.
41. Slater R.A.C.: Engineering Plasticity, The MacMillan Press, 1977.
42. Baker J., Heyman J.: Plastic Design of Frames I, II, Cambridge University Press, 1969, 1971.
43. Baker J.: The Steel Skeleton, Cambridge Univ. Press, 1956.
44. Neal B.G.: The Plastic Methods of Structural Analysis, 3rd Ed., Chapman and Hall, 1977.
45. Bleich F.: Buckling Strength of Metal Structures, McGraw Hill, 1952.
46. Goldsmith W.: Impact, E. Arnold Ltd., London 1960.
47. Johnson W.: Impact Strength of Materials, E. Arnold, 1972.
48. Hill R., Siebel M.: On Combined Bending and Twisting of Thin Tubes in the Plastic Range; Phil. Mag. 42, 722, 1951.
49. Hill R., Siebel M.: On the Plastic Distortion of Solid Bars by Combined Bending and Twisting; I.Mech.Phys. Solids, 1, 1953.
50. Siebel M.: The Combined Bending and Twisting of Thin Cylinders in the Plastic Range; I.Mech.Phys. Solids, 3, 189, 1953.
51. Hill R., Siebel M.: On the Plastic Distortion of Solid Bars by Combined Bending and Twisting, I.Mech.Phys. Solids, 1, 207, 1953.
52. Steele M.C.: The Plastic Bending and Twisting of Square Section Members, I.Mech.Phys. Solids, 3, 156, 1954.
53. Gaydon F.A., Nuttal H.: On the Combined Bending and Twisting of Beams of Various Sections; I.Mech.Phys. Solids, 6, 17, 1957.
54. Imegwu E.O.: Plastic Flexure and Torsion; I.Mech.Phys. Solids, 8, 144, 1960.
55. Green A.P., Hundy B.B.: Plastic Yielding of I Beams; Engineering, July, 1957.

56. Heyman J., Dutton V.L.: Welding and Metal Fabrication, 22, 564, 1954.
57. Radomski M., White D.J.: Some Theoretical Considerations Relating to Strain Concentration in Elastic-Plastic Bending of Beams; I. of Strain Analysis, 3, 4, 1968.
58. Strel'bickaya A.I., Yevsenko G.I.: Experimental Investigation into the Elastic-Plastic Behaviour of Thin Walled Structures; Naukova Dumka, Kiev 1968 (in Russian).
59. Santathadaporn S., Chen W.: Interaction Curves for Sections under Combined Biaxial Bending and Axial Force; WRC Bulletin 148, 1970.
60. Morris G.A., Fenves J.: Approximate Yield Surface Equations, Proc. Amer. Soc. Civ. Eng. (J. Eng. Mech. Div.), Aug. 1969.
61. Shakir-Khalil H., Tadros G.S.: Plastic Resistance of Mild Steel Rectangular Sections; Struct. Engineer, No. 7, Vol 51, 1973.
62. Shakir-Khalil H.: Plastic Resistance of Sections under Biaxial Bending and Torsion; The Struct. Engineer, No. 3 Vol 54, 1976.
63. Winter G.: Strength of Thin Steel Compression Flanges, Trans. ASCE, Vol 112, AISI, 1970.
64. Von Karman T., Sechler E.E., Donnel L.H.: Strength of Thin Plates in Compression; Trans ASME, 54, 53, 1932.
65. Chilver A.H.: The Stability and Strength of Thin Walled Steel Struts; The Engineer, Aug. 1953.
66. Rhodes J.: The Non Linear Behaviour of Thin Walled Beams subjected to Pure Moment Loading; PhD thesis, Univ. of Strathclyde, Glasgow 1969.
67. Rhodes J., Harvey J.M.: Design of Thin Walled Beams; Conf. Exp. Stress Analysis in Design, Cambridge, 1970.
68. Dawson R.G., Walker A.C.: A Proposed Method for the Design of Thin Walled Beams which Buckle Locally; The Struct. Engineer, No. 2, Vol 50, 1972.
69. Pugsley A., Macaulay M.: The Large-Scale Crumpling of Thin Cylindrical Columns; Quart. J. Mech. and Appl. Math., Vol 13, 1960.
70. Alexander I.M.: An Approximate Analysis of the Collapse of Thin Cylindrical Shells under Axial Loading; Quart. J. Mech. and Appl. Math., Vol 13, 1960.
71. Ohkubo Y., Akamatsu T., Shirasawa K.: Mean Crushing Strength of Closed-Hat Section Members; SAE Paper 760040.
72. Rawlings B., Shapland P.: The Behaviour of Thin-Walled Box Sections under Gross Deformation; The Struct. Engineer No. 4, Vol 53, 1975.

73. Johnson W., Soden P.D., Al-Hassani S.T.S.: Inextensional Collapse of Thin-Walled Tubes Under Axial Compression; J. of Strain Analysis for Eng. Design, No 4, Oct., 1977.
74. Wimmer A.: Einfluss der Belastungsgeschwindigkeit auf das Festigkeits- und Verformungsverhalten von Blechkonstruktionen am Beispiel von Kraftfahrzeugen; Congress FISITA, Tokyo 1976.
75. Wierzbicki T., Akerström T.: Dynamic Crushing of Strain Rate Sensitive Box Columns; II Int. Conf. on Veh. Struct. Mech., SAE, Mich., 1977.
76. Newman R.N., Rawlings B.: An Analysis of Impact Overload in a Simplified Vehicle Structural System; Conf. on Vehicle Safety Legislation, I.Mech.E., S.A.S. (Cranfield Inst. of Tech), 1973.
77. Molnar C.: Plastic Deformations and Energy Consumption at Dynamic (Impact) Loads; I.Mech.E./S.A.S. (Cranfield) Conf. on Design, Construction, and Service of PSV's, Cranfield 1977.
78. Davies P., Kemp K.O., Walker A.C.: An Analysis of the Failure Mechanism of an Axially Loaded Simply Supported Steel Plate; Proc. Instn. Civ. Eng., 59, 1975.
79. Johnson W., Reid S.R., Reddy T.Y.: The Compression of Crossed Layers of Thin Tubes; Int. J. Mech. Sci., Vol 19, No 7, 1977.
80. McIvor I.K., Anderson W.J., Bijak-Zochowski: An experimental Study of the Large Deformation of Plastic Hinges; Int. J. Solids and Structures, Vol 13, 1977.
81. McIvor I.K., Wineman A.S., Wang H.C.: Plastic Collapse of General Frames; Int. J. Solids Structures, Vol 13, 1977.
82. Prager W., Hodge P.G.: Theory of Perfectly Plastic Solids, John Wiley & Sons, Inc., New York, 1951.
83. Bulson P.S.: The Stability of Flat Plates, Chatto and Windus, 1970.
84. Stowell E.Z.: A Unified Theory of Plastic Buckling of Columns and Plates, NACA, Tech. Note 1556, 1948, and NACA Tech. Note 2020, 1950 or Rep. No. 1029, 1951.
85. Coan J.M.: Large Deflection Theory for Plates with Small Initial Curvature Loaded in Edge Compression, J. App. Mech. Vol. 18, 1951, p. 143-151.
86. Walker A.C.: The Post-Buckling Behaviour of Simply Supported Square Plates, Aero. Quarterly, Vol. 20, 1969, p. 203-222.
87. Tidbury G.H., Kecman D.: Investigation into the Behaviour of Hinges Produced by Bending Collapse of Vehicle Structural Components, Congress FISITA, Budapest 1978.
88. Tresca H.: Sur l'écoulement des corps solides soumis à de fortes pressions, C.R. Acad. Sci. Paris, 59, 754, 1864.

89. Von Mises R.: Mechanik der festen Körper im plastisch deformablen Zustand, Nachr. Ges. Wiss., Göttingen, 582, 1913.
90. Dallas D. (Editor-in-Chief): Tool and Manufacturing Engineers Handbook, 3rd Edition, McGraw Hill, 1976.
91. Bauschinger J.: Ueber die Veränderung der Elasticitätsgrenze und die Festigkeit des Eisens und Stahls, Mitt. a.d. Mech. Tech. Lab., München, No. XIII, 1886.
92. Backhofen W, et al (Editors): Fundamentals of Deformation Processing, Proc. of the 9th Sag. Army Mat. Res. Conf., Syracuse Univ. Press. 1964.
93. Tabor D.: Hardness of Metals, Oxford Univ. Press, 1952.
94. Experimental exercises carried out during the 1976/77 postgraduate course at the School of Automotive Studies, C.I.T.
95. Manjoine M.J.: Influence of Rate of Strain and Temperature on Yield Stress of Mild Steel, ASME Trans., Vol 66, 1944.
96. Bodner S.R.: Deformation of Rate-sensitive Structures Under Impulsive Loading, Conf. "Engineering Plasticity", Cambridge Univ. Press, Cambridge 1968.
97. Anderson W.J., McIvor I.K., Kimball B.S.: Modular Program Development for Vehicle Crash Simulation, Vol 2 - Plastic Hinge Experiments, Report to NHTSA, Contract No. DOT-HS-4-00855, Univ. of Michigan, 1976.
98. Livesley, R.: Matrix Methods of Structural Analysis, Pergamon Press, Oxford, 1964.
99. Bisshopp, K.E., Drucker K.C.: Large Deflection of Cantilever Beams, Quart. Appl. Math., Vol 3, p.272, 1945.
100. Frisch-Fay R.: A New Approach to the Analysis of the Deflection of Thin Cantilevers, J. Appl. Mech., 28, 87-90, 1961.
101. British Steel Corporation: "Hypress" steels pamphlet, Ref. No. SSD 874.

APPENDIX 1

The First Model of the Hinge Collapse Behaviour

The first model of the hinge collapse behaviour (87) was based on Figs. 5.12 and 5.13. The characteristic equations (5.24) ÷ (5.30) were simplified by assumptions, supported by experimental evidence, that $\xi = \rho = \theta/2$, $y_U = y_S$, $z_U = z_S$ (U coincides with A) and that $z_V = z_S$. This approximation was then used to derive the theoretical energy absorbed $W(\theta)$ in a square section tube of the depth "b", wall thickness "t" and rolling radius "R" which was approximately equal to the section corner radius in the case considered. The result was:

$$W(\theta) = \frac{\sigma_P t^2}{4} b_1 \left[2\pi - \theta - 4 \arcsin \left(1 - 2 \sin \frac{\theta}{2} \right) + 4\eta + \right. \\ \left. + 0.5 \frac{b'}{b_1} \left(\varphi + 4 \frac{BA_1}{R} \right) + \frac{8 BA_1 K_1 A}{3 b_1 R} \right]$$

where $b' = b - t$; $b_1 = b - 2R - t$

$$y_B = b' \left\{ \cos \frac{\theta}{2} - \left(0.5 - \sin \frac{\theta}{2} \right) \cot \left[\arcsin \left(1 - 2 \sin \frac{\theta}{2} \right) \right] \right\}$$

$$y_{A1} = \frac{(b' - 4R + y_B)(b' - y_B)}{4R - 2y_B + 2(b' - 2R) \sqrt{1 + \tan^2 \frac{\theta}{2}}} + 2R$$

$$\varphi = \frac{\pi}{2} + \arcsin \frac{(y_{A1} - 2R) \tan \frac{\theta}{2}}{(y_{A1} - y_B) \left(1 - 2 \sin \frac{\theta}{2} \right)}$$

$$BA_1 = \frac{(y_{A1} - 2R) \tan \frac{\theta}{2}}{\cos \left[\arcsin \frac{y_{A1} - y_B}{(y_{A1} - 2R) \tan \frac{\theta}{2}} \right]}$$

$$y_{AT} = \frac{y_{A1} - 0.5 b' \tan \frac{\theta}{2} - R}{1 + \tan^2 \frac{\theta}{2}}$$

$$\eta = \arcsin \frac{(y_{A1} - 2R) \tan \frac{\theta}{2}}{\sqrt{\left(0.5 b' - y_{AT} \tan \frac{\theta}{2} \right)^2 + (y_{AT} - y_{A1} + R)^2}}$$

and

$$K_1 A = \sqrt{0.25 b^2 + \frac{(y_{A1} - 2R)^2}{\cos^2 \frac{\theta}{2}}}$$

Discrete points on the M-θ curve were calculated using equation (5.69).

Comparison between the theoretical and experimental results for section 18 (Table 6.1) is given in Fig. A1-1. A constant average value of the rolling radius R was taken $R = 0.04 \cdot KL = 4 \text{ mm}$ (section 5.3). The two theoretical curves A and B in Fig. A1-1 were obtained by using σ_p or σ_{pu} in the energy equation and correspond to the two curves (B and A) in Fig. 6.9.

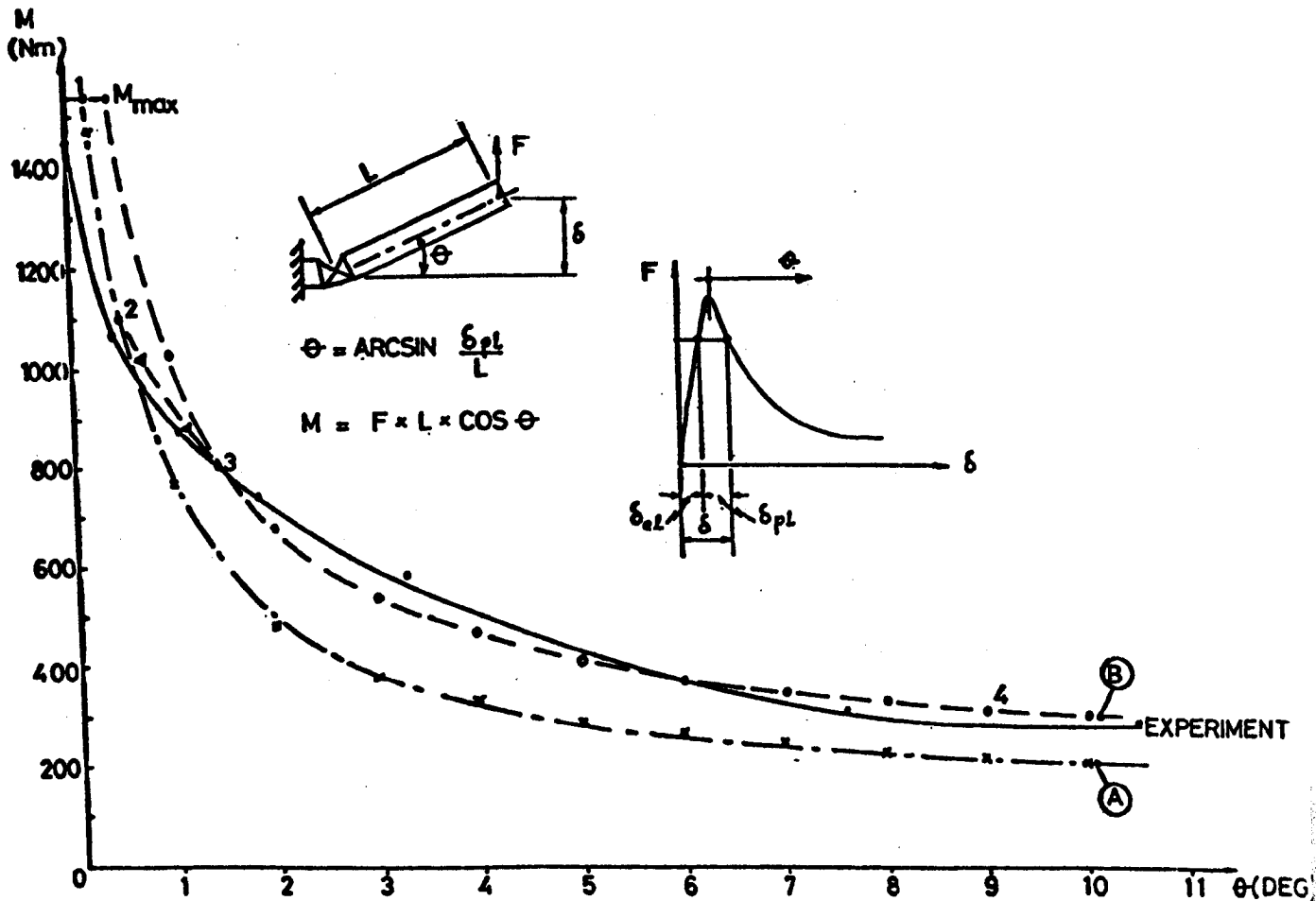


Fig. A1-1 (Ref. 87)

APPENDIX 2

The energy of rolling deformation (W_r) along the yield line GA is given by the equation (5.57) as:

$$W_r = m_p \frac{h}{r} \cdot z_A \quad (A2.1)$$

Co-ordinate z_A , corresponding to the model in Fig. 5.14 can be derived from the continuity condition:

$$b = z_A - r + r \cdot \frac{\pi}{2} + \sqrt{y_A^2 + z_A^2}; \quad \text{for } z_A \geq r \quad (A2.2)$$

$$\text{where } y_A = y_B - r \quad (A2.3)$$

and $y_B = y_B(\theta)$ is known from (5.34).

The last two equations are solved for z_A and substitution into (A2.1) yields:

$$W_r(r, \theta) = m_p \frac{h}{r} \frac{b^2 - (y_B - r)^2 + r(0.5\pi - 1) [2b - r(0.5\pi - 1)]}{2 [b - r(0.5\pi - 1)]} \quad (A2.4)$$

Derivations (5.31) and (5.32) of the expression (A2.4) indicated that the rolling radius tends to be as large as possible, but no zeros could be found within the limits of the problem considered.

APPENDIX 3

Diagrams within Appendix 3 represent the nominal stress (σ_o) - engineering strain (e) curves of the materials used in the tubes tested. Curves were obtained by uniaxial, quasi-static tensile tests on standard specimens. The numbers in the diagrams correspond to the values indicated in Fig. A3-1a.

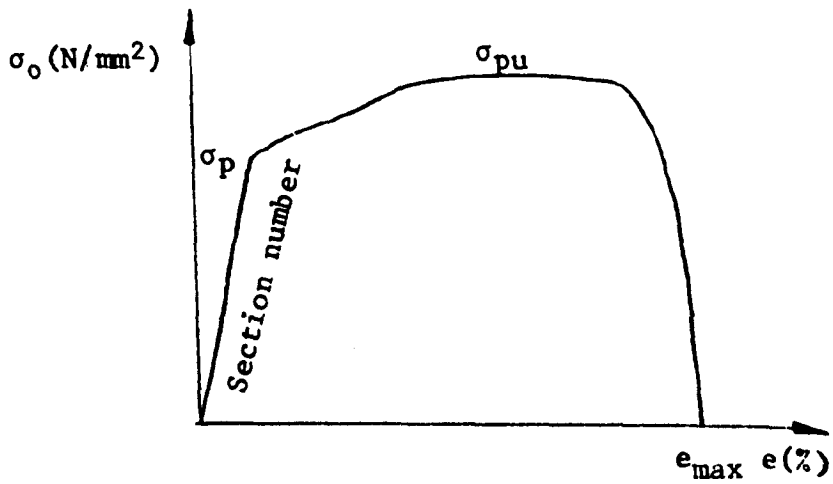


Fig. A3-1a

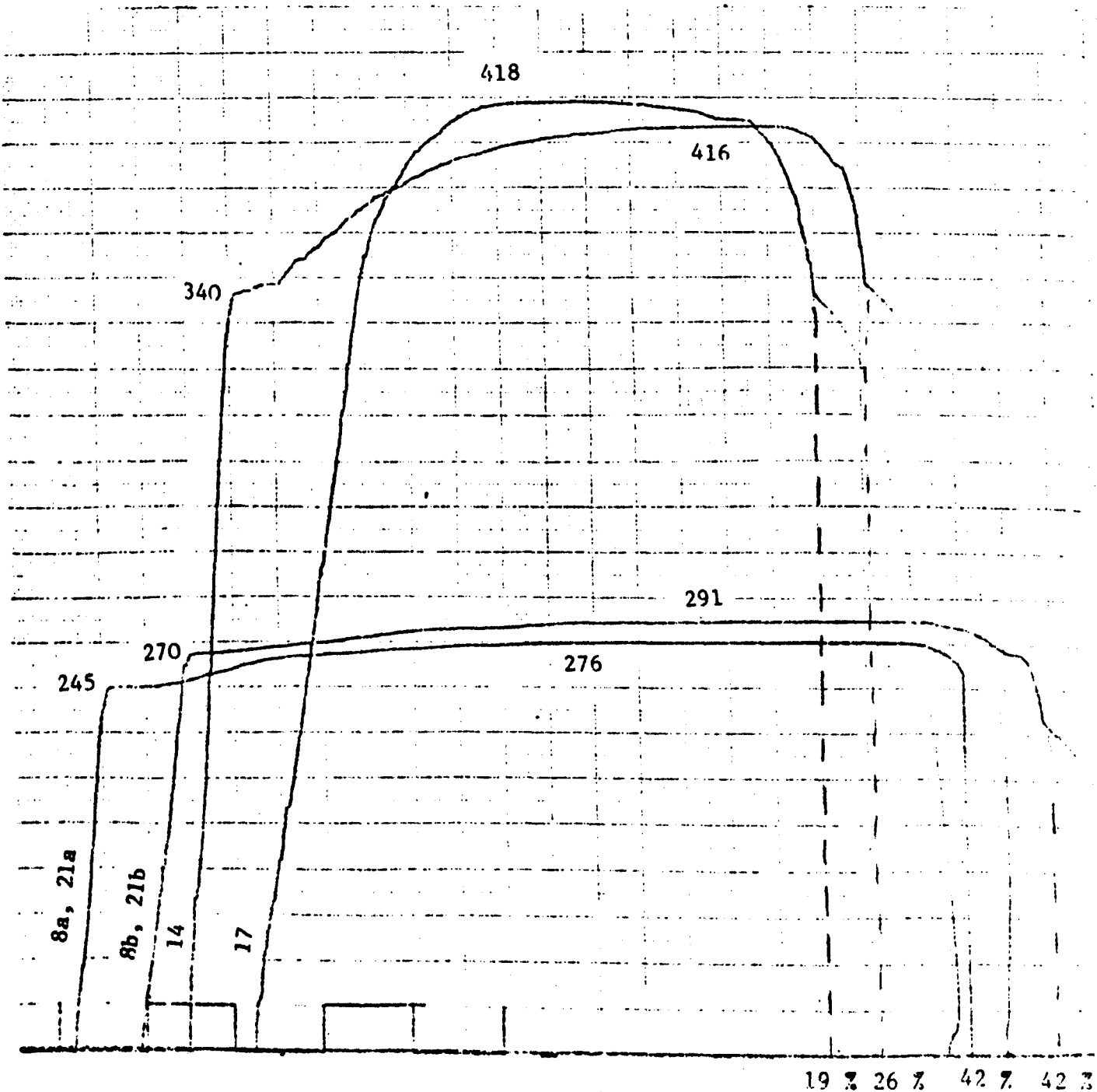


Fig. A3-1 SECTIONS 8, 14, 17 and 21

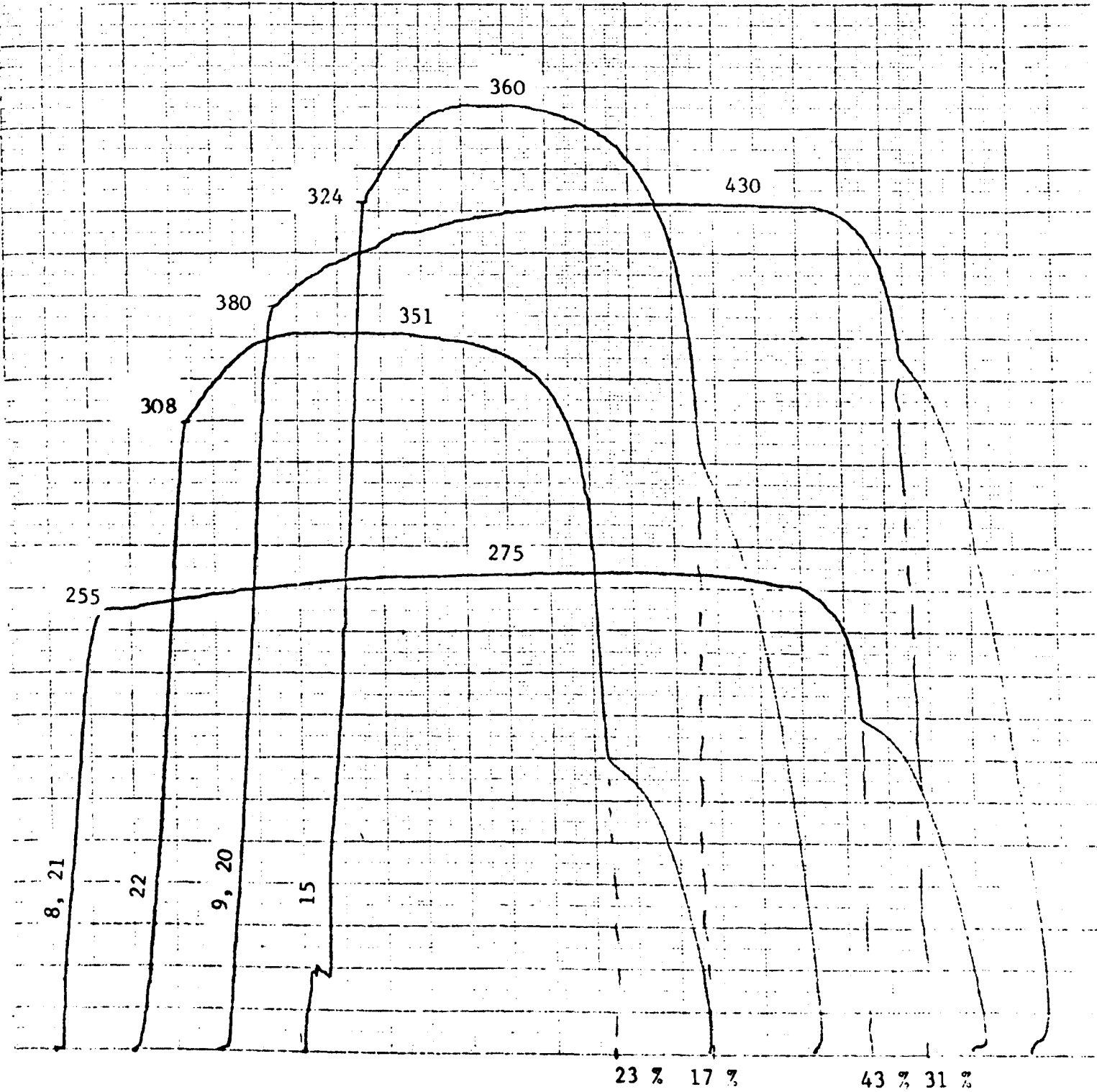


Fig. A3-2 SECTIONS 8, 9, 15, 20, 21 and 22

PRINTED IN ENGLAND

INSTROM LTD., HIGH WYCOMBE, BUCKS.

No. 101

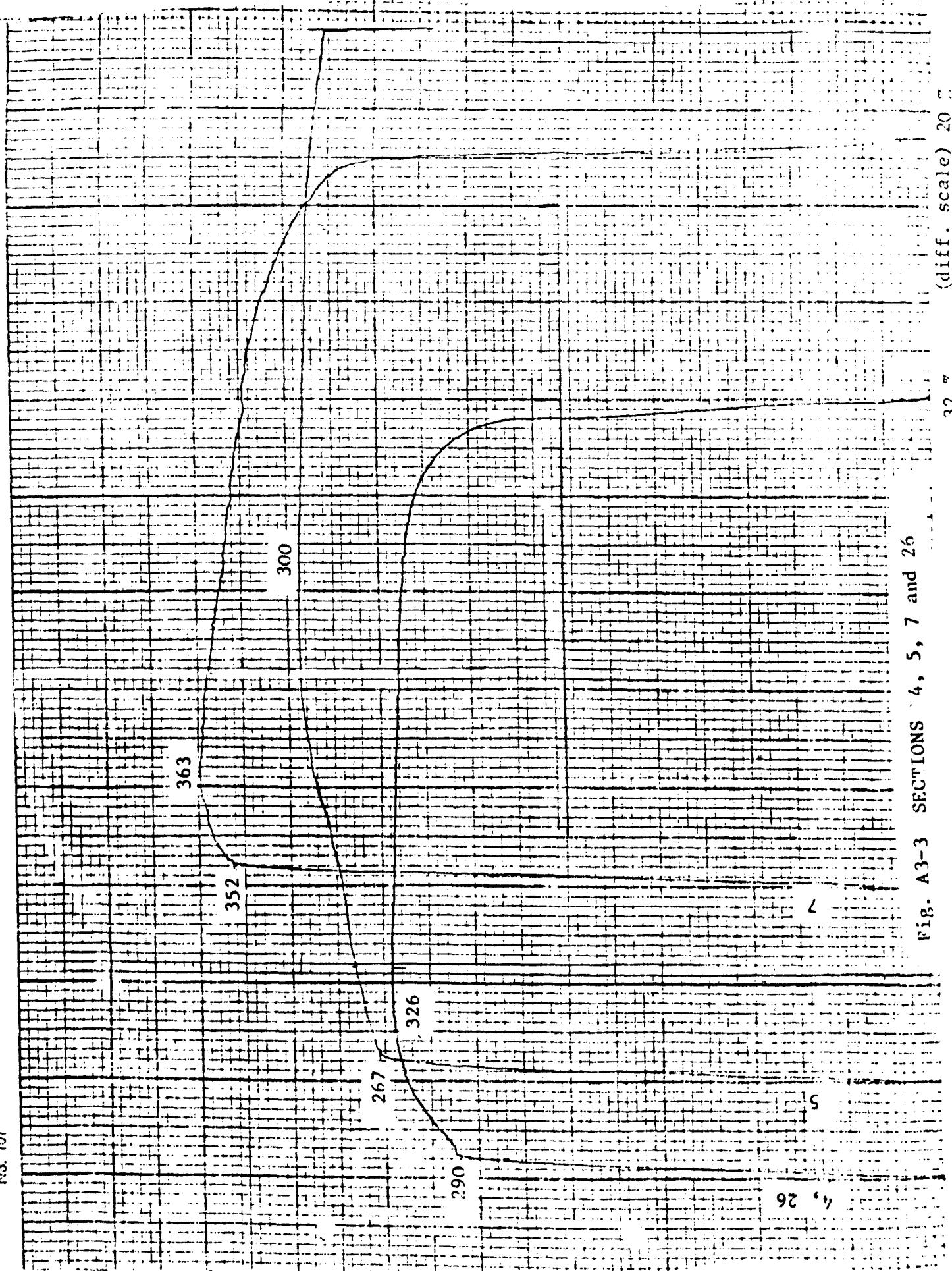


Fig. A3-3 SECTIONS 4, 5, 7 and 26

(diff. scale) 20

32

PRINTED IN ENGLAND

INSTON LTD., HIGH WYCOMBE, BUCKS.

No. 101

PRINTED IN ENGLAND

WYCOMBE, BUCKS.

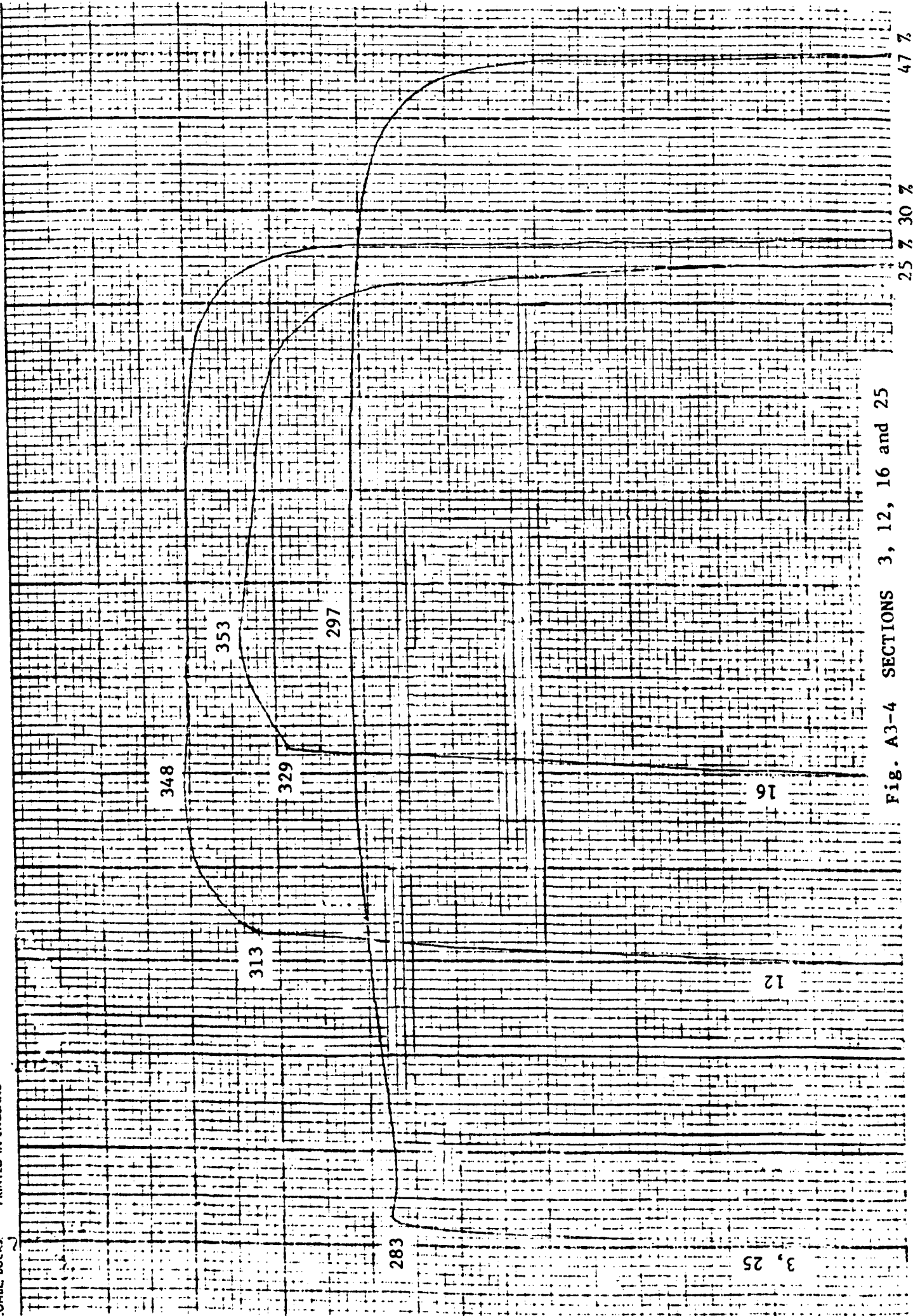


Fig. A3-4 SECTIONS 3, 12, 16 and 25

47 %

25 % 30 %

3, 25

No. 101

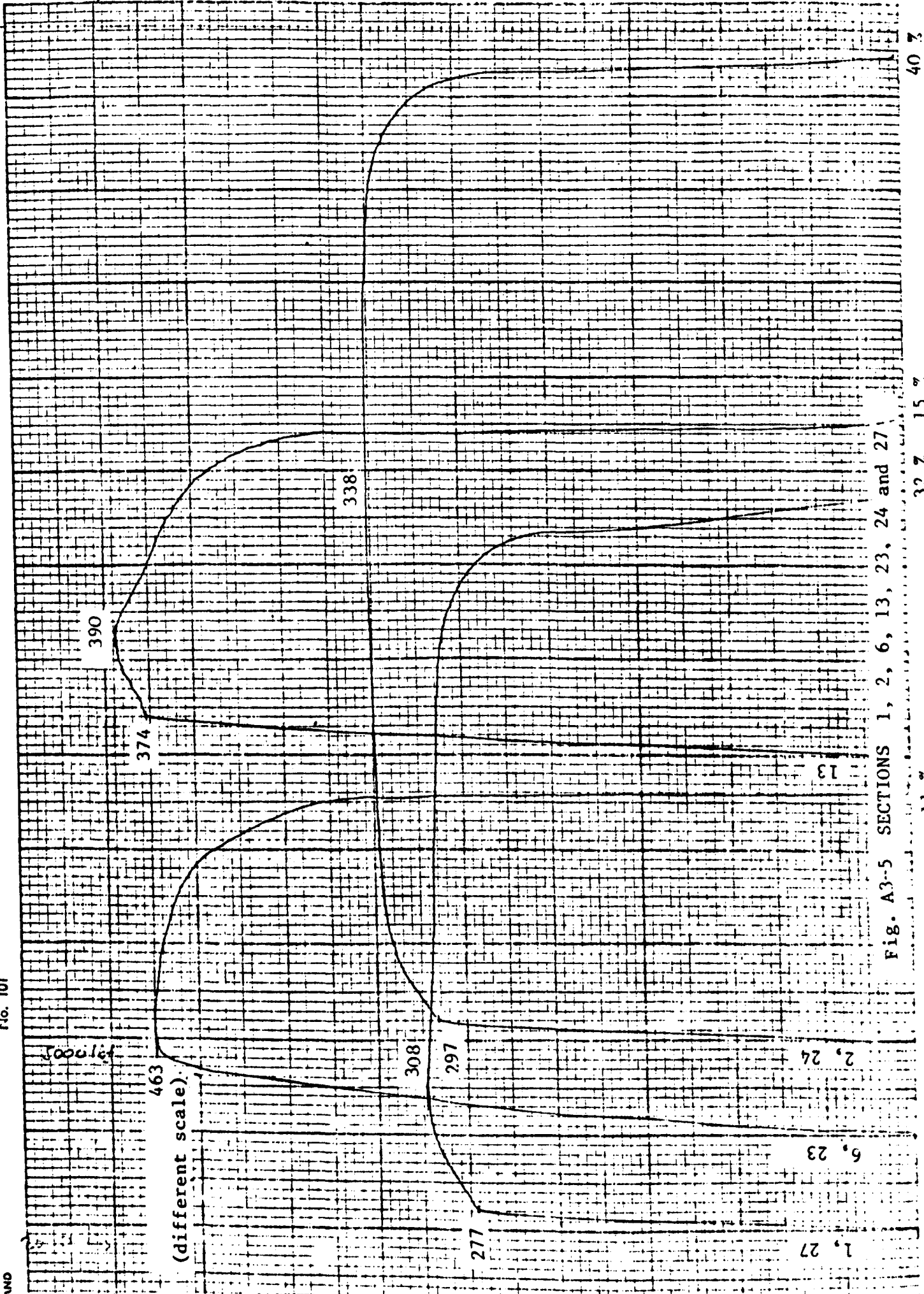
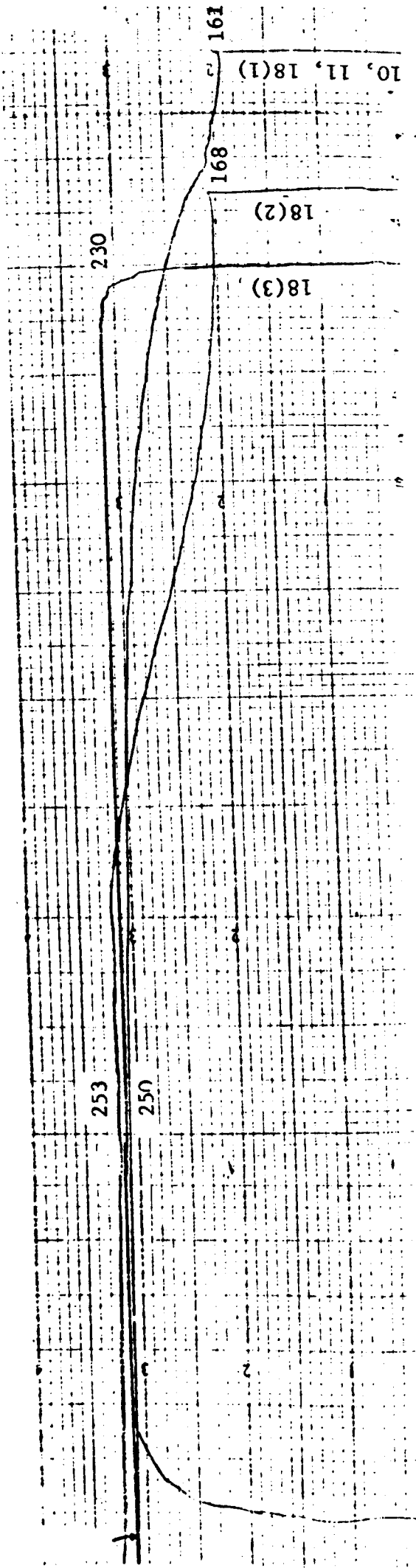


Fig. A3-5 SECTIONS 1, 2, 6, 13, 23, 24 and 27

11 3 32 7 15 7 40 7



30 %

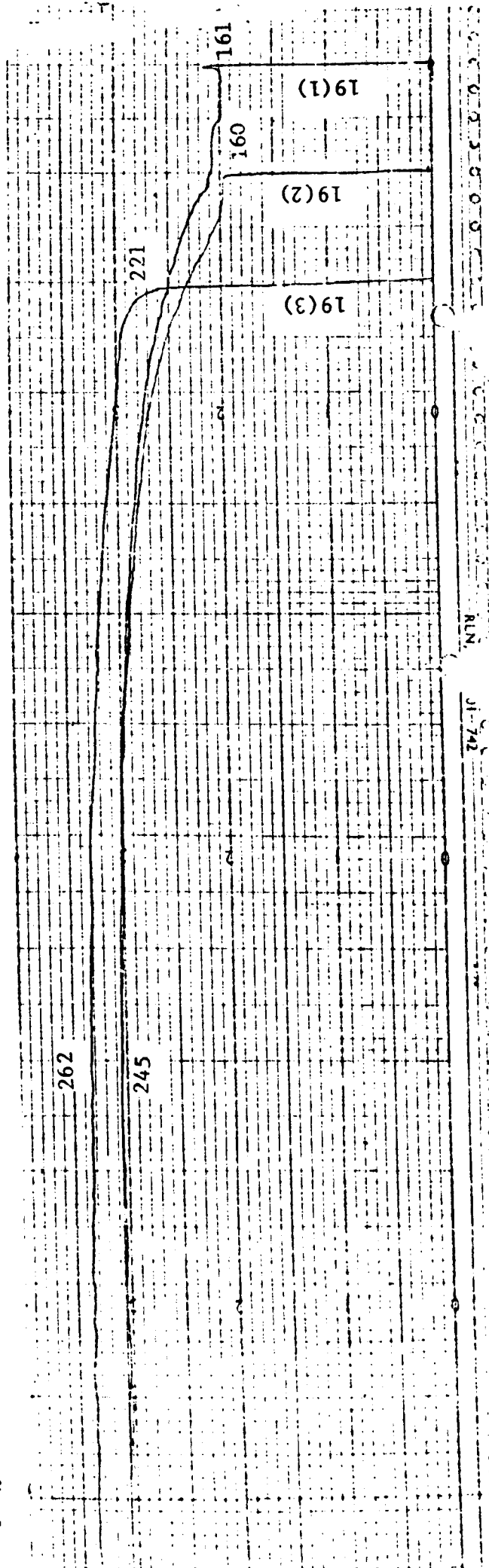


Fig. A3-6 SECTIONS 10, 11, 18(1,2,3) and 19(1,2,3)

APPENDIX 4

Histograms in Fig. 6.43 are obtained using the data from the table below:

Theory Experiment	θ (deg)	0	10	20	30	40
	Percentage	%	%	%	%	%
<0.75	Moment Energy	0 -	0 0	0 0	3.8 0	9.1 0
0.75±0.80	Moment Energy	0 -	0 0	0 0	3.8 0	0 0
0.80±0.85	Moment Energy	0 -	0 0	0 0	0 0	4.5 0
0.85±0.90	Moment Energy	7.4 -	0 0	7.4 3.7	19.2 0	9.1 0
0.90±0.95	Moment Energy	29.6 -	3.7 11.1	22.2 7.4	34.6 11.5	27.3 22.7
0.95±1.00	Moment Energy	44.4 -	18.5 25.9	33.3 14.8	23.1 34.6	22.7 31.8
1.00±1.05	Moment Energy	11.1 -	33.3 18.5	14.8 44.4	0 23.1	13.6 18.2
1.05±1.10	Moment Energy	3.7 -	25.9 29.6	14.8 14.8	0 19.2	0 18.2
1.10±1.15	Moment Energy	3.7 -	7.4 3.7	7.4 7.4	7.7 7.7	4.5 9.1
1.15±1.20	Moment Energy	0 -	7.4 3.7	0 3.7	3.8 0	0 0
1.20±1.25	Moment Energy	0 -	3.7 3.7	0 0	3.8 3.8	0 0
>1.25	Moment Energy	0 -	0 3.7	0 3.7	0 0	9.1 0
0.95±1.05	Moment Energy	55.6 -	51.8 44.4	48.1 59.2	23.1 57.8	36.3 50
0.90±1.10	Moment Energy	88.9 -	81.4 85.1	85.1 81.4	57.8 88.4	63.6 90.9
0.85±1.15	Moment Energy	100 -	88.8 88.8	100 92.5	84.8 96.3	77.2 100
0.80±1.20	Moment Energy	100 -	96.3 92.5	100 96.3	88.5 96.2	81.7 100
0.75±1.25	Moment Energy	100 -	100 96.3	100 96.3	96.2 100	81.7 100